Imperial College London

Melt processing and characterisation of lightweight metal composites reinforced by nanocarbon

MPhil Thesis

Daniel John William Markcoons

Supervisors:

Dr Qianqian Li

Prof Milo S P Shaffer

January 2021

Department of Aeronautics

South Kensington Campus

Imperial College London

London SW7 2AZ

U.K.

Declaration of Originality

I, Daniel Markcoons of Imperial College London, hereby declare that this thesis that I have presented for consideration for my MPhil degree is composed of my own work and all else is appropriately referenced.

Copyright Declaration

Abstract

Increasing the specific strength of lightweight structural metals such as magnesium, which has two-thirds the density of aluminium, has the potential to significantly widen their application and improve the system energy efficiency and performance across transport and defence industries. Reinforcing magnesium matrices with nano-sized particles to form metal matrix nanocomposites (MMNCs) has shown promise as a way of achieving an increase in specific properties, albeit without the traditionally associated decrease in ductility. This study manufactured and characterised magnesium-based MMNCs to investigate the impact of nanoparticle reinforcements on the mechanical properties of the composites, their microstructure and the theoretical models used for the potential strengthening mechanisms. Multi-walled carbon nanotubes (MWCNTs) can be considered as the ideal reinforcing nanoparticle due to their exceptional mechanical properties, geometry and low density, which can take full advantage of the proposed strengthening mechanisms that occur when nanoparticles are added to a metal matrix. MWCNTs are however notoriously difficult to be homogenously dispersed in a metal matrix and are poorly wetted by molten metal; therefore, nickel coated MWCNTs (NiCNTs) and silicon carbide nanoparticles are also investigated as a potential solution for wettability in this study.

Magnesium alloy AZ91D was used as the metal matrix material and the MMNCs were made using metal melt-stirring combined with a nanoparticle pre-dispersion technique. Melt processing and casting techniques are favoured in component manufacturing processes due their scalability and cost-effectiveness.

The melt stirring processing parameters such as casting temperature, stirring time and stirring speed were thoroughly examined and modified to successfully produce MMNC samples. The compression mechanical properties of the AZ91D-MWCNT composites showed no change for a range of MWCNT concentrations for the melt stirring processing parameters tested. Theoretical studies of nanoparticle dispersion and wettability combined with electron microscopy of the cross sections of the samples showed that the pre-dispersion and melt stirring processes were insufficient to homogenously disperse the MWCNTs in the metal matrix, therefore NiCNTs were utilised. Whilst no significant differences in compression mechanical properties were seen for the AZ91D-NiCNT samples, a 13% increase in hardness was achieved. An 11% and 20% increase in hardness was achieved for samples of AZ91D composites reinforced with equal concentration of silicon carbide nanoparticles and whiskers, respectively.

The poor wettability of MWCNTs by AZ91D melt, apparent from SEM imaging of the composite fracture surfaces, suggested that in order to take advantage of the superior mechanical properties of MWCNTs, a coherent interface between the MWCNT and the Mg matrix is necessary. The nickel coating and silicon carbide nanoparticles, known to wet with molten magnesium, may have provided a coherent interface that resulted in the measured increase in hardness.

Contents

List of Figures

List of Tables

1. Introduction

The automotive and aerospace industries have a perpetual need for advanced lightweight materials to enhance vehicle performance and to satisfy future legislation regarding greenhouse gas emissions. The aviation industry is one of the fastest growing sources of greenhouse gas emissions [1] and it is recognised that the uptake of emerging advanced materials is imperative for meeting future emission targets [2]. It has also been calculated that a 100kg weight reduction of an automobile can reduce the CO_2 emissions by around 1600kg over a 10 year lifetime [3], highlighting the importance of lightweight material development.

Metal matrix composites reinforced with microscale particles have been shown to be a competitive alternative to unreinforced metals due to their improved strength, stiffness and hardness. However, these superior properties usually come at the expense of the ductility and machinability of the metal, and so this has limited their widespread use. Recently, research has transitioned from micro to nanoscale reinforcements. The manufacture of metal matrix nanocomposites (MMNCs) has shown the potential of improving metal strength whilst maintaining or even improving the metal's ductility [4, 5]. Whilst the exact mechanisms underpinning the effects that nanoparticle reinforcements have on the metal matrix remain unclear, it is well understood that a homogenous dispersion is critical for the exploitation of the potential improvements in mechanical properties; however, homogenous dispersion is extremely difficult to achieve. Therefore, a host of manufacturing methods have been explored for their sound fabrication, of varying cost effectiveness and scalability.

Since 97% of all metal products have at least one solidification step within their manufacturing process [6], it is apparent that melt processing is a technique favoured by industry. Melt processing, and in particular casting, is an economical and scalable approach to making complicated 3D net shape components that can also lead to the light weighting of designs through part consolidation [7]. Magnesium (Mg) alloys could offer weight savings of 70 and 30% over steel and aluminium (Al) alloys, respectively. They also have favourable casting properties when compared to Al such as a higher fluidity, allowing the casting of intricate and thinner walled components, and a low specific heat per unit volume, which reduces the cast cool down time and therefore die tool wear[8] [9].

The focus of this MPhil project is to further enhance the specific properties of Mg and its alloys by utilising the superior mechanical properties exhibited by nanocarbon species, such as multi-walled carbon nanotubes (MWCNTs) and SiC ceramic nanoparticles. A Mg metal matrix nanocomposite melt-processing fabrication rig will be implemented and optimised in order to produce the Mg based composites. In addition, the mechanisms that lead to the change in mechanical properties, nanoparticle – metal matrix interfacial interactions and nanoparticle geometry effects will be explored.

1.1 Objectives

The objectives addressed in this thesis are:

- To fabricate and characterise Mg/AZ91D – MWCNT composites using a melt stirring technique, investigating the influence of casting temperature, stirring time and reinforcing particle volume fraction.
- To fabricate and characterise both Mg/AZ91D – Nickel coated MWCNT and AZ91D – SiC composites using a melt stirring technique, investigating the influence of the nanoparticle material on its wettability with molten Mg/AZ91D, subsequent level of dispersion and interfacial reaction mechanics.
- To use models given in the literature for the prediction of the increase in yield strength in a MMNC for a given volume fraction of nanomaterial to investigate the influence of nanoparticle geometry on MMNC yield strength.

2 Literature Review

The following review of literature begins with an introduction of the materials that are at the centre of this project, followed by an overview of the strengthening mechanisms anticipated on adding nanoparticles to a metal matrix and the models currently used to predict material properties for the given nanoparticle geometries and loadings. Furthermore, a discussion of the challenges behind the production of MMNCs for melt processing and the manufacturing methods currently used throughout literature that try to achieve homogenous nanoparticle dispersion, in order to take full advantage of the proposed strengthening mechanisms. A deeper review that was undertaken of some selected studies showing the potential of MMNCs and other key aspects that relate to this project will also be included. This chapter concludes with a summary of the gaps in the research that motivate this project.

2.1 Nanocomposite materials

2.1.1 Mg and its alloys

Magnesium is the lightest of all structural metals with a density of 1.74g/cm^3 in its pure form and ranging from 1.5 g/cm^3 to 1.8 g/cm^3 in Mg lithium and Mg – rare earth (RE) alloys, respectively [10]. The hexagonal lattice structure [11] of Mg dominates its physical metallurgy and restricts its initial deformation to slip in the $< 11\bar{2}0 >$ directions on the basal planes with pyramidal slip planes $\{10\bar{1}1\}$ only becoming active above approximately 498K [12]. Mg therefore fails to satisfy the Taylor criterion [13] of a minimum of five independent slip planes required for homogenous ductility of a polycrystal. Mg and its alloys are therefore, like body centre cubic metals, brittle and have poor cold workability, in comparison to face centre cubic metals that have a large number of available slip systems at room temperature. Figure 1 shows the directions of the principal planes in a Mg unit cell. Mg's atomic diameter allows it to be alloyed with a range of solute elements such as Al and Zn, the two main constituents of Mg alloy AZ91.

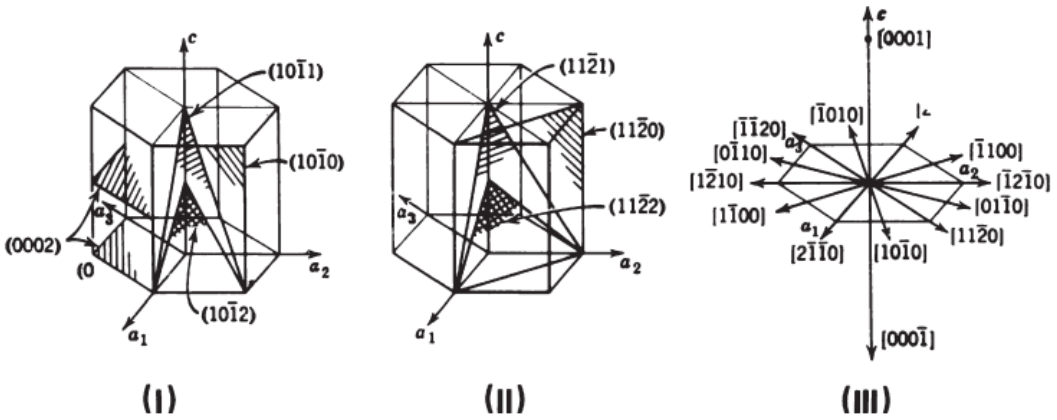

Figure 1 - Mg unit cell, principal planes and directions [7].

Mg alloys exhibit desirable properties such as high specific strength, fluidity for casting, recyclability and damping capacity[14], however they are also known for their poor high temperature strength and low creep resistance. The general temperature limit for satisfactory strength for Al-free Mg alloys is around 250°C[15] and 130°C for AZ91 acceptable creep resistance [16, 17], which limits their use to mostly room temperature applications. Several attempts

have been made to improve these properties by utilising different alloying elements such as calcium (Ca) and silicon (Si), however these methods reduce the castability with regards to hot cracking and tool sticking [18].

The majority of Mg alloy components in use today are manufactured via the high pressure die casting (HPDC) route [19], with capabilities of injecting a 10kg molten shot into a die in less than 100ms at up to 1500bar [8]. Although Mg and Al have very similar melting points of 650°C and 660°C, respectively, the casting of Mg alloys enjoys several advantages over the casting of similar Al components. Mg's higher fluidity allows the casting of more intricate components with walls as thin as 1-1.5mm instead of Al's 2-2.5mm [7]. Mg also has a latent heat of fusion per unit volume of approximately 2/3 that of Al's, resulting in faster cooling and therefore faster production rates and reduced tool wear, thus improving the cost effectiveness of the process.

2.1.2 Multi-walled carbon nanotube

MWCNTs were the first carbon nanomaterials to be synthesised [20]. Before Iijima's reclassification in 1991[21], MWCNTs were referred to as graphitic whiskers or fibrils, with the recognition of carbon nanomaterials as a new form of carbon materials triggered by the discovery of buckminsterfullerene in 1985 [22].

Carbon nanotubes (CNTs) have inspired the emergence of a wide range of research areas to identify and explore potential applications of their superior mechanical, electrical and thermal properties [23]. MWCNTs have been shown to exhibit tensile strengths and Young's modulus of up to 63GPa and 950GPa [24], respectively. However, these values can vary greatly from tube to tube due to the defects in the crystalline structure of the outermost layer. The high stiffness and strength of CNTs can be attributed to the sp^2 carbon-carbon bonds that exist in graphite's basal plane. The sp^2 bond is considered to be one of the strongest in solid materials. A CNT takes full advantage of the sp^2 bond strength as its structure is a rolled sheet of graphene with ends capped with fullerene-like structures, therefore, the basal plane is placed parallel to the tube axis [25]. In addition to the excellent mechanical properties, MWCNTs exhibit a high aspect ratio (~10^4) [26] and a large surface area (~250m^2/g) which could provide the opportunity for strong interfacial reactions with the metal matrix, especially when employing surface treated MWCNTs, thereby allowing for more effective load transfer to their exceptionally strong structure. The low density of CNTs (~1.7kgm^{-3}) [27] combined with their geometric and mechanical properties makes them ideal potential MMNC reinforcements.

2.1.3 SiC nanoparticles and whiskers

SiC nanoparticles and whiskers can be synthesised by a wide range of methods that can yield particles of varying size (<8nm-100nm [28, 29]), size distribution, atomic structure (α – SiC, β – SiC) and purity [30]. Commercially provided SiC nanoparticles and whiskers are mostly made by proprietary manufacturing methods [29, 31].

In addition to its favourable mechanical properties, density and cost, SiC is well wetted by Mg [5] and therefore can be used as an analogous system for a proof of concept for MMNCs reinforced by nanocarbon.

Whilst there have been numerous studies into melt-processed Mg based MMNCs reinforced with SiC nanoparticles [5, 32], studies into SiC whisker reinforced magnesium composites have been largely performed using a squeeze casting (pressure infiltration) technique [33, 34]. Squeeze casting can produce mechanically sound castings, however unlike stir casting, it is restricted in terms of cast shape, dimensions and suitability for mass production [35]. An investigation into the as cast properties of a melt stirred AZ91-SiC whisker composite has not been previously explored in the literature.

2.2 Strengthening mechanisms and models

The motivation for incorporating nanoparticles into a metal matrix stems from several proposed strengthening mechanisms that their presence induces. Models for each mechanism, which will be presented below, have been suggested to predict the magnitude of each mechanism's contribution to any increase in mechanical properties. The reviewed mechanisms include Orowan strengthening, load transfer, thermal mismatch strengthening and grain boundary refinement. This section will then finally discuss proposed models to predict how the different mechanistic contributions can be summed together and predict the overall strength of a given MMNC.

2.2.1 Orowan Strengthening

As nanoparticles are added to a metal matrix, they act as obstacles that will intersect slip planes in a random manner. Therefore, when there is an interparticle distance of approximately 1µm or less, a gliding dislocation must either cut through the nanoparticle, move to a prismatic plane of direction or bow between multiple obstacles to be able to further traverse through the matrix. Ceramic nanoparticles such as SiC and Al_2O_3, similar to MWCNTs, are incoherent with the metal matrix and therefore the bowing or looping mechanism is favoured [36]. The looping mechanism forces the gliding dislocation to take a higher energy path that therefore requires a higher applied stress to enable dislocation motion, thereby increasing the yield strength of the matrix and creates a new dislocation loop around the nanoparticle. Succeeding dislocation loops are generated around the nanoparticle inclusions that in turn compounds the strengthening by generating a higher back stress, which further inhibits dislocation motion. The increase in yield strength due to Orowan looping for a Mg-MWCNT nanocomposite was modelled by [37]:

$$\Delta\sigma_{y(O)} = \frac{0.8\, G_m b M}{L_p} \tag{1}$$

Where $\Delta\sigma_{y(O)}$ is the increase in yield strength due to Orowan looping, G_m is the shear modulus of the matrix, b is the Burgers vector, M is the Taylor factor (assumed to be 3)[38, 39] and L_p is the inter-particle distance. High aspect ratio nanoparticle inclusions such as MWCNTs are considered as rod like particles for which Kelly [40] defines rod interparticle spacing by:

$$L_{p-rod} = \sqrt{\frac{\pi d^2}{2 v_{re}}} \tag{2}$$

Where d is the rod diameter and v_{re} is the volume fraction of the reinforcement. From Equation 1&2, one can determine that the increase in yield strength due to Orowan looping increases with decreasing interparticle distance. Therefore, for MWCNT MMNCs, the effectiveness of the Orowan looping mechanism is diminished as the interparticle distance is increased if the MWCNTs are in large agglomerates for a given concentration in a matrix, compared to a matrix with individually dispersed MWCNTs, highlighting the criticality of a good particle dispersion.

Chen *et al* [41] produced a set of Al-MWCNT composites with each composite made with a different average MWCNT aspect ratio, from ~5 – 55, exploring the effect of particle aspect ratio on the strength contribution from the different strengthening mechanisms. The study showed that above an aspect ratio of around 10, the strength contribution to the composite from Orowan strengthening decreases until becoming negligible at aspect ratio > 40 , shown in Figure 2a. The Orowan strengthening was modelled using the Orowan-Ashby equation 3 [4, 42] that considers the aspect ratio of the reinforcing particle.

$$\Delta\sigma_{y(O)} = \frac{G_m b M}{2.36\pi} \ln\left(\frac{\varphi}{2b}\right)\left(\frac{1}{L_p - \varphi}\right) \tag{3}$$

Where

$$L_p = d\sqrt[3]{\frac{6\pi}{v_{re}}} \tag{4}$$

Where φ is the effective particle diameter, defined for MWCNTs as

$$\varphi = d\sqrt[3]{\frac{3h}{2d}} \tag{5}$$

Where h is the MWCNT length.

This breakdown in Orowan strengthening is credited to the lengths of the CNTs being above a 'critical' length that inhibits Orowan looping, forming pinned dislocations instead or successive Orowan loops that, whilst still leading to an increase in strength, could lead to decreased work hardenability and ductility, schematically shown in Figure 2b. However, the mechanism of forming a sunk dislocation due to the length of the MWCNT, that hasn't been reported elsewhere, seems like a very 2D, and most likely rare, case as a traversing dislocation would most likely 'see' a MWCNT as a point and still form a Orowan loop and prevent dislocation climb unless it is in a slip plane that is parallel with the MWCNT. Whilst the different grain sizes of the composite were considered in calculating the strength contribution from the Orowan looping and load transfer mechanisms, there could be an undiscussed interaction for the low aspect ratio MWCNT composites as the MWCNT length is similar to the grain size of the matrix. The MWCNT dispersion quality may also be significantly poorer for the shorter ball milling times used to create the relatively higher aspect ratio MWCNT composites. Nevertheless, this would suggest that moving towards spherically-shaped reinforcements provides superior strengthening than rod shaped reinforcements, especially as rod shaped particles would provide a larger L_p than spherical particles at a given concentration. Contrastingly, Kelly [40] carried out an analytical study to show that rod shape reinforcements of an equivalent volume to spherical reinforcements, offer approximately 1.75 times more the magnitude of strengthening due to an enhanced rod shape/slip plane interaction. The apparent conflict between these models provide the opportunity for further studies to be carried out to investigate the geometrical effect of the nanoparticle reinforcements to potentially establish the limits and validity of the current Orowan strengthening models whilst finding nanoparticle geometries that optimise Orowan strengthening.

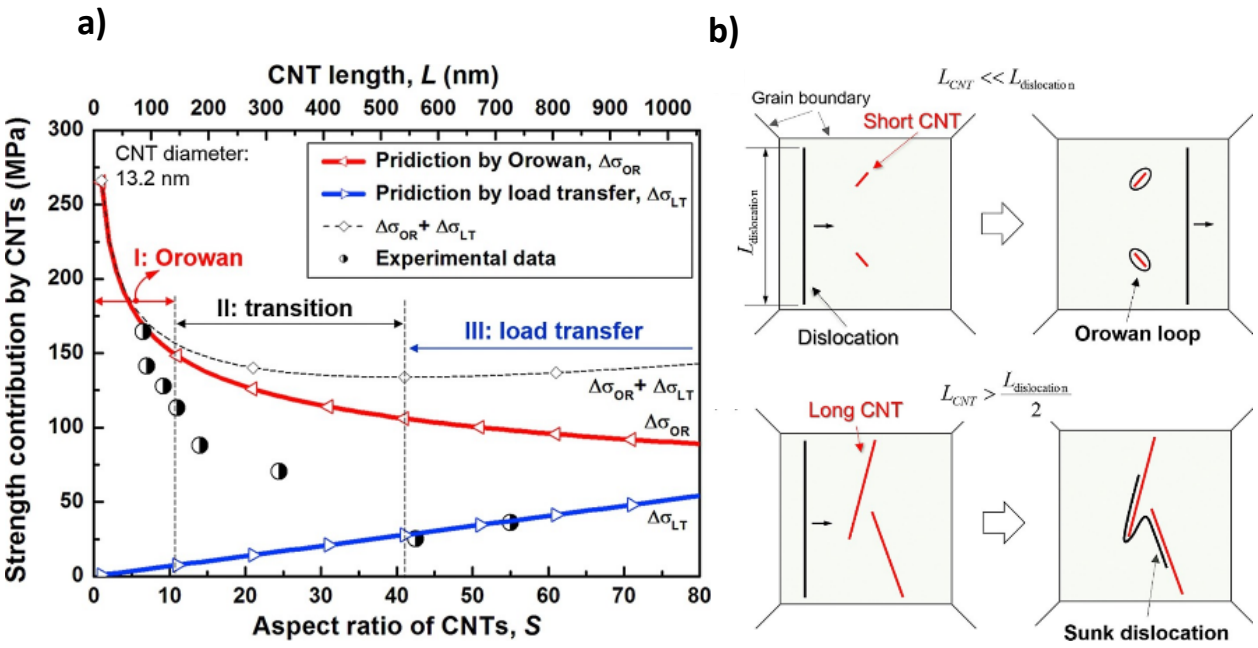

Figure 2. a) Plot to show how the strength contribution of MWCNT additions vary with aspect ratio. b) Schematic representation of how a dislocation interacts with MWCNTs with low aspect ratio and high aspect ratio [41]

2.2.2 Load Transfer

Load transfer occurs by the transfer of stress through interfacial shear from the relatively softer metal matrix to the stronger reinforcements. In its simplest form, the increase in yield strength due to fibre reinforcement is given by Li *et al* [38] that assumes the reinforcing fibres are uniaxial to the load direction as:

$$\Delta\sigma_{y(LT)} = \sigma_{re} v_{re} \tag{6}$$

Where $\Delta\sigma_{y(LT)}$ is the increase in yield strength due to load transfer, σ_{re} is the yield strength of the reinforcing material and v_{re} is the volume fraction of the reinforcing materials. However, this model assumes an ideal load transfer efficiency through an interface. The contact angle between Mg and the basal plane of graphite was determined to be 120^{o}, indicating that Mg does not in fact wet CNTs and therefore a poor interface is likely formed[43]. The surface tension of liquid Mg ≈575$\frac{mN}{m^2}$ [44], also exceeds the surface tension upper limit of 200$\frac{mN}{m^2}$ determined by Dujardin *et al* [45] to successfully wet CNTs. This would suggest that an ideal interface is not in fact formed by adding CNTs in Mg matrices, and substantially limit the magnitude of the transferable load.

The shear lag model, which was originally developed by Cox [46] for describing fibrous paper, has also been applied to MWCNT-MMNCs. Generally, throughout literature a model given by Kelly and Tyson based on the shear lag model [47] is used to calculate the load transferred to the short fibre reinforcement form the matrix.

$$\sigma_{c(KT)} = \sigma_{re} v_{re} \left(1 - \frac{l_c}{2l}\right) + \sigma_m v_m \qquad for\ l \geq l_c \tag{7}$$

$$\sigma_{c(KT)} = v_{re} \left(\frac{\tau l}{d}\right) + \sigma_m v_m \qquad for\ l < l_c \tag{8}$$

Where

$$l_c = \frac{\sigma_{re} d}{2\tau} \tag{9}$$

Where $\sigma_{c(KT)}$ is the composite yield strength, σ_m is the yield strength of the metal matrix, l_c is the critical length, l is the length of the nanoparticle reinforcement, d is the reinforcement diameter, and τ is the ultimate shear strength of the matrix. The critical length for fibre reinforcements is the minimum length at which the magnitude of the load transferred to the fibre can exceed its ultimate strength and can therefore be fully utilised as a reinforcement. The transferred load induces a stress on the fibre that varies along its length, with the maximum stress occurring towards the centre of the fibre and results in the formation to two shorter fibres if the ultimate strength of the fibre is exceeded. The Kelly and Tyson model assumes that every nanoparticle is load bearing, i.e well dispersed with a strong interfacial bond and are aligned with the loading direction.

Although secondary processes that induce alignment on high aspect ratio nanoparticle reinforcements are regularly used in MMNC production, such as extrusion, a variation of the shear lag model was suggested by Ryu *et al* [48] to account for the disorientation of the nanoparticle reinforcements with the loading direction:

$$\sigma_{y(LT)} = \sigma_m \left(v_{re} \left[\frac{S_{eff} + 2}{2} \right] + v_m \right) \tag{10}$$

Where v_m is the volume fraction of the metal matrix and S_{eff} is the effective aspect ratio of the nanoparticle reinforcement defined as:

$$S_{eff} = S \cos^2 \theta + \left(\frac{3\pi - 4}{3\pi} \right) \left(1 + \frac{1}{S} \right) \sin^2 \theta \tag{11}$$

Where S is the aspect ratio of the nanoparticle defined as $S = \frac{nanoparticle\ length}{nanoparticle\ width}$ and θ is the angle of misorientation of the nanoparticle with the loading direction. It can be seen from Equation 11, that when the nanoparticles are all perfectly aligned with the loading direction, and $\theta = 0, S_{eff} = S$. To determine the disorientation of the nanoparticles in the metal matrix, Park *et al* [49] assumed perfect aligned after their extrusion process of an extrusion ratio of ~37, however, Chen *et al* [41] used transmission electron microscopy (TEM) imaging to find that a misorientation of approximately 30^o was found for their extrusion process, albeit for a comparatively low extrusion ratio of ~3. 30^o was determined by performing TEM image analysis on an unmentioned sample size by comparing the orientation of an imaged MWCNT to the extrusion direction. This indicates that to use this model, it is important to take a measurement to more accurately estimate the misorientation angle to enhance or better judge the accuracy of the model. Again, Equation 11 assumes a perfect interfacial bond between the matrix and the reinforcing nanoparticle.

In order to more accurately predict the achievable load transfer in a metal – MWCNT system, where an idealistic interface may not be formed, the interfacial shear strength (IFSS) between the MWCNT and metal matrix could be directly measured. Zhou et al [50] were the first to attempt this measurement by using Al – MWCNT composites that were fabricated by high energy ball mixing (HEBM) ultrasonically dispersed, acid purified MWCNTs with Al powder. The powder was then consolidated by spark plasma sintering and subsequently hot extruded at 550°C [51] [52]. The resulting composite was shown to contain individualised and aligned MWCNTs with a good Al – MWCNT interface. A fracture surface of the composite was generated from a tension test that exposed pulled-out MWCNTs that were then clamped to an AFM tip using electron-beam-induced deposition (EBID), as shown in Figure 3. The MWCNTs were then pulled out of the matrix, and by adapting Equation 9 to replace l_c with the measured effective MWCNT embedded length and σ_{re} with the force required to pull-out the MWCNT divided by its area to calculate the IFSS. The IFSS between the Al matrix and MWCNT was calculated to be 24.8 ± 3.2 MPa that translated to a 60% load transfer efficiency. The UTS of composites made with 0.2 – 3vol.% MWCNT reinforcements were found to be in good agreement with the shear lag theory when the measured IFSS was used instead of assuming a perfect interface. A similar study by Yi et al [53] later determined the Al – MWCNT IFSS to be 28.7MPa that appeared to be in reasonable agreement with Zhou et al. However, both studies fail to determine the contribution of the radial compressive stresses to the IFSS that are induced due to the difference in coefficients of thermal expansion between the metal matrix and

MWCNT. The IFSS is a critical parameter in being able to confidently model and aid the design of future composites and has so far only being quantitatively measured in Al-MWCNT systems, thus presenting compelling opportunities to study similar Mg and other metal composites reinforced with MWCNTs and coated MWCNTs as an extension.

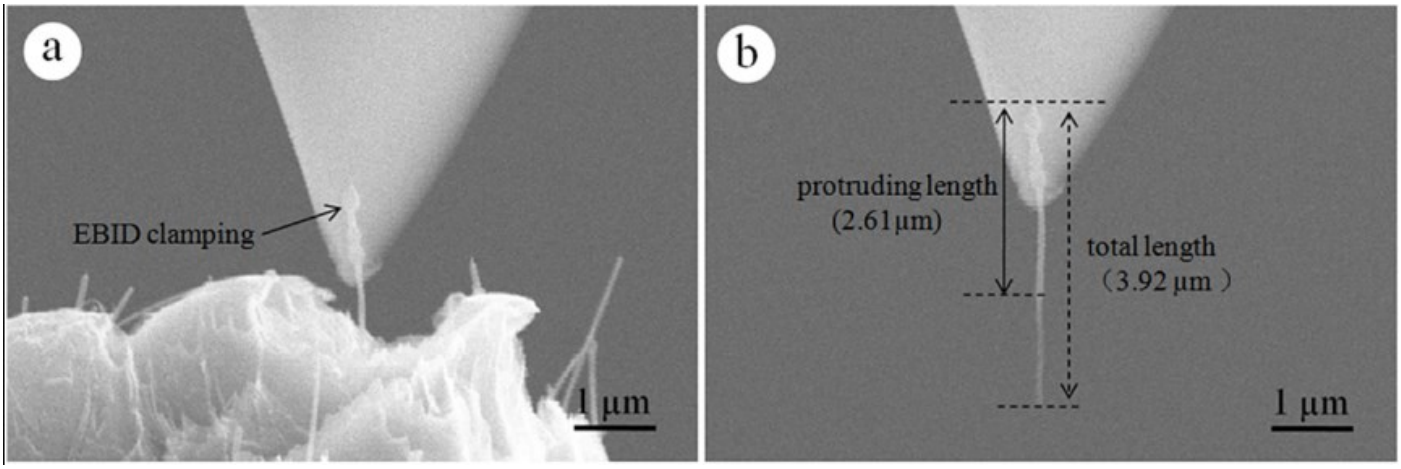

Figure 3. a) SEM imaging of pulled out MWCNTs exposed after a tension test of an Al – MWCNT composite attached to an AFM tip by EBID. b) MWCNT attached to an AFM tip after being pulled out from the Al matrix [50].

2.2.3 Thermal mismatch

Thermal mismatch strengthening occurs due to the increase in prismatically punched geometrically necessary dislocations (GNDs) at the nanoparticle-metal interface that accommodate the strain gradients generated by the difference in coefficient of thermal expansion between the reinforcing particle and the metal matrix, as the composite is cooled from its processing temperature. A model that is regularly used [49, 54, 55] to calculate the strengthening contribution due to thermal mismatch was first described by Hansen [56]:

$$\Delta\sigma_{y(T.M)} = \alpha G_m b\sqrt{\rho} \tag{12}$$

Where α is a geometric constant ≈1.25 (given for Al by [56] but also used for Mg [38]). ρ is the increase in dislocation density assumed to be due to residual plastic strain generated by the difference in the coefficients of thermal expansion between the matrix and reinforcing particle. ρ is given by [57, 58] as:

$$\rho = \frac{Bv_{re}\Delta CTE\Delta T}{bd(1-v_{re})} \tag{13}$$

Where B is a geometric constant ([57]), ΔCTE is the difference in coefficient of thermal expansion between the reinforcing phase and matrix, ΔT is the difference in process and testing temperature and *d* represents the smallest dimension of the reinforcing phase.

This model, however, was developed by Arsenault *et al* [57] for (5-7µm x 2-3µm diameter x thickness) micro-scale SiC platelets as opposed to 1D CNTs, with the assumptions that the SiC platelets demonstrate equally isotropic behaviour and parallelepiped geometry, qualities not exhibited by MWCNTs in metal composites. The SiC platelet dimensions far exceed, by approximately three orders of magnitude, that of the nanoscale reinforcements that will be the subject of this study in two dimensions, i.e NC7000 MWCNT (9.5nm x1.5µm diameter x length) supplied by Nanocyl, meaning that it is possible that this model is inapplicable to nanoparticle/matrix regime. Chen *et al*[5], found that upon TEM analysis, there was no significant local increase in dislocation density around SiC nanoparticles in a Mg matrix, suggesting that the particles used were too small (60nm diameter) to generate enough strain to form GNDs. The dislocations in this particular study, however, could have been annealed away during slow cooling. It has also been shown numerically and experimentally [59, 60] that thermal mismatch strengthening only occurs in typically coarse-grained metal composites (grain size ≳250nm) as the GNDs can be distributed throughout the matrix as opposed to nanostructured interfacial boundaries that inhibit strain hardening [61]. Although this mechanism appears to be critical in understanding and modelling MMNCs, it is rarely discussed in detail with even some CNT-MMNC review literature failing to mention it [62, 63].

2.2.4 Grain Refinement

Metal grain refinement has been long regarded as an effective way of improving the strength of alloys, without reduction of the elongation to failure, described by the Hall-Petch equation [64]:

$$\sigma_{y(HP)} = \sigma_o + kd^{-\frac{1}{2}} \tag{14}$$

Where $\sigma_{y(HP)}$ is the yield strength of the metal matrix related to the corresponding grain size, σ_o is the frictional stress of the matrix or the strength of a single crystal, k is the strengthening coefficient and a material constant and d is the grain size.

Grain refinement in Mg alloys is a very efficient way of improving their mechanical properties due to its high strengthening coefficient, exceeding that of Al by approximately a factor of two [65, 66]. Grain boundaries are areas that separate crystals that have different crystallographic orientations in polycrystalline materials. For a dislocation to traverse a grain boundary, it would have to change direction, a process that requires more energy than if it was to stay on its current trajectory. The amount of energy required for a change of direction increases with increased crystal misorientation, thus inhibiting dislocation motion. Decreasing the grain size, and therefore increasing the total grain boundary area to impede dislocation motion, improves the mechanical properties of the metal. It is important to note, however, that a recent study [67] has shown that the Hall-Petch strengthening relationship may start to break down at grain sizes less than 100nm due to grain boundary rotation, a grain size regime regularly reached when using severe plastic deformation (SPD) processing techniques such as high pressure torsion and equal-channel angular pressing.

The addition of nanoparticles to molten metals could act to refine grains upon solidification through nucleation and/or the Zener pinning effect. Kim and Cantor [68, 69] developed an adsorption model for nucleation around inoculants whereby an initial layer of atoms can absorb onto an inoculant surface with no undercooling, providing the embryo for a crystal from which to grow. This model was termed as the free growth model by Quested and Greer [70] who then went on to determine the undercooling necessary for grain growth from the embryo as:

$$\Delta T = \frac{4\sigma_{p-liquid}}{\Delta S_v d} \tag{15}$$

Where $\sigma_{p-liquid}$ is the nanoparticle-liquid interface energy, ΔS_v is the entropy of fusion per unit volume and d is the diameter of the adsorbed layer of atoms (usually taken as the particle diameter). This relationship was originally derived for a Al – TiB_2 microparticle system; however, Cicco *et al* [71] showed a remarkable agreement between the free growth model and experiment results obtained for Al – SiC/TiC/Al_2O_3 nanoparticle systems with diameters for each nanoparticle material ranging from 10 – 100nm. It was also highlighted that a nanoparticle having a small lattice disregistry with the matrix would increase its nucleation catalyst potency. Günther *et al* [72] also examined a AZ31-SiCp system and developed a successful model for predicting the fine grain size of a gravity cast composite, based on the free growth model.

The Zener pinning effect is the impedance of grain growth by their interaction with dispersed second phase particles upon solidification. Uniform and monosized particles impart a drag force defined by [73]:

$$F_D = \frac{aV_f}{d} \tag{16}$$

Where a is constant ≈1, d is the particle diameter and V_f is the particle volume fraction. It can be seen from Equation 16, for the same volume fraction of particles of 10µm and 100nm, that the drag force exerted by the nanoparticles would be 100 times greater than that of the micro sized particles. In order to stabilise a grain size of diameter D, a maximum particle diameter for a given volume fraction can be calculated by [74]:

$$d = \frac{3}{4}DV_f \tag{17}$$

Mokhtari *et al* [75] found that gold coated silica nanoparticles of 100nm diameter significantly reduced the grain boundary movement and dynamic grain growth during hot compression tests up to a homologous temperature of approximately 0.5. Figure 4 shows a schematic given to explain the improvement assuming effectual pinning. However, limited work has investigated how the pinning effect changes with different aspect ratio particles such as plates or rods, as in the case of graphene or MWCNTs. Han *et al* [76] found that the grain size of AZ31-MWCNT composites were reduced compared to monolithic AZ31 after casting and extrusion processes, which was attributed to the MWCNTs in the melt acting as heterogeneous nucleus substrates, stimulating the nucleation process (Figure 5). Morisade *et al* [77] also found reduced dynamic recrystallisation during friction stir processing of an AZ31-MWCNT composite and attributed it to the pinning effect of the MWCNTs. These studies suggest that nanoparticle additions can act as grain refiners by catalysing the grain nucleation and growth and thus improving the mechanical properties of the composite. Additionally, the reduced dynamic recrystallisation could further enhance the composites mechanical properties after forming processes such as rolling or extrusion when compared to the monolithic unreinforced matrix.

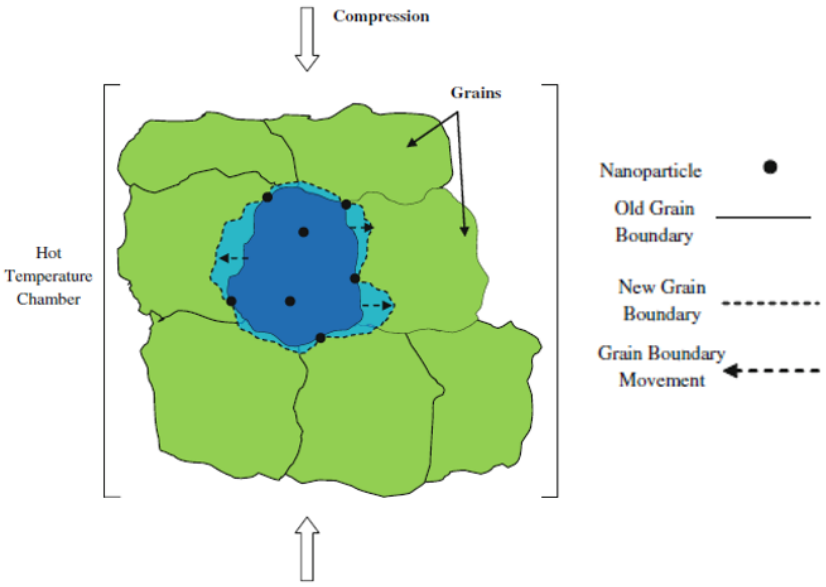

Figure 4 – Schematic representation of the grain pinning effect imparted by nanoparticle reinforcements during hot compression [75].

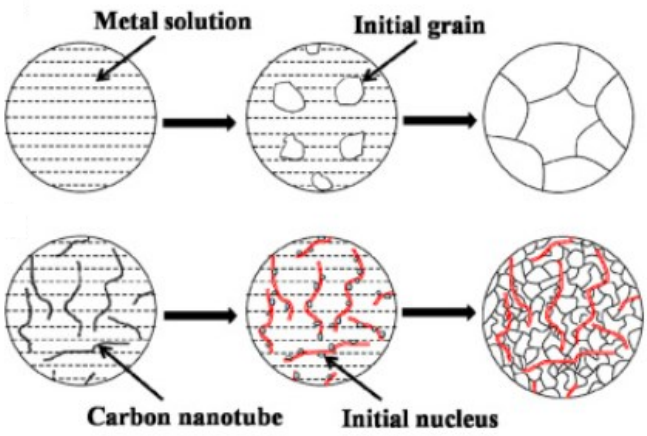

Figure 5 – Schematic representation of MWCNTs acting as heterogeneous nucleation sites in molten AZ31, stimulating the nucleation process and thereby decreasing the grain size of the solidified ingot compared to monolithic AZ31 [76].

2.2.5 Summation models

In addition to the models that have been developed for calculating the change in yield stress for each of the proposed strengthening mechanisms, different summation models that include each mechanism have also been considered. The most simple method is a linear summation of each of the strengthening effects assuming that each of the mechanisms are independent of one another, given by [38]:

$$\sigma_{c(l)} = \sigma_m + +\Delta\sigma_{y(LT)} + \Delta\sigma_{y(O)} + \Delta\sigma_{y(T.M)} \quad (18)$$

Where $\sigma_{c(l)}$ is the yield strength of the composite predicted by the linear summation model.

The Modified Clyne method developed by Sanaty-Zadeh [78], built upon what Clyne [79] had originally proposed, that similar strengthening mechanisms that act unevenly throughout the matrix are combined most suitably as the root of the sum of the squares to give the predicted composite yield strength. Clyne's model was first applied to microscale composites and to only similar strengthening mechanisms, whereas the Modified Clyne method assumes that all strengthening mechanisms are dependant and therefore defined as:

$$\sigma_{c(MC)} = \sigma_m + \sqrt{\Delta\sigma_{y(T.M)}{}^2 + \Delta\sigma_{y(LT)}{}^2 + \Delta\sigma_{y(O)}{}^2} \quad (19)$$

Where $\sigma_{c(MC)}$ is the yield strength of the composite predicted by the Modified Clyne Method. This method was shown to fit well with a sample of experimental results given for a Mg-Y_2O_3 nanoparticle composite, shown in Figure 6, albeit the sample size was small [80].

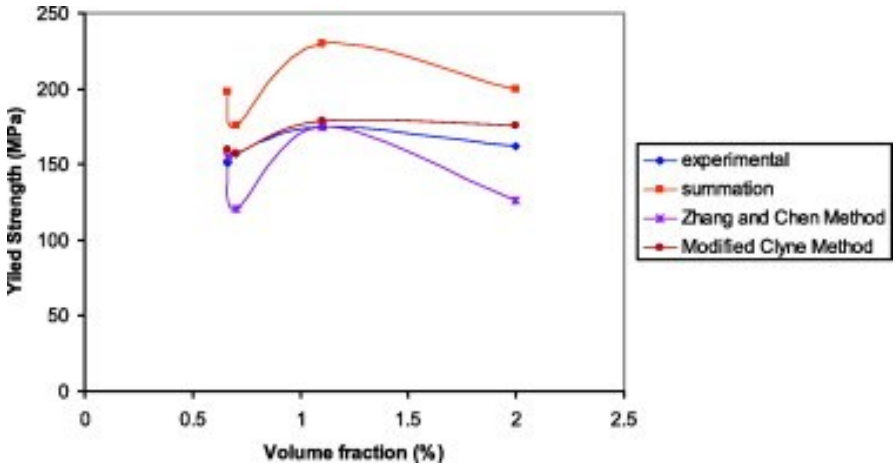

Figure 6. Experimental values vs theoretical values calculated using the Modified Clyne Method for Mg-Y_2O_3 nanocomposites.

Zhang *et al* [55] developed a model building on what was originally developed for microscale composites by Ramakrishnan [81] who in turn had built upon Nardone's modified shear lag theory [82, 83]. Ramakrishnan's model for the composite yield strength is given as:

$$\sigma_{C(R)} = \sigma_m(1 + f_l)(1 + f_d) \tag{20}$$

Where $\sigma_{c(R)}$ is the predicted yield strength of the composite calculated by Ramakrishnan's model and f_l and f_d are the improvement factors due to the load bearing and the enhanced dislocation density strengthening, respectively, defined as [82]:

$$f_l = \frac{v_{re}}{2}(S - 2) \quad or \;\; 0.5v_{re}\, for\, equiaxed\, particles \tag{21}$$

$$f_d = \frac{kG_m b\rho^{0.5}}{\sigma_m} \tag{22}$$

Zhang *et al* [55] further incorporated Orowan looping into Ramakrishnan's model to account for the additional strengthening mechanism that occurs in particle nanocomposites when compared to micro-composites to give:

$$\sigma_{C(Z)} = \sigma_m(1 + f_l)(1 + f_d)(1 + f_{Orowan}) \tag{23}$$

Where f_{Orowan} is the improvement factor due to Orowan looping given by:

$$f_{Orowan} = \left(\frac{0.13G_m b}{L_p}\ln\frac{d}{2b}\right)\frac{1}{\sigma_m}$$

Equation 23 can be simplified to:

$$\sigma_{C(Z)} = (1 + 0.5v_{re})\left(\sigma_m + A + B + \frac{AB}{\sigma_m}\right) \tag{24}$$

Where

$$A = 1.25G_m b\sqrt{\frac{Bv_{re}\Delta CTE\Delta T}{bd(1 - v_{re})}} \tag{25}$$

$$B = \frac{MG_m b}{L_p}\ln\left(\frac{d}{2b}\right) \tag{26}$$

$$L_p = d\left(\left(\frac{1}{v_{re}}\right)^{\frac{1}{3}} - 1\right) for\, equiaxed\, particles \tag{27}$$

Zhang *et al*'s model [55] was compared to a small set of yield strength results for a Mg-Al_2O_3 nanoparticle composite, showing good agreement, and importantly, better agreement than Ramakrishnan's original model as shown in Figure 7, suggesting that it is important to consider the strengthening effects of Orowan looping for nanocomposites.

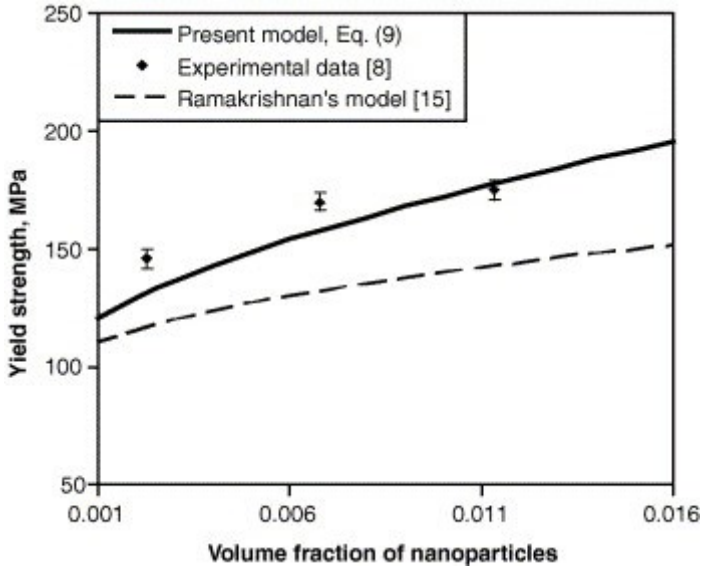

Figure 7. A plot that compares experimental yield strength values for a Mg-Al_2O_3 nanocomposite with Zhang et al's, presented as the 'Present model' here, and Ramakrishnan's predicative model.

Mirza *et al* [84], using Li *et al*'s [85] adaption of Equation 14 that considers the dynamics of interacting dislocations and Equation 17, obtained a modified Hall-Petch relationship with a consideration for the Zener pinning effect:

$$\sigma_{y(HP-Z)} = KG_m\sqrt{\frac{3bV_f}{4d}} \tag{28}$$

Where $\sigma_{y(HP-Z)}$ is the yield strength due to grain size considering the Zener pinning effect and K is a constant. Mirza *et al* [84] aimed to account for the Zenner pinning effect and the composite porosity, a symptom of both casting and powder metallurgy manufacturing techniques. Mirza el al adapted Zhang *et al*'s [55] model (Equation 23 & 24) to further include porosity [86] and Hall-Petch effects:

$$\sigma_{C(M)} = \sigma_m(1+f_l)(1+f_d)(1+f_{Orowan})(1+f_{Hall-Petch-Zener})\left(1-f_{Porosity}\right) \tag{29}$$

Where

$$f_{Hall-Petch-Zener} = \left(KG_m\sqrt{\frac{3bV_f}{4d}}\right)\left(\frac{1}{\sigma_m}\right) \tag{30}$$

$$f_{Porosity} = 1 - e^{-nP} \tag{31}$$

$$n = \frac{0.405l}{d} + \frac{0.318d}{l} + 1.22 \tag{32}$$

Equation 29 can be then simplified to give:

$$\sigma_{C(M)} = (1 + 0.5v_{re} - P)\left(\sigma_m + A + B + \frac{AB}{\sigma_m}\right)\left(1 + \frac{C}{\sigma_m}\right)e^{-nP} \tag{33}$$

$$C = KG_m\sqrt{\frac{3bV_f}{4d}} \tag{34}$$

Where $\sigma_{C(M)}$ is the yield strength of the composite predicted by Mirza *et al*'s model, $f_{Hall-Petch-Zener}$ is the improvement factor due to Hall-Petch strengthening with Zenner pinning considered, $f_{Porosity}$ is the deterioration factor due to porosity, P is the volume fraction of porosity and n is an empirical constant assuming the pore is cylindrical in shape, orientated between 45^o and 90^o to the loading axis.

Figure 8 shows Ramkrishnans's and Zhang *et al*'s model compared to Mirza *et al*'s model which is named as the 'Present model' at different porosity levels, plotted against Mg-MWCNT composites manufactured and investigated by Goh *et al* [87-89]. Mirza *et al* claim their model represents the data well, which is interesting as the improvement factor due to load transfer is developed from Nardone's [82] expression for equiaxed particles instead of fibres. The interparticle distance is also calculated for point like particles instead of rods, where rods would most appropriately model MWCNTs. This could suggest that the particle geometry has little impact on the final mechanical properties of the composite as the model should most accurately represent equiaxed particle reinforced composites, but also well represents data for fibre like MWCNT composites.

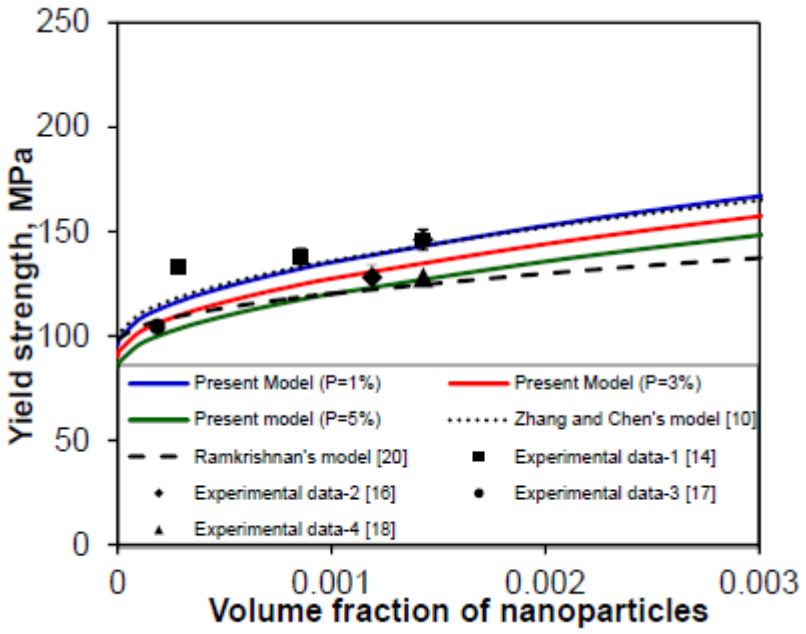

Figure 8. Mirza et al's model, listed here as the 'Present Model', compared against predictions made by previous iterations of a similar model and experimental data for Mg-MWCNT composites. [84]

Multiple models exist for calculating the incremental yield strength for each of the strengthening mechanisms discussed in this section, as well as for their summation. With the growing number of studies, and therefore experimental data, into Mg nanocomposites there exists an opportunity to explore the most accurate and representative models in terms of their individual contributions and their summation. The increased accuracy of the prediction of nanocomposite properties could potentially reduce the number of expensive trials required to produce optimised nanocomposites.

2.3 State of the art - manufacturing techniques

Since their inception, a multitude of manufacturing methods have been developed for a range of reinforcing nanoparticles and metal matrices and their alloys. Each method, with their own advantages and drawbacks, is specifically employed to produce MMNCs in an attempt to overcome the challenges that their sound manufacture presents. A homogeneous dispersion of the nanoparticle reinforcements is necessary to maximise any improvements that would result from the proposed strengthening mechanisms whilst also reducing potentially negative effects such as nanoparticle agglomeration leading to crack initiation sites. MMNC production can mostly be divided by bulk MMNC production and surface metal matrix nanocomposite (SMMNC) coatings that are in the order of µm to mm thick usually for improved corrosion and wear resistance. This review will focus on the production of bulk MMNCs.

The manufacture of bulk MMNCs can then be further divided mainly by melt and powder/solid processing routes, with SMMNCs most commonly being made by laser deposition or electrodeposition.

The greatest number of studies on carbon based MMNCs, have been performed on Al-CNT nanocomposites. This is most likely due to how the use of Al alloys in industry, particularly in the aerospace industry, have been well established for decades following widespread and in-depth metallurgical and processing studies carried out by industry and the research community. However, Mg nanocomposites present an exciting alternative to their Al counterparts, being approximately 30% lighter than Al ($\rho Al = 2.70 kgm^{-3}$, $\rho Mg = 1.74\ kgm^{-3}$), having good recyclability [90, 91] and an excellent damping capacity [92], which make it an attractive structural material for transport industries attempting to satisfy legislative requirements for fuel efficiency and end of life impact.

2.3.1 Pre-Dispersion

MWCNT systems are notoriously difficult to disperse due to their high surface area, high aspect ratio and the strong van der Waals interactions among them that stimulate and enable agglomeration and bundling. The as-produced state of commercially available MWCNTs (Baytube C150P MWCNTs produced by Bayer Science with an average diameter of 13nm and a length of 1-10µm) are usually in large entangled agglomerates, as shown in Figure 9, therefore steps are taken to well disperse the tubes before a secondary or final processing step. The two most widely used techniques are ultrasonification and HEBM.

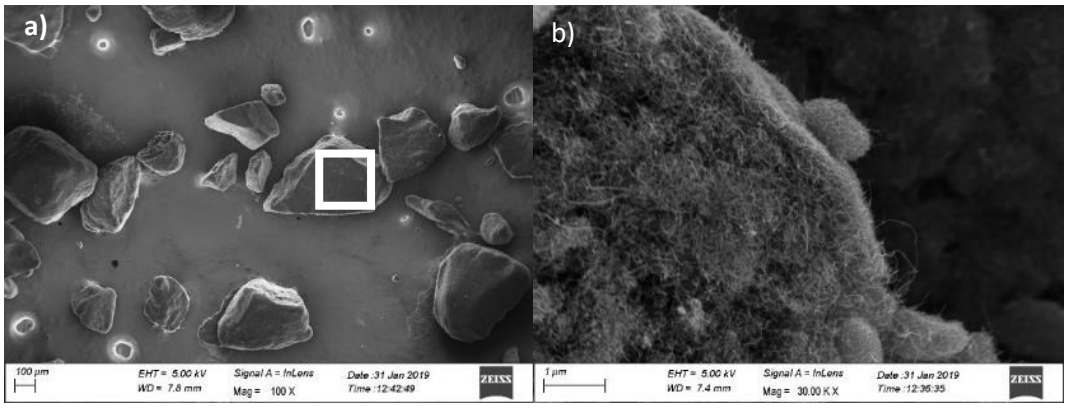

Figure 9. HRSEM images of as-received Baytube C150P MWCNTs, a) showing the large bundles and b) their surface morphology.

2.3.1.1 Ultrasonification

Ultrasonification provides the local shear stress that is required to overcome the mechanical entanglements of the MWCNTs that cannot always be provided by mechanical shear mixing, i.e. 20kPa of shear stress can be delivered to a viscous polymer by a commercially available high shear mixer opposed to 100MPa by a cavitation implosion event that occurs during ultrasonification [93]. Studies have been done to disperse the initially large MWCNT bundles in a solvent with an ultrasonic bath prior to a secondary process, for example, Li *et al* [38] ultrasonically dispersed MWCNTs in ethanol with a block copolymer before drying the dispersion over AZ91 chips, which was followed by a melt stirring process. Han *et al* [76, 94], using a similar technique, drying dispersed MWCNTs in ethanol with Mg powder to also make a precursor for a melt stirring process. The mechanics of ultrasonic dispersion are further discussed in section 2.3.2.2.

2.3.1.2 High energy ball milling (HEBM)

HEBM is usually used as a powder preparation method prior to powder metallurgy manufacturing techniques, popular with Al-CNT matrix studies [41, 49]. Usually, a steel or zirconia jar is filled with steel or zirconia balls, respectively, in addition to powdered metal and the nanoparticle reinforcement. The jars are then vigorously mechanically manipulated so that there are high energy impacts between the balls themselves and the jar walls, with the powder mixture caught in-between. The series of high energy impacts can lead to cold welding, fracturing (due to work hardening of the metal) and re-cold welding of the metal matrix powder, and the deagglomeration of the nanoparticles, leading to the nanoparticles on the surface of the powder being well mixed and embedded into the matrix [95]. The morphology of the CNTs can be drastically changed by certain ball milling parameters. Chen *et al* [41] varied HEBM time from 4 to 48hours and saw a significant decrease in length, shown in Figure 10. However, no measure of the defect density and therefore structural quality of the milled MWCNTs were made. In addition to MWCNT scission, defects could be introduced to compromise the nanoparticles mechanical performance that would in-turn reduce the magnitude of transferrable load and reduce the composites mechanical properties. However, this phenomenon has not been studied in MWCNT-MMNCs. Additionally, Mg powders require extremely careful process control due to its explosive nature and therefore is rarely used with HEBM. The flammability of Mg powders could impede its widespread use in industry, making melt processing the more attractive fabrication method for Mg composites.

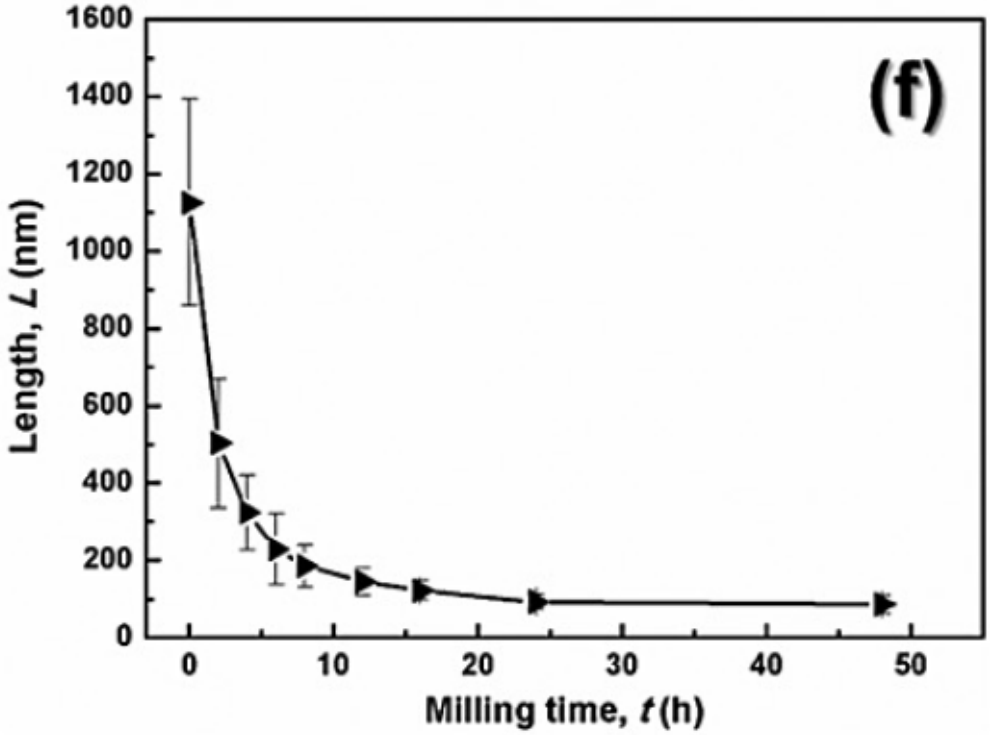

Figure 10. The variation of MWCNT length with HEBM time [41].

2.3.2 Composite production - Melt processing

In terms of the production of MMNCs transitioning from the lab to the industrial scale, melt processing is currently widely used for the mass production of bulk metal components with complex geometries and would therefore be the simplest and most economical way of integrating their manufacture with current conventional casting equipment and knowledge. Mg alloys show a greater castability when compared to other Al and copper casting alloys due to excellent fluidity [7] and a reduced susceptibility to hydrogen solubility that leads to porosity [9].

2.3.2.1 Stir Casting

Stir casting is an economic, scalable and adaptable method and is the most cost-effective method that has been currently utilised for the production of MMNCs in the literature. It has been seen as the commercial application for Al metal matrix composites [96, 97] and is quite simply the incorporation of reinforcing particles into a metal melt by the means of an impeller, schematically shown in Figure 11. Despite the economic benefits of stir casting, stirring processing difficulties still exist, such as the inclusion of air bubbles and miscellaneous surface impurities that can lead to porosity and material quality compromising defects.

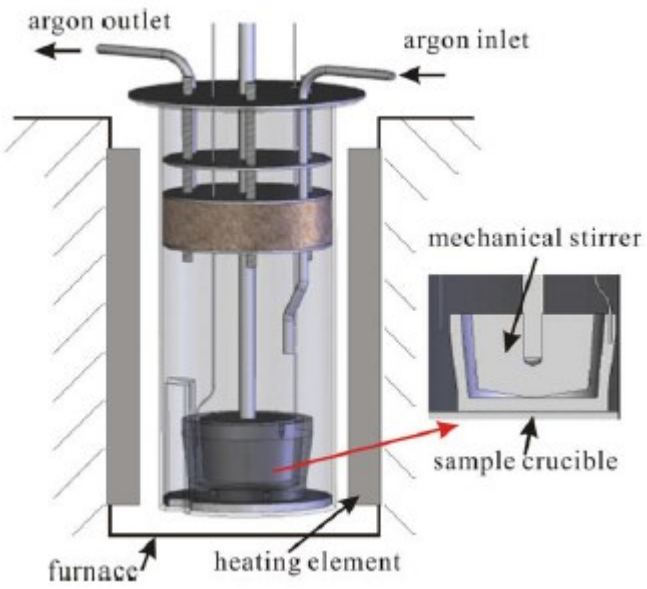

Figure 11. Schematic of the melt stirring apparatus used in this study [38].

Dr Qianqian Li, the PI for this project, and her group developed a two-step process by which Baytube C150P MWCNTs were 'pre-dispersed' covering AZ91 chips before being melted for casting to produce AZ91 0.1wt.%CNT composites [38]. The MWCNTS were first dispersed in ethanol using an ultrasonic bath and the block copolymer Disperbyk-2150. AZ91 chips were then added to the dispersion and stirred until the ethanol had evaporated. SEM images showed a homogenous coating of dispersed MWCNTs on the AZ91 chip surfaces. The chips were then melted in a resistance furnace under a protective argon (Ar) atmosphere and vigorously stirred in an attempt to further disperse the MWCNTs. The molten mixture was then poured into a mould preheated to 200°C for rapid solidification. Samples were then compression tested and an increase in ductility, ultimate compressive strength (UCS) and 2% compressive yield strength (CYS) were found to be 36%, 10% and 20%, respectively. Li *et al* [98] continued to study the process by varying the concentration of MWCNTs in the composite, investigating 0.1, 0.5 and 1 wt.% AZ91-MWCNT composites. Similar

mechanical properties were seen for the composites of different weight loadings of MWCNTs, all showing an improvement of up to 40% and 20% for compression to failure and UCS, respectively. The similar composite properties for a range of MWCNT concentrations were attributed to the pre-dispersion being insufficient for dispersing higher loadings of MWCNTs and the agglomerates that reside in the melt do not contribute to any strengthening mechanisms. Another explanation was that the MWCNTs were separating from the AZ91 melt during the processing stage and that a similar concentration of MWCNTs that were inside the final casting were similar for the different weight loadings.

Zeng *et al* [97] utilised HEBM and a simple consolidation step to manufacture a highly concentrated MWCNT (10wt.%), Al and zinc (Zn) precursor that was later added and mechanically stirred to a measured composition of metal melt to give 0.5 – 1.5wt.% MWCNT – AZ31 composites that were then vacuum cast at 690°C. Significant grain refinement was achieved, with a reduction from 125.6µm to 21.6 µm from AZ31 to 1.5wt.% MWCNT – AZ31, respectively. However, no final sample dispersion analysis was carried out. The maximum increase in hardness, tensile strength and elongation to failure were found for the 1wt.% MWCNT composite to be 59%, 31% and 75%, respectively, whilst the increase in Young's modulus was the maximum for the 1.5wt.% MWCNT sample at 68%.

It is difficult for a mechanical stirring method alone to disperse nanoparticles within a melt uniformly due to their high surface to volume ratio and, especially in the case of MWCNTs, low wettability with the metal melt [99]. Low wettability can lead to reagglomeration and therefore limit the increase or even decrease the mechanical properties of the final composite. A potential method for overcoming this problem is to use ultrasonic assisted stirring.

2.3.2.2 Ultrasound assisted stirring

Ultrasonic treatment (UST) has been recognised for the past few decades as a way of degassing the molten metal in order to produce higher quality, less porous casts [100] . It was also found that UST encouraged grain refinement in the final casting, which in turn results in stronger components with a strengthening factor defined by the Hall-Petch relationship [101]. The difficulty of dispersing nanocarbons in metal melts stems from the fact that, even if initially well dispersed, due to the poor wettability of nanocarbons with the molten Mg, it will be energetically favourable for the nanocarbons to reagglomerate than remain dispersed in the melt. This challenge will be discussed in more detail in section 2.3.2.3.

UST has been repeatedly proven to be an effective way of dispersing nanoparticles in a liquid media [102-105]. Through cavitation and acoustic streaming, UST can fragment nanoparticle clusters and aid with their homogeneous dispersion throughout the melt. As the sonotrode oscillates at a given frequency and amplitude, alternating compression and expansion waves are transmitted into the melt directly below the sonotrode tip. If the local stress field generated by the expansion wave exceeds the attractive forces between the liquid metal constituents, a cavitation bubble will be formed. As the bubble pulsates, grows and reaches a critical radius, the bubble implodes in the order of pico-seconds [107] and reaches temperatures up to ~5000K, pressures up to 1000bar and cooling rates of $> 10^{10}$ Ks^{-1}, creating an exceptional physical environment[108]. This mechanism is called cavitation. Acoustic streaming is the macroscopic flow of the melt due to the attenuation of a propagating ultrasonic wave that generates pressure differences and has

been found to depend on ultrasound intensity, melt viscosity, melt sound absorption ability and crucible geometry [102]. The attractive forces in the melt are disrupted and therefore weakened by the presence of nanoparticles and impurities, encouraging cavitation at their location. Nanoparticle agglomerates will include gas entrapments in their structure, upon cavitation, if the explosive environment generated within the nanoparticle cluster provides a large enough force to overcome the agglomerating van der Waals force, the cluster will be fragmented, as shown in Figure 12 [102].

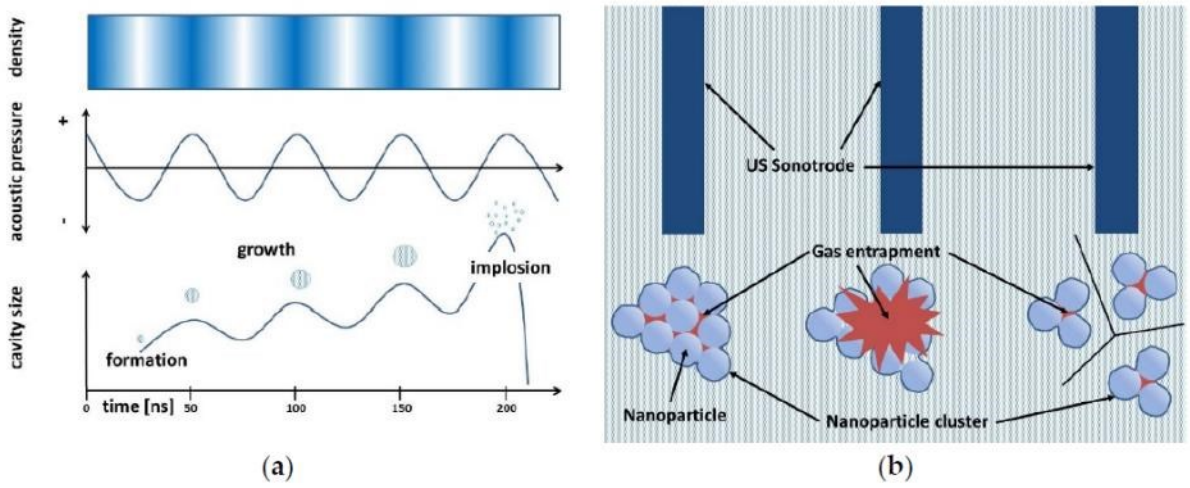

Figure 12 – a) Schematic showing the formation and life cycle of cavitation bubbles. B) Schematic showing how cavitation that is induced under the sonotrode tip can fragment nanoparticle agglomerates. The gas trapped inside the agglomerate under the cavitation effect can provide an explosive environment to overcome the agglomerating van der Waals forces. Adapted from [102].

An ultrasonic dispersion mechanism, specific to the MWCNT case proposed by Huang *et al* [93], describes how the shear stress imparted on a nanotube due to the high strain rate induced by an imploding bubble can overcome MWCNT binding energy or induce separation by tube fracture. The maximum shear stress that can be imparted on a MWCNT, for a cavitating system, is determined by the accessible length of the MWCNT. Tube fracture will occur as long as the length of tube allows a shear stress to be applied that exceeds the tubes ultimate tensile strength. Therefore, a critical tube length, below which tube scission can no longer occur, exists, which can be calculated by:

$$L_{Lim} = \sqrt{\frac{d^2\sigma^*}{2\eta\left(\frac{\dot{R}_i}{R_i}\right)}} \tag{36}$$

Where L_{Lim} is the length below which the MWCNT will no longer experience scission, d is the MWCNT diameter, σ^* is the ultimate tenisle strength of the MWCNT, η is the media viscosity and $\frac{\dot{R}_i}{R_i}$ is the rate of bubble implosion (10^8) [93]. L_{Lim} will be 3.68µm in ethanol and 1.04µm in liquid Mg (for NC7000 nanotubes d = 9.5nm, σ^* = 30GPa, $\eta_{ethanol} = 0.001Pas$ [109] and $\eta_{l-magnesium} = 0.0124Pas$) [110].

Eskin [111] claims that there are three cavitation regimes: pulsating cavities that maintain a constant gas vapour content; cavities that grow during pulsation that allows gas to diffuse only into the cavity; and finally, imploding cavities. Cavities that grow, allowing gas to diffuse out of the metal melt, can reach a large enough size to float out and thereby reduce the gas content of the melt. As previously mentioned, it is also stated throughout literature that UST of metal melts results in castings with reduced grain size. The exact grain refinement mechanism is not agreed upon [112], with a predominant theory revolving around cavitation induced dendritic fragmentation, which generates a higher density of nucleation sites.

An equation for ultrasonic intensity has been proposed by Eskin [111], Equation 37, where I is the ultrasonic intensity (W/m^2), ρ is the liquid density (kg/m^3), c is the speed of sound in the medium (m/s), f is the ultrasonic frequency (Hz) and A is the amplitude of oscillation (m). For a sonotrode oscillating at 20kHz with an amplitude of 60µm, the ultrasonic intensity would be ~3 times greater in a Mg melt (ρ = 1800kg/m^3 and c = 1500m/s) than in ethanol (ρ = 789kg/m^3 and c = 1127m/s). This higher intensity suggests the cavitation and streaming effects are amplified in a Mg melt when compared to solvents such as water or ethanol. However, Equation 37 does not consider the influence of medium viscosity, and molten Mg has a viscosity of ~12.4Pas at 650°C[110], approximately 12 times that of ethanol at room temperature [109], which may impede macroscopic flow.

$$I = \frac{\rho c}{2}(2\pi f A)^2 \tag{37}$$

Numerical studies have been conducted to produce models that can be used to optimise UST parameters without having to perform a costly number of experiments and characterisations. Song *et al* [113] varied the power (1.5-2.5kW), frequency (20kHz-40kHz), immersion depth (20-40mm) and sonication time (80s-160s) in a 2D geometry space, with a 20mm wide probe in a "crucible" containing molten AZ91D at 900K that is 100mm wide and 150mm tall dispersing 30nm – 50nm SiC nanoparticles. The optimal sonication parameters were a power, frequency, probe immersion depth and sonication time of 2kW, 20kHz, 20-30mm and 120s, respectively. AZ91D 1 vol% SiC nanocomposites were then fabricated with parameters of 1.5kW for 50s and 2kW for 120s at 20kHz, with the latter using simulated parameters, to guide an experimental study to produce a composite with the better mechanical properties due to a better dispersion of the SiC nanoparticles as a way of verifying the numerical model. There is, however, no measurement of grain size or porosity to confirm that the increased mechanical properties are only attributed to an enhanced dispersion. Pasumarthi *et al* [107] created a numerical model to explore and optimise geometric parameters that produced the largest acoustic cavitation zone. An analysis of the variance study of three factors, the ratio of the crucible diameter (D) and ultrasonic probe diameter (D_p), the ratio of the immersion depth (d) to the probe diameter (D_p) and the volume of melt to be processed with a 20kHz sonotrode of an unmentioned power. It was found that the volume was the least significant factor effecting the cavitation zone size, so it was kept constant at 50ml for the remainder of the study, with focus remaining on the diameter ratio and immersion depth ratio. D/D_p and d/D_p ratios that produced the largest acoustic cavitation zones were found to be 2.8 and 2.0, respectively, which was within the parameter range considered (D/D_p and d/D_p was varied from 1.25 – 3 and 0.25 – 3, respectively). These

ratios can act as guidelines for designing a system that can optimise the ultrasonic dispersion of nanoparticles in metal melt.

2.3.2.3 Challenges and possible solutions of melt processing

In order to take full advantage of the strengthening mechanisms that nanoparticle reinforcements induce, as previously discussed, a homogenous dispersion is necessary. A homogenous dispersion requires the nanoparticles being well dispersed within the metal grains. A major challenge for the melt processing of bulk MMNCs is to ensure that the nanoparticles are captured by the solidification front instead of being pushed and aggregated together at grain boundaries. The detrimental effect of a nanoparticle not being captured by the solidification front is compounded by the unstable nature of the suspended nanoparticles that are not wetted by the metal melt. Forces, exerted by their high difference in surface energy, are driving them to re-agglomerate in an environment where traditional nanoparticle stabilisation techniques such as surface modification are not effective [114]. The unstable nanoparticle – melt mixture leads to the distribution of nanoparticles being very different in the composites solidified state when compared to its liquid state, potentially making any steps taken to disperse the nanoparticles obsolete.

A number of studies were conducted in an attempt to model the solidification front capture of micro sized particle dispersions, however, they failed to match well with experimental results [115]. Xu *et al* [115] carried out a theoretical study that presented three potential models for nanoparticle capture: viscous capture, Brownian capture and spontaneous capture.

For viscous capture, a defined critical velocity describes the point at which the solidification front speed is large enough to capture the nanoparticle due to the viscous drag force, imposed on the nanoparticle due to its velocity away from the solidification front, is larger than the repulsive forces on the nanoparticle when the nanoparticle and solidification front interfaces are incident. Brownian capture can occur when the absolute value of the Hamaker constant for a given system is small and the Brownian potential can initiate a spontaneous movement of the nanoparticle into the oncoming solidification front with enough energy to overcome the energy barrier presented by the repulsive forces. The Hamaker constant is an inherent material property that gives a measure of the van der Waals forces between two surfaces that is seen to be key in the study of the dynamics of solidification front capture or pushing of nanoparticles [116]. Spontaneous capture is the most favoured pathway as it removes the need for viscous or Brownian capture, and it occurs when, as can be seen from Equation 38 [115], the Hamaker constant of the nanoparticle exceeds that of the molten metal, leading to attractive van der Waals forces between the melt and the nanoparticle.

$$W_{vdw}(D) = -\frac{\left(\sqrt{A_{solid}} - \sqrt{A_{liquid}}\right)\left(\sqrt{A_{nanoparticle}} - \sqrt{A_{liquid}}\right)R}{6D} \tag{38}$$

Where $W_{vdw}(D)$ is the van der Waals potential, D is the distance between the metal-ceramic interface, A is the Hamaker constant and R is the nanoparticle radius. Equation 38 is valid for when D << R. D and R are schematically shown in Figure 13.

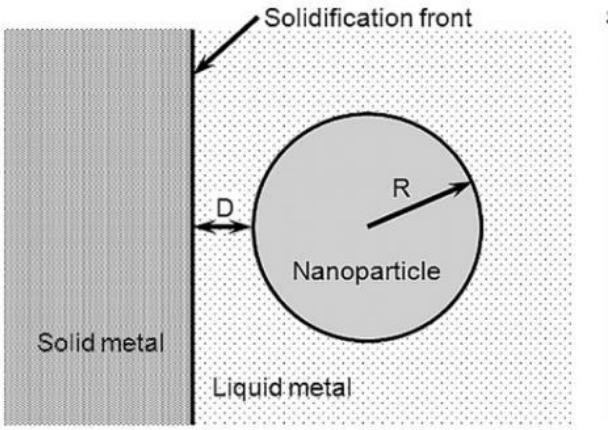

Figure 13. Schematic representation of a nanoparticle and an incident solidification front [115]

An interesting method to ensure SiC nanoparticle capture in an Al matrix system has been shown by Boostani *et al* [117], which encapsulated the SiC nanoparticles in graphene to exhibit a modified Hamaker constant of 387zJ, making it larger than the SiC and most importantly Al Hamaker constants of 287zJ and 266zJ[118], respectively. It can be seen from Figure 14 that molten Mg has a lower Hamaker constant than molten Al, meaning that Mg will be spontaneous capture compatible with a larger range of reinforcing particles. However, Xiang *et al* [119] found that ultrasonically dispersed graphene nanoplatelets in Mg melt were found in higher concentrations around grain boundaries than within the grain upon solidification, suggesting that the graphene nanoplatelets were pushed by the solidification front instead of being captured even though graphene's Hamaker constant (387zJ) is larger than Mg's (206zJ). The conflicting results require further study into the nanoparticle-solidification front interaction.

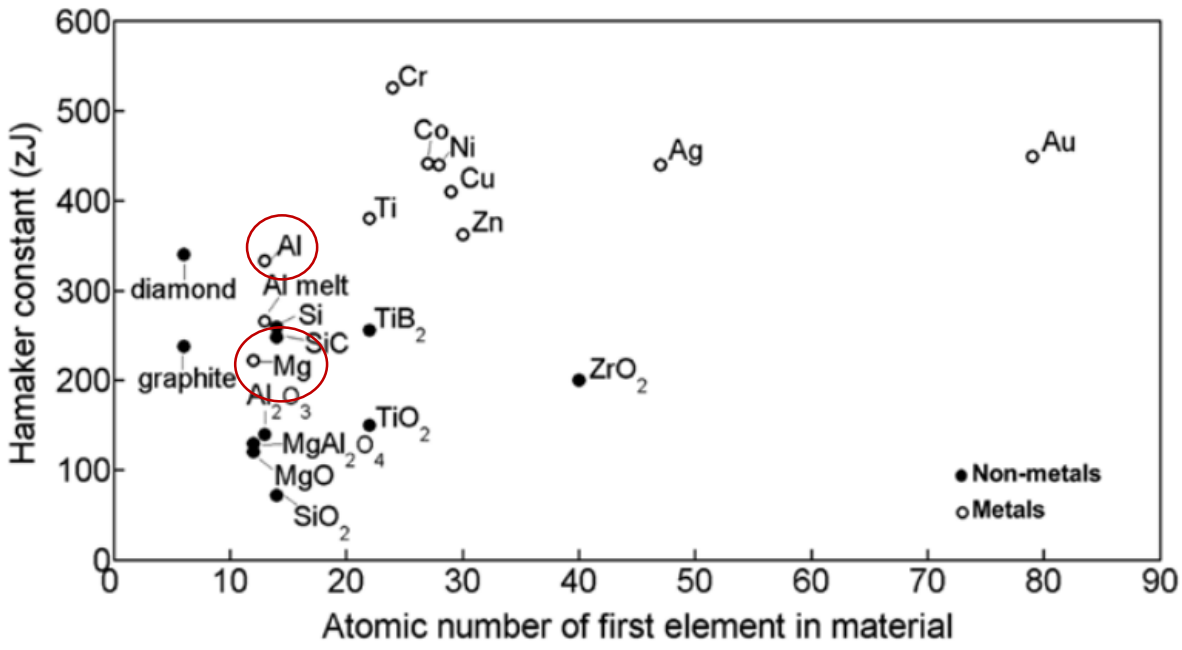

Figure 14. Hamaker constant vs main element atomic number for given materials. Taken from [115] .

Chen *et al* [5] used similar concepts to propose how they achieved an extremely dense (14% vol), uniform dispersion of SiC nanoparticles in a Mg6Zn alloy through a nanoparticle self-stabilisation mechanism in molten metal. They attributed the stabilisation of the nanoparticles to a reduced van der Waals between the SiC nanoparticles, energetic

Brownian motion and a high energy barrier to nanoparticle sintering induced by the favourable wettability between the SiC nanoparticles and molten Mg. Equation 39 [5] [120] can be used to determine the van der Waals interaction between two nanoparticles in a liquid:

$$W_{vdw}(D) = -\frac{\left(\sqrt{A_{np}} - \sqrt{A_{liquid}}\right)^2}{6D}\frac{R}{2} \tag{39}$$

Where D is larger than approximately 2 atomic layers (~0.4nm, where $W_{vdw}(D)$ is at its minimum and therefore represents that maximum attraction between the nanoparticles), A_{np} and A_{liquid} are the Hamaker constants for the nanoparticle and liquid, respectively, and R is the nanoparticles radii. For the SiCnp-liquid Mg system where $A_{SiC} = 248zJ$ [121] and $A_{l-Mg} = 206zJ$ [122](thereby also satisfying the spontaneous capture criteria outlined by [115]), a maximum van der Waals attraction is estimated to be -12.17zJ. The nanoparticles also have an associated thermal energy for Brownian motion that is increased by the high processing temperatures used for metal melt processing. The energy for Brownian motion can be calculated by

$$E_b = kT \tag{40}$$

Where k is the Boltzmann constant and T is the absolute temperature. For a processing temperature of 1000K, E_b = 13.8zJ, suggesting that through Brownian motion alone, the SiC nanoparticles submerged in Mg6Zn melt can overcome the maximum van der Waals (-12.17zJ) between them, inhibiting their reagglomeration. In micro particle systems, Brownian motion didn't have to be considered as it was negligible compared to the interactive van der Waals force that would be three orders of magnitude larger [115].

Lastly, the stabilisation of the SiC nanoparticles in the Mg6Zn melt was also attributed to the high energy barrier that inhibits their contact and sintering. The sintering process can be driven by the significant drop in interfacial energy, schematically shown by section 3 in Figure 15.

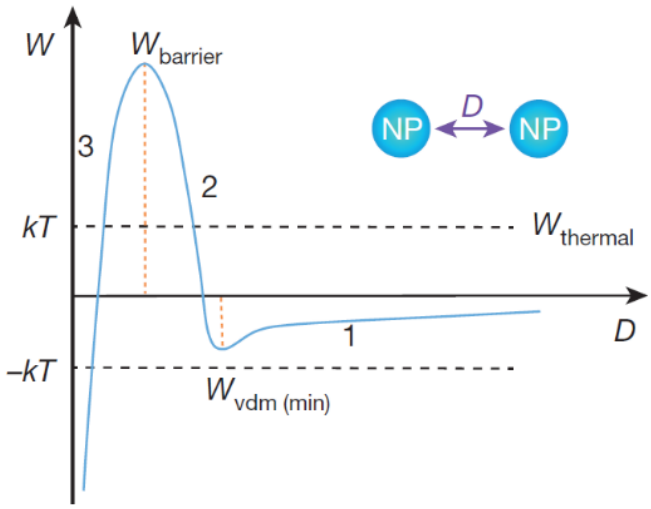

Figure 15. Interaction potential curve for two SiC nanoparticles separated by a distance D in a metal melt. Segment 1 is mainly the van der Waals interaction, 2 represents the energy increase of displacing liquid Mg from in between the SiC nanoparticles and being replaced with SiC surfaces and 3 is the interfacial energy drop due to contact and sintering [5].

The maximum energy barrier ($W_{barrier}$), which occurs at an interparticle distance of one atomic layer of separation by the liquid (at D = 0.2nm for liquid Mg), can be defined as [5]:

$$W_{barrier} = S(\sigma_{np} - \sigma_{np-l}) = S\sigma_l \cos\theta \quad (41)$$

Where S is the effective interaction area, σ_{np} is the surface energy of the nanoparticle, σ_{np-l} is the interfacial energy between the nanoparticle and the liquid, σ_l is the surface tension of the liquid and θ is the contact angle between the liquid and the nanoparticle. It can be therefore deduced from Equation 41 that as $\theta \rightarrow 0$ with increased wettability between the liquid and the substrate, $W_{barrier}$ increases, further acting against the nanoparticles contacting one another. The effective interaction area between two spheres, S, can be calculated using the Langbein approximation [120]:

$$S = \pi RD \quad (42)$$

Derjaguins approximation for two cylinders of equal radius crossing at 90^o [120]

$$S = 2\pi RD \quad (43)$$

Using a measured contact angle, the interfacial energy between the nanoparticle and the liquid can be calculated using the Young's equation [120] :

$$\sigma_{np} = \sigma_{np-l} - \sigma_l \cos\theta \quad (44)$$

The implications of this study are discussed in section 3.2.4.

The challenge of the poor wettability and interface of carbon morphologies with molten metal was encountered during research into metal matrix composites reinforced with carbon fibres (CF), particularly Al-CF composites. Even when methods such as vacuum infiltration or squeeze casting were employed to infiltrate the CFs, the poor wettability resulted in inadequate bonding and material properties [123, 124]. In order to overcome this wettability issue, graphite particles and fibres were coated with Ni before being mixed with the molten matrix metal. Ip et al [124] found that when they coated a graphite surface with 3.2µm of Ni, the contact angle with pure Al reduced from 140^{o} with uncoated graphite to 4^{o} after 1 hour at 740°C, tested with the sessile drop method. The enhanced wettability was accredited to a mechanism of the Ni coating being dissolved into the Al drop at the Al drop perimeter that allows the triple point to advance and the formation of Al-Ni intermetallics at the interface, shown in Figure 16. The mechanism of intermetallic formation would suggest that a continuous, rather than discontinuous, coating would be the ideal coating regime when trying to achieve MWCNT-molten metal wetting, as a continuous interface would be formed instead of a series of wetted anchor points to benefit from effective load transferring. Rams et al [125] found that the wetting behaviour of Ni coated CFs was improved in an AA6061 Al alloy due to the formation of Al-Ni intermetallic that limited fibre segregation during casting and ageing when compared to the uncoated CF composite. Whilst the as-cast hardness and elastic modulus were similar for both AA6061 Al - CF composites, following T6 heat treatment, the Ni coated CF composite exhibited an 18 and 10% increase in hardness and elastic modulus compared to the uncoated CF composite.

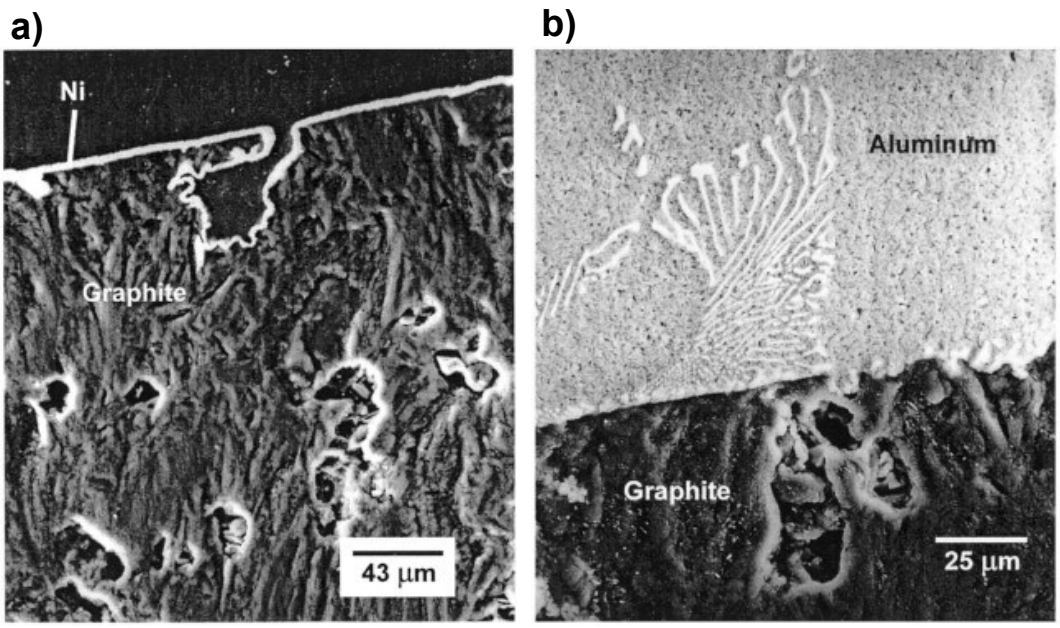

Figure 16. a) Graphite substrate coated with a 3.2µm thick layer of Ni. b) A micrograph showing the interface between the pure Al droplet and graphite. The Ni coating had completely dissolved into the Al potentially with small Al-Ni intermetallics formed at the interface [124].

With the advent of MMNC's reinforced with MWCNTs and the modest success shown in Ni coated CF reinforced metal composites, molecular dynamic (MD) simulations were used to investigate the impact of coated MWCNTs. Nasiri et al [126] developed a simulation to estimate the energy required for Ni coated/ non-coated CNT pull out of an Al matrix, for different coating regimes. To do this, they created a unit cell where a MWCNT was coated with Ni nanoparticles in a similar way to what is currently generally achieved using an electroless plating method, whereby discrete Ni nanoparticles were chemisorbed at random locations on the MWCNT surface, instead of monolayers being coherently placed onto a graphene surface. This coated nanotube was then placed into a solid aluminium cylinder, of equal length to the nanotube and a radius equal to approximately 10 nanotube diameters. All aluminium atoms within 3 angstroms of C or Ni atoms were then removed. This unit cell then undergoes some melt quench cycles that did not alter the Ni but relaxed the aluminium matrix. This unit cell is schematically shown in Figure 17.

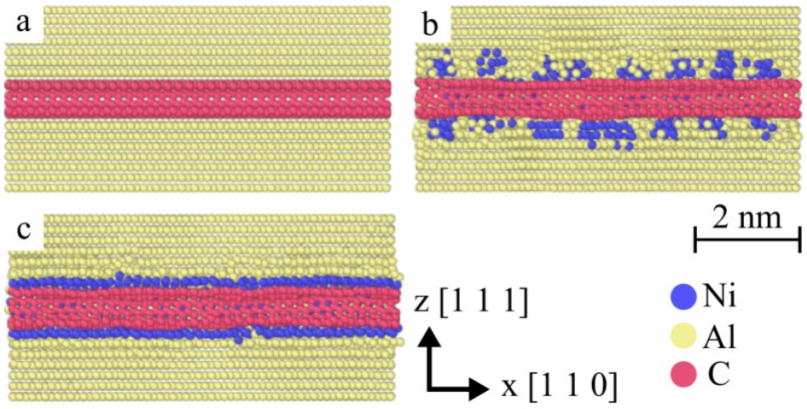

Figure 17 –Ni nanoparticles decorated on a CNT (5,5) surface with a) 0% coverage, b) 80% coverage and c) 100% coverage [126].

As shown in Figure 18, fully and partially chemisorbed Ni coated nanotubes exhibited a significantly higher pull out force. The increased pull out force was due to the large energy variations that occur as the nickel was moved relative to the CNT surface. However, the simulation was also performed assuming that the Ni coating was physisorbed onto the surface of the CNT showing that there was only a slight increase in required pull-out energy of 0.2eV/Å when compared to a pure CNT pull out energy of 0.4eV/Å, as the Ni-CNT interface was of a slightly lower energy than that of the Al-CNT interface. The energy for pull out of approximately 20 eV/Å for CNTs with a chemisorbed Ni coating indicates that the IFSS between the metal matrix and the CNT surface can be improved, thereby enhancing the magnitude of the load that can be transferred and making more effective use of the CNTs mechanical properties. The nature of the bond between the Ni nanoparticles and the CNT needs to be experimentally determined in order to validate this MD simulation. This study was also more likely to be applicable to solid state processed MMNCs as the Ni coating would most likely dissolve away from the CNT surface into the molten metal to either sit interstitially or form intermetallics in melt processed MMNCs. Therefore, an interesting avenue of study that has not currently been explored in the literature would be to investigate the use of SiC coated MWCNTs as a reinforcement in Mg and its alloys, as SiC is known to wet with Mg [5] and will be less likely to dissolve into the metal matrix due to its ceramic nature.

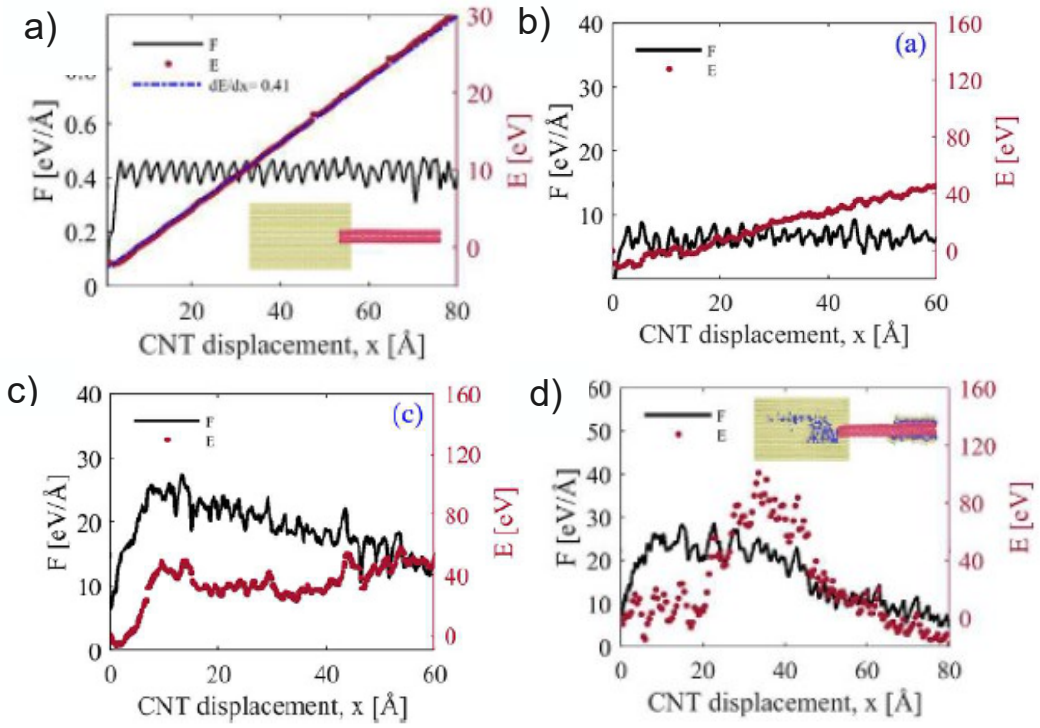

Figure 18. Simulation of the energy required for pull out of a CNT with a) 0% Ni coverage, b) 10% Ni coverage, c) 40% Ni coverage and d) 100% Ni coverage [126].

2.3.3 Solid state processing

2.3.3.1 Powder Metallurgy

Powder metallurgy has been the favoured method and successfully used for the manufacture of Al-CNT composites [127-130] with few studies into Mg-CNT composite [87, 94, 131]. It allows a number of phases and constituents to be mixed together in the solid state, usually through optimised HEBM, to form a homogenous powder that then has to be consolidated or densified usually by either sintering or forming processes. By processing in the solid state, the challenges of melt processing and the criticality of the wettability between the matrix and nanoparticle can be omitted. Active dispersion of the nanoparticles only occurs during the powder mixing phases. The extensive use of HEBM with nanocarbons can lead to significant nanoparticle damage [132, 133] and under-milled mixtures can limit the distribution of nanoparticles to the metal grain boundaries[134], thus emphasising the importance of optimising the HEBM parameters used. In terms of industrialising powder metallurgy, the HEBM process is both time and resource consuming and difficult to economically scale up. Furthermore, the requirement for sintering limits the process to simple geometries and therefore would require further expensive post processing. However, an interesting processing philosophy may be to use HEBM to produce well dispersed, high nanoparticle concentration 'master composites' that could be coupled with melt processing, perhaps eliminating the need for ultrasonic assisted stirring.

Goh *et al* [87] used a V-blender, a low shear mechanical powder mixer, to mix MWCNT powders with pure Mg powders with loadings of 0.06%, 0.18% and 0.3wt.%, followed by compaction, sintering and hot extrusion. They observed a maximum increase of 33% of elongation to failure with no significant differences in the mechanical properties between the monolithic Mg and the Mg-MWCNT composites. Clusters were found in the matrix and the work to fracture of the

samples decreased with increased CNT loading, suggesting a higher proportion of clustering that effectively behave as pores. The increase in ductility was attributed to the activation of prismatic slip planes. The minimal effect of the MWCNTs on the mechanical properties of the composite suggest that a V blender does not provide adequate mixing conditions and more rigorous techniques are required. Whereas studies by Fukuda *et al* [135] and Shimizu *et al* [136], who used HEBM with Mg-MWCNT powders, sintering and hot extrusion, achieved improvements in ultimate tensile yield strength of up to 33%, indicating the importance of the dispersion of the MWCNTs during the initial mixing phase.

2.3.3.2 Surface treated CNT – Mg composites

An advantage of powder metallurgy is being able to fabricate the composites at lower temperatures than required for melt processing. Low temperature processing is especially important when trying to manipulate the interface between the nanoparticle and the metal matrix that would otherwise be unfavourable and more difficult to achieve a homogeneous dispersion. A method [94, 137]of improving the interface between nanocarbons and Mg matrix is to coat the nanocarbons with nickel (Ni), so an intermetallic is formed at the interface as previously discussed for the MD simulation presented in section 2.3.2.3. To form a suitable interfacial intermetallic, an important consideration for using Ni coated CNTs within a Mg matrix is to be able to ensure that the Ni coating will stay adhered to the CNT surface, instead of dissolving into the Mg matrix that will occur at ≈923K due to a solubility limit of ≈1wt.% Ni in Mg according the Mg-Ni binary phase diagrams [138]. This temperature and above is regularly used for the melt processing of Mg alloys, thus either making this method unsuitable or limiting the materials that can be used for nanocarbon coating for melt processing or requiring accurate temperature control.

Han *et al* [94] made an attempt to produce bulk pure Mg ingots reinforced with Ni coated MWCNTS using a two-step process. Using a similar philosophy to Li *et al* [38, 98], outlined in [76], MWCNTs pre-treated with dimethyl sulfoxide (DMSO) were added to ethanol and placed into an ultrasonic bath for 1 hour. Pure Mg powder was then slowly added at the mixture and bath ultrasonicated for 10 mins, followed by stirring with an impeller at 500rpm for 1 hour. Ethanol was then removed from the solution using vacuum distillation for 2 hours at 333K and 600KPa. The powder was then heated to 793K in a quartz tube in an annealing furnace to remove DMSO from the MWCNTs. Finally, the powder was compacted and hot extruded. Ni-coated MWCNT composites were prepared in the same way for comparison. The Ni coated MWCNT composites were produced following a method that oxidised, sensitised and activated the MWCNTs, prior to their addition to a “nickel plating solution” that achieved a 3nm “coating”, shown in Figure 19. Figure 19a would suggest that a sparse and inhomogeneous Ni coating was achieved.

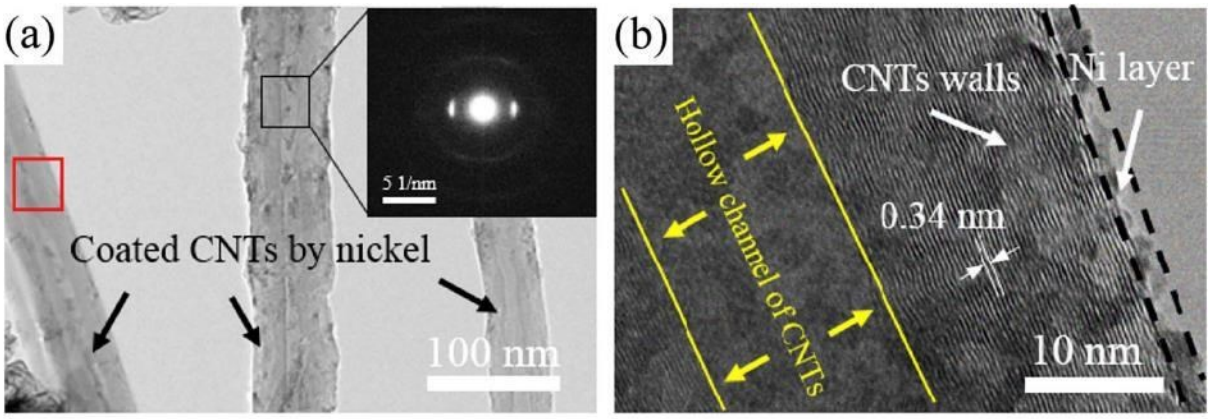

Figure 19 – TEM images of Ni coated – MWCNTs from [94].

Significant improvements in mechanical properties in terms of tensile yield strength (TYS) and ultimate tensile strength (UTS) were seen when comparing equal weight loadings of MWCNTs and Ni-MWCNTs, most notably, the 2% wt Ni-MWCNT composite showed a 77% and 48% increase in TYS and UTS over a 2% wt MWCNT composite, respectively. EBSD was used to accurately measure the grain size of the different composites, showing that they were all very similar (using Hall-Petch, the increase in yield strength for the 2wt.% Ni-MWCNT would have accounted only 3% of the total increase in TYS observed) and therefore leads to their conclusion that any increase in properties should be mainly credited to a strong interface bonding. However, in the particular case of this study, it is difficult to determine whether a fair comparison between a 2wt.% MWCNT and 2wt.% Ni – MWCNT composite can be made. It is not clear as to whether the mass of the Ni coating has been accounted for in producing the composite so that an equivalent number of MWCNTs are being dispersed within the matrix, as for example, if the same mass of MWCNT powder and Ni-MWCNT powder was used for a given mass of Mg powder to achieve a given concentration, the Ni-MWCNT composite would have significantly less MWCNTs within a given mass of matrix. For a given system with perfectly dispersed nanoparticles, a change in the number of nanoparticles would lead a change in the number of load bearing reinforcements and to a change in interparticle distance that would therefore lead to difference mechanical properties due to Orowan looping as in Equation 1. Additionally, without a pure metal control sample, it is difficult to conclude whether the strengthening is due to the Ni addition or even whether it is due to the presence of less MWCNTs, if the mass of the Ni coating was not accounted for. Nevertheless, a significant improvement was seen for both 0.3wt.% and 2wt.% Ni – MWCNT composites over the MWCNT composites. Two interesting interface regimes were observed between the Ni-MWCNTs and the Mg matrix shown in Figure 20. It was stated, but not shown, that no interface was observed for the MWCNT-Mg composites. Figure 20a-b shows a coherent interface between Mg_2Ni and Mg matrix, which has low energy due to the low lattice disregistry and therefore most likely to form. Figure 20c-d shows what the authors claimed to be a Mg_2Ni phase that is partially interstitially located within the MWCNT walls and the Mg matrix, behaving as an analogous chain link between the MWCNT and the Mg matrix. However, the interference pattern could be generated by the Mg_2Ni crystal being above or below the MWCNTs plane instead of actually being interstitially located with the MWCNT. The interfacial regimes shown in Figure 20 could both contribute to achieving a system that can efficiently transfer load from the matrix to the stiffer MWCNT reinforcements.

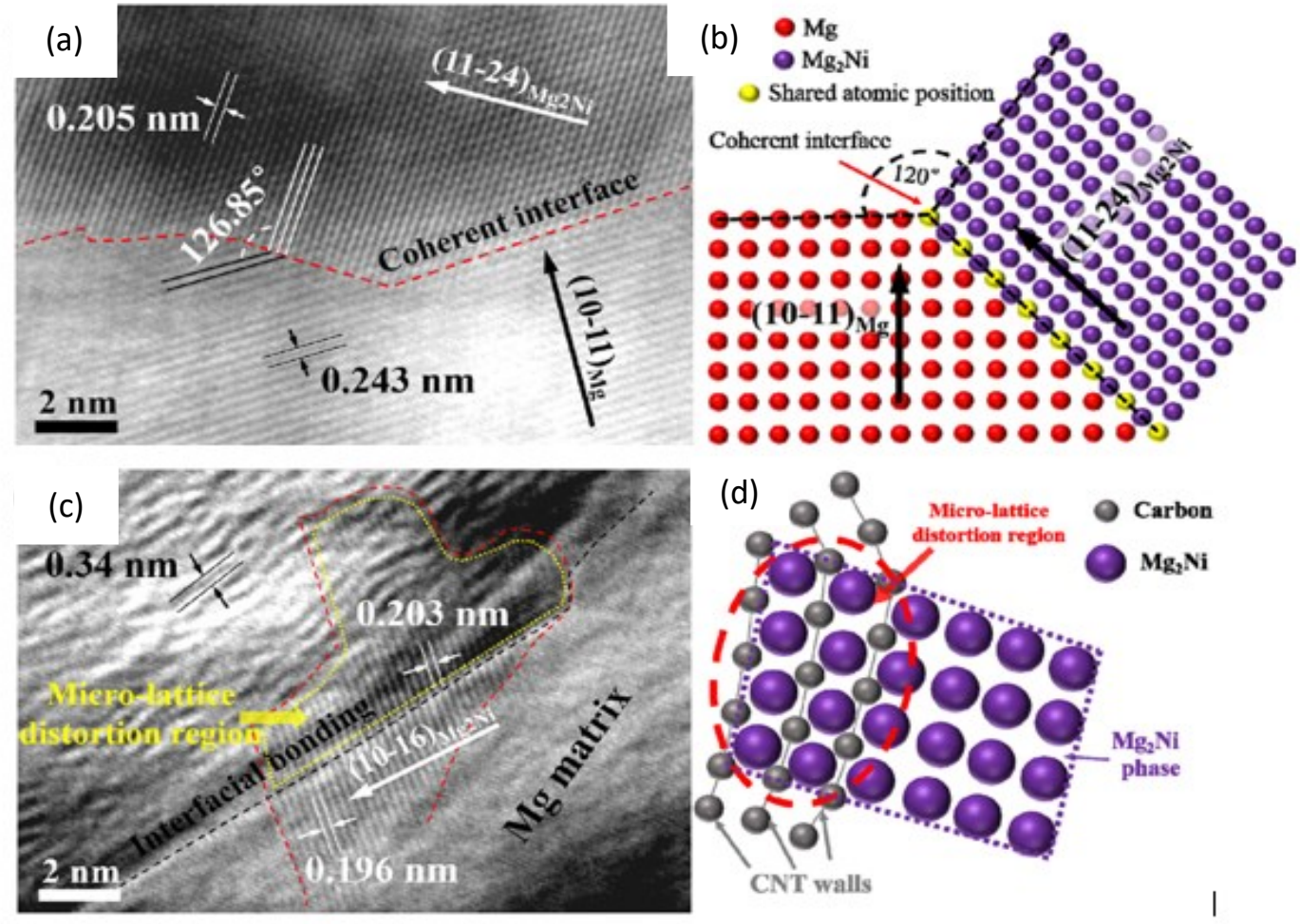

Figure 20. a) showing a coherent Mg-Mg2Ni interface, b) schematic view of a). c) is suggested as showing an Mg2Ni phase interstitially located within the outer walls of a MWCNT and forming a coherent interface with the Mg matrix, d) is a schematic view of c) [94].

2.3.4 Alternative techniques

The challenges presented by trying to manufacture MMNCs has led to a myriad of advanced manufacturing techniques being investigated, mainly revolving around severe plastic deformation (SPD) such as equal-channel angular pressing (ECAP) [139], high-pressure torsion (HPT) [5] or advanced casting techniques that are usually both expensive and limited in their industrial application.

Gupta *et al* [140-143] carried out studies on Mg- MWCNT MMNCs and other Mg – nanoparticle combinations using what was called a disintegrated melt deposition technique. Molten Mg heated to 750°C and the reinforcing nanoparticles were mechanically stirred before being poured from the bottom of the crucible into Ar jets that disintegrated the melt and deposited it to form an ingot that was then extruded. At MWCNT concentrations above 1.3wt.%, mechanical properties were seen to drastically reduce due to MWCNT agglomeration, however, in samples <1.3wt.% an increase in tensile ductility of up to 68% was seen [142] that was attributed to activation of prismatic and cross-slipping dislocations.

Friction stir processing (FSP) or solid state stirring, is the most utilised SPD technique in the literature in the realms of MMNC production [144-147]. Studies originally followed a method similar to cutting a groove along the to-be stirrer path and depositing MWCNT or nanoparticle powder directly into the groove. Chen *et al* [148] used ultrasonification to first disperse graphene nanoplatelets in molten Mg before casting a Mg- 1.2wt.% graphene plate, schematically shown in Figure 21, but micro sized graphene clusters were still observed in the as cast plate. Although this could be due to reagglomeration during solidification as previously discussed, nevertheless, the final dispersion could be improved, hence the employment of FSP. The final composite was 78% harder than the monolithic Mg prepared in the same way. SEM images clearly show an enhanced dispersion after FSP. Unfortunately, comparisons between the as cast composite and the FSP'd composite in terms of microstructure and hardness were not carried out that could have provided valuable information about the source of the increase in hardness as to whether it was due to enhanced induced grain refinement by the graphene additions, or indeed other strengthening mechanisms such as load transfer or Orowan strengthening.

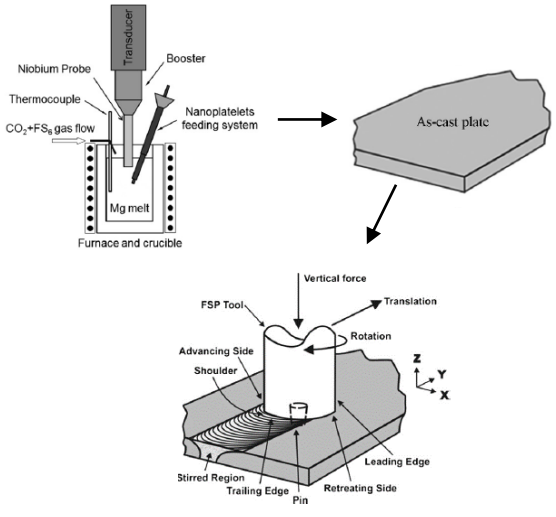

Figure 21. Schematic representation of the fabrication route used to produce 1.2wt.% – Mg MMNC using ultrasonification and friction stir processing [148].

2.4 Properties of nanoparticle reinforced Mg and Mg alloys

So far in this literature review, the benefits of reinforcing Mg and Mg alloys with nanoparticles has been discussed from a theoretical point of view and the difficulties in their manufacture. This section will provide a summary of the Mg MMNCs that have been fabricated and presented in the literature, showing any measured changes in mechanical properties with a focus on Mg MMNCs reinforced with MWCNTs and SiC nanoparticles in Table 1 and Table 2, respectively. It will also discuss the impact of nanoparticle reinforcements on the ductility and creep properties of the Mg MMNCs.

2.4.1 Literature summary

Table 1. A summary of the effect of MWCNT reinforcement on Mg/Mg alloys reported in the literature.

Primary Manufacturing method	Composite	MWCNT content	YS %	US %	Ductility %	Hardness	Ref
Melt Stirring	AZ91 - MWCNT	0.1% wt	Compression: 10%	Compression: 20%	Compression: 36%		[38]
Melt Stirring	AZ91 - MWCNT	0.1% wt	Compression: -4%	Compression: 20%	Compression: 41%		[38]
Melt Stirring	AZ91 - MWCNT	0.5% wt	Compression: -11.5%	Compression: 14%	Compression: 35%		[38]
Melt Stirring	AZ91 - MWCNT	1% wt	Compression: -4%	Compression: 22%	Compression: 47%		[38]
Melt stirred, disintegrated melt deposition and hot extrusion	Mg - MWCNT	0.3% wt	Tensile: 2%	Tensile: 1%	Tensile: 59%	7%	[89]
Melt stirred, disintegrated melt deposition and hot extrusion	Mg - MWCNT	1.3% wt	Tensile: 11%	Tensile: 9%	Tensile: 69%	2%	[89]
Melt stirred, disintegrated melt deposition and hot extrusion	Mg - MWCNT	1.6% wt	Tensile: -4%	Tensile: 4%	Tensile: 53%	-7%	[89]
Melt stirred, disintegrated melt deposition and hot extrusion	Mg - MWCNT	2% wt	Tensile: -3%	Tensile: 3%	Tensile: -4%	-13%	[89]
disintegrated melt deposition and hot extrusion	AZ31 - MWCNT	0.5%wt MWCNT	Tensile: 10%	Tensile: 17%	Tensile: 68%		[142]
disintegrated melt deposition and hot extrusion	AZ31 - MWCNT	0.5%wt MWCNT	Compression: 58%	Compression: 3%	Compression: 5%		[142]
disintegrated melt deposition and hot extrusion	AZ31 - MWCNT	1%wt MWCNT	Tensile: 17%	Tensile: 3%	Tensile: 24%	45%	[140]

disintegrated melt deposition and hot extrusion	AZ81 - MWCNT	1.5%wt MWCNT	Tensile: -7%	Tensile: -2%	Tensile: 73%	-4%	[143]
Ball milling to form master block and melt stirring	AZ31 - MWCNT	0.5%wt MWCNT	Tensile: 13%		Tensile: 50%	29%	[97]
Ball milling to form master block and melt stirring	AZ31 - MWCNT	1%wt MWCNT	Tensile: 31%		Tensile: 124%	59%	[97]
Ball milling to form master block and melt stirring	AZ31 - MWCNT	1.5%wt MWCNT	Tensile: 19%		Tensile: 75%	50%	[97]
Melt stirring with compacted master alloy, cast and hot extrusion	AZ31 - MWCNT	0.05% vol	Compressive: 53%	Compression: 9.5%	Compression: -66%		[76]
Melt stirring with compacted master alloy, cast and hot extrusion	AZ31 - MWCNT	0.1% vol	Tensile: 22.7%	Tensile: 7%	Tension: -20%	10%	[76]
Melt stirring with compacted master alloy, cast and hot extrusion	AZ31 - MWCNT	0.2% vol				9%	[76]
Powder compaction and hot extrusion	Mg - NiCNT	0.3% wt MWCNT 0.3% wt Ni-MWCNT	Improvement from 0.3% MWCNT to 0.3% Ni-MWCNT: 26.2%	Improvement from 0.3% MWCNT to 0.3% Ni-MWCNT: 16.1%	Improvement from 0.3% MWCNT to 0.3% Ni-MWCNT: 13.0%	Improvement from 0.3% MWCNT to 0.3% Ni-MWCNT: 19.9%	[94]
Powder compaction and hot extrusion	Mg - NiCNT	2% wt MWCNT 2% wt Ni-MWCNT	Improvement from 2% MWCNT to 2% Ni-MWCNT: 77.1%	Improvement from 2% MWCNT to 2% Ni-MWCNT: 47.9%	Improvement from 2% MWCNT to 2% Ni-MWCNT: -52.9%	Improvement from 2% MWCNT to 2% Ni-MWCNT: 29.9%	[94]
V-blender powder mixing, compacted and hot extruded	Mg - MWCNT	0.06% wt	Tensile: 5%	Tensile: -1%	Tensile: 33%	0%	[87]
V-blender powder mixing, compacted and hot extruded	Mg - MWCNT	0.18% wt	Tensile: 9%	Tensile: 0%	Tensile: 22%	0%	[87]
V-blender powder mixing, compacted and hot extruded	Mg - MWCNT	0.3% wt	Tensile: 15%	Tensile: 2%	Tensile: -11%	0%	[87]
Ball milling, compaction, microwave sintered, furnace soaked and hot extrusion	Mg - MWCNT - SiCnp	0.3%wt MWCNT 0.7%wt SiC	Tensile: 37%	Tensile: 25%	Tensile: -44%	12%	[149]
Ball milling, compaction, microwave sintered, furnace soaked and hot extrusion	Mg - MWCNT - SiCnp	0.5%wt MWCNT 0.5%wt SiC	Tensile: 36%	Tensile: 1%	Tensile: -61%	10%	[149]

Ball milling, compaction, microwave sintered, furnace soaked and hot extrusion	Mg - MWCNT - SiCnp	0.7%wt MWCNT 0.3%wt SiC	Tensile: 25%	Tensile: 17%	Tensile: -64%	7%	[149]
Ball milling, compaction, microwave sintered, furnace soaked and hot extrusion	Mg - MWCNT - SiCnp	1%wt MWCNT	Tensile: 5%	Tensile: -1%	Tensile: -75%	5%	[149]
ball milling, compaction and hot extrusion	AZ91 - MWCNT	0.5%wt MWCNT	Tensile: 21%	Tensile: 22%	Tensile: -57%		[136]
ball milling, compaction and hot extrusion	AZ91 - MWCNT	1%wt MWCNT	Tensile: 27%	Tensile: 23%	Tensile: -64%		[136]
ball milling, compaction and hot extrusion	AZ91 - MWCNT	3%wt MWCNT	Tensile: 22%	Tensile: 15%	Tensile: -79%		[136]
ball milling, compaction and hot extrusion	AZ91 - MWCNT	5%wt MWCNT	Tensile: 19%	Tensile: -3%	Tensile: -93%		[136]
Ball milling, sintered and hot isostatic pressing	AZ91 - MWCNT		Tensile: 0%	Tensile: 0%	Tensile: 0%		[150]
Ball milling, compaction and melt stirring	AZ91 - MWCNT	1%wt MWCNT	Tensile: 47%	Tensile: 64%	Tensile: 112%		[151]

Literature shows that when MWCNTs are used to reinforce Mg and its alloys, there is generally an increase in mechanical properties and, perhaps most interestingly, a simultaneous increase in ductility. However, some studies still report the traditional trade of a decreasing ductility with increasing mechanical properties. The majority of the studies use solid state processing techniques that also tend to see higher strengthening improvements than melt-processing techniques. The variety of trends reported in the literature and the lack of robust, explanatory evidence of the MWCNTs influence on the metal matrix highlight the need for continued scientific investigation.

Table 2 A summary of the effect of SiC nanoparticle reinforcement on Mg/Mg alloys reported in the literature.

Primary Manufacturing method	Composite	MWCNT content	YS %	US %	Ductility %	Hardness	Ref
Ultrasonic stirring	AZ91 - SiCnp	2% wt				33%	[99]
Ultrasonic stirring	AZ91 - SiCnp	5% wt				66%	[99]
Ultrasonic stirring	AZ91 - SiCnp	0.1%wt	Tensile: 9%	Tensile: 9%	Tensile: 67%		[104]
Ultrasonic stirring	AZ91 - SiCnp	0.3%wt	Tensile: 13%	Tensile: 17%	Tensile: 83%		[104]
Ultrasonic stirring	AZ91 - SiCnp	0.5%wt	Tensile: 18%	Tensile: 23%	Tensile: 127%		[104]
Ultrasonic stirring, vacuum evaporation of liquid melt	Mg6Zn	14%vol	Micropillar compression: 102%				[5]
Melt stirring with squeeze casting	AZ31 - SiCnp	1%wt	Tension: 72%	Tension: 81%	Tension 63%		[152]
Melt stirring with squeeze casting	AZ91 - SiCnp	0.5%vol	Tension: 5%	Tension: -17%		16%	[32]
Melt stirring with squeeze casting	AZ91 - SiCnp	1%vol	Tension: 10%	Tension: -8%		17%	[32]
Melt stirring with squeeze casting	AZ91 - SiCnp	1.5%vol	Tension: 15%	Tension: 0%		20%	[32]
Melt stirring with squeeze casting	AZ91 - SiCnp	2%vol	Tension: 30%	Tension: 1%		22%	[32]
Melt stirring with squeeze casting	AZ91 - SiCnp	3%vol	Tension: 60%	Tension: -3%		24%	[32]
Melt stirring with squeeze casting	AZ91 - SiCnp	5%vol	Tension: 70%	Tension: -10%		39%	[32]
Ball milled	Mg - SiCnp	3%vol	Tension: 25%	Tension: 23%		34%	[153]

The majority of studies investigating SiC nanoparticle reinforced Mg alloys show an increase in mechanical properties compared to the monolithic counterpart. Melt-processing techniques are much more popular for the Mg-SiC composite system than for the Mg-MWCNT composites, most likely due to the ease of production, relevance for real-world application and the wettability of the SiC by molten Mg. SiC particles are available in a range of shapes and sizes and so the Mg-SiC system provides an excellent opportunity to investigate the effect of different particle size geometries and how well these changes are represented by the current strengthening models.

2.4.2 Creep improvement

Improving the strength of Mg and its alloys at elevated temperatures is a challenge [154, 155]. This challenge combined with their low creep resistance has impeded the expansion of their use throughout transport and defence industries [156]. The dominant creep mechanisms for the steady state creep of metal alloys can be determined from the activation energy for creep, Q_c, and stress exponent, n, defined by the following relationship [157]:

$$\dot{\varepsilon}_{SS} = A_0 e^{\left(-\frac{Q_c}{kT}\right)} \left(\frac{\sigma_{SS}}{E}\right)^n \quad (35)$$

Where $\dot{\varepsilon}_{SS}$ is the steady stress-strain rate, A_0 is a constant, k is Boltzmann's constant, σ_{SS} is the steady state stress and E is the Young's modulus. The stress exponent and the creep activation energy can be obtained by a $\log \dot{\varepsilon}_{SS}$ - $\log \sigma_{SS}$ plot and a $\ln \dot{\varepsilon}_{SS}$ - $\frac{1}{T}$ plot, respectively. The creep rate controlling mechanism can be deduced from the stress exponent according to Table 3, [157-159].

Table 3. The rate controlling creep mechanism for a given stress exponent, n. [157-159].

Stress exponent, n	Rate controlling creep mechanism
1	Diffusional
2	Grain boundary sliding
3	Solute drag creep
5	Dislocation climb and glide
6	
7	

The creep resistance of Mg is inherently higher than Al [160], and yet Al alloys largely make up the bulk of powertrain systems where a good creep resistance is required [18]. The root cause of the poor creep resistance related to Mg-Al based alloys is the low thermal stability of the β phase $Mg_{17}Al_{12}$ [161], which has a low melting temperature of 458°C. The β phase $Mg_{17}Al_{12}$ promptly softens and coarsens at temperatures above 120°C, which stimulates grain boundary sliding and provides reduced dislocation motion resistance, respectively [18]. Approaches to try to overcome the low creep resistance of Mg alloys to date has been to either make small changes to improve the widely popular AZ91 [162], by employing the use of RE elements such as yttrium and gadolinium, or more recently, develop Mg – alkaline element alloys such as Mg-Al-Ca or Mg-Al-Sr.

Increased creep resistance can be achieved by adding elements such as REs and Ca that reinforce the grain boundaries. Elemental additions can form thermally stable intermetallics that offer a pinning effect and strengthen the α-Mg through solid solution strengthening and/or precipitation hardening; however, the wider use of REs is restricted due to their high cost, reduced recyclability [163] and increased density, and Mg-Al-Ca alloys have been associated with casting defects such as cold shuts, hot cracking and die sticking [18]. When improving the creep resistance of an Mg-

Al alloy, a key strategy is reducing the volume of β phase $Mg_{17}Al_{12}$ and instead forming secondary phases of a higher thermal stability.

The addition of nanoparticles, such as graphene nanoplatelets, to the metal matrix have the potential to add exciting creep resistance properties by acting as barriers to diffusional material flow [148], inhibiting grain boundary sliding and acting as barriers to dislocation motion for when the composite is subjected to an environment that induces dislocation climb and glide (n = 5-7) whilst being thermally stable to temperatures exceeding the temperature creep limit for a metal matrix (>523K [164]). Katsarou *et al* [165] manufactured Elektron 21 -1wt.% AlN nanoparticle composites using ultrasound-assisted stirring and conducted creep tests at 240°C at stresses from 70MPa to 200MPa. As can be seen from Figure 22, the minimum creep rate for the MMNC was almost an order of magnitude lower for lower stresses between 70-120MPa, with the difference decreasing as the applied stress increases. Ferkal *et al* [153] used high energy ball milling (HEBM) to produce Mg-SiC nanoparticle composites that exhibited creep resistance at 200°C stressed to 35 and 45MPa equal to or better than specially designed creep resistance alloys such as QE22, WE43 and WE54. The increased creep resistance was attributed to the SiC nanoparticles decorating the grain boundaries, a symptom of HEBM and powder metallurgy manufacturing techniques, which inhibits grain boundary sliding. From these early studies, it appears that nanoparticles can have a significantly positive effect on the creep resistance of Mg alloys, even in addition to purely metallurgical creep resistant alloys. The research findings in this section present an important opportunity to explore the impact of nanocarbon additions on the creep resistance of Mg alloys that, to the author's knowledge, has not been previously explored.

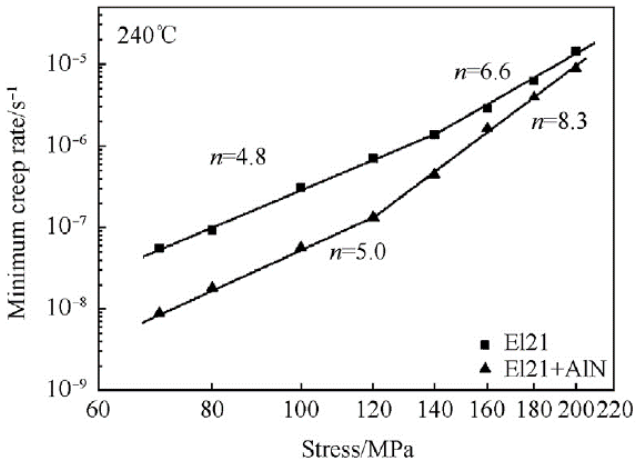

Figure 22. Minimum creep rates at different applied stresses for Elektron 21 and Elektron 21+1wt.% AlN tested at 240°C [165].

2.4.3 Ductility improvement

Mg and its alloys traditionally exhibit poor formability at ambient temperatures due to the limited deformation characteristics that a hexagonal close packed lattice (HCP) provides [141, 166]. The HCP structure leads to a reduced work to fracture and increased processing costs due to the requirement of a controlled elevated temperature, which sometimes result in necessary secondary processes to remove surface cracks. Generally, the techniques used by material scientists and metallurgists to manipulate material properties result in a trade-off between an increase in strength and a reduction in ductility and vice versa, with grain refinement being the exception. A range of Mg-MWCNT [38, 97, 98, 140, 142, 143], Al-MWCNT [167] and other nanocomposite studies have found a mutual increase in strength and ductility using varied manufacturing techniques. A relatively early study by Goh *et al* [87] explained that the observed increase in ductility of the Mg-MWCNT composite they produced was due to the MWCNTs activating cross slip in non-basal planes. Goh [141] later went on to capture TEM images of extruded monolithic Mg and a Mg 1.3wt.% MWCNT composite, showing the existence of dislocation structures in non-basal planes in Mg 1.3wt.% MWCNT and their absence in the pure Mg samples. Similar TEM dislocation studies [141] were conducted on the tensile tested monolithic Mg and Mg 1.3wt.% MWCNT showing that whilst non-basal slip was present in both samples, prismatic slip was absent in the monolithic Mg, with the suggestion that the local strain fields introduced by MWCNTs facilitate the dislocations changing of slip systems. A later study by Chen *et al* [5] discovered activation of non-basal slip systems were discovered as shown in Figure 23 in samples cut from compression test micropillars, and claimed that the SiC nanoparticle reinforcements suppressed basal slip by bringing the effective critical resolved shear stress close to unity for different slip systems, also discussed by [168].

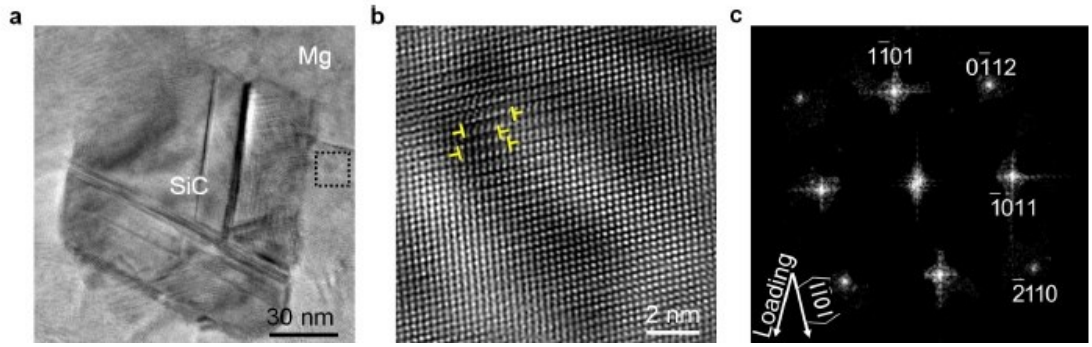

Figure 23 a) Bright field TEM image of a SiC nanoparticle embedded in a Mg matrix. b) High resolution – TEM image of the region highlighted in a) showing dislocations (yellow) terminated at stacking faults on pyramidal planes. c)Fast Fourier transform showing the angle between the loading and pyramidal directions is around 30°.

2.5 Conclusions of the literature review

The fundamental challenge in the development and widespread uptake of bulk MMNCs is to develop a fabrication route that can repeatedly enable homogeneous, individualised nanoparticle dispersions within a metal matrix to produce composites with properties that surpass that of current commercial materials in a cost-effective way. Nanocarbons exhibit excellent specific mechanical properties, which make them ideal reinforcements for MMCs. Melt processing offers a cost-effective manufacturing method that can be easily integrated into well-established techniques currently used, however, the nanocarbon-metal melt interaction offers difficulties in producing stable nanoparticle dispersions, which also must be maintained through solidification, due to the poor wettability of the nanocarbon with the metal melt. Melt processing of Mg nanocomposites reinforced with appropriately surface coated nanocarbons is a potential way of producing stable metal melt-nanocarbon dispersions that can also stimulate solidification front capture due to the enhanced wettability between the surface coating and Mg. An additional potential benefit of a suitable coating on nanocarbon that may form a strong and coherent interface with the Mg matrix, as shown by Han *et al* [94] in section 2.3.3.2, is to achieve enhanced mechanical properties due to more effective load transfer.

SiC nanoparticles and nano-whiskers offer a chance to study the effect of nanoparticle geometry on the mechanical properties of the composite by allowing a comparison between nanoparticles whilst removing the wettability variable, to potentially determine important nanoparticle characteristics such as surface area. In addition to conventional mechanical properties such as ultimate tensile strength, tensile yield strength and elongation to failure, other mechanical properties such as the creep resistance must also be studied and understood. Mg alloys could offer a step change in the light weighting of vehicles by replacing heavier Al and steel alloys currently used, however, their application has been restricted due to poor formability and elevated temperature properties. At present, very few studies, as discussed in section 2.4.2, have investigated the creep properties of Mg-MMNCs, with no creep studies performed for Mg-nanocarbon composites. Such a study could also provide insight into the influence of the nanoparticle geometry on diffusional flow and dislocation interaction. The creep properties of Mg-MMNCs therefore present a research gap, that could provide an alternative solution to, or even enhance the creep resistance of, Mg-RE alloys whilst also providing an a deeper upstanding of the dislocation – nanoparticle interactions.

The room temperature ductility of Mg- nanocomposites have been seen to increase in comparison to their monolithic material. An increase in ductility could lead to enhanced Mg alloy forming procedures that are less likely to initiate surface cracks that require more, expensive, crack removal procedures. The source of this ductility has been attributed to the activation of non-basal prismatic slip planes, that are normally only active at elevated temperatures, observed by Goh[141] and Chen [5]. In addition to this enhanced ductility for formability, nanoparticle additions have been shown to reduce the magnitude of dynamic recrystallisation during forming processes, leading to smaller grain sizes and therefore improved mechanical properties. At present, no studies exist that investigate the efficacy of different nanoparticle geometries ability to pin grain boundaries and therefore reduce dynamic recrystallisation.

The myriad of models for the strengthening mechanisms in particle reinforced metal matrix composites, as previously discussed in section 2.2, were originally developed for microscale reinforcements and it is unclear as to whether these

models can be applied at the nanoscale. With the growth of experimental data for nanocomposites, a systematic study could be undertaken to compare literature results with all combinations of strengthening models and their summation to determine which models best explain the experimental data to date, to guide future experimental work.

3 Mg/AZ91D – MWCNT and Mg/AZ91D - NiCNT alloy nanocomposites

3.1 Experimental

3.1.1 Materials

3.1.1.1 Mg alloy AZ91

The matrix material used in this study was Mg alloy AZ91D, of a composition given in Table 4 provided by non ferrum GmbH. The alloy was supplied as chips of an irregular geometry measuring approximately 5x3mm width x length, shown in Figure 24a. They have a rough and cracked surface providing an increased surface area for the entrapment of nanoparticles.

Table 4. AZ91D Composition used in this study, given by non ferrum GmbH data sheet.

Element	Al	Zinc	Manganese	Silicon	Copper	Nickel	Iron	Beryllium	Others	Mg
% mass	8.9100	0.5334	0.2067	0.0373	0.0052	0.0010	0.0026	0.0010	<0.010	Balance

3.1.1.2 Pure Mg

Pure Mg chips similar in size and shape to that of the AZ91D chips used in this study were provided by Glentham Life Sciences and had a purity of 99.9%, shown in Figure 24b.

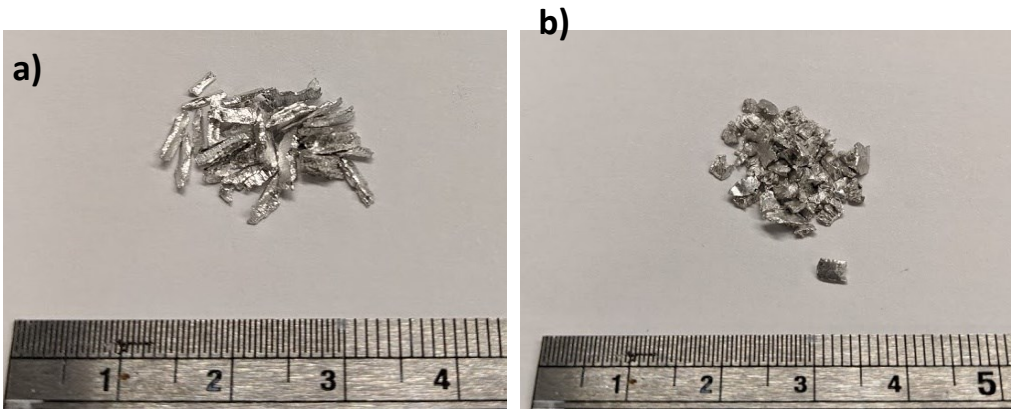

Figure 24. a) AZ91D chips and b) Pure Mg chips used in this study.

3.1.1.3 Multi-walled Carbon Nanotubes

The results presented in this report were for AZ91D – MWCNT composites fabricated with Baytube C150P MWCNTs provided by Bayer Science with an average diameter of 13nm and a length of 1-10µm that were synthesised via catalytic chemical vapour deposition (CCVD). However, as Baytube C150P MWCNTs were no longer in production, NC7000 MWCNTs manufactured by Nanocyl, also via the CCVD method, were used for the pure Mg – NC7000 composites, detailed in Table 6-Table 8. Figure 9 and Figure 25 show the as received state of the Baytubes C150P and NC7000 MWCNTs, respectively.

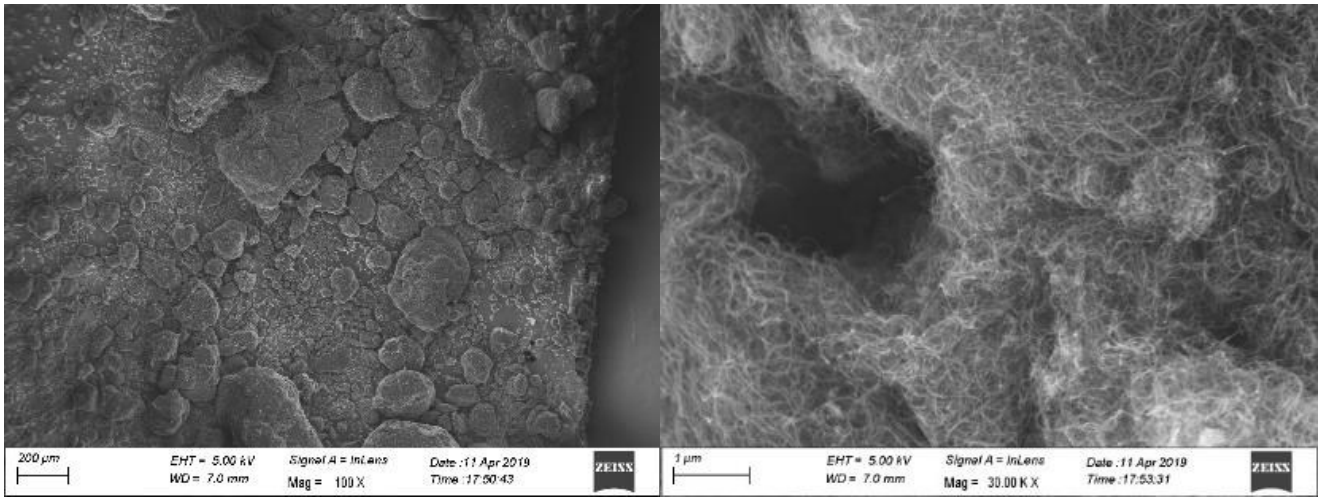

Figure 25. SEM images of as-received NC7000 MWCNTs

3.1.1.4 Nickel coated MWCNTs (NiCNTs)

NiCNTs with an average outside diameter of 8-15nm and length of 10-50µm were used in this study, which were purchased from Nanostructured & Amorphous Materials. Table 5 shows the provided NiCNT composition. The as-received state of the NiCNTs are shown in Figure 26.

Table 5 – Composition of as-received NiCNTs provided by Nanostructured & Amorphous Materials.

Element	Carbon	Aluminium	Chlorine	Sulphur	Nickel
% mass	39.90	0.012	0.036	0.048	Balance

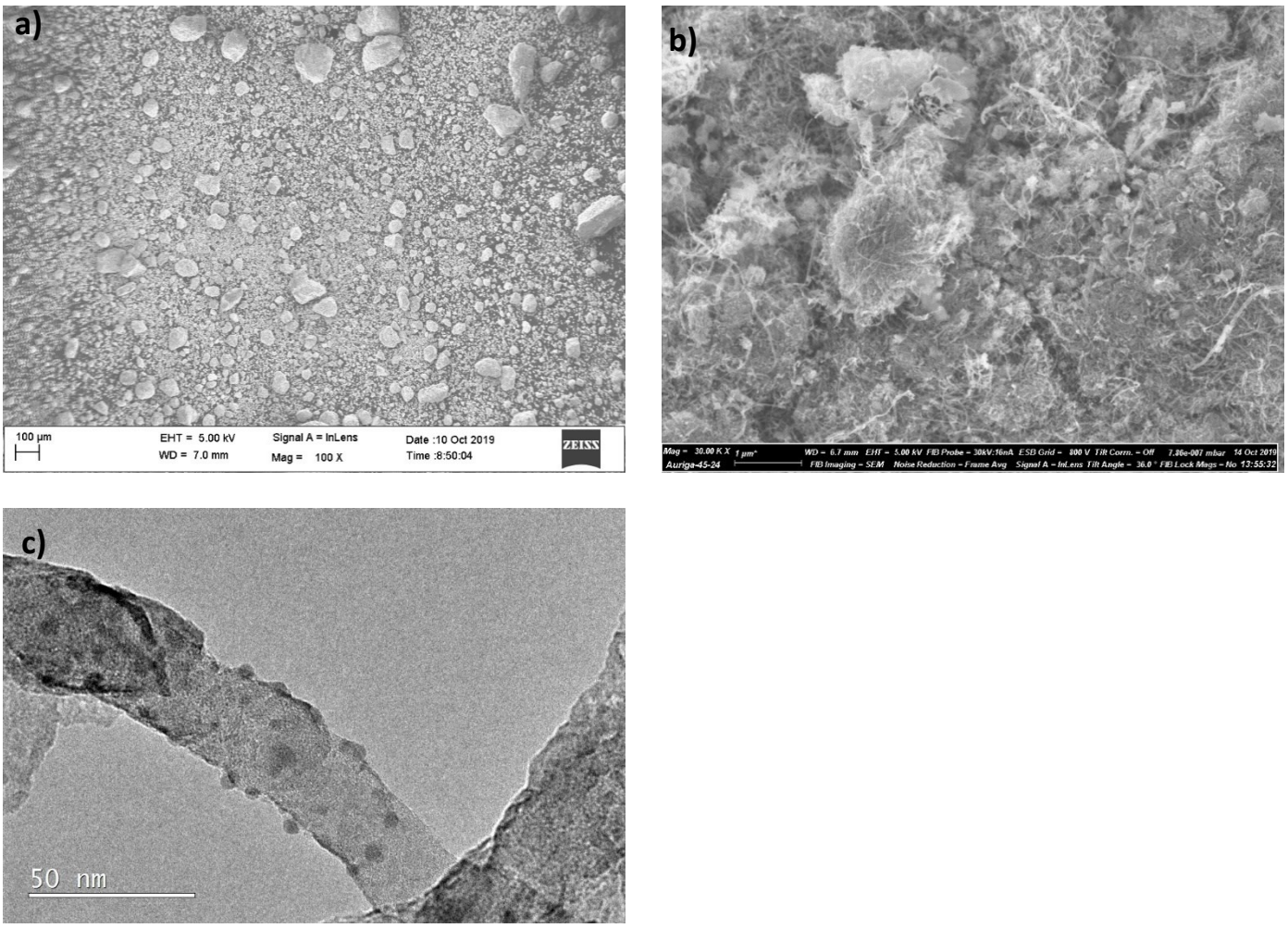

Figure 26. a & b) SEM images of the NiCNTs in their as-received powder form. c) TEM image of Ni nanoparticles decorated on the MWCNT surface.

3.1.1.5 Dispersing Agent

Block copolymer (BCP) Disberbyk 2150, provided by BYK Chemie GmbH, was used as a dispersing agent in an attempt to form stable, well dispersed MWCNT-ethanol dispersions. Adding the BCP to the MWCNT-ethanol mixture provides mechanisms through which MWCNTs can be dispersed and stabilised in ethanol. The opposing ends of the BCP chains are lyophobic and lyophilic, with one end therefore being attracted to the MWCNT and the other attracted to the polar solvent. The steric hindrance and electrostatic repulsion provided by the BCP hampers MWCNT reagglomeration, however, the as-received tight MWCNT bundles need to be separated before the block copolymer can adsorb onto the tube surface and maintain its individualised state. For this reason, ultrasonification was utilised during the pre-dispersion process.

3.1.2 Experimental methods

3.1.2.1 Pre-dispersion

To aid the dispersion of the MWCNTs in the final composite, a pre-dispersion step was taken to initially break up the large bundles of MWCNTs from their as-manufactured state. Firstly, 80ml of ethanol was measured into a 250ml borosilicate beaker, then Disperbyk 2150 was weighed into the ethanol and dissolved with magnetic stirring for 5 minutes at 250rpm. The mass of MWCNTs needed for the target composite composition was then weighed using a ±0.001g VWR scale and added to the BCP-ethanol solution in a ratio of 1:1 with the BCP. The solution was then transferred to a sealable glass bottle that was sealed and placed in an ultrasonic bath for 15 minutes. The solution was afterwards transferred to a 250ml beaker and the weighed AZ91 chips were added to the dispersion. The beaker was in the end placed on a hot plate heated to 50°C and magnetically stirred until the ethanol had evaporated, leaving dry AZ91 chips coated with MWCNTs as shown in Figure 32.

3.1.2.2 Melt stirring and casting

80g of AZ91 MWCNT coated chips were added to a boron nitride coated H13 tool steel crucible, crucible dimensions are shown in Appendix A1. The crucible was then loaded into a vertical tube furnace, as shown in Figure 27a. The crucible was loaded into the furnace from the bottom of the tube, with the stirrer being placed in position at the top of the furnace tube, forming a loose seal around the crucible provided by alumina wool. A flushing cycle was then carried out, schematically shown in Figure 28. After Ar/2% H_2 was flushed at room temperature for 30 minutes, the furnace was raised to 400°C to stimulate the release of oxygen from the system and flushed further for an hour. Disperbyk 2150 decomposes at around 146°C, therefore the BCP on the surface of the chips will be removed during this flushing stage. The flushing gas was then switched to pure Ar to avoid hydrogen embrittlement of the Mg melt and the furnace was raised to the target casting temperature. The pre-heated stirrer is then lowered into the crucible and the semi molten melt is stirred at 780RPM for 30 minutes. After the stirring, the crucible is lowered from the furnace and cast into a permanent steel mould preheated to 200°C producing cylindrical ingots of approximately 11.5 x 120mm diameter x width. The ingots were then machined to 5x7mm diameter x length compression test coupons, labelled as shown in Figure 27c.

Even though at 650°C, AZ91 is approximately 50°C above its liquidus temperature. The chips do not spontaneously form a molten mixture, most likely due to the oxide layer on the surface of the chips, highlighting the need for the melt stirring. After initially varying the casting temperature, it was found that the molten AZ91 was easily castable at 650°C. As this was the lowest possible temperature, a parameter that is favourably minimised by industry, it was used as the temperature to explore the effect of stirring time and nanoparticle reinforcement concentration.

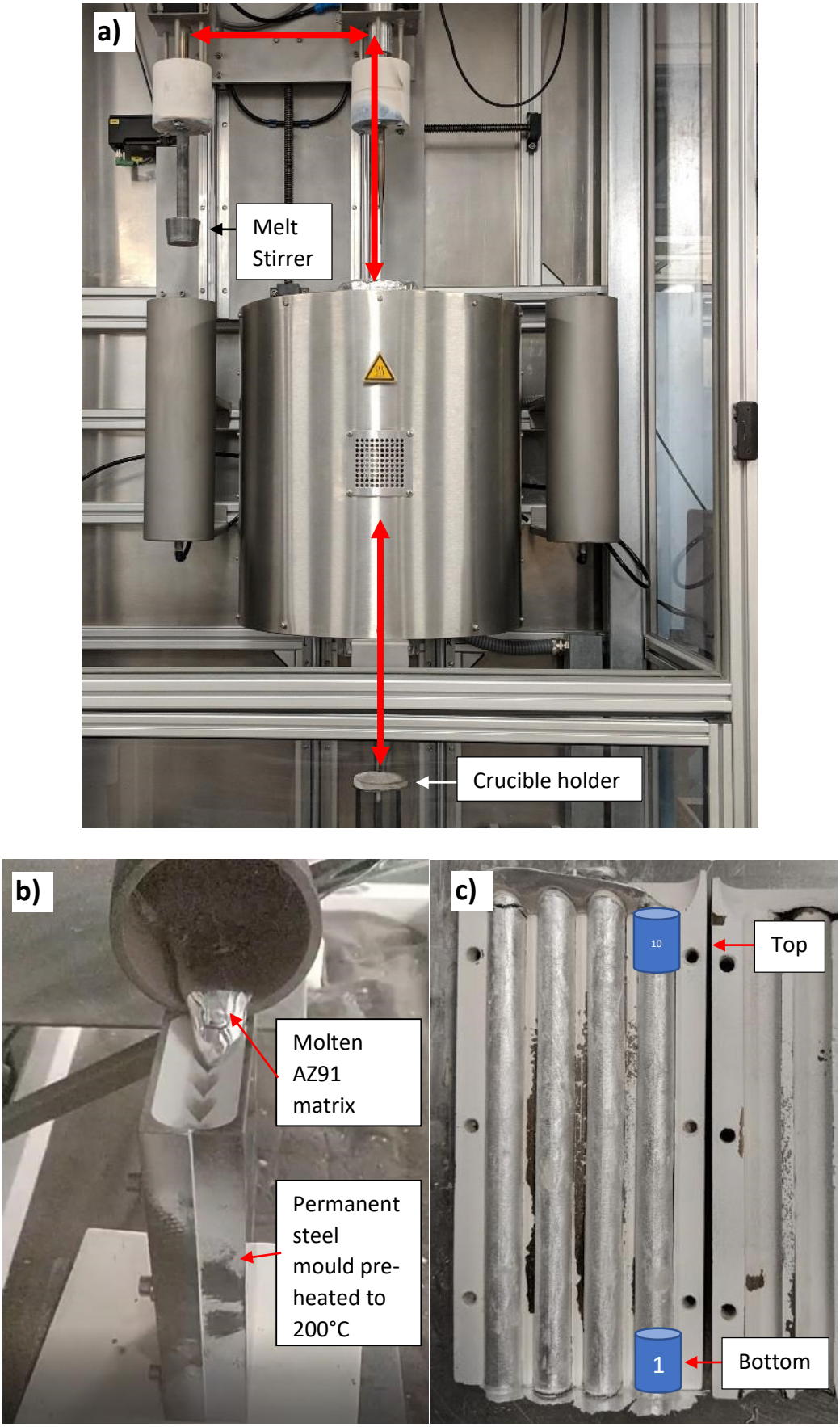

Figure 27. a) Vertical tube furnace showing the bottom loaded crucible and top lowered melt stirrer, with red arrows indicating how the melt stirrer and crucible are loaded into the furnace b) Gravity casting method. C) Cast AZ91D ingots showing how the samples are labelled and the origin of their location from within the cast.

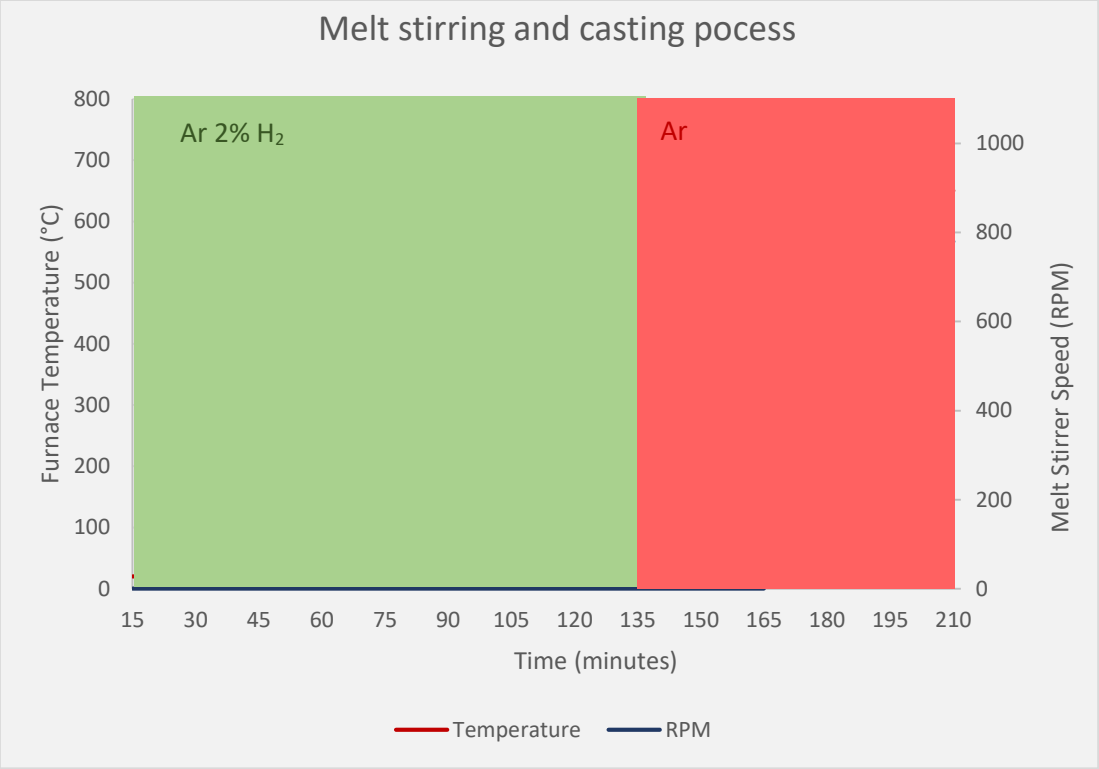

Figure 28. Schematic representation of the furnace flushing cycle and stirring parameters

3.1.2.3 Mg/AZ91D – MWCNT composites – Parameters for fabricated samples

Initial screening experiments, casting AZ91 alloys and AZ91-MWCNT composites, attempted to determine important factors in the processing of the materials. The parameter space initially explored is outlined in Table 6. Only the AZ91_T650_S30_0.1C150 sample, where AZ91, T650, S30 and 0.1C150 represent the matrix, processing temperature (°C), stirring time and 0.1vol% of C150P MWCNT used as reinforcement, respectively, was fabricated 3 times to gain a measure of repeatability. 80g of AZ91 was usually able to produce two 11.5 x 120mm length x diameter cylindrical ingots.

The melt stirring time impact on the mechanical properties was investigated to determine whether longer times was able to produce better dispersions or if it effected the melt quality due to additional oxide inclusion, and by extension, the cast quality.

The MWCNT concentrations interaction with the mechanical properties was investigated to give insight into whether a higher loading of MWCNTs can be well dispersed into the matrix and lead to improved mechanical properties, as the models from section 2.2 suggest.

Following analysis of the results gathered for the samples from Table 6, pure Mg was used instead of AZ91D and NC7000 MWCNTs were used instead of C150P MWCNTs to further explore the effects of melt stirring time and MWCNT vol.% outside the parameter upper and lower bounds used for Table 6 samples. The parameters used for the Mg-MWCNT samples are given in Table 7 & Table 8. A processing temperature of 700°C was used for the Mg samples for the same reason as AZ91, maintaining a 50°C overheat above the liquidus temperature.

Table 6. Processing parameters for the AZ91D – MWCNT samples produced

Materials	Sample ref	Casting Temperature (°C)	Melt Stirring Time (mins)	CNT vol%
AZ91	AZ91_T650_S30	650	30	0
AZ91	AZ91_T700_S30	700	30	0
AZ91	AZ91_T750_S30	750	30	0
AZ91 + Baytubes C150P	AZ91_T650_S30_0.1C150	650	30	0.1
AZ91 + Baytubes C150P	AZ91_T700_S30_0.1C150	700	30	0.1
AZ91 + Baytubes C150P	AZ91_T750_S30_0.1C150	750	30	0.1
AZ91 + Baytubes C150P	AZ91_T650_S15_0.5C150	650	15	0.5
AZ91 + Baytubes C150P	AZ91_T650_S15_0.5C150	650	15	0.5
AZ91 + Baytubes C150P	AZ91_T650_S45_0.05CNT	650	45	0.05
AZ91 + Baytubes C150P	AZ91_T650_S45_0.05CNT	650	45	0.05

Table 7. Processing parameters for the Mg – MWCNT samples produced to explore the effect of melt stirring time.

Materials	Sample ref	Casting Temperature (°C)	Melt Stirring Time (mins)	CNT vol%
Mg	Mg_T700_S2	700	2	0
Mg	Mg_T700_S60	700	60	0
Mg	Mg_T700_S120	700	120	0
Mg + NC7000	Mg_T700_S2_0.1NC7000	700	2	0.1
Mg + NC7000	Mg_T700_S60_0.1NC7000	700	60	0.1
Mg + NC7000	Mg_T700_S120_0.1NC7000	700	120	0.1

Table 8. Processing parameters for the Mg – MWCNT samples produced to explore the effect of MWCNT vol.%.

Materials	Sample ref	Casting Temperature (°C)	Melt Stirring Time (mins)	CNT vol%
Mg	Mg_T700_S30	700	30	0
Mg + NC7000	Mg_T700_S30_0.05NC7000	700	30	0.05
Mg + NC7000	Mg_T700_S30_0.1NC7000	700	30	0.1
Mg + NC7000	Mg_T700_S30_0.5NC7000	700	30	0.5
Mg + NC7000	Mg_T700_S30_1NC7000	700	30	1

3.1.2.4 Mg/AZ91D - NiCNT composites - Parameters for fabricated samples

The methodology used to manufacture the AZ91D-NiCNT and Mg-NiCNT samples is very similar to the method described in section 3.1.2.2, with the exception being that the Disperbyk – 2150 block copolymer was no longer used. When weighing the NiCNTs in preparation to add them to the metal chips, the mass of Ni was considered when calculating what mass of NiCNTs would provide a known volume of carbon that would allow a fair comparison with the previous composites reinforced with raw MWCNTs. The NiCNT manufacturers estimate of a mass ratio of 60:40 for Ni:MWCNT was used.

Table 9 and Table 10 show the manufacturing parameters used for the AZ91D/Mg – NiCNT composites. An AZ91_T650_S30_0.1NiCNT sample was produced to allow a comparison with the raw NC7000 MWCNT reinforced composite; whilst an AZ91_T650_S30_0.8NiCNT sample was produced to accentuate and therefore more easily observe any NiCNT – molten AZ91 interactions that may occur. A Mg_T650_S120_0.8NiCNT
sample was also made for the similar reasons of clarity as the AZ91_T650_S30_0.8NiCNT, however, without the intermetallics formed in AZ91D, the complexity of the resultant microstructure can be further reduced and therefore more easily understood.

Table 9. Processing parameters for the AZ91D – NiCNT samples produced

Materials	Sample ref	Casting Temperature (°C)	Melt Stirring Time (mins)	CNT vol%
AZ91	AZ91_T650_S30	650	30	0
AZ91 + NiCNT	AZ91_T650_S30_0.1NiCNT	650	30	0.1
AZ91 + NiCNT	AZ91_T650_S30_0.8NiCNT	650	30	0.8

Table 10. Processing parameters for the Mg – NiCNT samples produced

Materials	Sample ref	Casting Temperature (°C)	Melt Stirring Time (mins)	CNT vol%
Mg	Mg_T650_S120	700	120	0
Mg + NiCNT	Mg_T650_S120_0.8NiCNT	700	120	0.8

3.1.2.5 AZ91D – MWCNT Enhanced Pre-Dispersion

A method of enhanced pre-dispersion of MWCNTs over the surface of AZ91 chips to investigate whether the extent of the pre-dispersion had any impact on the resultant composite mechanical properties. The initial pre-dispersion method, described in section 3.1.2.1, was followed except for tip sonication replacing the use of an ultrasonic bath, and for rotary evaporation, shown in Figure 29a, replacing the use of magnetic stirring on a hot plate for the removal of ethanol from the AZ91/MWCNT slurry.

A Sonics and Materials VCX 750 ultrasonic system, shown in Figure 29b and c, which utilises an oscillating probe directly in contact with the solution, was used instead of an ultrasonic bath. The ultrasonic power transferred to the solution from a probe can usually achieve much higher cavitation intensities than that of ultrasonic baths due to the localisation of the energy transfer, resulting in enhanced particle dispersion for a given timeframe and dispersed MWCNT bundles that require an energy density not achievable by an ultrasonic bath. A result of the increased intensity can be significant solution heating that can lead to solvent evaporation and influence the cavitation. In order to omit this heating, the solution was suspended in an ice bath and the probe was pulsed for a period of 20 seconds “ON” followed by 10 seconds “OFF” at an amplitude of 50% for 30 minutes in total.

Figure 29.a) Rotary evaporator used in this study [169] b) Sonics and Materials VCX 750 ultrasonic system [170] c) Sonics and Materials VCX 750 ultrasonic processing system used with a MWCNT - ethanol dispersion.

The tip sonicated MWCNT dispersion was then added to a beaker containing weighed AZ91 chips, as before. For the initial pre-dispersion method, the beaker was placed on a hot plate and heated to 50°C and magnetically stirred until the ethanol had evaporated. The beaker was left overnight as the evaporation process took approximately 10 hours, leaving the solution for this long could allow the re-agglomeration of dispersed MWCNTS or significant build-up of MWCNTs in cracks/ridges on the AZ91 chip surface and therefore uneven coating of the AZ91 chips. Therefore, to minimise the evaporation time, a rotary evaporator was employed. The AZ91/0.1vol % MWCNT dispersion slurry was put into a round bottomed flask that could be attached to the rotary evaporator. The pressure inside the flask was then reduced to 250mbar whilst also being submerged in a water bath at 50°C. The round bottomed flask had internal ridges that encouraged the tumbling effect of the chips through the dispersion and even mixing. The ethanol was completely evaporated within approximately 30 minutes and a random sample of MWCNT covered AZ91 chips were inspected using a SEM to inspect the extent of MWCNT dispersion.

3.1.2.6 NiCNT Wettability test

Some simple wetting experiments were conducted with pure aluminium and nickel coated NiCNTs. The aim of these experiments was to investigate whether the nickel coating assisted with the NiCNTs wetting by molten magnesium. Pure Al was used as it could be easily formed into testable coupons, whereas the brittleness of Mg would present extra difficulties, whilst still representing an analogous system to potentially show how molten metal interacts with the NiCNTs. The first attempt was carried out by dispersing 14mg of NiCNTs in 10g of ethanol for 15 minutes in an ultrasonic bath in order to have a well dispersed suspension. The NiCNT dispersion was then dropped onto a strip of aluminium foil and allowed to dry in a HEPA cabinet for approximately 3 hours, as shown in Figure 30a. The strip was then folded up into an approximately $1cm^2$ parcel with two more strips of aluminium foil that were the same length but slight wider than the strip shown in Figure 30a were wrapped around the parcel to ensure the NiCNTs were sealed inside the parcel. The parcel was then placed into a mild steel crucible coated with boron nitride, as shown in Figure 30b. The crucible was then loaded into a furnace at held at 700°C for 60 minutes in an argon atmosphere before being removed from the furnace and allowed to cool to room temperature.

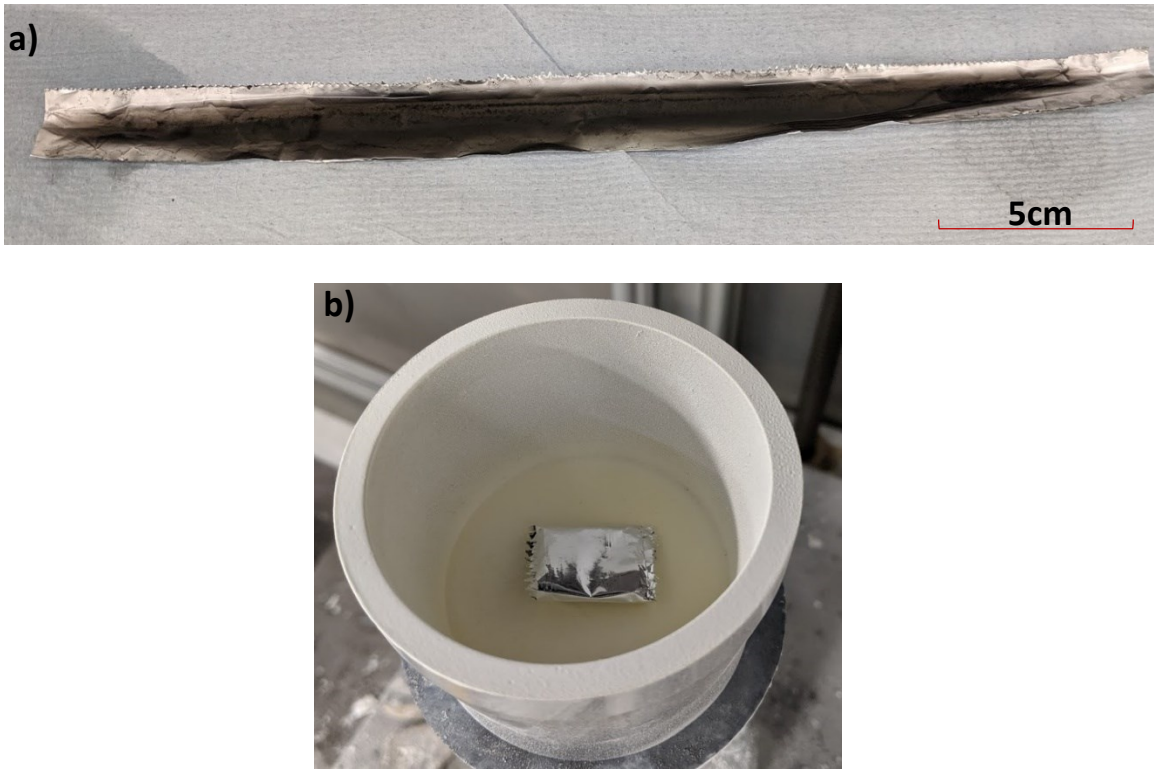

Figure 30. a) Al foil strip with an ethanol-NiCNT dispersion dropped onto and allowed to dry. b) The Al foil folded into a parcel and loaded into a boron nitride coated mild steel crucible.

3.1.3 Characterisation

3.1.3.1 Mechanical and physical properties

Compression tests

The high levels of porosity associated with the current method of casting would result in highly variable results in tension, and the results would only reflect the material properties as a function of porosity, making it difficult to detect the effects of the nanoparticle additions. Thus, compression testing was used to provide more reliable information, by determining the ultimate compression strength (UCS), 0.2% compression yield strength (CYS) and the compressive strain to failure. Compression tests were performed on an Instron 5960 with a 50kN load cell, shown in Figure 31, at a strain rate of $0.01s^{-1}$ to failure on cylindrical coupons cut from the as-cast ingots that were 5x7mm (diameter x length). Approximately 10-11 samples were cut from each ingot for testing. After some initial tests, it was seen that there was a geometrical dependence on the mechanical properties of the tested coupons relative to their location in the as-cast ingot. For all compression results presented in this report, the machined test coupon taken from the bottom of a cast ingot was labelled 1 as in Figure 27c, from 1 (bottom of the cast ingot) → x with x being the number of samples machined from the ingot.

Figure 31. Compression test experimental set-up.

Microhardness

To determine the microhardness of the as cast ingots, a Wilson Tukon 1102/1202 Micro-Hardness Tester was used. 10 measurements were taken from polished cross sections of the top, middle and bottom of an as-cast ingot along a straight line from opposite edges of the circular cross section, passing through the centre. After applying 1kg for 10seconds to the square pyramid Vickers indenter with opposing sides forming an angle of 136°, the diagonals of the indentation were measured, and the Vickers hardness was calculated using:

$$HV = \frac{2\sin(68)F}{d^2} \approx 1.854\frac{F}{d^2} \tag{45}$$

Where d is the length of the diagonal, F is the applied force on the sample and HV is the Vickers hardness.

Density

Initially, the density of each 5x7mm cylindrical coupon was measured by using a micrometer to geometrically determine the volume and using a scale to determine the mass, thereby allowing the density to be calculated. The density measured in this way was then compared to the density of the coupons tested using the Archimedes method. Whilst the geometric method is more time efficient, the Archimedes method is more widely used in literature and less susceptible to inaccuracies such as a slight taper on the cylinder that could lead to an incorrectly used effective diameter. To calculate the density using the Archimedes method, some simple lab equipment was used to determine the necessary variables in the following equation:

$$\rho = \frac{A}{A - B}(\rho_0 - \rho_L) + \rho_L \tag{46}$$

Where

$\rho =$ Density of sample

A = Mass of sample in air

B = Mass of sample in auxillary liquid (water)

ρ_0 = Density of the auxillary liquid (water)

ρ_L = Air density (0.0012g/cm^3)

3.1.3.2 Microstructure

Metallographic sample preparation

To observe the microstructure of the cast samples using different microscopy techniques, cross sections of the as-cast ingot were cut and mounted in a Bakelite puck and ground with SiC sandpaper to P2000 with water, and to P4000 with ethanol to avoid possible oxidation and corrosion. For the polishing stage, 0.04µm silica suspension OP-S NonDry supplied by Struers GmbH was used, being diluted in a ratio of 1:4 with ethanol with a MD-Chem polishing cloth. The sample was ultrasonically cleaned in-between and following the grinding and polishing stages. In order to determine the grain structure of the samples, which would otherwise require a tedious heat treatment process, the polished surfaces were colour etched using a 1:50:150 ratio solution of glacial acetic acid, distilled water and ethanol, respectively. Samples were gently agitated in the etchant for approximately 180 seconds before being rinsed with ethanol and then dried with compressed air. As a final step, warm, humid air was supplied to the etched surface for approximately 30 seconds to improve the grain contrast. Unfortunately, a method for safe polishing the nanoparticle reinforced composited was only agreed recently due to the safety measure in the College and so the composites could not be prepared for colour etching in order to compare the effect of nanoparticle inclusion on grain size for AZ91D castings. This will become an imperative characterisation technique for future work.

Optical microscopy

An Olympus BX53M was used to study the polished cross sections of the as-cast ingots. A U-POTP3 polarising filter was used to generate the colour contrast required for imaging the colour etched samples, enabling grain size measurement.

Scanning electron microscopy (SEM)

A JEOL 6010LA SEM was used to analyse the porosity morphologies of the polished cross sections of the as-cast ingot. Zeiss Auriga and Zeiss Leo Gemini 1525 SEMs were used for the high-resolution imaging of the fracture surfaces of the monolithic and MWCNT AZ91 compression test samples, as received states of MWCNTs and for qualitative representation of the MWCNTs dispersed on AZ91 chips.

3.2 Results and Discussion - Mg/AZ91D – MWCNT/NiCNT nanocomposites

3.2.1 Pre-Dispersion

The aim of the pre-dispersion process was to break up the tightly packed bundles that the various as-received MWCNTs form during their manufacturing process and leave them well dispersed over the surface of the Mg/AZ91 chips. From Figure 32, the coated chips have an even black colour that shows the chips are macroscopically evenly covered. The degree of separation or individualisation of the nanotubes requires high resolution SEM imaging to achieve a clearer qualitative idea of the dispersion state of the tubes. When the dispersion was transferred to the beaker from the bottle after ultrasonification, visible black agglomerates were left behind in the bottle, indicating that the ultrasonification bath was not sufficient in fully dispersing all of the MWCNT agglomerates.

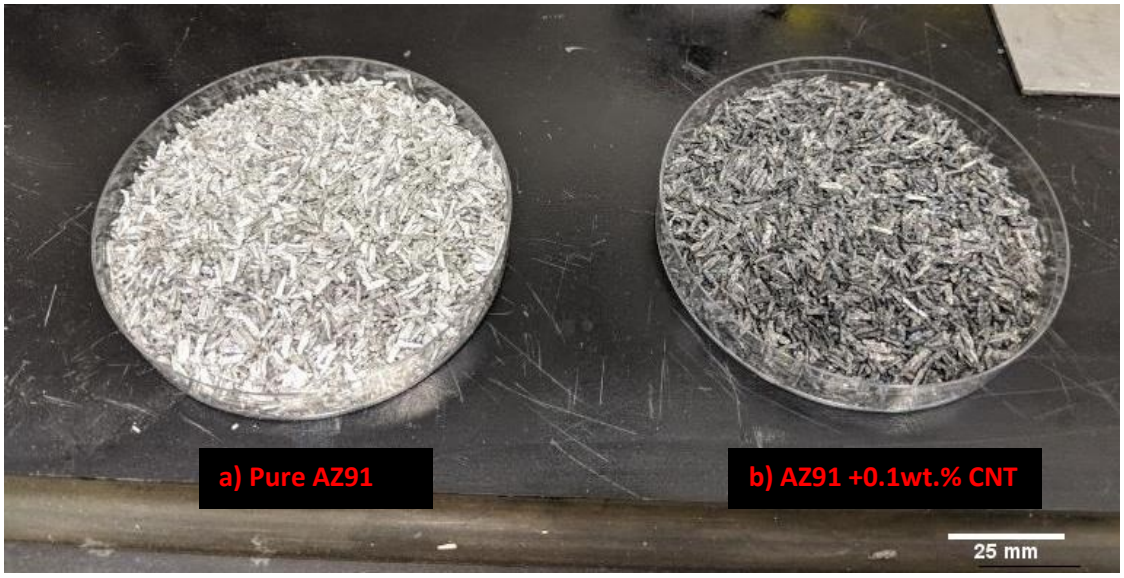

Figure 32. a) Pure AZ91 chips. b) Blackened MWCNT coated chips after the pre-dispersion process.

Whilst there were areas of individualised tubes for the 0.1wt.% CNT chips, bundles were still observed on the surface surrounded by sometimes large areas with no MWCNT deposits, shown in Figure 33a and b, respectively. There were also dense areas of bundles MWCNTs, predominantly where they had the chance to collect, in such areas as cracks and crevices, shown in Figure 34.

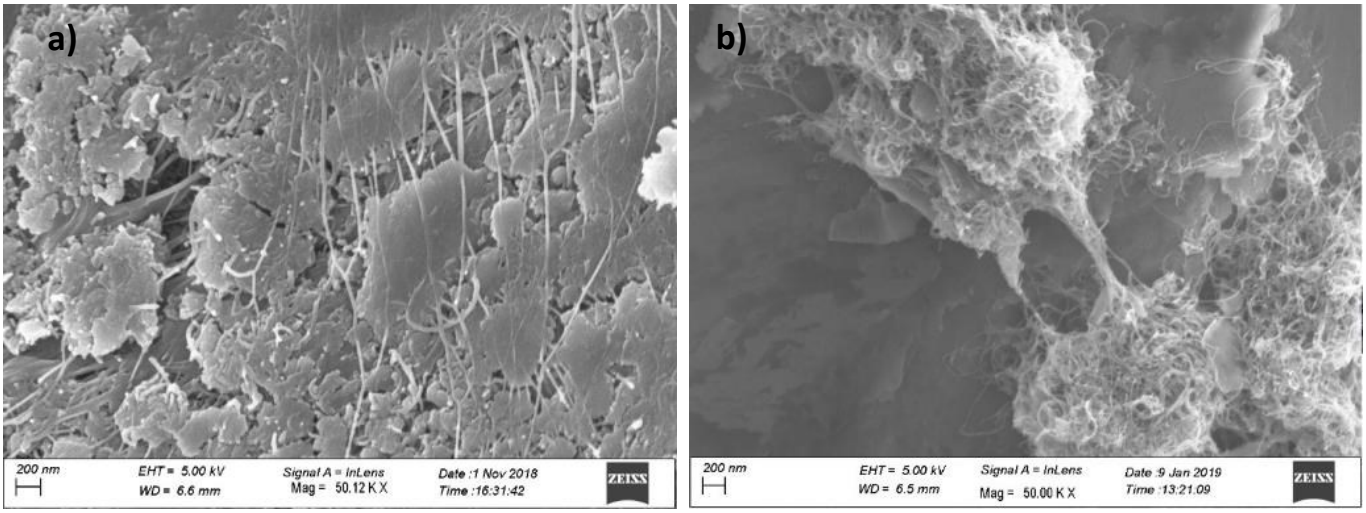

Figure 33. a) areas of well individualised MWCNTs. B) agglomerates that are still present on the surface next to areas of no coverage.

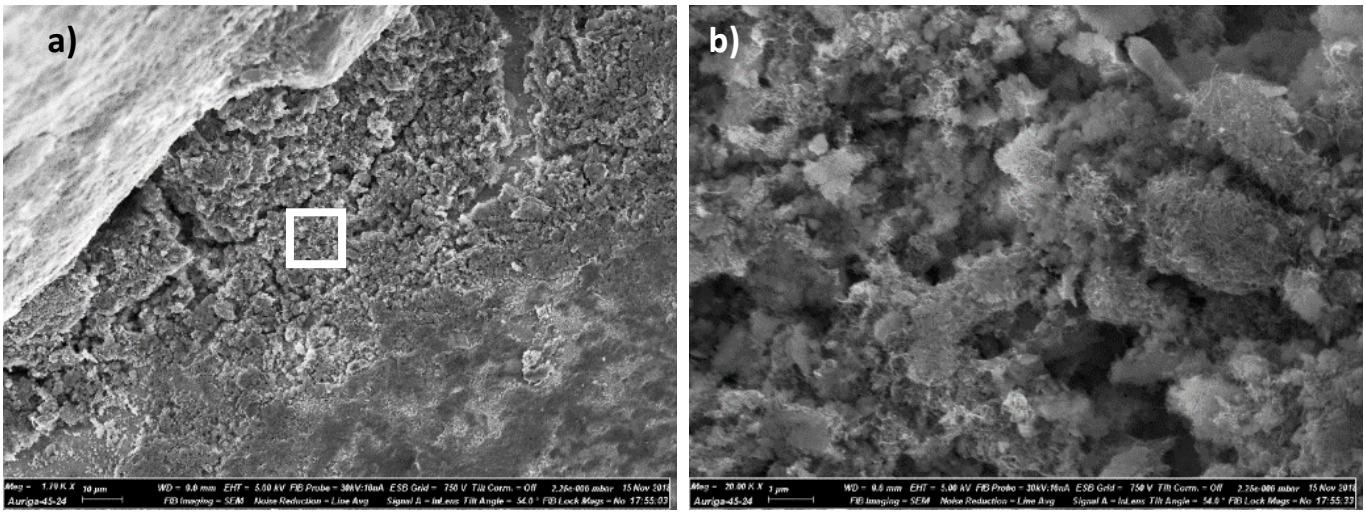

Figure 34. a) Crevice on the chip surface showing a build-up of MWCNT bundles. b) Higher magnification of the highlighted area in a).

3.2.2 AZ91D – C150P Composites

Microstructural Analysis of Cast Quality

The microstructure of as-cast monolithic AZ91 was characterised to establish the baseline properties of the material and to investigate the quality of the casting to understand the degree of shrinkage and/or gas porosity that may be present. The following analysis was conducted on pure AZ91 that was cast at 650°C after being stirred for 30 minutes.

Cross sections from the bottom (Figure 35) and the top (Figure 36) of an as-cast cylindrical ingot were taken and polished without etching and inspected using an optical microscope and a SEM. Gas and shrinkage porosities were observed, the gas porosities shown in Figure 35b and c show a rounded voided that could be up to 50µm across, whereas shrinkage porosity shown in Figure 36b and c, occurs with a network like geometry in the inter-dendritic regions. Gas porosities can be seen throughout the casting. However, shrinkage porosity is only seen in the middle and the top of the casting shown in Figure 36(middle section in Appendix A.2). The gas porosities can originate from either hydrogen gas that was dissolved in the melt that then resolved as its solubility limit in Mg decreases with decreasing temperature, or from gas that is trapped during casting. As the Mg melt starts solidifying through nucleation and growth, dendritic arms form and grow in the direction of a solidification front, forming secondary and tertiary arms as growth continues, consuming the melt and forming a solid polycrystal.

Shrinkage porosity occurs when the supply of molten metal for the solidification front is exhausted, resulting in areas of porosity occurring between incident growing dendritic arms, as shown in Figure 36b and c. Shrinkage is usually found to be most predominant in the centre of the casting, as the solidification fronts follow the thermal gradients generated by the relatively cold mould walls to the hot cavity centre, however, in Figure 36a, it appears to be concentrated in an area off centre (as circled in red in Figure 36a). The off-centre location of the porosity could be due to the unsymmetrical nature of the mould that creates a thermal gradient that is perpendicular to the pouring direction, due to the ‘centre’ of the mould not being the same as the centre of the mould cavity, but elsewhere. These two types of porosities can significantly affect the mechanical properties of the material by facilitating crack generation and growth.

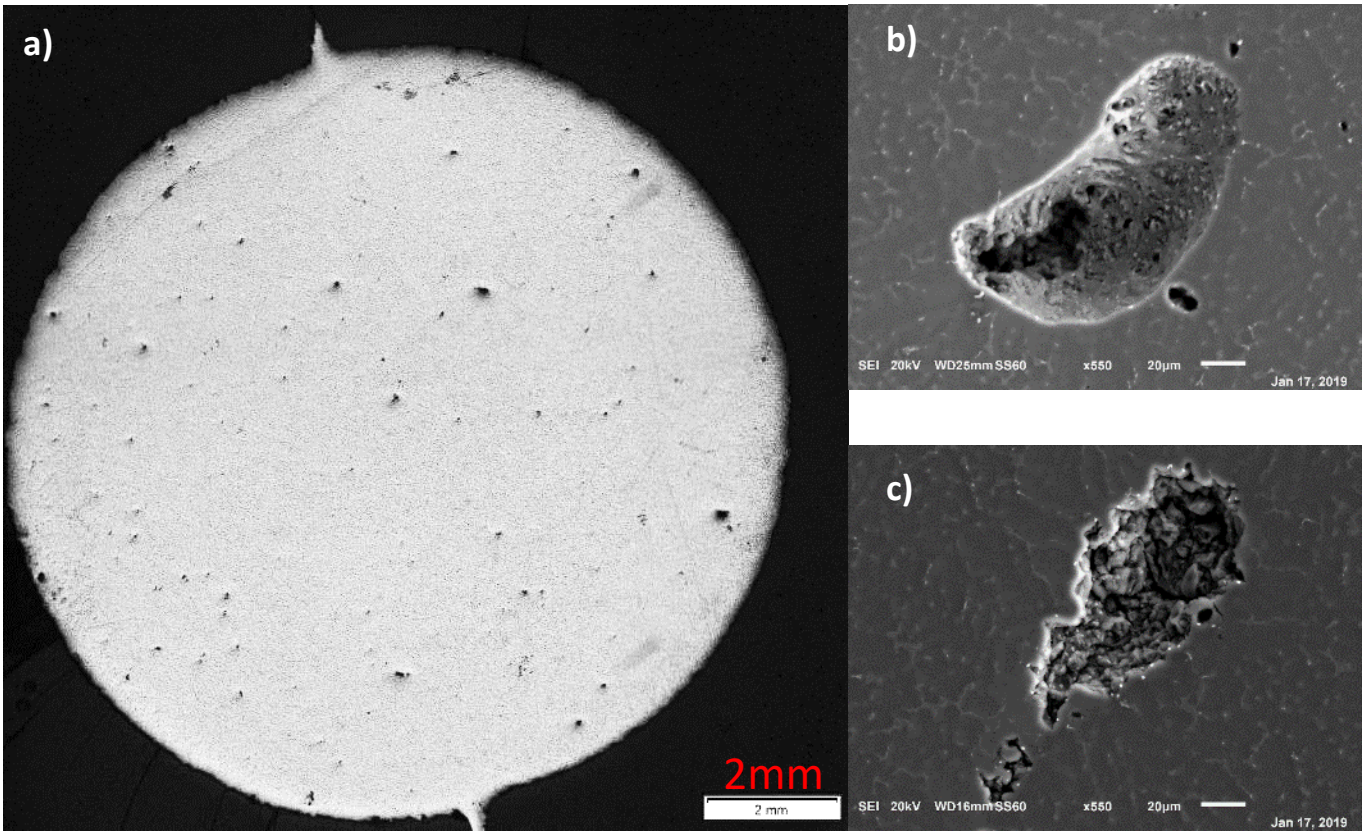

Figure 35. a) Bottom of the cross section of an as-cast ingot. b&c) representative images of the types of porosities seem in the cross section.

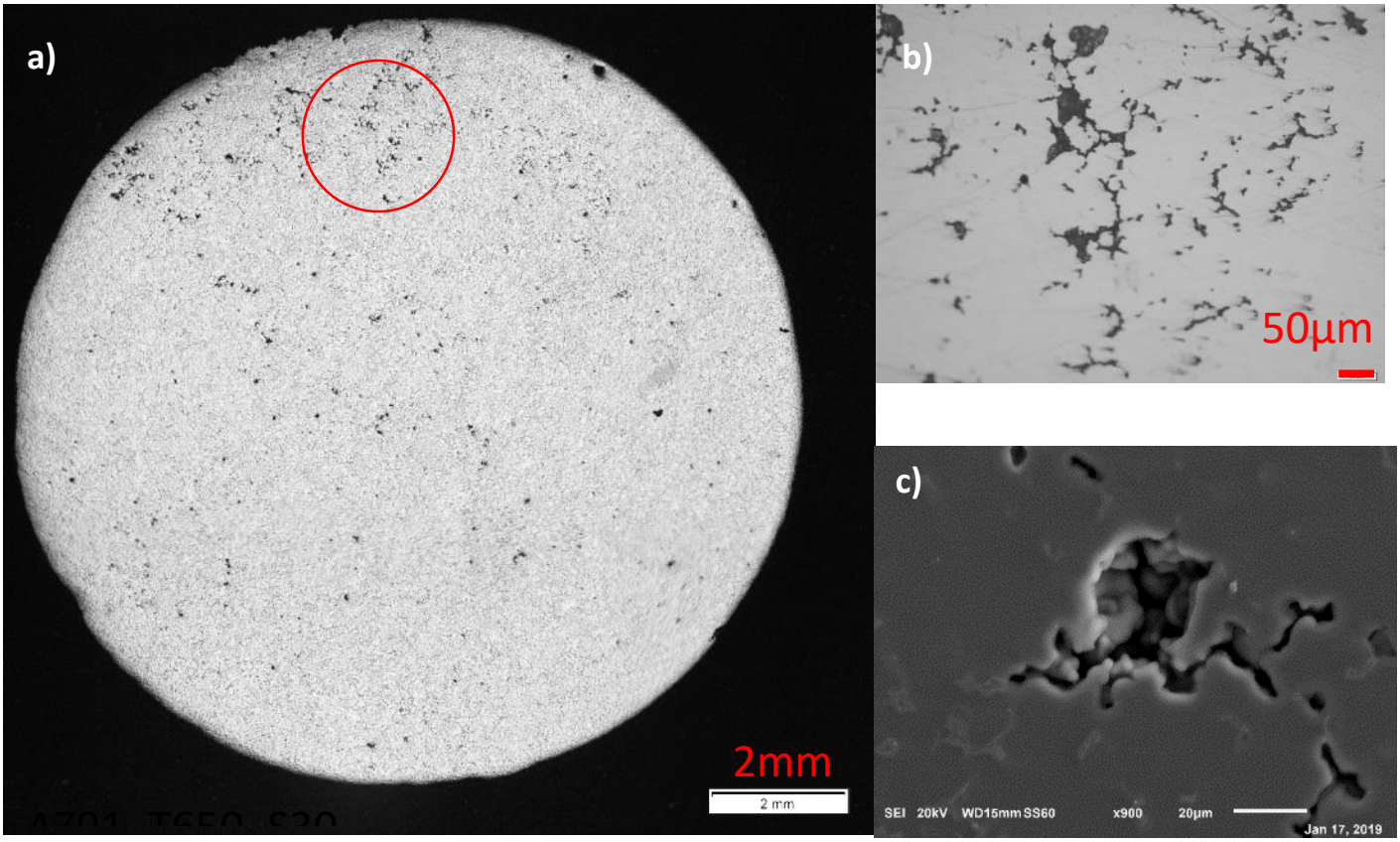

Figure 36. a) A cross section taken from the top of an as-cast ingot showing gas porosities as well as shrinkage porosity. b) Optical micrograph of the shrinkage porosity highlighted by red circle in a). c) representative SEM image of the shrinkage porosity, showing an air gap between dendrite arms.

Compression Test

The UCS, CYS, compression at failure and representative stress strain curves for the pure AZ91D and composite comparison cast at 650°C are shown in Figure 37a. It should be noted that for each sample set, an as-cast ingot contained approximately 2 to 3 test coupons that failed at very low stresses and or exhibited very high porosity, for this reason a filter was applied, throughout this study, to the compression testing results that omitted coupons that failed at or below 350 MPa and had a porosity of >5%.

Samples were cast at 650, 700 and 750°C to find the optimum processing and casting temperature. The casting temperature was varied due to its effect on several aspects of the process, such as when the temperature of molten Mg is increased above 650°C, the rate of surface oxidation increases rapidly [7]. Oxidation is a concern when using only Ar as a flushing gas in the metal furnace, which is not strictly an air tight system, instead of a cover gas such as SF_6 to provide a protective atmosphere, especially during melt stirring when a fresh melt surface is continuously exposed and then incorporated back into the melt. Increasing the casting temperature can also lead to increased fluidity for casting and potentially reduce the impact of shrinkage porosity due to higher solidification rates.

It is apparent that the monolithic AZ91 alloy exhibits slightly higher UCS values than their 0.1wt.% MWCNT composite counterparts for all casting temperatures, however, the maximum difference occurring at a casting temperature of 650°C is a slim 3.9% decrease. The casting temperature and addition of Baytube C150P MWCNTs seems to have little effect on the 0.2% CYS and elongation to failure of the AZ91 alloy.

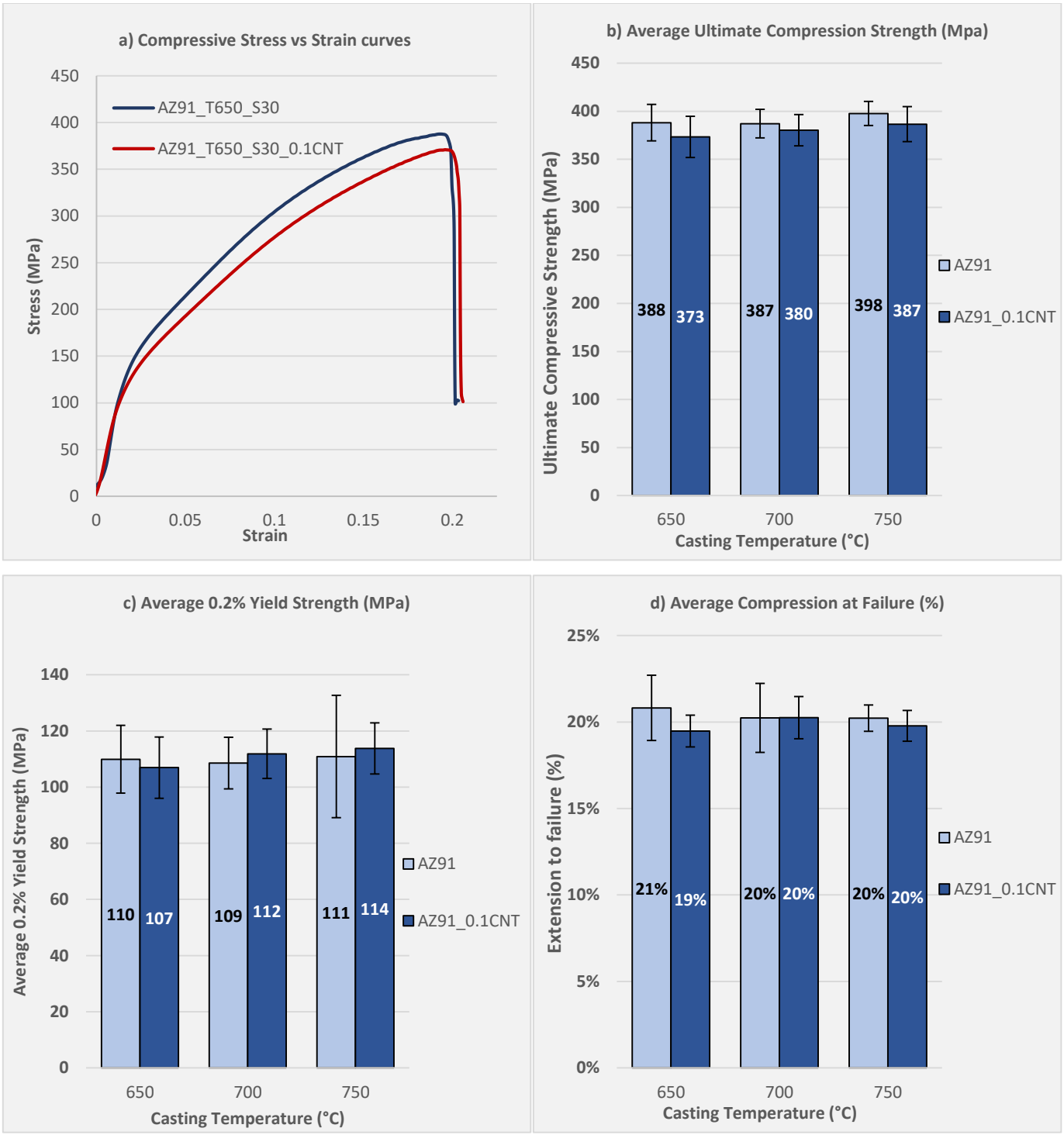

Figure 37. a) Representative stress vs strain curves for AZ91_T650_S30 and its 0.1% C150P counterpart composite. b,c,d) Average UCS, 0.2% yield strength and compression to failure values, respectively, for pure AZ91 and 0.1vol.% C150P composite at different casting temperatures. Error bars represent standard deviation.

A screening experiment was conducted to investigate the influence of stirring time and MWCNT concentration on the mechanical properties of the as cast alloy. Figure 38 shows that an increase in stirring time for both MWCNT concentration leads to a slight increase in both UCS and 0.2% CYS, whilst the increase in vol.% loading has no effect on the mechanical properties for the 15-minute stirred composites, but a slight decrease for the 45-minute stirred composites.

The screening experiment, shown in Figure 38, into the AZ91D melt stirring time and MWCNT loading was conducted to initially determine the extent of, if any, the effect that they have on the final mechanical properties of the composite. The mechanical properties of the AZ91-MWCNT composites were found to be similar when compared to their monolithic counterparts, for all processing parameters. The UCS of the MWCNT composites showed a slight decrease across all casting temperatures, with the largest decrease found to be 3.9% for the samples casted at 650°C. The 0.2% yield stress, as with the UCS, is similar for all samples with the largest difference between comparable composites being a 2.7% decrease from the monolithic AZ91 to the equivalent 0.1wt.% MWCNT composite. The standard deviation on almost all measurements lead to a substantially overlap between results, that subsequent t-tests determined no significant difference between them. The mechanical properties of the samples with varied stirring time and MWCNT concentration were, again, very similar. The resultant properties could be similar due to the boundaries used for the melt stirring time and MWCNT concentration are not wide enough to reliably detect their effect on the mechanical properties or due to processing factors discussed shortly, even though if the same theoretical models are followed for AZ91D-MWCNT composites as shown in Figure 46, increasing the MWCNT concentration from 0.05vol% to 0.5vol% should result in an increase in yield strength of approximately 50%.

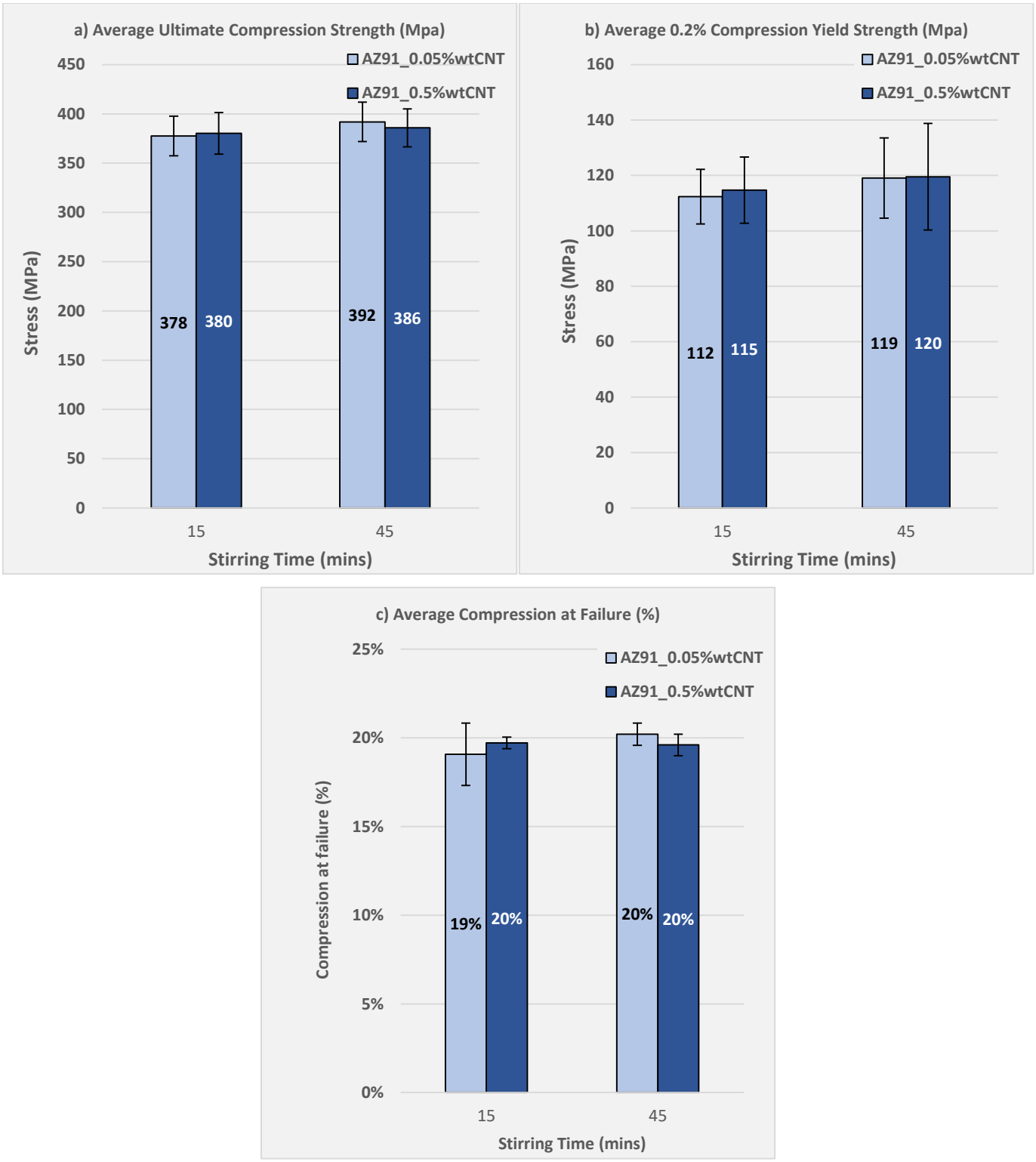

Figure 38. a,b,c) Average UCS, 0.2% yield strength and compression to failure values, respectively, For AZ91 CNT composites at different stirring and MWCNT concentrations.

Density

As previously mentioned, after some initial tests, a dependence on the mechanical properties of the compression test coupons on their position within the cast ingot became apparent. Each coupon was labelled as shown in Figure 27, from 1 (bottom of the cast ingot) → x with x being the number of samples machined from the ingot. Across the repeated AZ91_T650_S30_0.1CNT samples cast, the average density measured for each coupon by position was converted into a percentage of the density of pore-free AZ91, plotted in Figure 39a. The lowest density is consistently found to be in the middle section of the ingot, which could be explained by this being the area where the solidification rate is the slowest and would therefore be supplying the solidification of the top and bottom of the melt. The relationship of the density with the sample position is also reflected across all 12 cast samples, shown in Figure 39b, regardless of the slightly different parameters used, suggesting the relationship is a symptom of the casting technique and mould design instead of any other parameters. The change in density of the composite compared to the monolithic material is negligible.

The overall trend of decreasing density as the coupons were tested from the bottom to the top of the ingot, with the lowest density measured in the middle of the ingot, is also reflected in the measured UCS with the minimum for density and UCS values being found for sample 6, in the region of the middle of the casting. The compressive stress-strain curve for samples from position 1 and 6 for an AZ91_T650_S30_0.1CNT sample can be found in Appendix A.2. After the samples of Table 6 (AZ91D-MWCNT) were made, a preheated ceramic plate was placed under the preheated permanent steel mould. The ceramic base led to much more consistent mechanical properties throughout the ingot, as reflected in Figure 42, with the lowest still observed in the centre of the ingot, most likely due to reduced thermal gradients within the mould and therefore also the solidifying material.

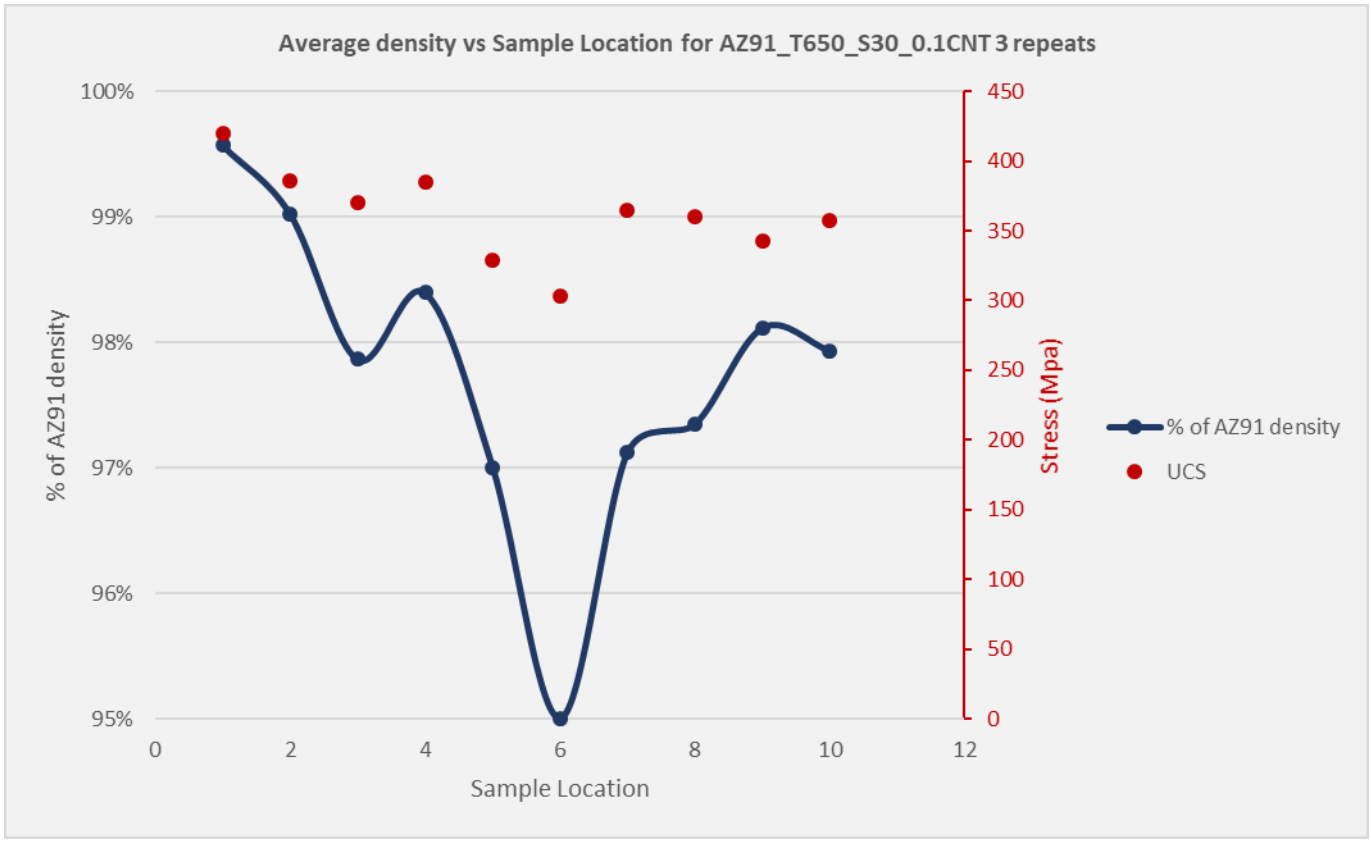

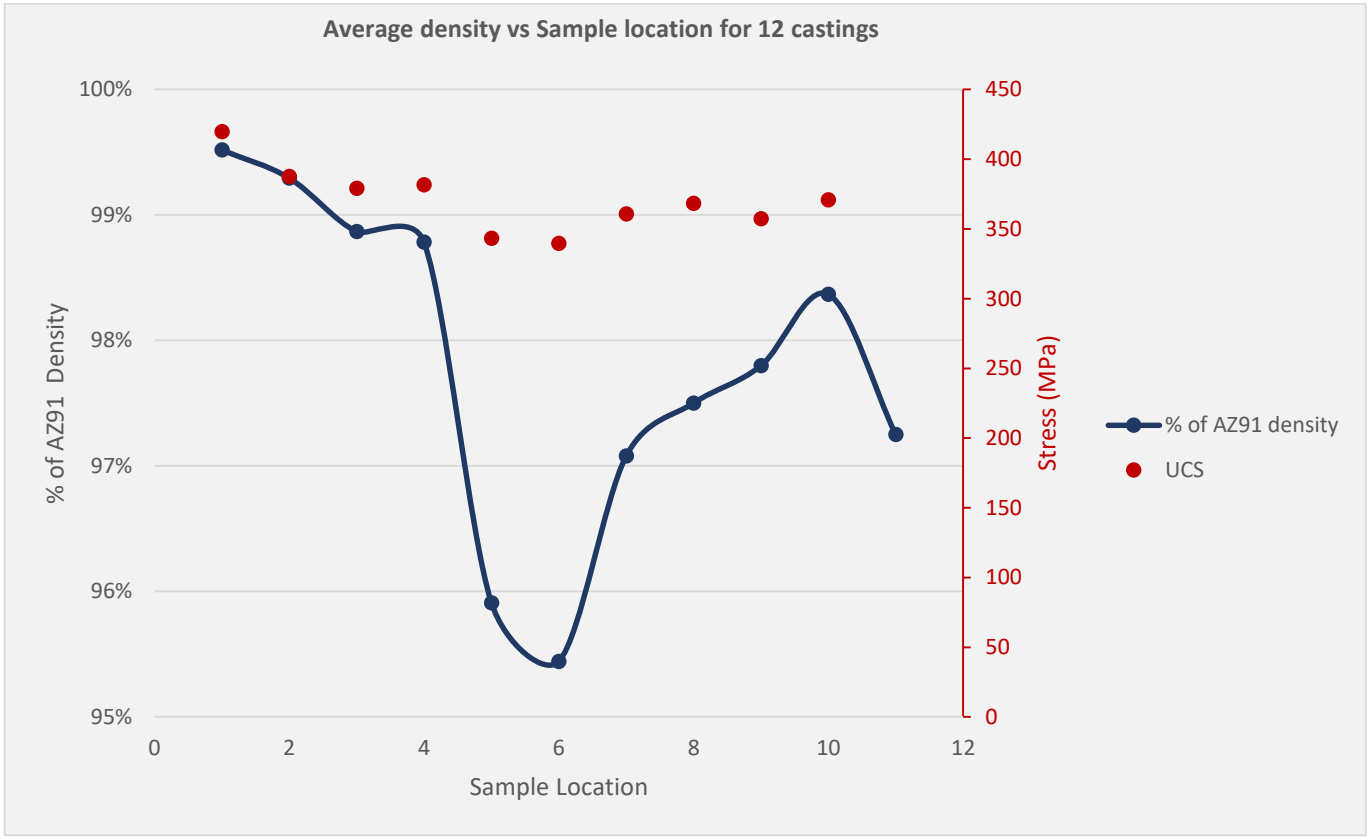

Figure 39. a,b) A plot showing how the average density for 3 cast AZ91_T650_S30_0.1CNT ingots vary from the bottom to the top of an as-cast ingot (1 taken from the bottom – 10 from the top) and for all casted samples, respectively.

Fracture surface after Compression Tests

As expected, the cylindrical coupons usually failed with a single crack propagating approximately 45^{o} through the material from opposing edges as this is the angle of the maximum resolved shear stress, shown in Figure 40e. SEM was used to inspect the fracture surfaces of samples AZ91_T650_S30 and AZ91_T650_S30_0.1CNT taken from the bottom of the cast. From a macroscopic point of view, there appears to be little difference between the monolithic AZ91 and the composite, with both showing brittle failure; however, this is most likely due to the nature of the compression test causing significant surface deformation due to friction between the fracture surfaces post fracture. At higher magnification, whilst pits and crevices were still found in the monolithic fracture surface, in the MWCNT composite these pits and crevices were regularly found to include MWCNT bundles up to more an 1µm in diameter. Figure 40c shows such a bundle with a clear separation with the metal matrix, indicating that the metal melt had not wetted the bundles of MWCNTs and therefore would have likely, from the metal matrix's point of view, acted as a defect.

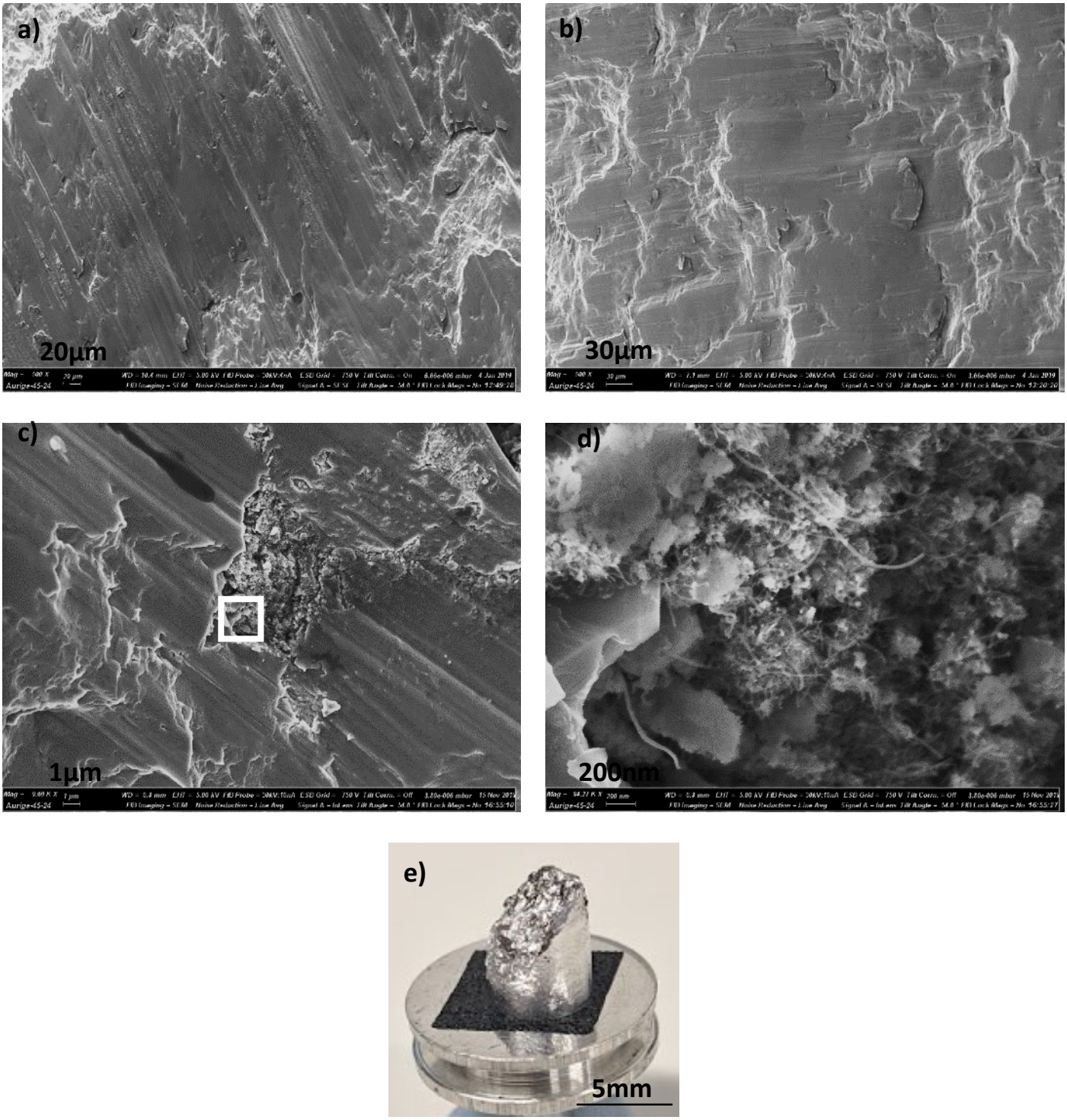

Figure 40. a,b) Fracture surface of the monolithic and AZ91-MWCNT, respectively. C) SEM image of a MWCNT agglomerate found in the fracture surface of the AZ91_MWCNT composites. D) Magnified image of the highlighted section in c). e) Compression test sample fracture.

Enhanced Pre-Dispersion

Figure 41a and b show the dispersion of NC7000 MWCNTs on the surface of AZ91 chips using the original pre-dispersion method dispersed with an ultrasonic bath and magnetic stirring. MWCNT agglomerates were regularly found on the AZ91 chip surface with individualised tubes sometimes only found in close proximity. However, there were large areas of chip surface were MWCNTs could not be found. Using the enhanced pre-dispersion method with the sonotrode, whilst agglomerates could still be found, as shown in Figure 41c and d, the significant difference when compared to the original method was that in the large areas between agglomerates, and even coating of individualised MWCNTs were found almost everywhere, best shown in Figure 41e and f. AZ91 chips were also prepared in the same way without MWCNTs.

The chips were then melt stirred for 30 minutes at 650°C using the process that is outlined in Figure 28 and the resultant as cast ingots were then machined into compression test coupons and subsequently mechanically tested. The values determined for the UCS, CYS and compression at failure for the sample with enhanced pre-dispersion are similar to that of pure AZ91 processed in the same way, shown in Figure 42. The similar mechanical properties suggest that the MWCNTs are in fact having little impact and an aspect of the current fabrication method makes the pre-dispersion of the MWCNTs redundant. The melt stirring stage could be reagglomerating the MWCNTs within the melt, which is explored in the section 3.2.4, or a significant amount of MWCNTs could be being rejected from the melt.

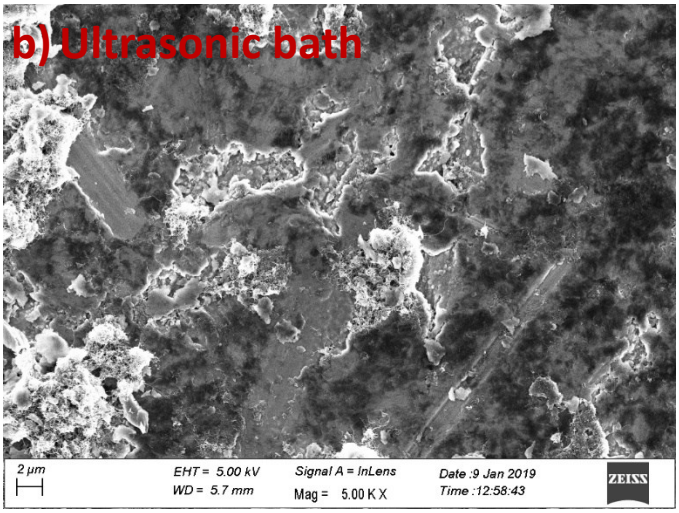

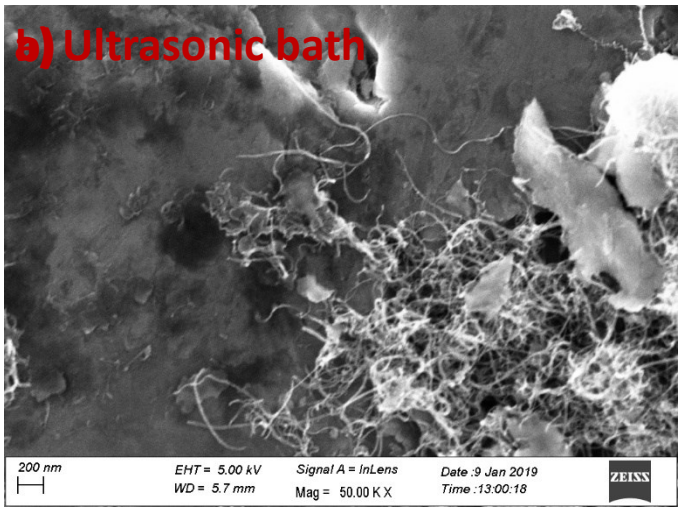

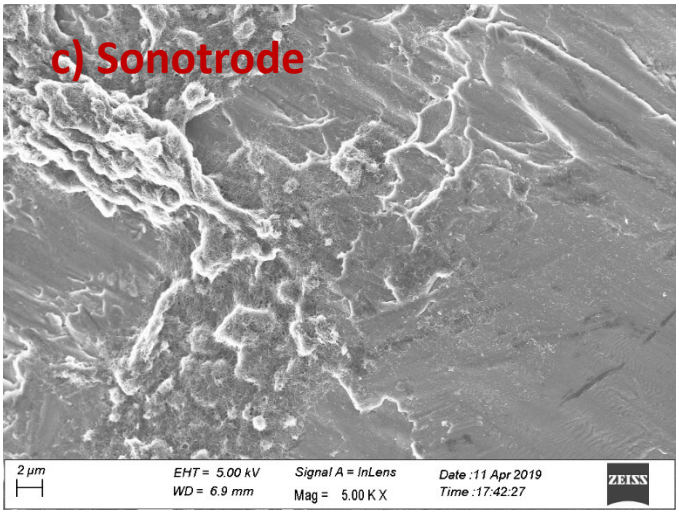

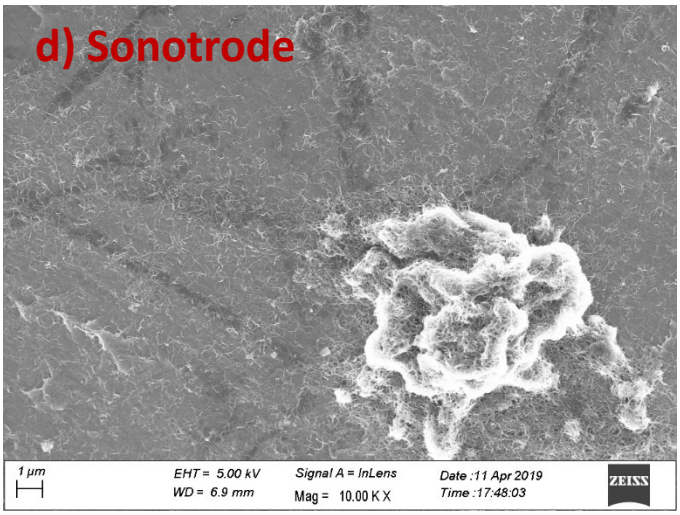

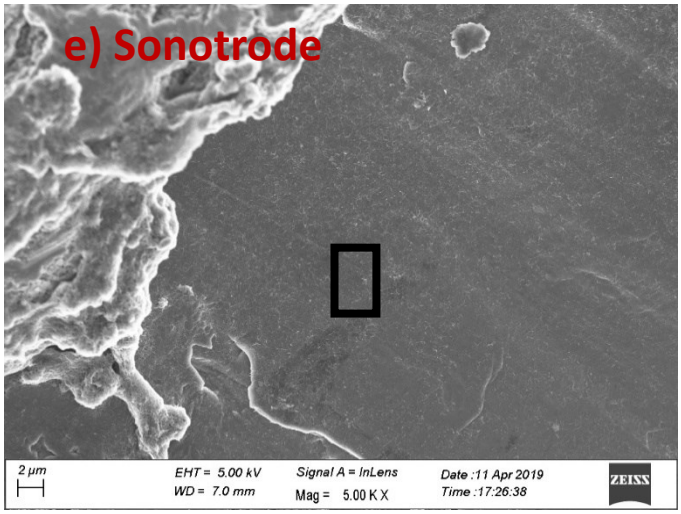

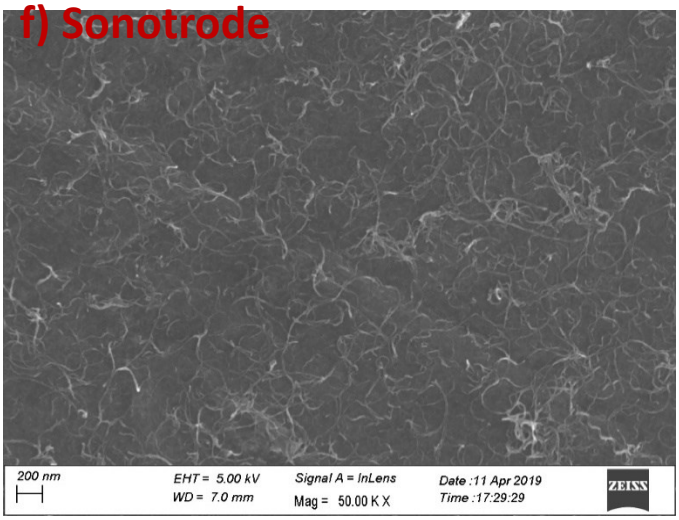

Figure 41 a) and b) show the dispersion of NC7000 MWCNTs on AZ91D chips using the original pre-dispersion method described in section 3.1.2.1. c),d),e) and f) show that even though bundles do still exist on the AZ91D chip after the enhanced pre-dispersion method, there are also vast areas covered with individualised MWCNTs, that is not found previously.

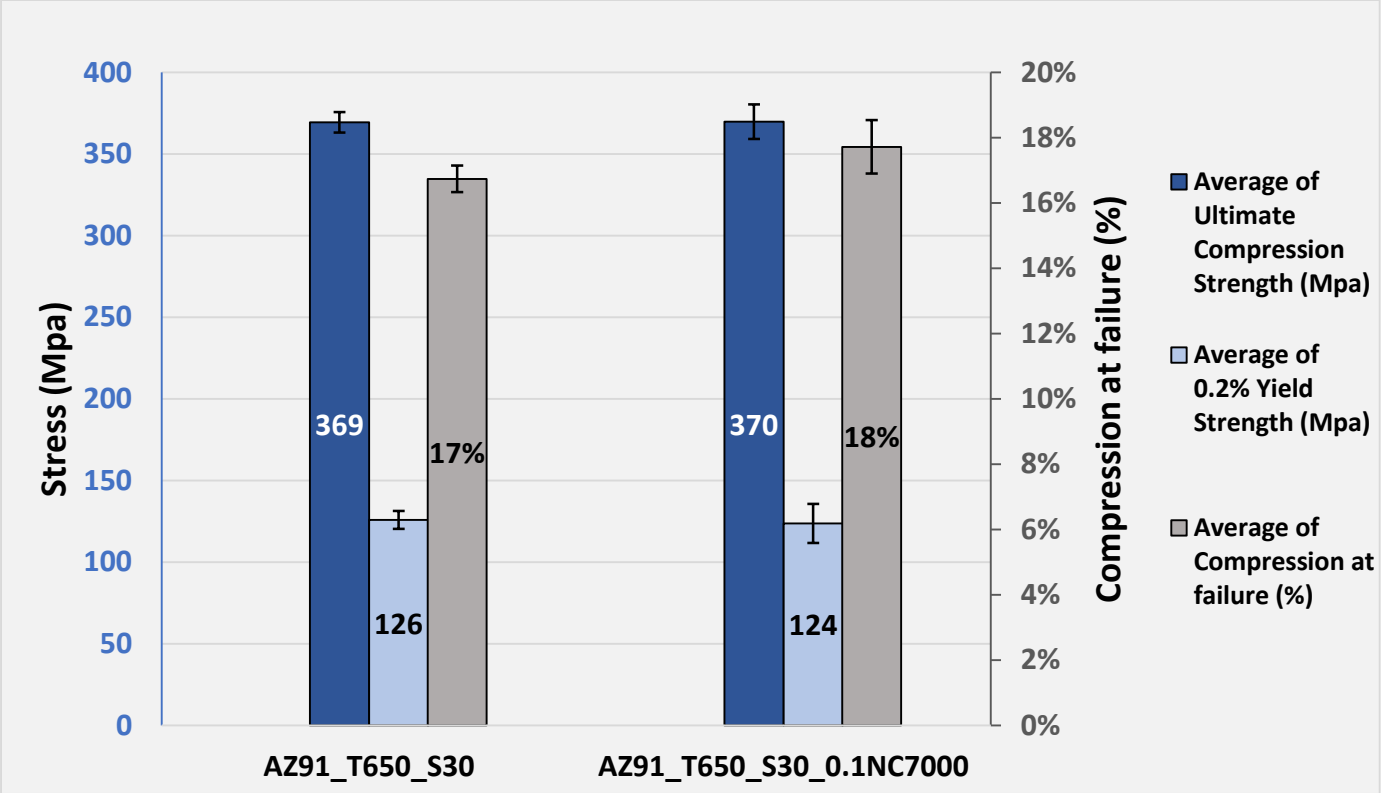

Figure 42. Average UCS, 0.2% yield strength and compression to failure values, respectively, for pure AZ91 and 0.1wt.% CNT composite at different casting temperatures. Error bars represent standard deviation.

3.2.3 Pure Mg – NC7000 composites

The results of the compression mechanical testing of all of the AZ91D – MWCNT composites were very similar. Due to the significant mechanical effects of the $\beta - Mg_{17}Al_{12}$ intermetallic network that is formed during the casting of AZ91D and how it can vary from cast to cast, pure Mg was tested as a matrix material to remove the intermetallic as a variable that is associated with the as-cast mechanical properties of the samples. Whilst a casting temperature of Mg – liquidus (650°C) + 50°C of overheat was maintained, the effects of %.vol MWCNT and stirring time were investigated with extended upper and lower boundaries of the parameters explored for AZ91D-MWCNT composites. The vol.% of MWCNT was varied from 0.05 – 1%.vol and the melt stirring time was varied from 2 -120 minutes. The pre-dispersion process for the pure Mg samples was carried out using the ultrasonic bath.

Following the analysis of the interaction between the MWCNTs and the Mg melt, discussed in section 3.2.4, suggesting that the combination of the potential attractive van der Waals forces between the MWCNTs in the Mg melt and the melt stirring would likely result in the reagglomeration of the MWCNTs, the effect of the melt stirring time was tested over a long range to investigate whether this effect could be detected. It was deduced that the MWCNTs would be in their most dispersed state following the pre-dispersion step, before any melt stirring, so the melt stirring time of 2 minutes was used as the minimum stirring time as some initial trails showed that at least 2 minutes was required to ensure the homogenous melting of the Mg chips. The following detailed study of the effect of the MWCNT loading allowed any found trend in yield strength to be compared with the theoretical prediction model that is used throughout literature for metal matrix nanocomposites.

3.2.3.1 Mechanical Properties

Figure 43 shows the compressive mechanical properties of the samples fabricated with 0.1%.vol of MWCNTS over a wide range of stirring times. When lower stirring times of 2 and 30 minutes are used, there appears to be an increase of 11% and 8% in UCS of NC7000 reinforced samples, respectively. The NC7000 reinforced samples with the longer stirring times of 60 and 120 minutes show a very small decrease in UCS compared to the pure samples. The decrease in UCS for the longer stirred samples could be due to the discussed re-agglomeration effects or the increased time allowed for the NC7000 tubes to separate or be rejected from the melt. The UCS for the pure Mg samples increased slowly with increased stirring time, potentially due to increased Mg oxide formation and strengthening. There is no obvious relation between compression strain at failure and MWCNT loading, however, both the pure and composite samples seem to have an increased compression at failure for 30 and 60 minutes of stirring as opposed to 2 and 120 minutes, suggesting the effect is most likely due to processing parameters that influence the quality of the casting instead of the presence of MWCNTs. Compression at failure is a metric that is very sensitive to cast quality, reflected by the large standard deviations and therefore small changes will be difficult to detect with the characterisation and manufacturing methods used for this study.

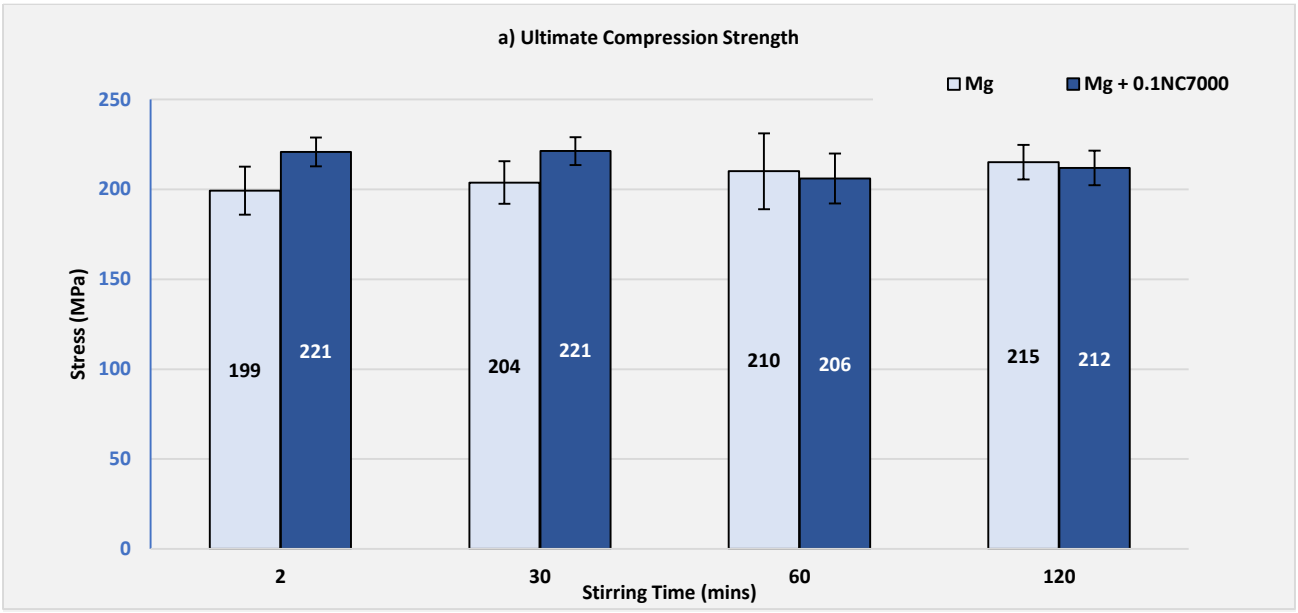

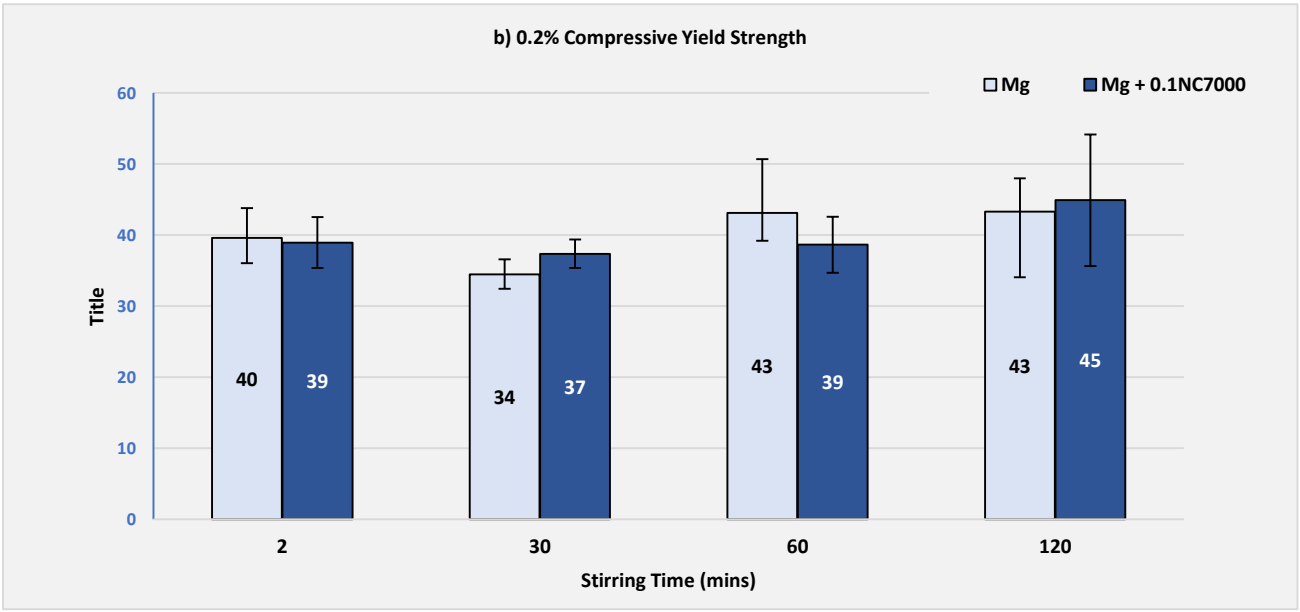

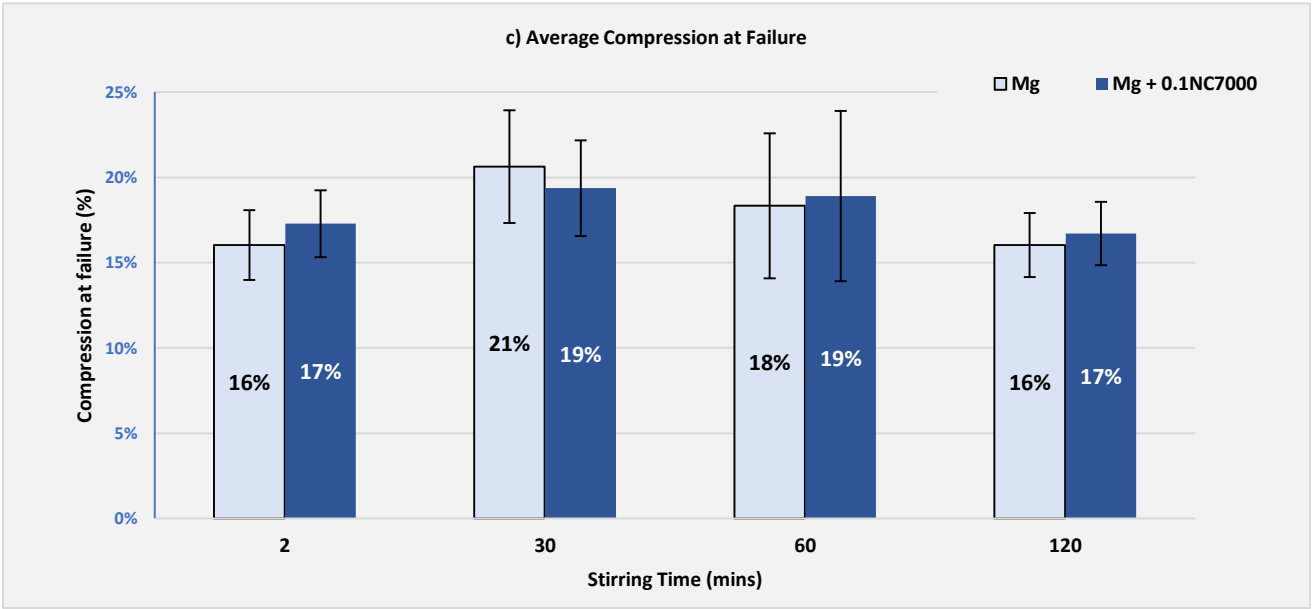

Figure 43. a), b) and c) Average UCS, 0.2% CYS and compression to failure values, respectively, for pure Mg and 0.1vol.% NC7000 composite at melt stirring times of 2 – 120 minutes. Error bars represent standard deviation.

The samples reinforced with 0.05 – 0.5vol.% NC7000 MWCNTs show approximately an 8% increase in UCS when compared to pure Mg and a 6% increase for 1vol.% NC7000 MWCNTs, showing that adding MWCNTs in the concentration range presented does offer some reinforcement to the Mg matrix as in Figure 44. A 21% increase in 0.2% CYS was achieved for Mg-0.05vol.% NC7000 sample, with a t-test determining a significant difference between the results. Interestingly, the largest increase in ultimate and compression strength measured for the NC7000 concentration range tested was the sample with the lowest concentration of MWCNTs. A low MWCNT concentration could potentially lead to a reduction in the number of large MWCNT agglomerates that can act as defects for a given number of MWCNTs that can in fact act as reinforcement or only a fixed amount of MWCNTs are incorporated into the matrix, such as a maximum of 0.05vol.%. Again, no relationship can be found between MWCNT concentration and the compression at failure of the resulting composite.

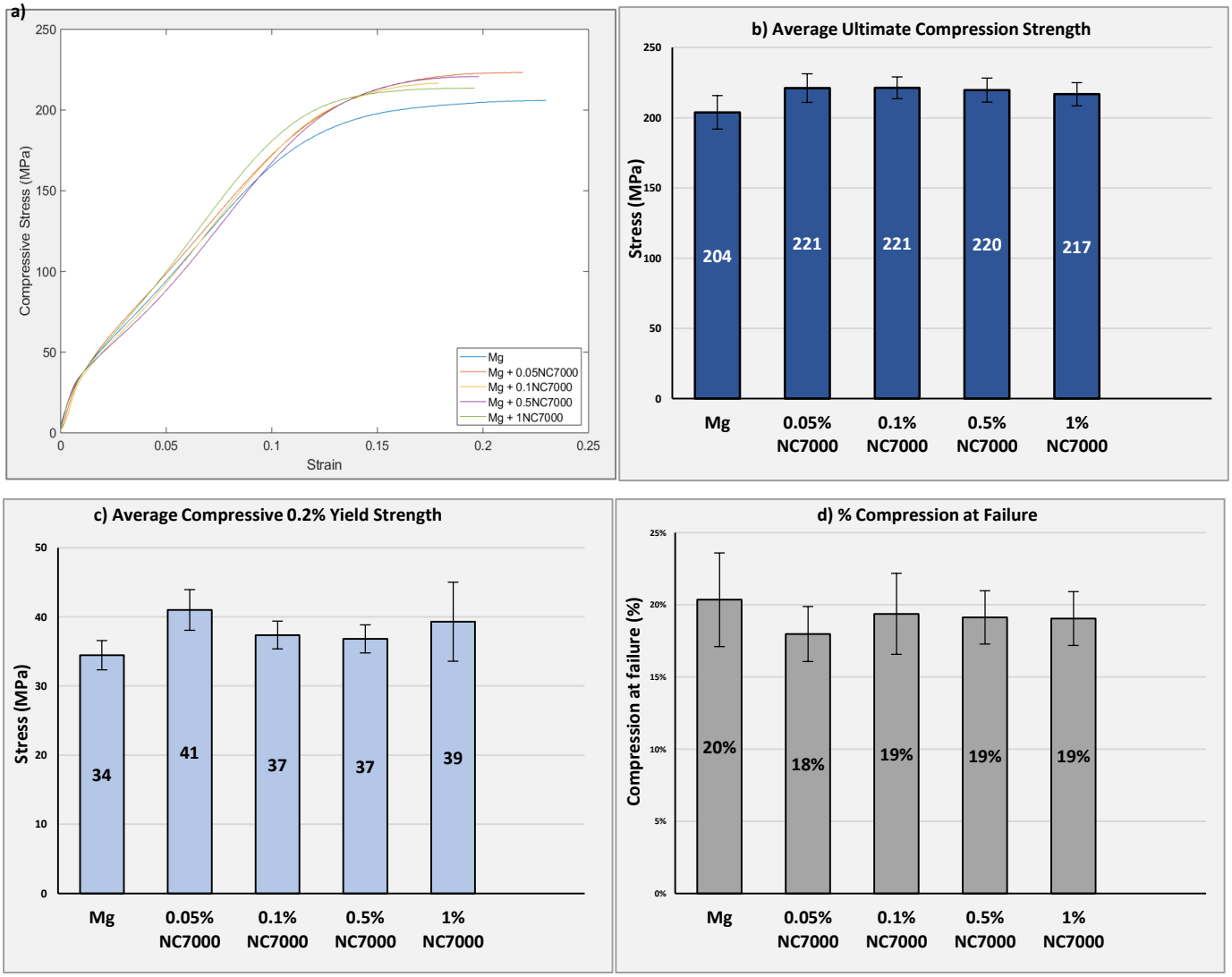

Figure 44. a) Representative stress strain curves for the average values for the samples tested. b), c) and d) Average UCS, 0.2% CYS and compression to failure values, respectively, for pure Mg and Mg - 0.05 – 1 vol.% NC7000. Error bars represent standard deviation

3.2.3.2 Solidification

An interesting artefact contained within an as-cast Mg – 0.1wt.%MWCNT composite ingot melt stirred for 30 minutes at 700°C was found. The ingot was fractured using a hammer, to reveal a tension induced fracture surface that contained a large porosity in the middle of the cross section, shown in Figure 45a and b. The cause of the pore is most likely to be due to shrinkage porosity, owing to its location being on the centre of the ingot as the melt would initially solidify at the relatively cool mould walls and travel along the thermal gradient towards to centre of the mould cavity. SEM images of the surface of the pore show a significant amount of MWCNTs/MWNCT agglomerates that have therefore been rejected by the melt and pushed there by the solidification front, shown in Figure 45c and d. The solidification front pushing would have a further negative impact of the homogeneity of the MWCNT dispersion, as the MWCNTs would most likely at least be pushed to the grain boundaries instead of being incorporated within the grains. Grain boundary accumulation has been reported by Xiang et al [119] that found that the graphene they had used to reinforce a melt processed Mg alloy accumulated preferentially at grain boundaries.

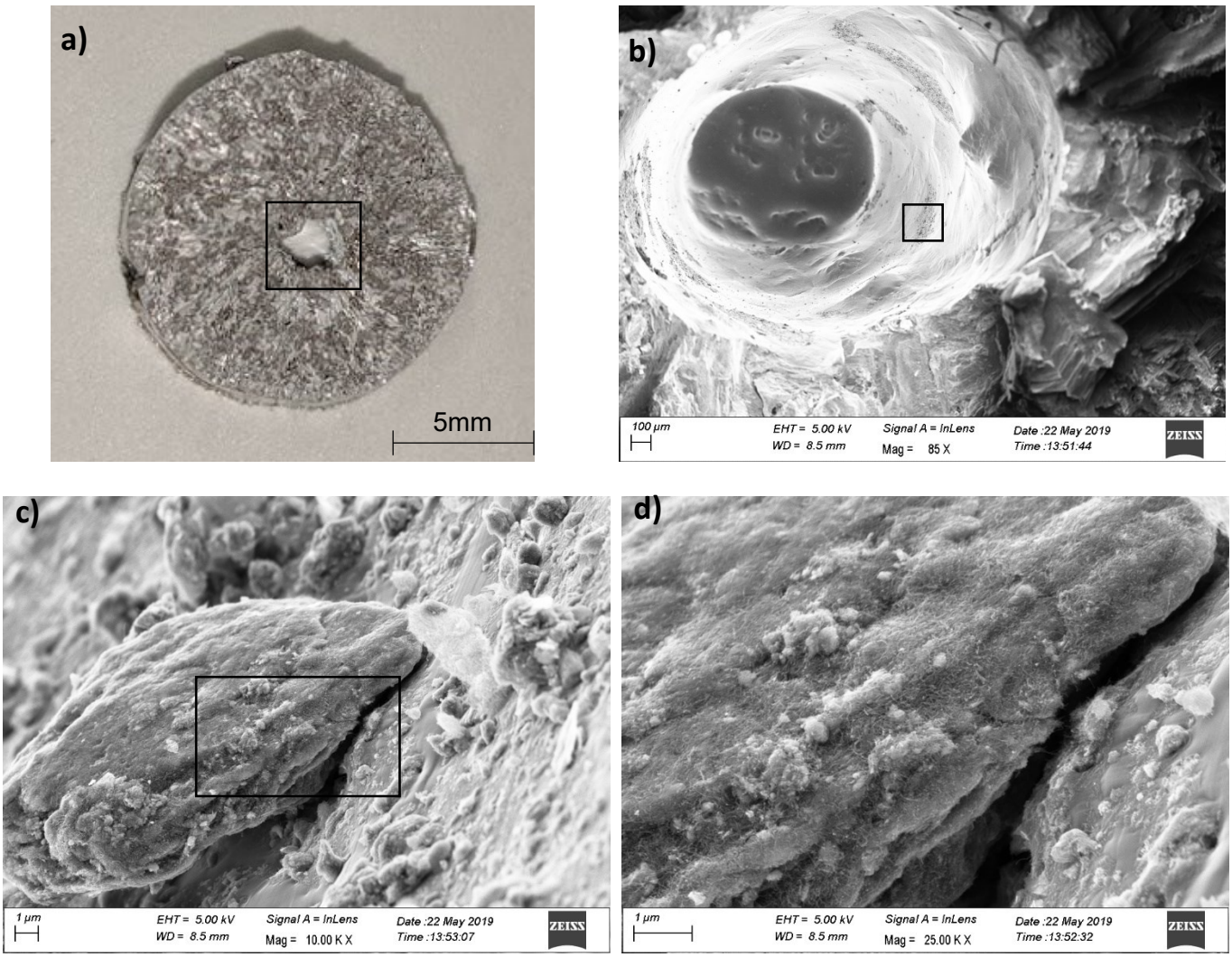

Figure 45. a) Cross section of a hammer fractured Mg – 0.1vol.% NC7000 composite with a large shrinkage pore at its centre. b) SEM image of the shrinkage pore, highlighted in a). c) SEM image of MWCNT agglomerates sitting on the surface of the pore in the area highlighted in b). d) High resolution SEM image of the area highlighted in c).

3.2.3.3 Theoretical strength predictions

As discussed in section 2.2, various models have been proposed in the literature for predicting the increase in yield strength of a metal composite for a given nanoparticle volume fraction. Using the results presented in Figure 44, for pure Mg reinforced by a range of vol.% of NC7000 MWCNTs, allowed for a comparison between the predicted and observed mechanical properties.

Critical fibre length

In order to calculate the maximum transferable stress, the critical fibre length can be determined using equation 9. If the length of the reinforcing particle exceeds its calculated critical length, then the maximum transferable stress is equal to the yield strength of the reinforcing material. The dimensions of NC7000 MWCNTs and the ultimate shear strength (USS) of a pure magnesium matrix were used. The USS of pure magnesium was determined by using the von Mises criterion applied to the measured ultimate tensile strength of pure magnesium [171] and a tensile strength of 33GPa was used for NC7000 as this value represents the average tensile strength of MWCNTs measured by Yu et al [24].

$$l_c = \frac{\sigma_{re} d}{2\tau} = \frac{(33 \times 10^9)(9.5 \times 10^{-9})}{2 \times \frac{1}{\sqrt{3}} \times (120 \times 10^6)} = 2.26\mu m$$

The calculated critical fibre length exceeds the average length of NC7000 tubes of 1.5µm and therefore the NC7000 MWCNTs should fail by pull-out before fracture. Equation 8 therefore becomes the most appropriate model to use for predicting the magnitude of the load transfer, however, it is important to recognise that this model assumes a perfect interface with well aligned, individually dispersed nanoparticles and therefore most likely represents an overestimation.

Yield strength

Figure 46 shows how the yield strength of a Mg-MWCNT composite should vary with %.vol of NC7000 MWCNTs assuming that the MWCNTs are perfectly aligned and individually dispersed with an ideal interface with the matrix. The increase in yield strength due to thermal mismatch ($\Delta\sigma_{th}$), Orowan strengthening ($\Delta\sigma_o$) and load transfer ($\Delta\sigma_{lt}$) are calculated using Equations 1, 8 and 12, respectively. The total predicted increase ($\Delta\sigma_{sum}$) was calculated using Equation 19, the root square summation, the most popular method used in the literature. The experimental results that were presented in Figure 44 are also plotted in Figure 46 to compare the achieved yield strength of the samples produced with their theoretical maximum yield strength. Although the yield strength of the Mg-0.1NC7000 was increased by 21% when compared to pure Mg, this increase is only 22% of the increase predicted by current theoretical models. This large deficit between the achieved and theoretical yield strength of the composites can be explained by the idealistic assumptions that are used in the models to calculate the yield strength contributions from the different mechanisms cannot be applied to the samples manufacturing in this study. The dispersion techniques used in manufacturing the samples have been shown to not be 100% effective due to the presence of MWCNT agglomerates, combined with poor wettability between the molten Mg and MWCNTs, lack of MWCNT alignment and solidification

front pushing. However, if these challenges can be overcome, Figure 46 highlights the huge potential of metal matrix composites reinforced with MWCNTs.

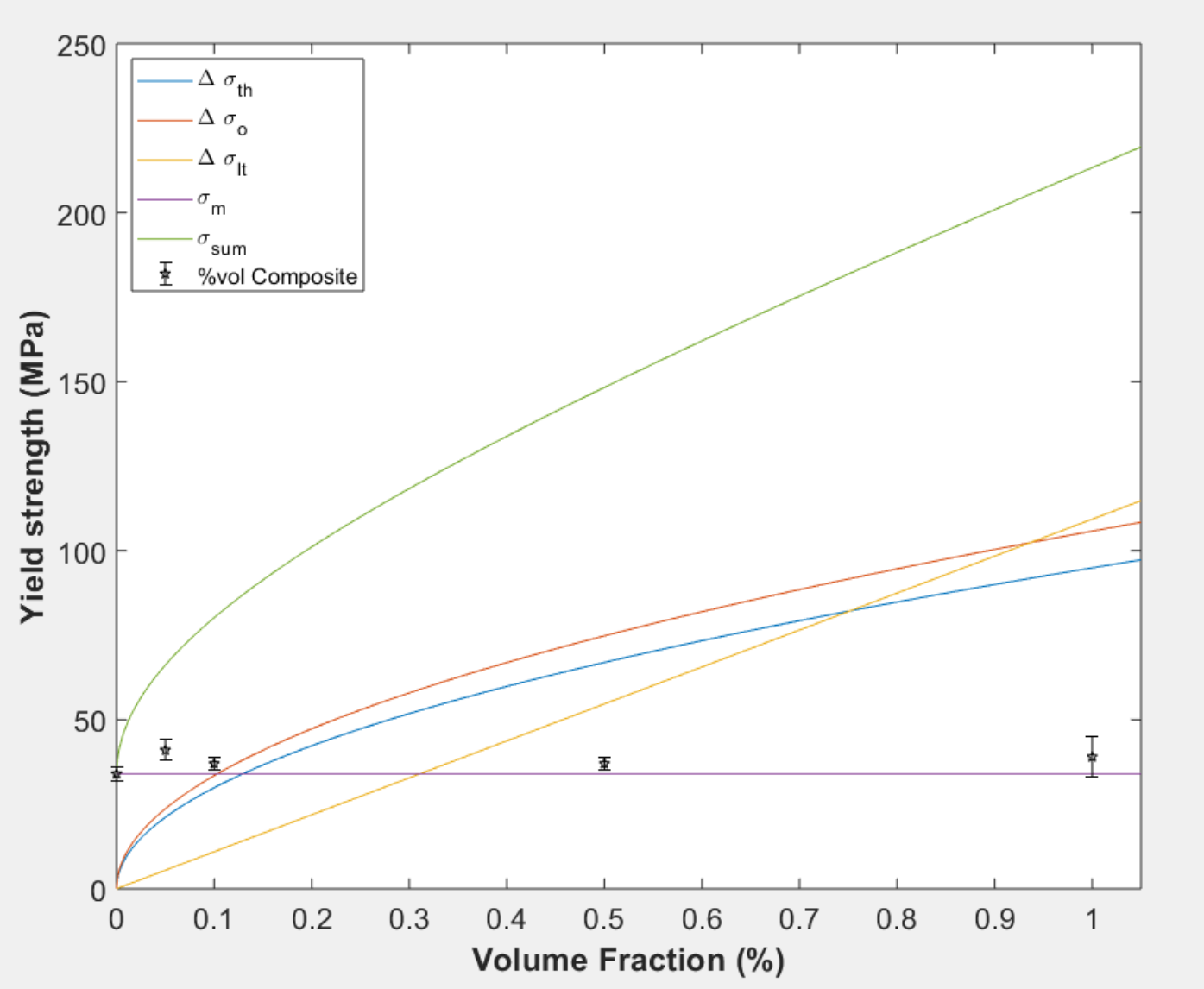

Figure 46. Comparison of the theoretical Incremental increase in yield strength for Mg – NC7000 composites as a function of MWCNT vol.% and the experimentally determined 0.2% CYS for the Mg – 0.05 – 1vol.% NC7000 composites produced in this study.

3.2.4 Theoretical analysis of the melt stirring process

After achieving similar mechanical properties for AZ91D / pure Mg castings and their respective MWCNT composites, a theoretical analysis of the manufacturing process was undertaken and to understand potential reasons why the method used could not produce samples with increased yield strengths as is theoretically predicted. SEM images of the composite fracture surfaces indicate that nanoparticle dispersion and wettability should be the area of focus and as a result are discussed in this section.

3.2.4.1 Nanoparticle – Metal melt interaction

Table 11 shows a comparison between the Mg-SiC system used in Chen's study [5] and a Mg-MWCNT system of equivalent diameter MWCNTs and NC7000-MWCNTs. Equation 43 was also used for the MWCNTs as from Derjaguins approximation, we can determine the effective area of interaction for two cylinders of equal radius crossing at 90^{o} [120], the most likely case of MWCNT contact. A study [43] that measured the contact angle between molten Mg and the basal plane of graphite to be 120^{o} was used for the Mg-MWCNT contact angle. Chen *et al* [5] used the logic that the $W_{barrier}$ was over 2000 times the Brownian motion energy at their processing temperature(13.8zJ), so that the SiC particles, once individually dispersed and wetted by the Mg melt, wouldn't be able to climb this energy barrier to contact and subsequently sinter with one another.

Table 11 also shows that the $W_{barrier}$ for the Mg-NC7000 system has a negative energy barrier, suggesting that the NC7000 MWCNTs will favourably re-agglomerate and therefore represents an unstable system. Figure 47 shows how the energy barrier varies for spherical nanoparticles and nano-whiskers that form a given contact angle with liquid Mg, showing the significance that a contact angle of 90^{o} or less between liquid Mg and the reinforcing nanoparticle for creating a stable (negative $W_{barrier}$) nanoparticle-metal melt system. In order to decrease the contact angle and achieve wetting of the MWCNTs by liquid Mg, a suggested method within the literature is to coat the MWCNT with a material that is wetted by the liquid Mg, such as nickel. An investigation into nickel coated MWCNTs and SiC whiskers was carried out in an attempt to overcome the wetting challenge.

Table 11 – Numerical comparison of the energy barrier to of nanoparticle contact and sintering

	$Mg_{(liquid)}$ – SiC $_{nanoparticles}$	$Mg_{(liquid)}$ -MWCNT of equivalent diameter	$Mg_{(liquid)}$ -NC7000 MWCNT
R (nm)	30	30	4.75
D (nm)	0.2	0.2	0.2
S (am^2)	18.8	37.7	6.0
$\sigma_{np}\ (Jm^{-2})$	1.45 [172]	0.045 [173]	0.045 [173]
$\sigma_{np-l}(Jm^{-2})$	0.422	0.345	0.345
$\sigma_{l}(Jm^{-2})$	0.599 [174]	0.599 [174]	0.599 [174]
θ (°)	83 [175]	120 [43]	120 [43]
$W_{barrier}$**(zJ)**	3.87 x 10^4	-1.13 x 10^4	-1.80 x 10^3

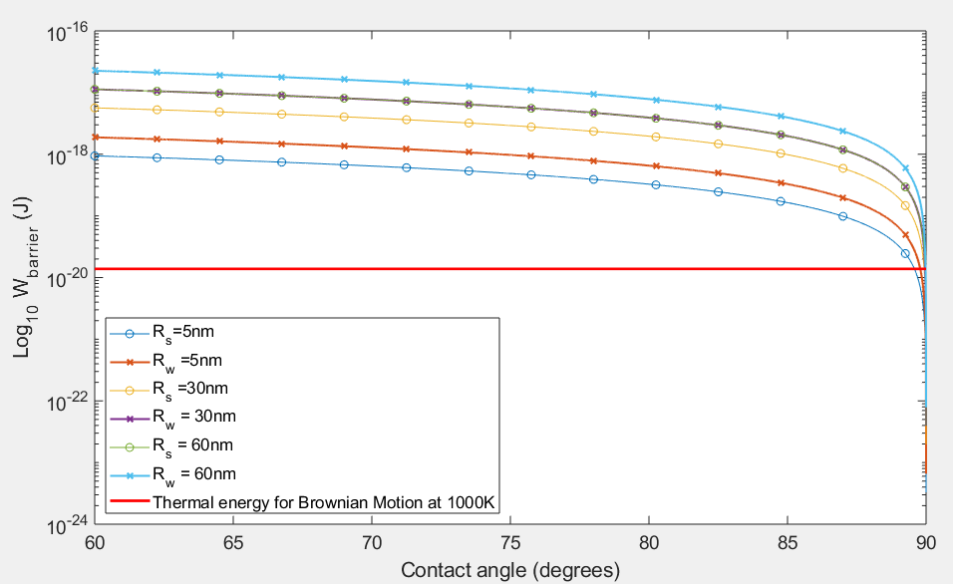

Figure 47. Plot to show how maximum energy barrier for particles that form a given contact angle with liquid Mg with regards to their diameter and particle geometry.

3.2.4.2 Mechanical Melt Stirring

Due to the topics discussed in section 2.3.2.2, it is unlikely that the melt stirrer is going to be able to provide the energy density to further disperse MWCNT bundles. Huang *et al* [93] estimated, using van der Waals interactions and the density of MWCNT contact points in a CVD grown MWCNT bundle, that the shear stress required to separate a MWCNT bundle was 16kPa. The shear stress generated by a Couette cylinder, that is well approximated by our crucible-stirrer geometry can be calculated by

$$\sigma_s = \eta\dot{\gamma} = \eta\frac{R\omega}{h} \tag{47}$$

where R is the radius of the container (35mm), ω is the rotational speed of the mixer in rads^{-1} (82 for 780rpm), h is the spacing between the mixer and the inner wall of the container (~6mm) and η is the viscosity of the medium (0.012Pas [110]).

From Equation 47, a shear stress of approximately 6Pa is imparted by the mixing medium, orders of magnitude less than what is required for separating MWCNTs. Figure 48 shows the required stirrer speeds and stirrer-container gap width required to generate an adequate shear stress in 650°C Mg melt in a container with a radius of 35mm to individualise MWCNTs. The physical processing parameters required for MWCNT dispersion through melt stirring is unobtainable with the current equipment being used in the project, alternative dispersion methods such as ultrasonic assisted stirring should be utilised instead. Furthermore, due to the poor wettability of the MWCNTs and melt, melt stirring most likely induces re-agglomeration by bringing individualised or MWCNT bundles into contact with one another, shown in section 3.2.4.1. The melt stirring duration was varied from 15 to 45 minutes, around the original 30 minutes used by Li *et al* [38].

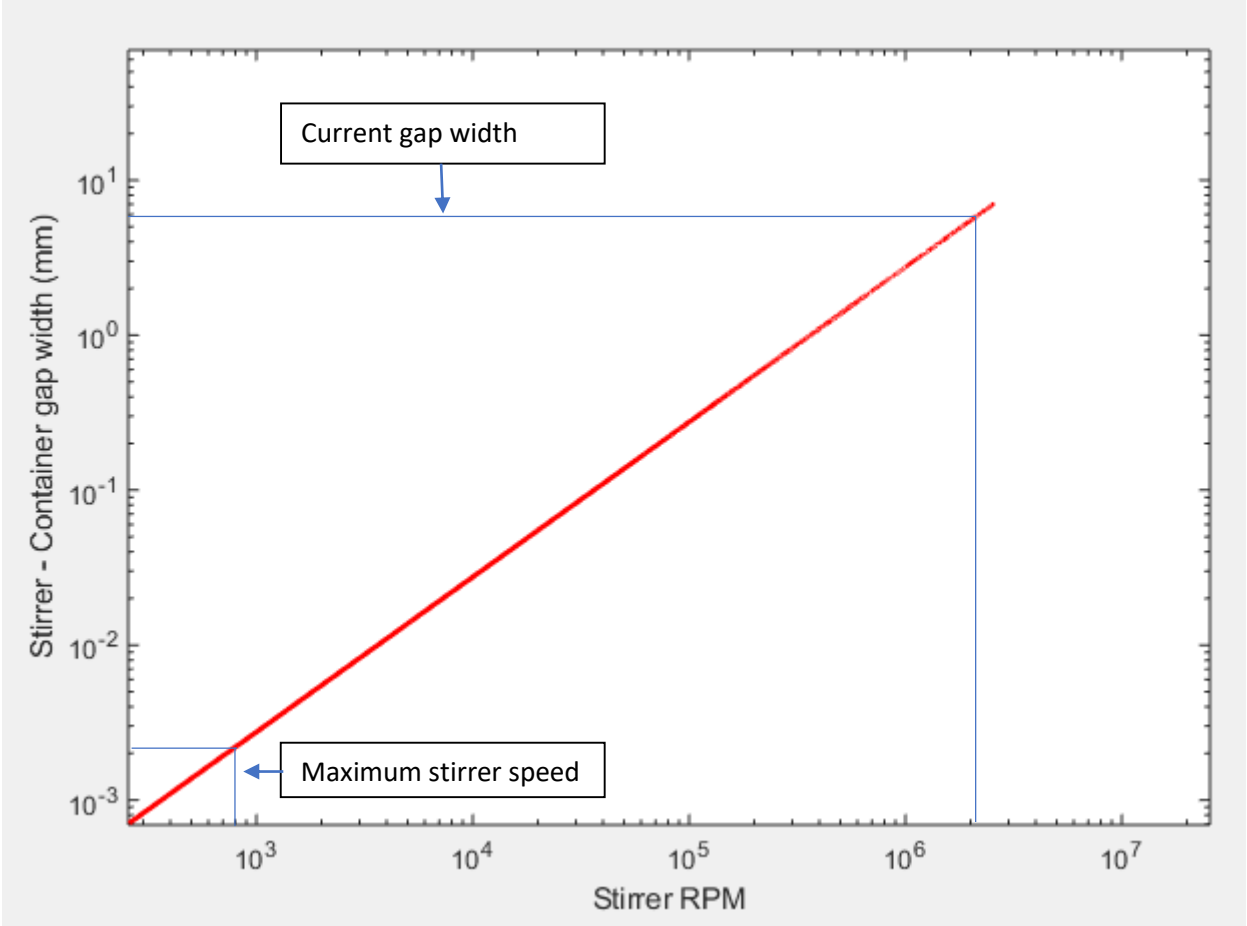

Figure 48. A logarithmic plot to show the required stirrer RPM and stirrer-container gap width to provide an adequate shear rate to further disperse MWCNT bundles in 650°C liquid Mg in a container with a radius of 35mm. Calculated from Equation 47.

The above analysis indicates that the mechanical stirring is unable to impart a shear force of a large enough magnitude to disperse the nanoparticles; in addition, as MWCNTs are not wetted by molten magnesium, the MWCNTs will favourably reagglomerate. Two methods to overcome these challenges are to use sonication in the molten metal as a way of delivering enough shear force to disperse the MWCNTs and to coat the MWCNTs in a material that is wetted by molten magnesium, such as Ni or SiC. Whilst efforts to establish a metal melt sonication rig were being made, AZ91D / Pure Mg - Ni coated MWCNT composites were investigated that were manufactured with the same melt stirring technique as the sample presented so far.

3.2.5 Nickel coated MWCNT reinforced metal matrix nanocomposites

Analysis of the results presented so far in section 3 suggest that the wettability between the molten metal and MWCNTs is a critical factor in determining the final microstructure of the composite. In order to overcome the non-wetting behaviour of the molten metal and MWCNTs, commercially available MWCNTs that were coated by nickel (NiCNTs), a material that is generally known to be wetted by molten Mg [123] and AZ91D with a contact angle of 51° [176], were used as reinforcements. Ni also has a much higher Hamaker constant than that of Mg [115], as shown in Figure 13, and therefore satisfies the theoretical requirements for spontaneous solidification front capture, instead of solidification front pushing, which allows the nanoparticle state of dispersion in the molten metal be maintained through solidification. Whilst 5 or more ppm of Ni in a Mg matrix abruptly increases its corrosion rate and would

therefore not be suitable for mass-produced as-cast use [7] , NiCNTs provide a proof of concept system that could be used to guide further studies with other coating materials that are known to wet with Mg, such as SiC. To the author's knowledge, this investigation of as-cast, melt processed, magnesium and its alloys reinforced with NiCNTs has not been reported in the literature.

3.2.5.1 Wettability test

Prior to melt stirring experiments, some simple wettability experiments were conducted to explore whether molten magnesium infiltrated/wetted the NiCNTs in way that wasn't seen with raw MWCNTs. As described in section 3.1.2.6, approximately 14mg of NiCNTs were dispersed on some aluminium foil surface, which was then folded into a parcel and melted at 700°C for 60 minutes. Aluminium foil was chosen for this experiment due to it being readily available and synonymous to magnesium in terms of melting temperature and being known to form intermetallics with Ni at the processing temperatures, so the interaction mechanics between the Al foil and NiCNTs should be very similar to Mg and NiCNTs. Al foil is also much easier to handle as magnesium foil would be very difficult to form a parcel due to its brittleness. The cross section of the parcel can be seen in Figure 49b, c and d.

From Figure 49c and d, there are solid areas of aluminium that are much thicker than the sheet thickness of the starting foil, suggesting that they have fused together under the heating conditions. However, towards the centre of the parcel that contains the foil layers that have a covering to NiCNTs appear to have not fused together. The NiCNT covered layers not fusing would suggest that the NiCNTs played a role in inhibiting the fusion of different the aluminium foil sheets, most likely due to the residual oxygen that is adsorbed into the NiCNT bundles that encourages enhanced oxidation of the surrounding aluminium, so the aluminium oxide formed would act as a barrier between adjacent pools of molten aluminium.

These layers were carefully exposed and studied in an SEM. Figure 50 shows some of the different NiCNT agglomerate morphologies that were found in between the layers of aluminium foil. Figure 50b shows what could be small metal crystals forming around the NiCNTs, with the EDS spectrum showing that potentially aluminium or a nickel/aluminium intermetallic has crystallised around the MWCNTs, possibly due to contact with molten aluminium or aluminium that has evaporated from the foil layer. The EDS spectrum could, however, be detecting aluminium from the underlaying foil layer that is within the penetration depth of the electron beam so further characterisation would be necessary to support this suspicion.

Due to the large amount of visible oxidation, it is difficult to draw any conclusions from this wettability test. It was then decided that the stirring of molten magnesium and NiCNTs was the best method to ensure the contact of molten metal with the NiCNTs, allowing their interaction to be better investigated.

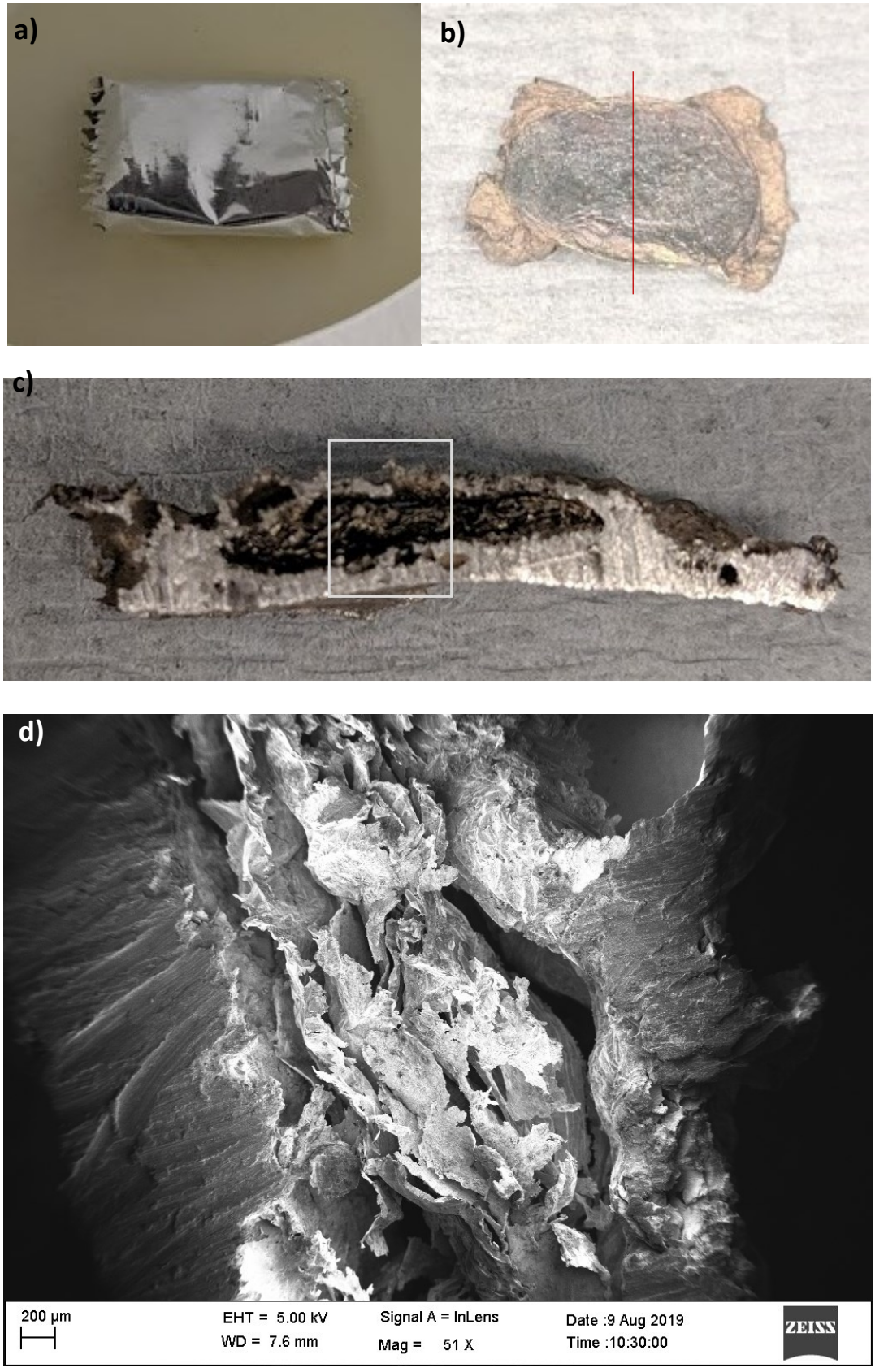

Figure 49. a) Al foil parcel containing ultrasonically dispersed NiCNTs before and b) after heat treatment at 700°C for 60 minutes. c) shows the cross section of the Al foil at the red line shown in b). d) SEM image of the cross section shown in the highlighted region in c).

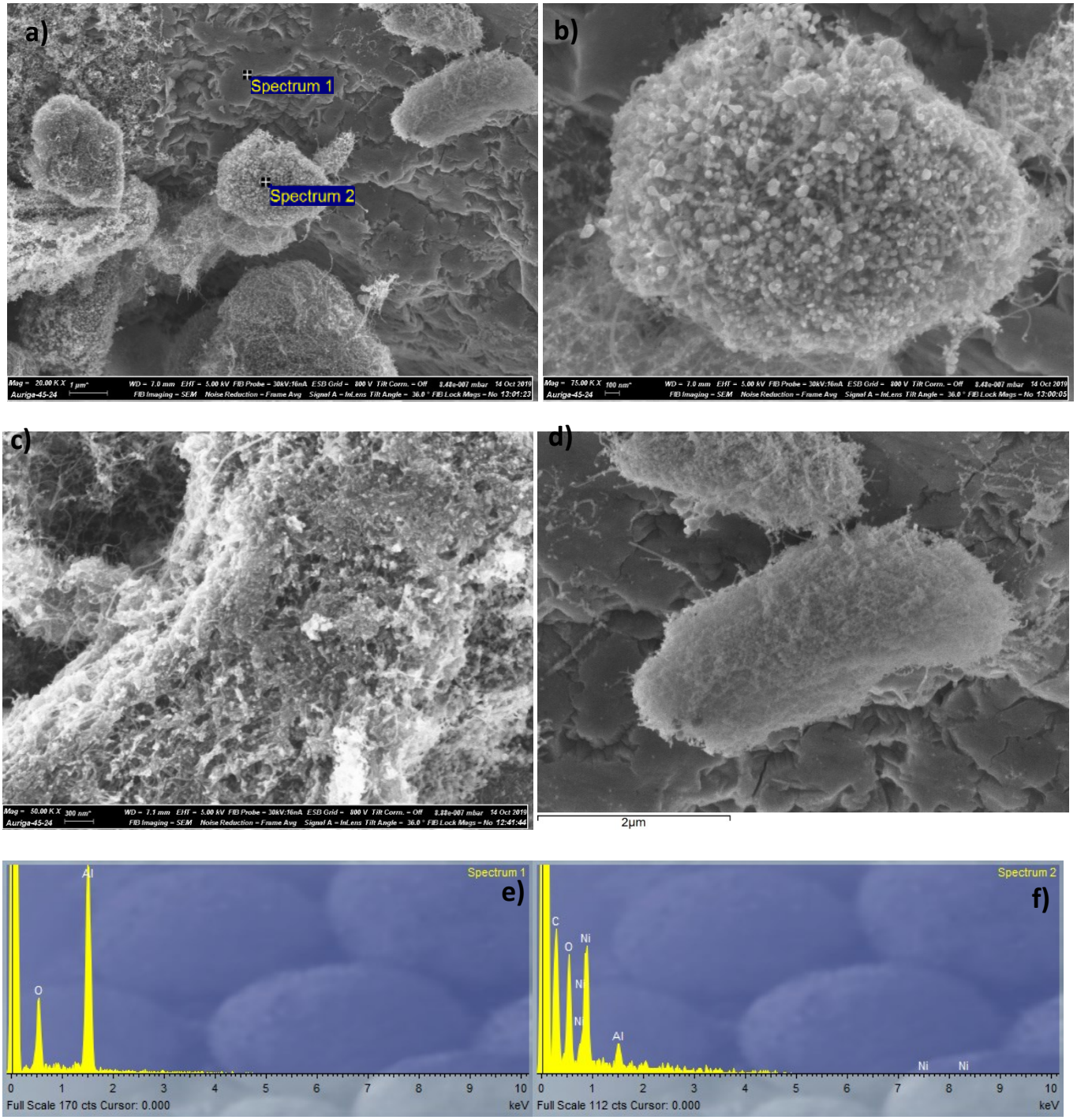

Figure 50. a) SEM image of the range of NiCNT morphologies observed within the unfused Al foil layers. b). c) and d) are high magnificaiton images of the morphologies shown in a). e) and f) show the EDS spectra measured in the highlighted areas in a).

3.2.5.2 Pre-dispersion

The NiCNTs appeared to disperse more easily into the ethanol with ultrasonic treatment, this is most likely due to the extra Ni material around the nanotubes that provides a larger space between the nanotubes that can therefore reduce the magnitude of the van der Waals interaction between them as well as minimising how tightly bundled they can become. Figure 51b shows that the metal chips are blackened and thus well covered with the NiCNTs, Figure 51c-g show that the covering is even. EDS measurements suggest that the Ni coating has potentially survived the ultrasonic treatment.

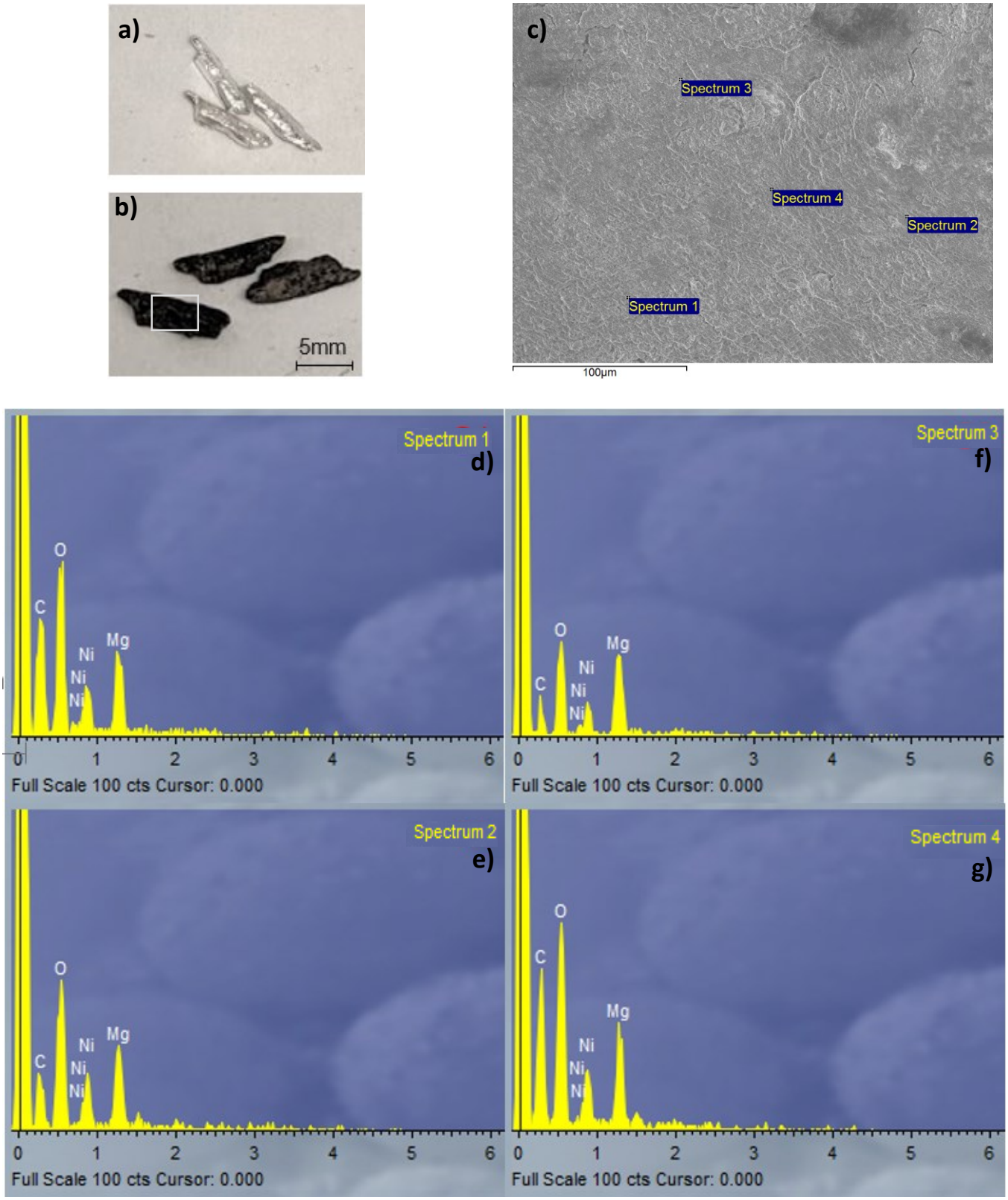

Figure 51. a) Pure AZ91D chips. b) AZ91D – 0.8vol.%NiCNT covered chips. c) SEM image of the AZ91D – NiCNT chips in b). d), e), f) and g) show the EDS spectra measured at the points highlighted in c).

3.2.5.3 AZ91 – NiCNT Composites

3.2.5.3.1 Microstructure

The cross sections of the bottom of the as cast ingots were taken and polished. The nanoparticle containing samples had to be hand polished within a HEPA filtered fume cupboard to ensure that any nanoparticles released from the matrix during the abrasive polishing and grinding stages were captured. Scratches on the cross-sections are associated with the difficulties of polishing without the use of a polishing machine and are therefore not linked to any changes in material composition and are to be ignored.

Figure 52 shows the cross sections of samples AZ91_T650_S30, AZ91_T650_S30_0.1NiCNT and AZ91_T650_S30_0.8NiCNT. Unfortunately, severe shrinkage porosity can be observed in the cross section of AZ91_T650_S30_0.1NiCNT, however, significantly more 'darker' material can be observed that is well macroscopically dispersed when comparing pure AZ91D with AZ91D-0.8vol.% NiCNT. A higher magnification image of the darker material can be seen in Figure 52f, which are most likely to be NiCNT agglomerates as shown in Figure 57, or Ni-Al intermetallics shown in Figure 53. Due to the presence of Ni-Al intermetallics, it can be concluded that at least some amount of Ni will have dissolved away from the NiCNTs into the matrix which could allow for the mechanism described by Ip et al [124], whereby the action of the Ni coating dissolving into the matrix allows the wetting of the underlying carbon by the molten Mg. Ideally, a comparison with a AZ91_T650_S30_0.1NC7000 sample would have been made, however unfortunately the nanoparticle metal composite polishing process was developed late in the project and the sample was unable to be prepared in time.

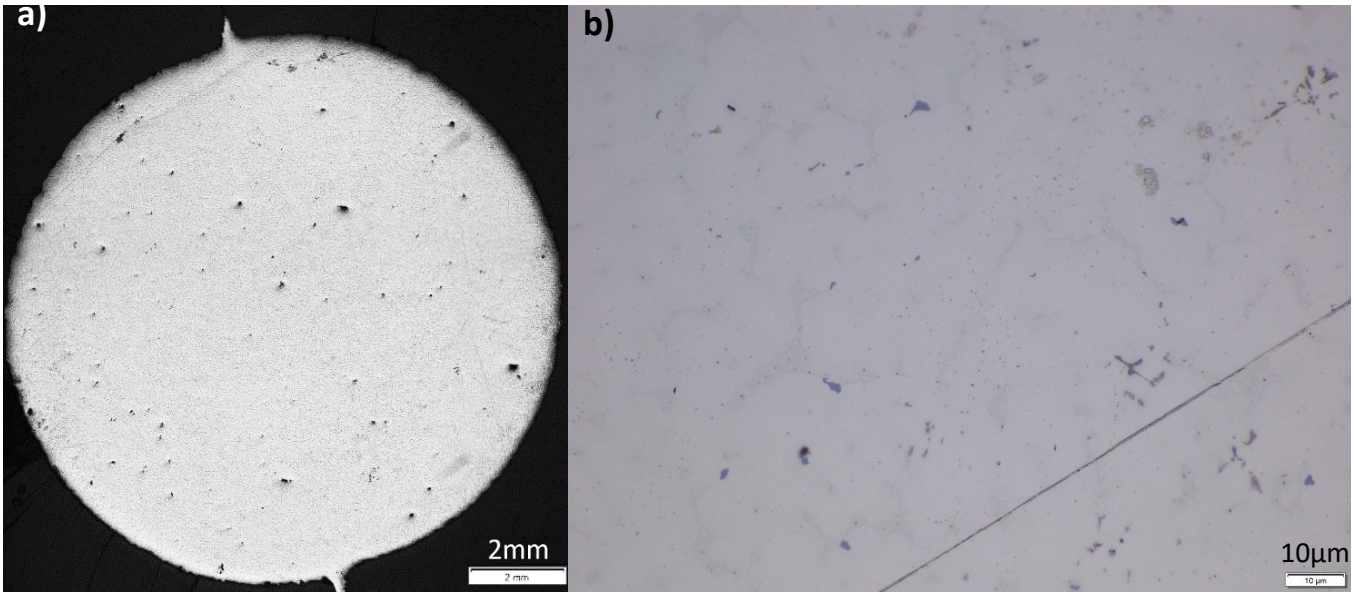

d)

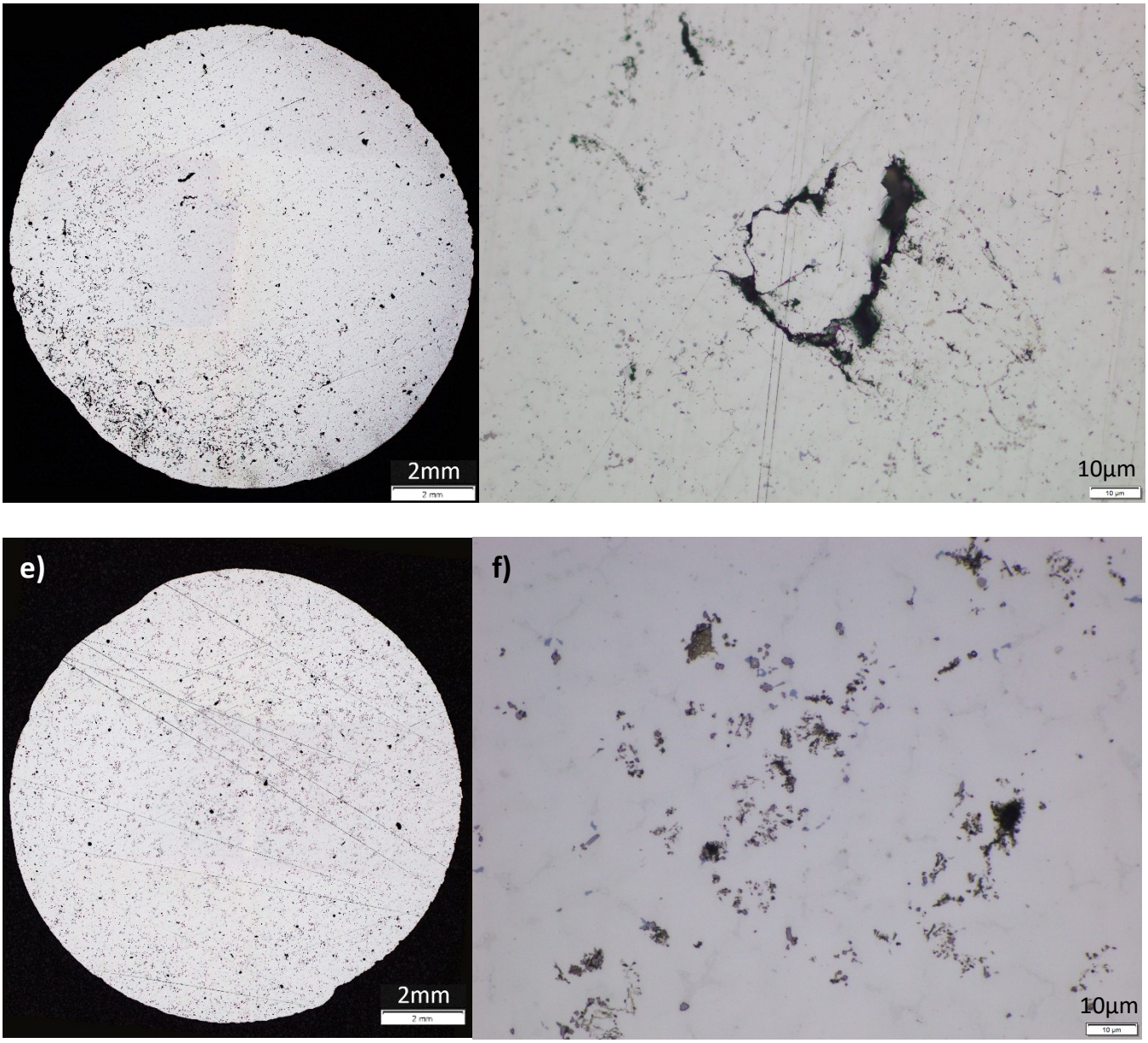

Figure 52. a) AZ91_T650_S30, c) AZ91_T650_S30_0.1NiCNT and e) AZ91_T650_S30_0.8NiCNT cross section. b), d) and f) x50 optimal microscopy image of representative microstructure of a), c) and e), respectively.

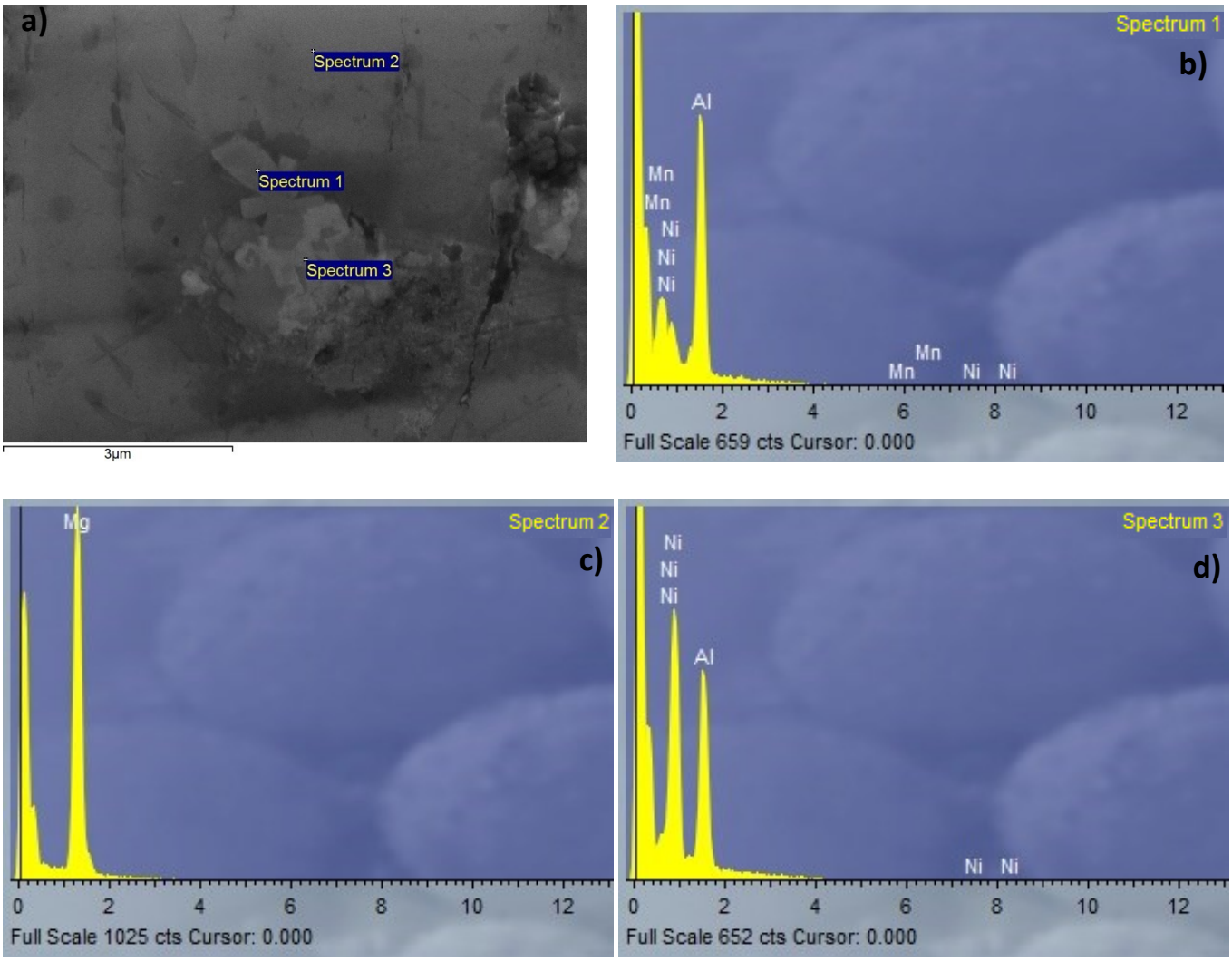

Figure 53. a) Al – Ni intermetallic detected in the cross section of AZ91_T650_S30_0.8NiCNT. b), c) and d) show the EDS spectra measured at the respective highlighted points in a).

3.2.5.3.2 Mechanical properties

Compression testing

The measured UCS, CYS and compression at failure for the AZ91-NiCNT composites produced are presented in Figure 54, including an AZ91-NC7000 composite for comparison. It can be seen that the addition of either raw MWCNTs or NiCNTs seem to have no significant impact on the resultant mechanical properties when made with the described melt stirring method. The similar mechanical properties could be considered as surprising, as even if the MWCNTs had no impact on the mechanical properties, it would be reasonable to assume that the formation of additional intermetallics would indeed have a measurable impact. The measured increase in compression at failure could be potentially be due to the replacement of the brittle $\beta - Mg_{17}Al_{12}$ [177] intermetallic with relatively less brittle Ni-Al intermetallics.

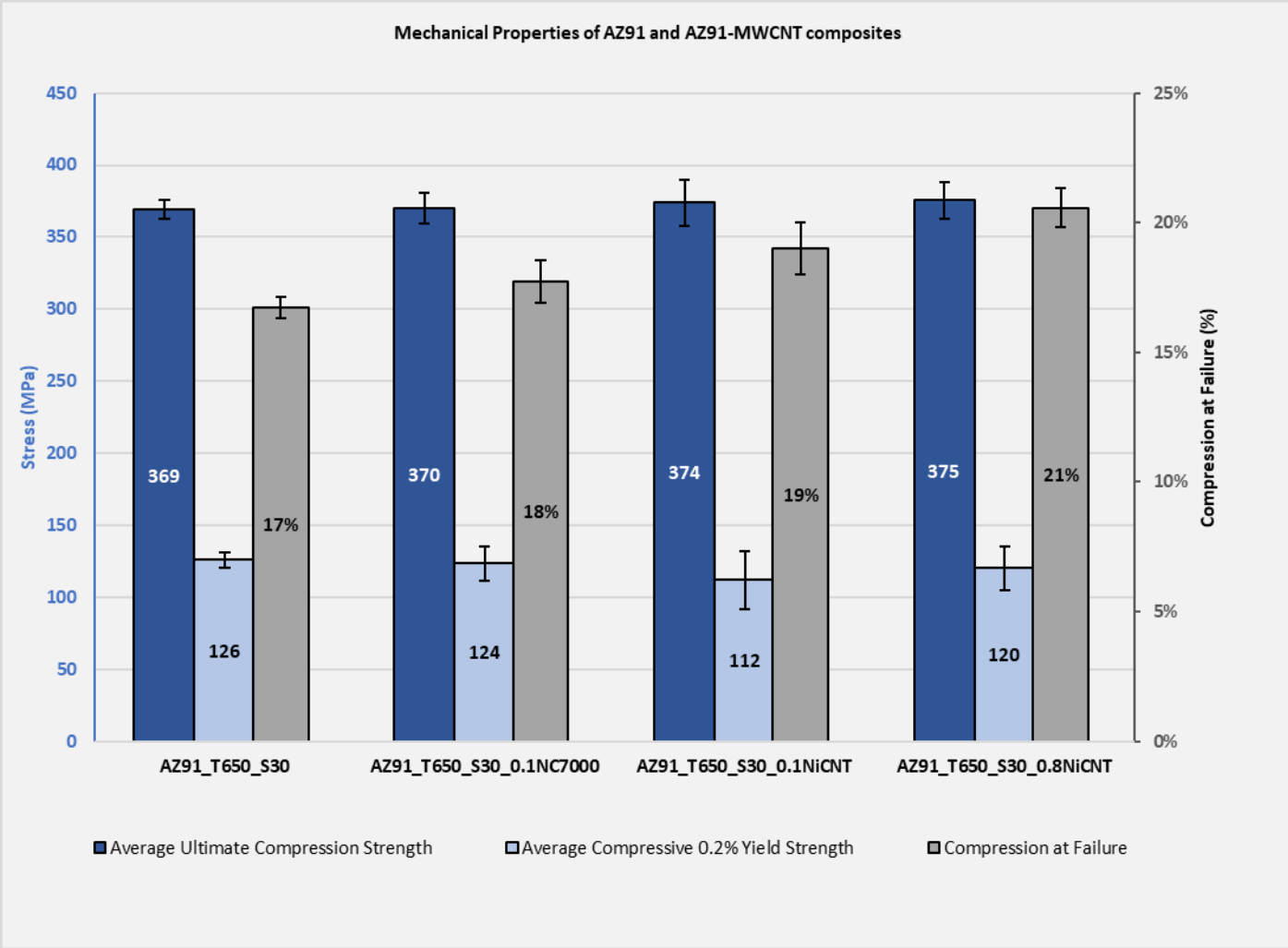

Figure 54. Average UCS, 0.2% CYS and compression to failure values for pure AZ91, AZ91 - 0.1vol.% NC7000 and AZ91D – NiCNT composites. Error bars represent standard deviation.

Hardness

To mitigate the effect of the potential variation, such as differing levels of porosity, which can exist between different cast samples due to the casting process itself, hardness testing was used, as areas of porosity could be avoided. Figure 55 shows that for pure AZ91D, for which an average hardness of 69.9 Hv1/10 was measured, a measurement taken in an area of shrinkage porosity was 30% lower than the average. The samples were polished using the processed described in section 3.1.3.2 prior to hardness testing. Little difference is observed between the pure AZ91D sample and the samples reinforced with 0.1vol.% MWCNTs, Ni coated or raw as in Figure 56. However, a 13% increase was seen for the AZ91D reinforced with 0.8vol.% NiCNTs. Whilst this could be due to NiCNT reinforcement, the 0.8vol.% NiCNT composite is now also 1.2wt.% Ni, as opposed to only 0.15wt.% Ni for the 0.1vol.% NiCNT reinforced sample. This significant addition of Ni and subsequent formation of new intermetallics would most likely have an influence on the hardness of the composite and therefore, in the future, an AZ91D – 1.2wt.% Ni alloy would have to be prepared and tested as a control to confirm that any increase is due to MWCNT reinforcement instead of the new matrix composition.

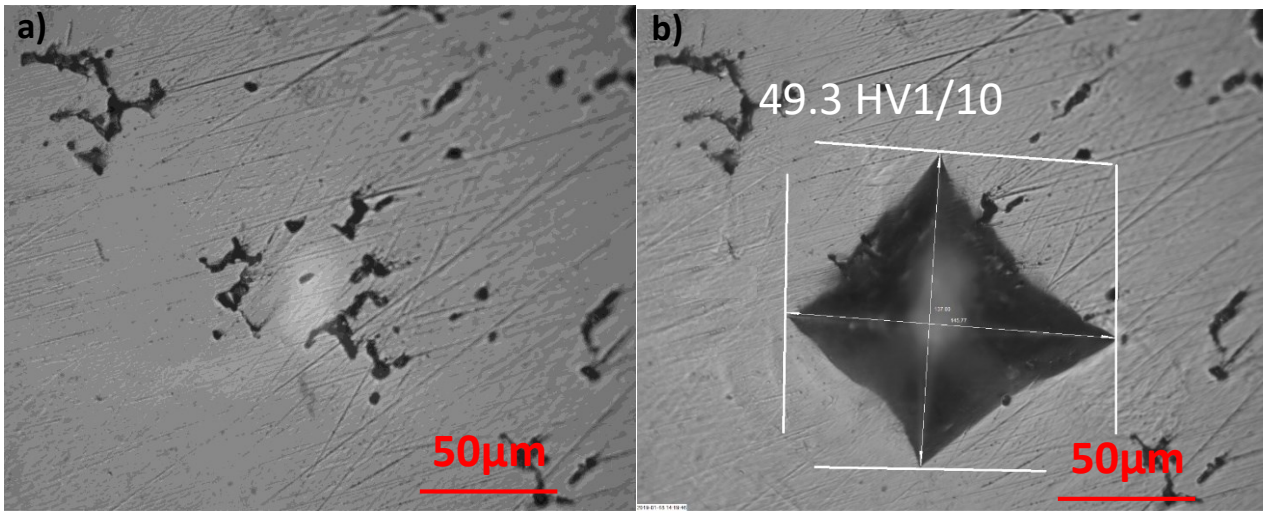

Figure 55. a) An area of shrinkage porosity in the polished cross section of an AZ91_T650_S30 sample. b) Indentation made for a HV1/10 hardness test showing a hardness value of 49.3Hv1/10 for a sample that had an average hardness measued of 69.9HV1/10, demonstrating that change in hardness between areas with and without shrinkage porisity.

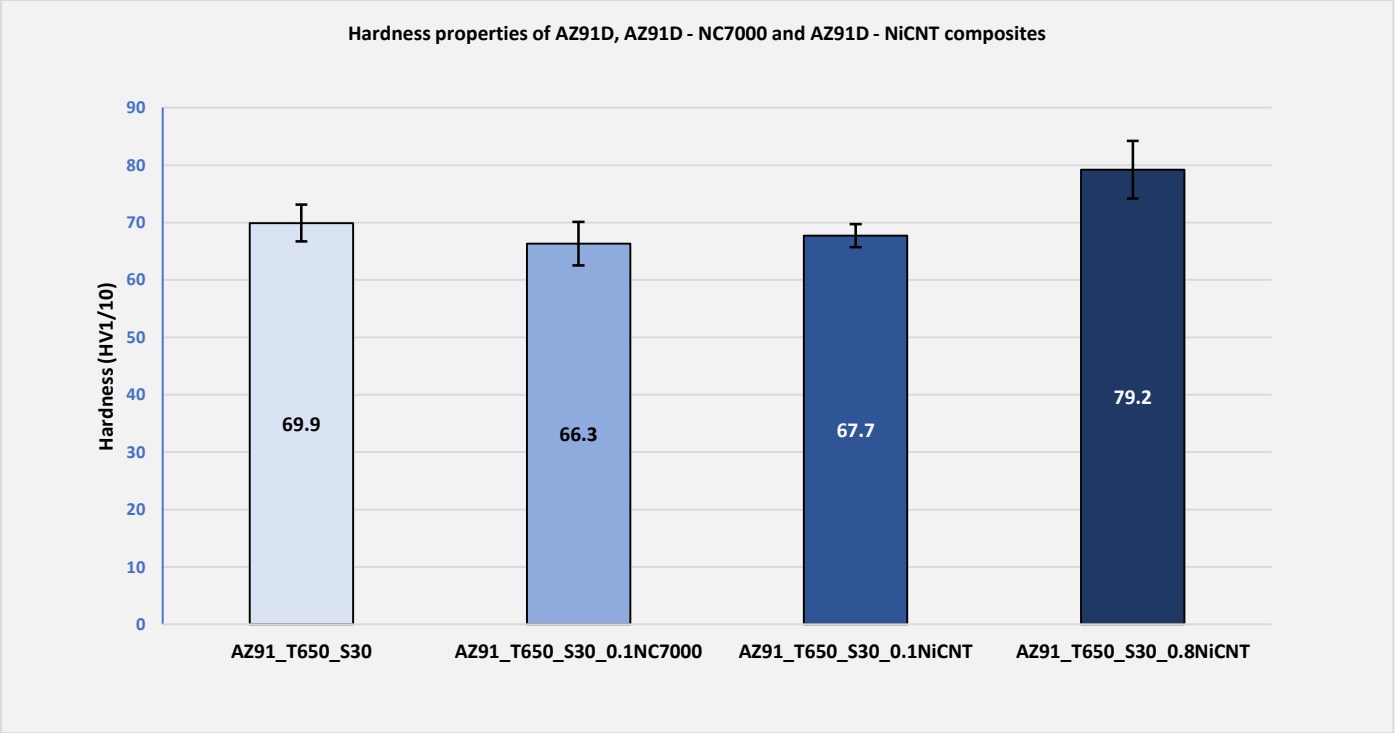

Figure 56. HV1/10 hardness values measured for AZ91D alloy, AZ91D – NC7000 and AZ91D – NiCNT composites.

Fractography

The fracture surface from an AZ91-0.8vol.% NiCNT composite compression test coupon and from a hammer fractured as-cast ingot, to simulate a tension like fracture, were inspected using SEM. Figure 57a and b show a morphology found in the compression fracture surface that was not seen in the AZ91-MWCNT composite where unwetted MWCNT agglomerates were regularly observed. Instead a smoother area that shows what could be individual MWCNTs fully surrounded by a matrix protruding from the surface, potentially indicating wetted MWCNTs, was observed.

However, the hammer fracture surface shown in Figure 57c and d, showed that numerous NiCNT agglomerates were still present in the composite that had not been fully infiltrated with molten metal. The higher contrast of the NiCNT agglomerate in Figure 57d can also be seen around the surface the pore within which it sits, suggesting NiCNTs are located there as well. A potential mechanism for this formation could be the NiCNT agglomerate experiencing partial infiltration at the surface of the agglomerate that is then pulled away from the unwetted section of the agglomerate during the contraction of solidification. The surface of such a pore was investigated for a Mg_T700_S120_0.8NiCNT sample, where the extra stirring time should have accentuated the infiltration and shrinkage effect and is discussed in more detail in section 3.2.5.4.

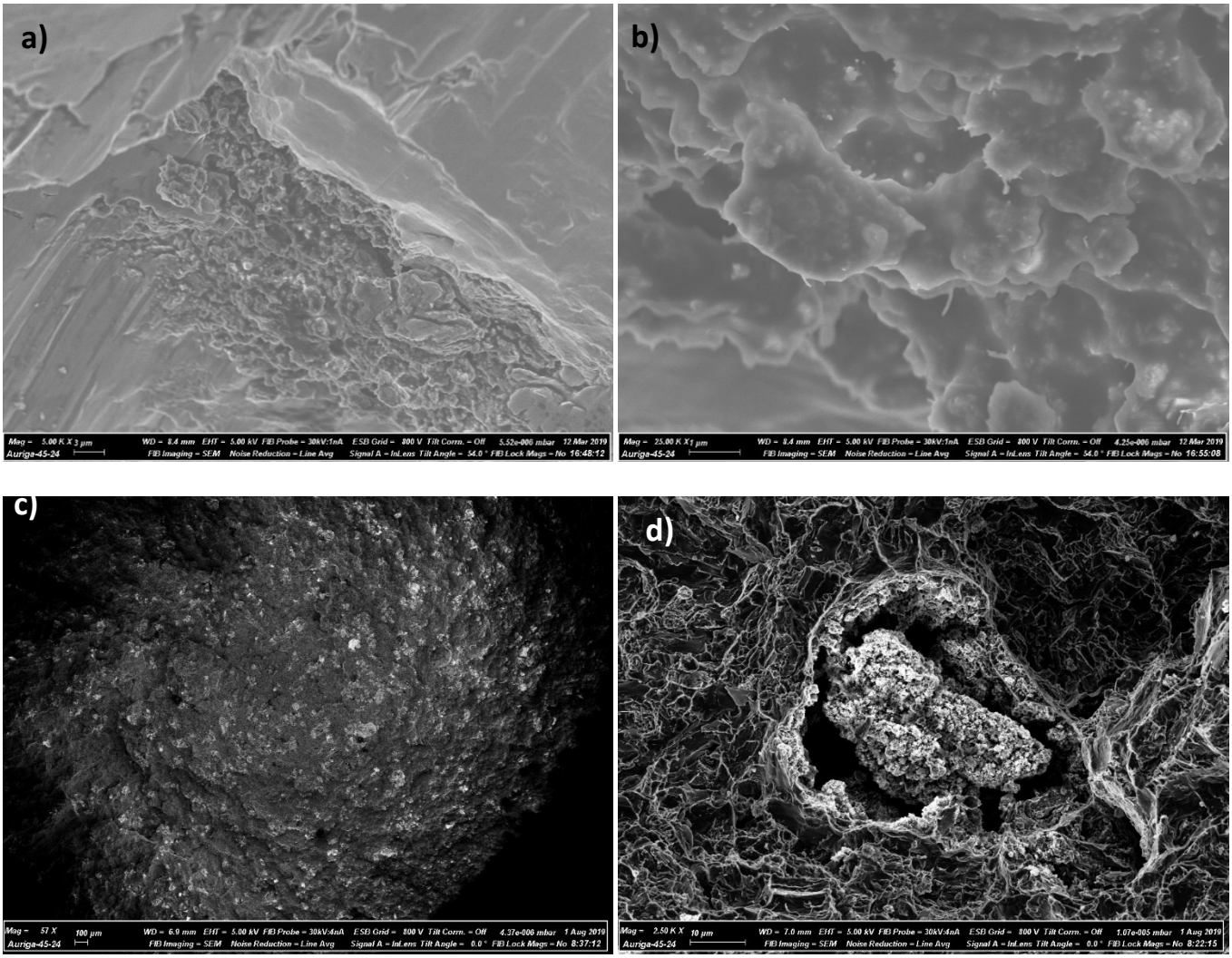

Figure 57. a) and b) SEM images of a fracture surface of AZ91-0.8vol.% NiCNT composite generated by compression testing. c) and d) SEM images of an overview and a NiCNT agglomerate found in a hammer fracture surface of AZ91-0.8vol.% NiCNT composit.

3.2.5.4 Pure Mg – NiCNT Composites

Cross-sectional analysis

The simple microstructure of the pure Mg polished cross section shown in Figure 58a and b allow the impact of adding 0.8vol.% NiCNTs to a pure Mg matrix to be clearly observed. The Mg-0.8vol.% NiCNT microstructure exhibited two predominant morphologies, more clearly shown in Figure 58e, of a network like structure of material that is mostly likely a solidification driven feature and round, dark inclusions. The network structure is therefore most likely to be a Ni-Mg intermetallic that's formed during solidification and further confirmed by EDS analysis shown in Figure 59. The round, dark inclusions were found to be either almost completely infiltrated NiCNT agglomerates, as shown in Figure 60, or pores that originally contained a NiCNT agglomerate, as seen in Figure 57d, that was subsequently removed during the polishing stage, shown in Figure 61.

As seen in the AZ91D-NiCNT samples, it appears as though the Ni is dissolving away from the MWCNTs into the metal melt and then matrix to sit interstitially within the matrix or form new intermetallics. It is therefore unlikely that a C-Ni-Mg interface would be formed, like that seen by Han et al [94] during the solid state processing of Mg-NiCNT composites. A TEM investigation of the NiCNT-Mg interface would be required for confirmation.

However, Figure 61 shows the surface of a pore that has a layer of infiltrated MWCNTs, suggested by a solid material that appears to surround the individual MWCNTs and that some degree of wetting has therefore taken place. An EDS study of the area cannot detect any Ni, again implying that the Ni has dissolved away from the MWCNTs. This potential sign of wetting is significant as it means that MWCNTs can in fact be stabilised in the Mg melt with an interface that is capable of transferring load, and therefore an enhanced MMNC can be realised if combined with a dispersion technique that can further disperse the MWCNTs within the melt. Unfortunately, due to time constraints, only a limited search was done for these types of morphologies, shown in Figure 60 and Figure 61, in the AZ91D-MWCNT composites polished cross-section; it is necessary to confirm their absence in order to attribute the potential wetting to the Ni coating.

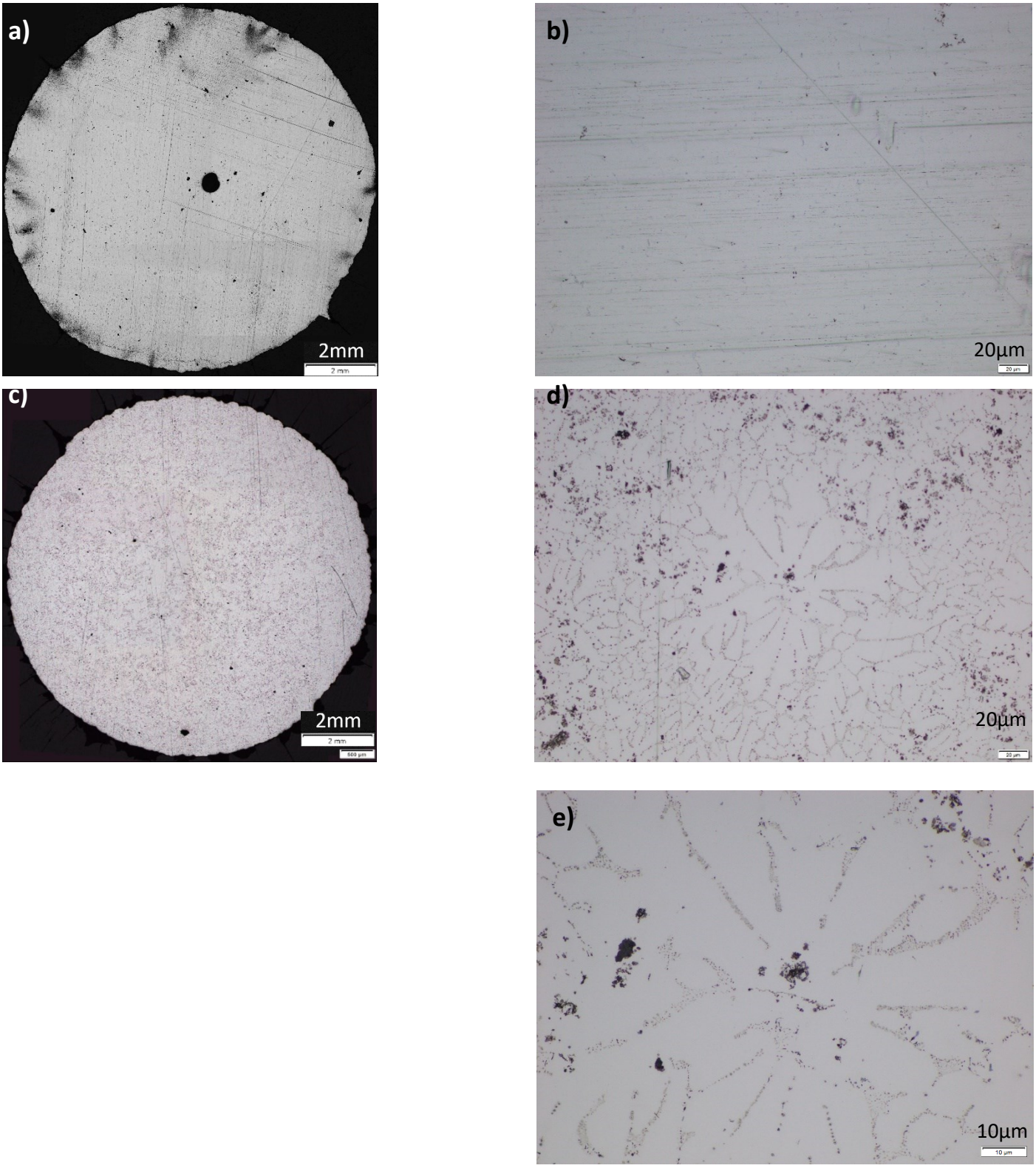

Figure 58. a) Mg_T700_S120 as-cast ingot cross section. b) microscture of a). c) Mg_T700_S120_0.8NiCNT as-cast ingot cross section. d) microstructure of c). e) high magnification image of the microstructure shown in d).

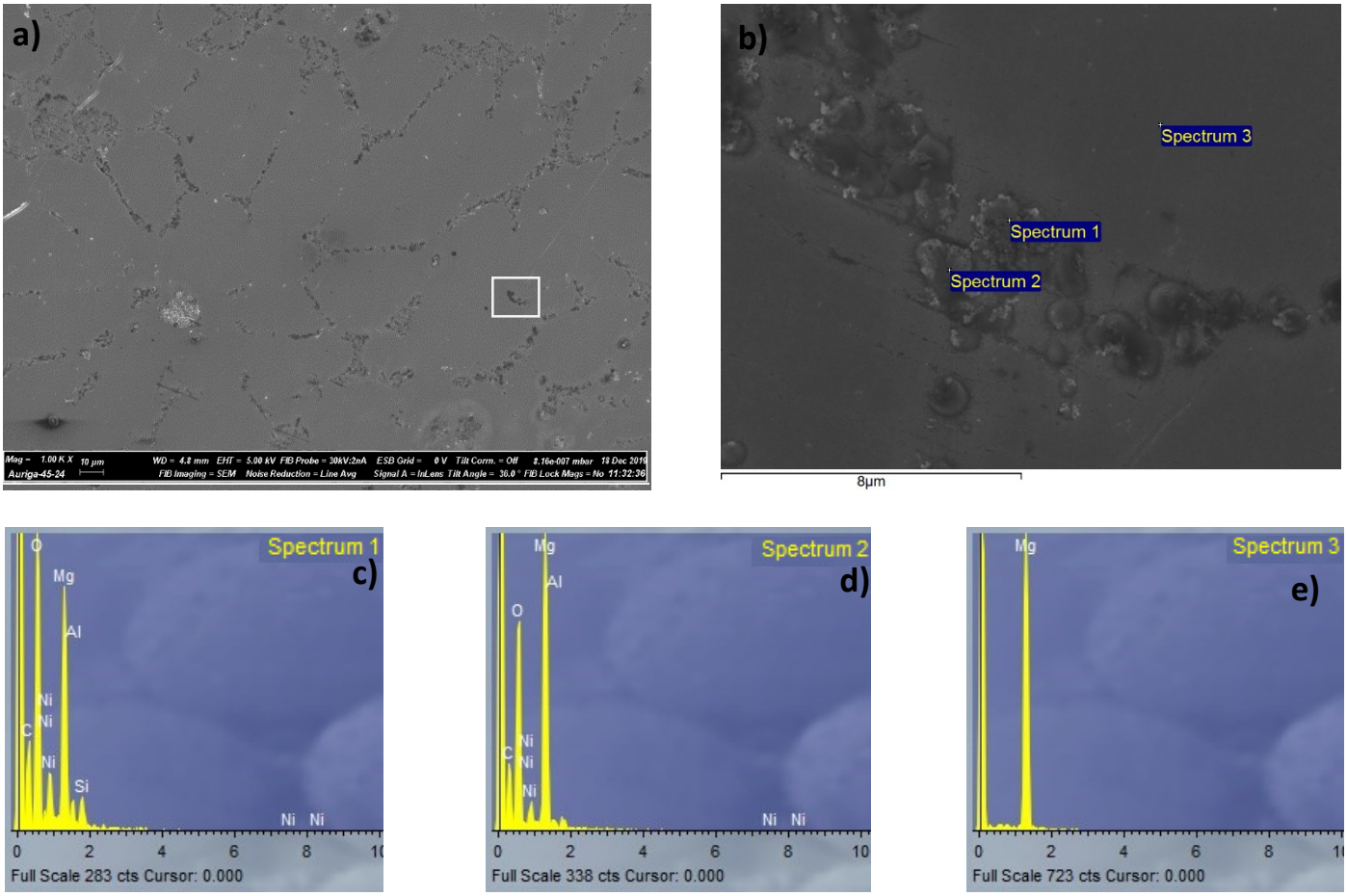

Figure 59. a) SEM image of the intermetallics form in Mg_T700_S120_0.8NiCNT same, optically shown in Figure 60d and e. b) SEM image of the intermetallic highlighted in a). c), d) and e) EDS spectra measured at the locations highlighted in b).

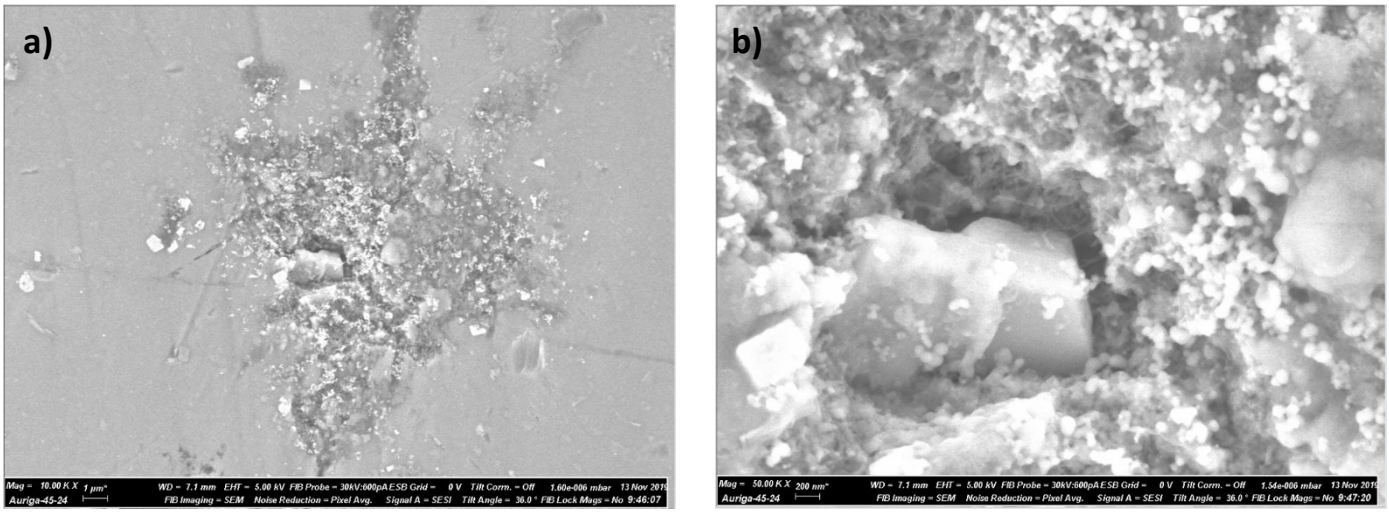

Figure 60. a) and b) SEM image of what appears to be an almost fully infiltrated NiCNT agglomerate within the Mg matrix in the Mg_T700_S120_0.8NiCNT composite.

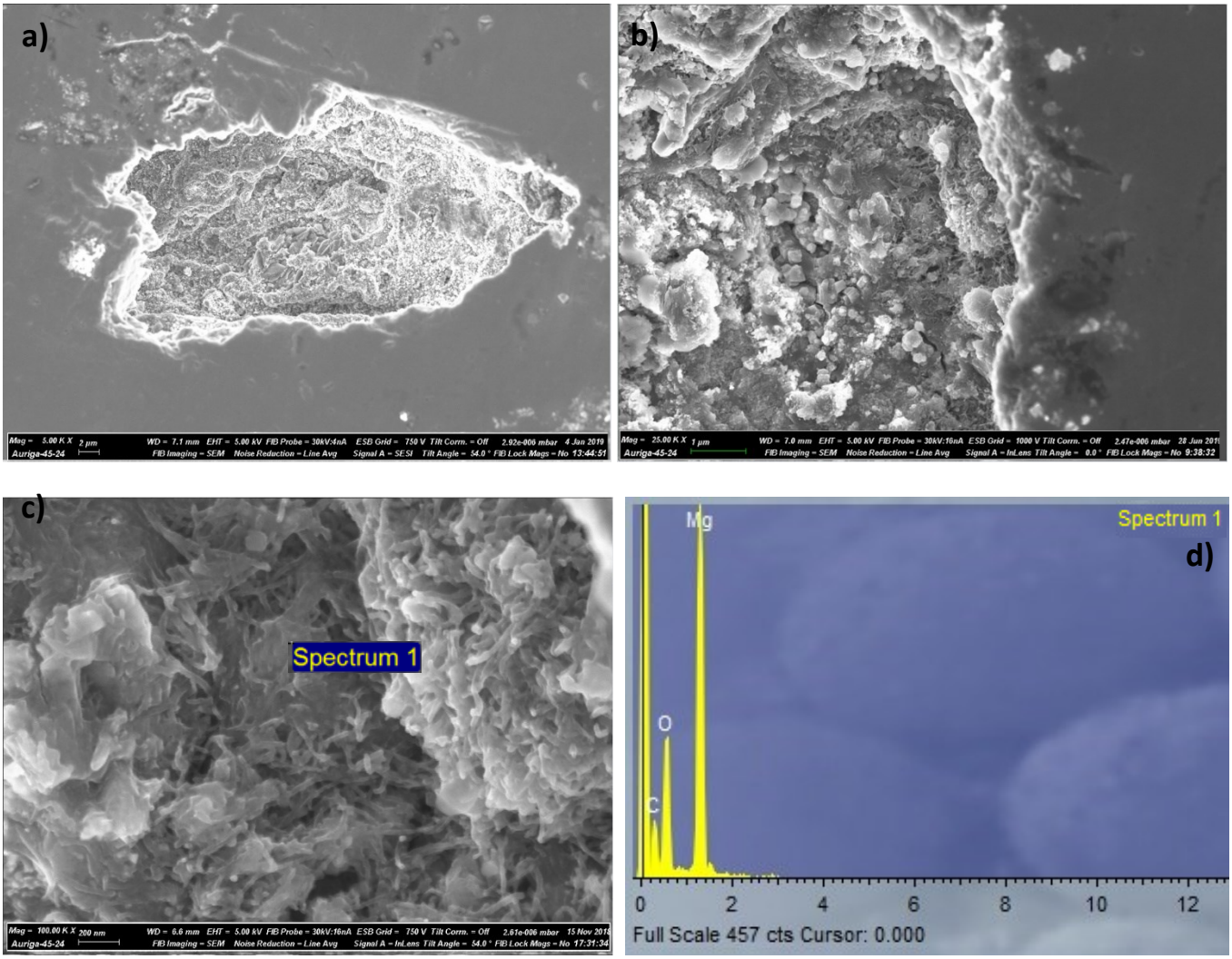

Figure 61. a) An empty pore found in the polished cross-section of Mg_T700_S120_0.8NiCNT. b) and c) show a the surface of a similar pore with a layer of wetted MWCNTs. d) EDS spectrum of the location highlighted in c) shows that no Ni can be detected.

Hardness

The hardness of the Mg_T700_S120 and Mg_T700_S120_0.8NiCNT samples was measured and presented in Figure 62. A 15% improvement was seen in the NiCNT reinforced sample, however, as discussed in section 3.2.5.3.2, the influence of the intermetallic formation on the hardness cannot be decoupled from any potential influence from the reinforcing NiCNTs without a control sample of Mg-1.2wt.% Ni.

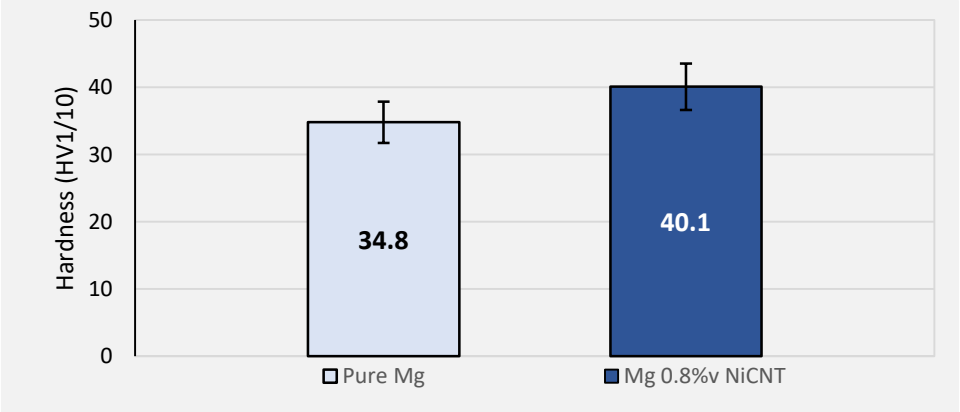

Figure 62. HV1/10 hardness values measured for pure Mg and Mg – 0.8vol.% NiCNT composites.

Fractography

A hammer fracture surface was generated for the Mg_T700_S120_0.8NiCNT sample and studied using SEM, shown in Figure 63. Figure 63a shows an interesting area where a NiCNT agglomerate could have been pulled apart during solidification or fracture, due to wetting at the agglomerate surface shown in Figure 63b, suggested by the tangled NiCNTs bridging the distance between the pore surfaces. Figure 63c and d show individualised NiCNTs within the Mg matrix with what appears to be a nano-gap between the NiCNT and the matrix Mg, similar to what has been observed by Zhou et al [50] in Al-MWCNT composites following a tension test. This gap could be due to poor wettability between the NiCNT and the matrix or, as theorised by Zhou et al [50], a degradation of the interface that occurs during the fracture of the sample.

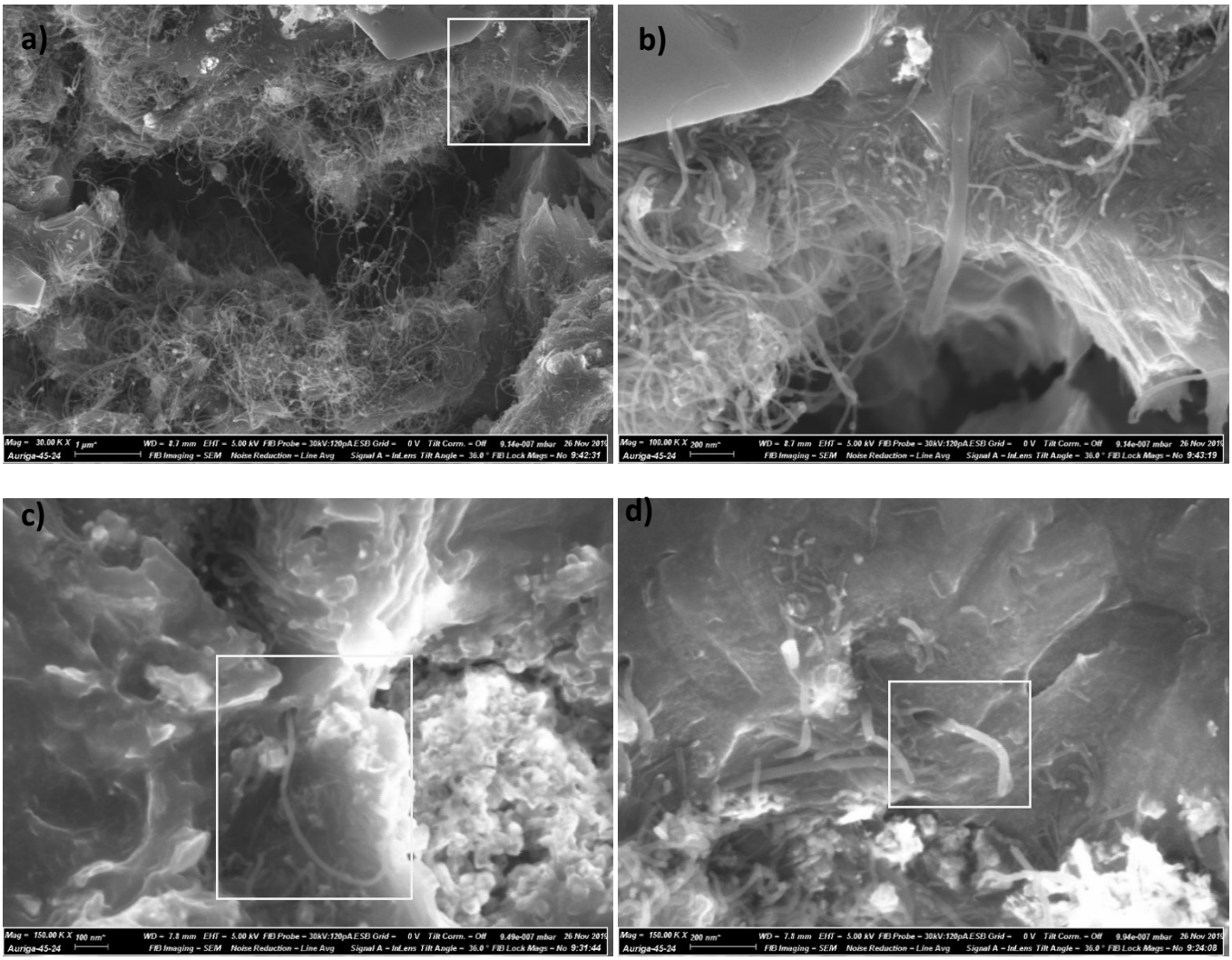

Figure 63. a) SEM image showing NiCNTs bridging the distance across a pore in the fracture surface that could have occurred as a result of solidification or the fracture. b) magnified SEM image of the area highlighted in a). c) and d) highlighted areas show individualised nanotubes in the fracture surface with a 'nano-gap' seperating them from the Mg matrix.

4 SiC reinforced metal matrix nanocomposites

For the final investigation as a part of this thesis, SiC whiskers and SiC nanoparticles were used as reinforcements in the manufacturing of AZ91D metal matrix composites. AZ91D – SiC composites were produced using a melt stirring method very similar to the method described in section 3.1.2.2 and the hardness properties were measured and compared. The results from this section also aim to assist in a complementary project being conducted within Dr Qianqian Li's research group, which is investigating how different MWCNT coatings affect their wettability with metal matrices. SiC coated MWCNTs have been selected for study as the SiC coated overcomes the coating dissolution problem that is encountered when using NiCNTs, and the following experiments present an analogous system to help guide the initial investigation.

4.1 Experimental

4.1.1 Materials

4.1.1.1 Matrix material

For the results presented in this chapter, AZ91D chips described in sections 3.1.1.1 were used as the matrix material.

4.1.1.2 SiC Whiskers

Haydale provided polycrystalline β-SiC whiskers that were used in this study, shown in Figure 64, which have a mean diameter and length of 0.65µm and 10µm, respectively.

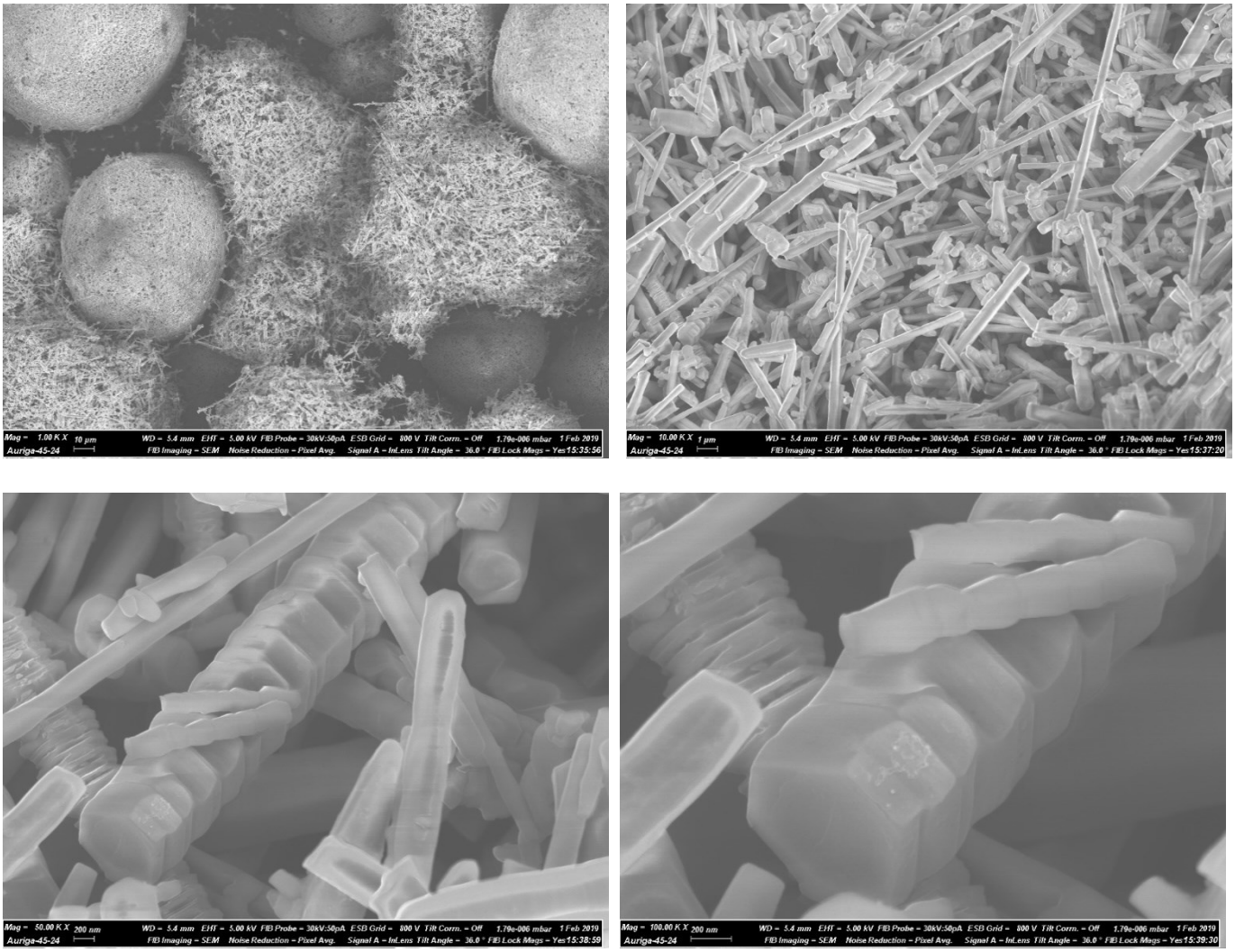

Figure 64. SEM images of the β-SiC whiskers in their as-received state.

4.1.1.3 SiC Nanoparticles

SiC nanoparticles were provided by Sigma Aldrich with an average particle size of 100nm were used in this study, with SEM images of their as received state shown in Figure 65.

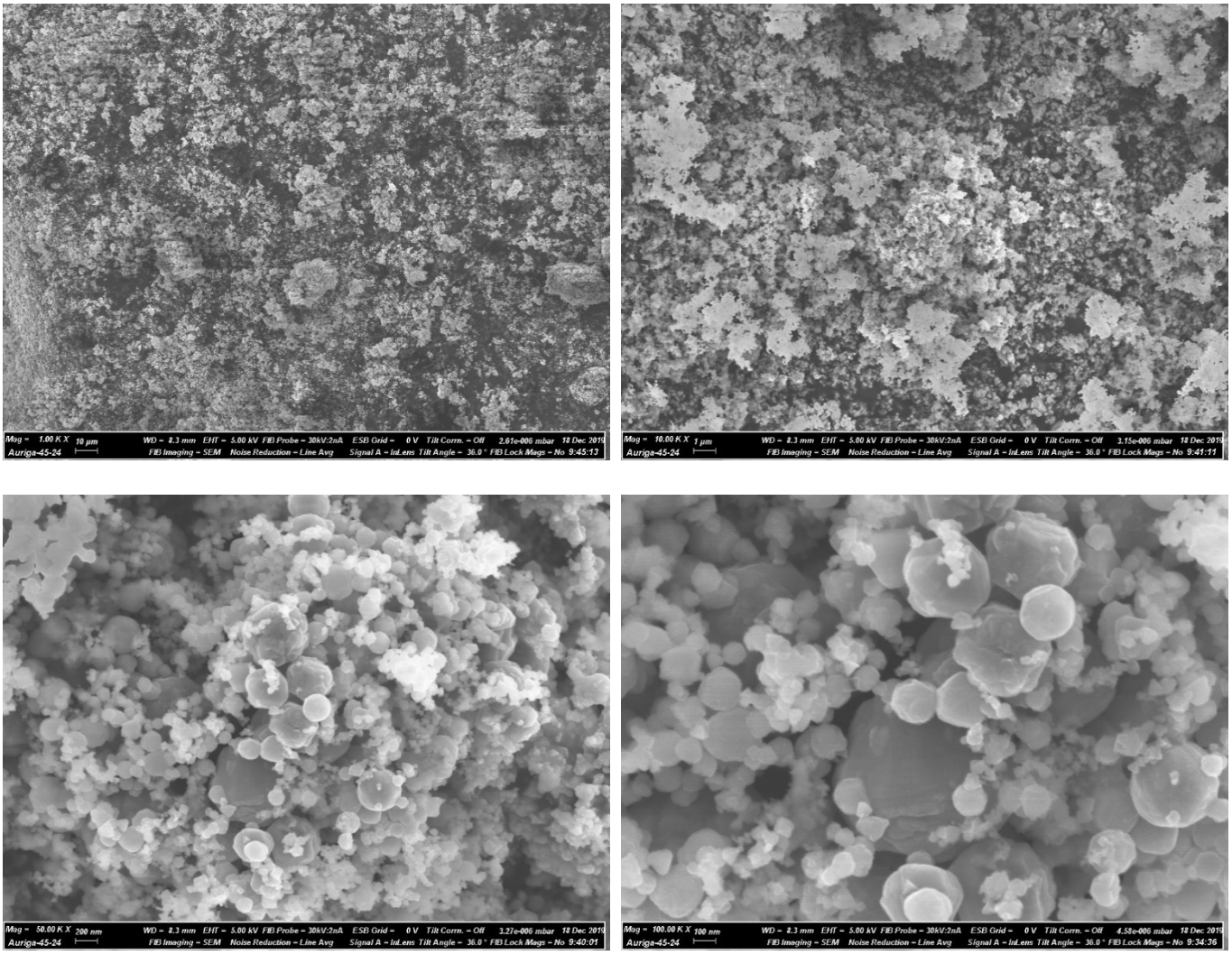

Figure 65. SEM images of SiC nanoaprticles in their as-received state.

4.1.2 Experimental Methods

SiC whiskers and nanoparticles are unable to form the tightly mechanically bound agglomerates that MWCNTs can and are instead bound together by van der Waals alone. Also considering the self-stabilisation mechanisms, discussed in section 2.3.2.3, that are available to SiC reinforcements due to their wettability with molten magnesium, the pre-dispersion technique was not used for incorporating the reinforcing particles into the metal matrix. Instead, SiC particles were weighed, wrapped and sealed in two aluminium foil parcels which have exactly the same weight and properties, each containing half of the total mass of SiC particles used for the composite. One aluminium parcel was then wrapped again in another layer of aluminium foil, so that one aluminium foil parcel had twice the mass of aluminium than the other. This extra layer of aluminium foil, which mass has a negligible impact on the alloy composition, was used in order to delay the release of SiC into the melt as double wrapped aluminium parcel would melt more slowly therefore release the contained SiC particles later than the single wrapped aluminium parcel. This delayed release mechanism would hopefully reduce the extent of SiC nanoparticle reagglomeration and encourage SiC-Mg contact and therefore wetting, self-stabilisation and dispersion. The aluminium parcels were then placed into a vacuum oven at 200°C and held at a pressure of 0-100mbar for 2 hours to ensure the parcels and SiC particles were dry.

The AZ91D chips were raised in the melt stirring furnace and held at 650°C for 30 minutes in an Ar atmosphere. The crucible containing molten AZ91 was then lowered out of the furnace and the aluminium parcels were dropped into the crucible. The crucible was then promptly placed back into the furnace and the molten mixture was stirred at 390RPM for 2 hours. The samples naming convention are similar to what was used in Chapter 3, for an AZ91D sample that is stirred for 2 hours and reinforced with 0.8%vol SiC whiskers would have the name AZ91_T650_S120_0.8SiCwh, as shown in Table 12. The relatively long stirring time of 2 hours was again used to ensure that the molten Mg would have time to infiltrate any SiC agglomerates that existed in the melt and to accentuate any interfacial reactions that may be occurring that could be essential for wetting and also so they become obvious in the microstructural analysis. After 2 hours of stirring, the molten mixture was then cast into a steel mould preheated to 200°C as described in section 3.1.2.2.

Table 12. Processing parameters for the AZ91D – SiC samples produced.

Materials	Sample ref	Casting Temperature (°C)	Melt Stirring Time (mins)	SiC vol%
AZ91	AZ91_T650_S120	650	120	0
AZ91 + SiC whisker	AZ91_T650_S120_0.8SiCwh	650	120	0.8
AZ91 + SiC nanoparticle	AZ91_T650_S120_0.8SiCnp	650	120	0.8

4.1.3 Characterisation

The microstructure, hardness and fractography studies were conducted for the AZ91D – SiC samples the same way as they were in Chapter 3.

4.2 Results

4.2.1 Microstructure

Figure 66a and b, Figure 67a and b and Figure 68a and b show the cross section of the as-cast ingots for samples AZ91_T650_S120, AZ91_T650_S120_0.8SiCwh and AZ91_T650_S120_0.8SiCnp, respectively. The AZ91_T650_S120 sample does show more non-matrix material represented by black specs than AZ91_T650_S30 shown in Figure 52a, which is most likely due to the higher levels of oxide particle inclusion that would be generated by the sample stirred for 120 minutes instead of 30 minutes. The high level of oxidation is also reflected in the 9% decrease in hardness measured for AZ91_T650_S120 when compared to AZ91_T650_S30.

The AZ91_T650_S120_0.8SiCnp sample also shows quite a homogenous microstructure except for darker areas that after SEM analysis were shown to be SiC nanoparticle agglomerates in Figure 68d. With further SEM examination, SiC nanoparticles were not found outside of these agglomerates apart from in areas of shrinkage porosity, discussed in section 4.3, and therefore poorly dispersed through the matrix. Even after acknowledging the SiC nanoparticles were poorly dispersed, one would expect to see a much larger amount of agglomerates throughout the matrix, given by the volume fraction. The sparsity of the SiC nanoparticles suggests that there may have been some larger scale separation of the melt during the melt stirring operation. However, interestingly, the AZ91_T650_S120_0.8SiCwh sample shows a macroscopically homogenous distribution of SiC whiskers throughout the cross section.

The SiC whiskers appear to be fully infiltrated and wetted by the Mg matrix, however, are only clustered together on a microscopic scale. Figure 67e shows SiC whiskers that are embedded parallel to the polished cross-section but have been shattered at multiple intervals along their length. The fracture of the SiC whiskers could have happened during the contraction of solidification or as a result of the mechanical forces generated during the grinding and polishing steps. Figure 70 and Figure 71 show whiskers with lengths longer than the fracture intervals shown in Figure 67e found within the matrix from SEM analysis of a fracture surface, suggesting that the SiC whisker fracture is indeed as a result of grinding and polishing, instead of solidification.

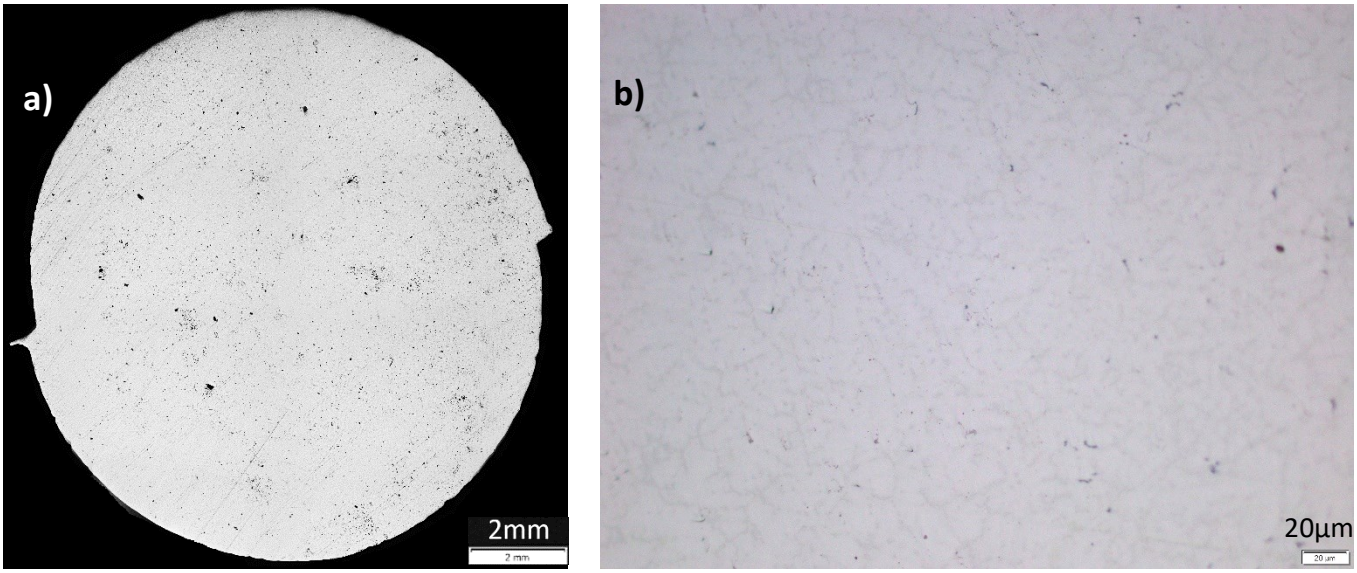

Figure 66. a) and b) show the cross-section and microstructure of AZ91_T650_S120, respectively.

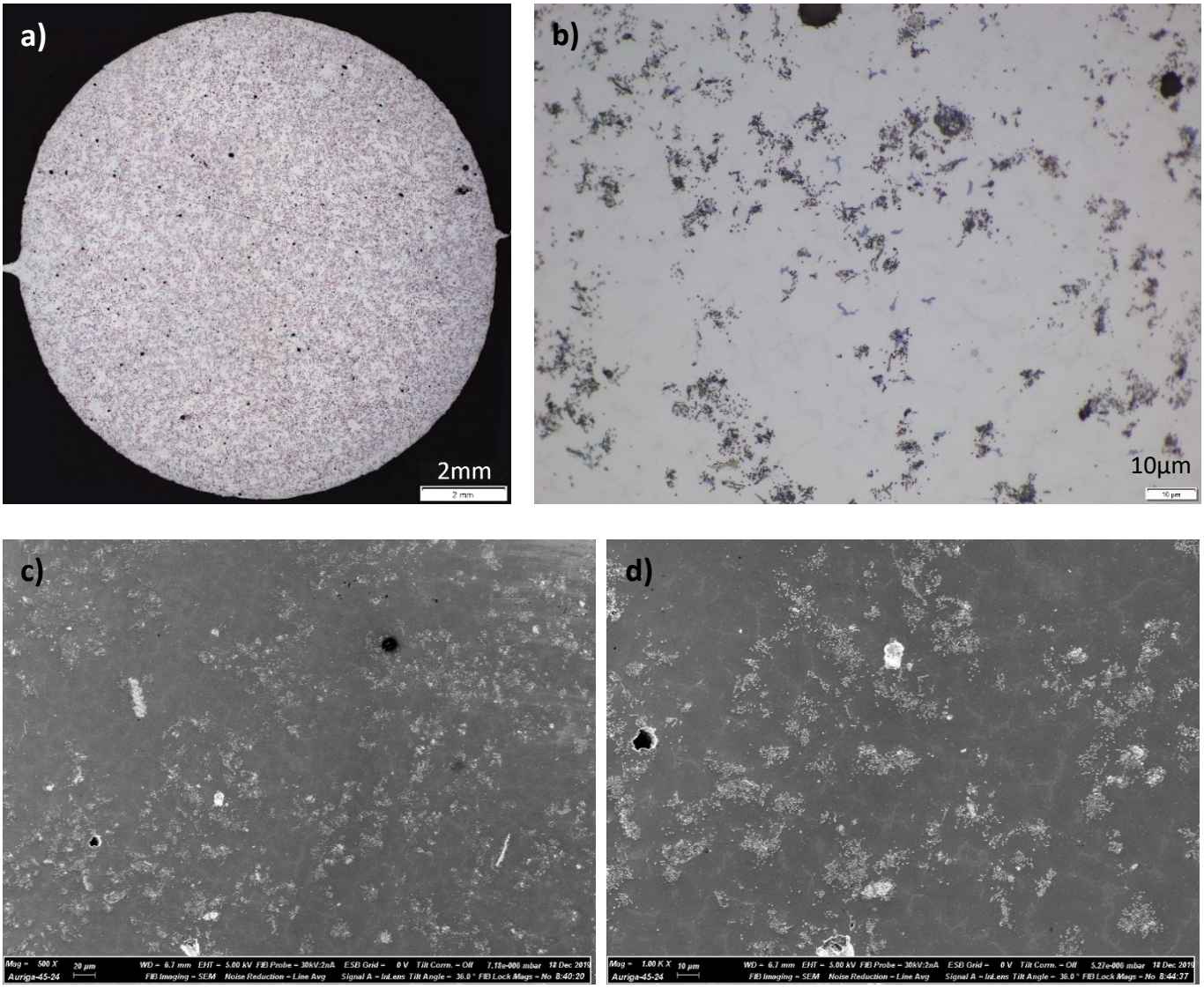

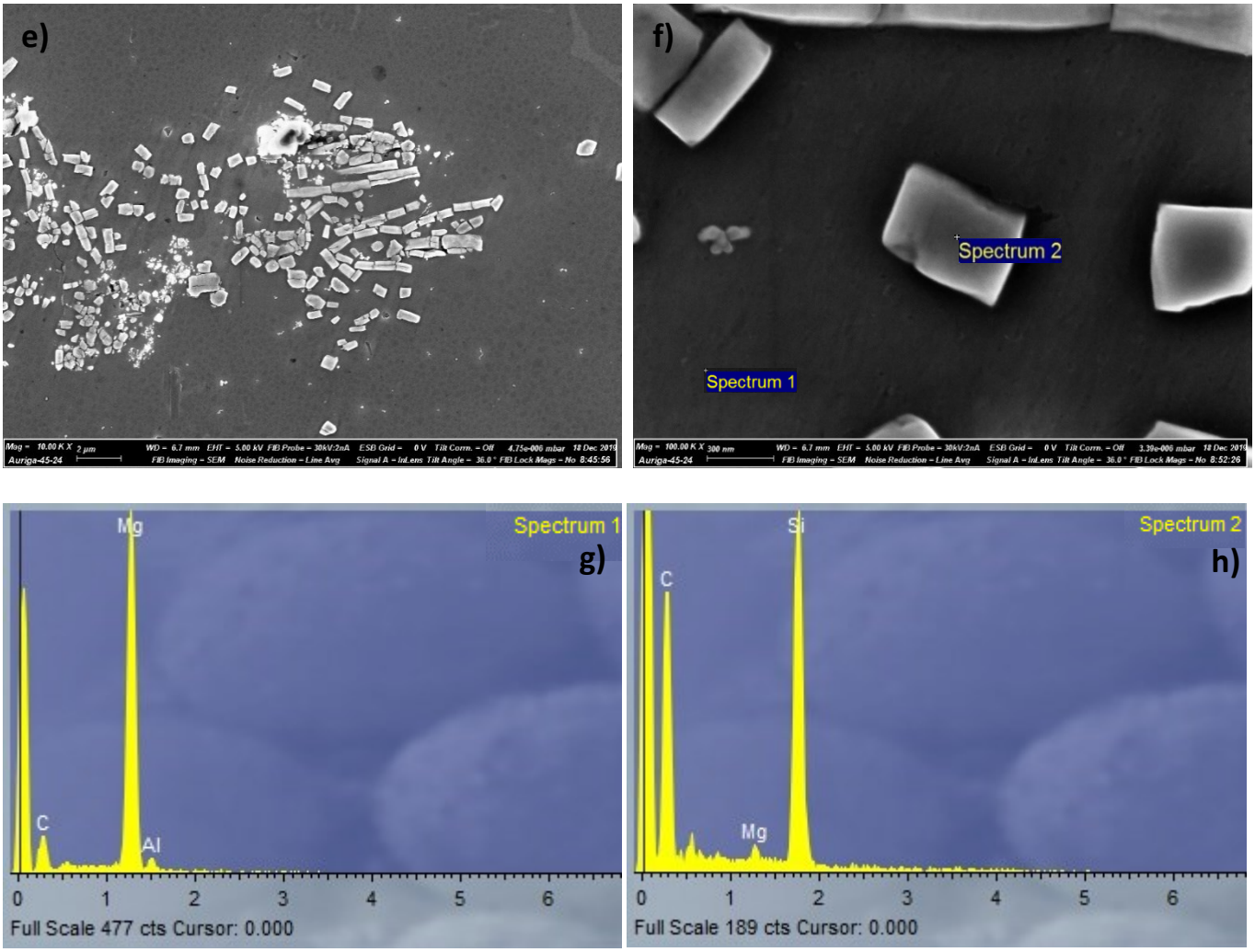

Figure 67. a) and b) show the cross-section and microstructure of AZ91_T650_S120_0.8SiCwh, respectively. b), c), d) and e) SEM images showing the dispersion state and clean interface of the SiC whiskers within the AZ91D matrix. g) and h) EDS spectra measured in locations highlighted in f).

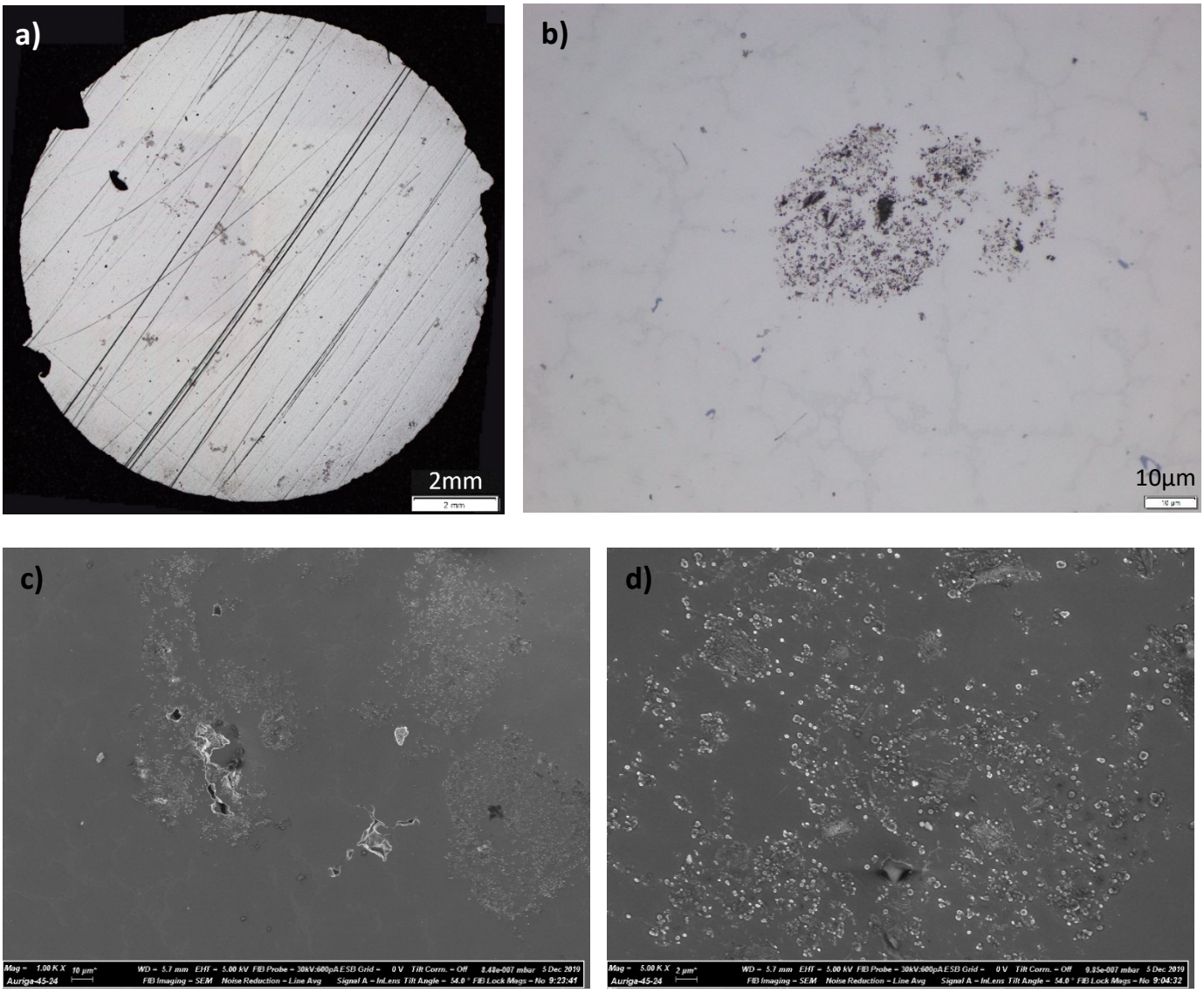

Figure 68. a) and b) show the cross-section and microstructure of AZ91_T650_S120_0.8SiCnp, respectively. c) and d) SEM images of a representative area of what is shown in b), showing an agglomeration of well wetted SiC nanoparticles.

4.2.2 Hardness

The measured hardness for the samples in Table 12 are given in Figure 69. An 11% and 20% increase in hardness was achieved for samples AZ91_T650_S120_0.8SiCnp and AZ91_T650_S120_0.8SiCwh, respectively.

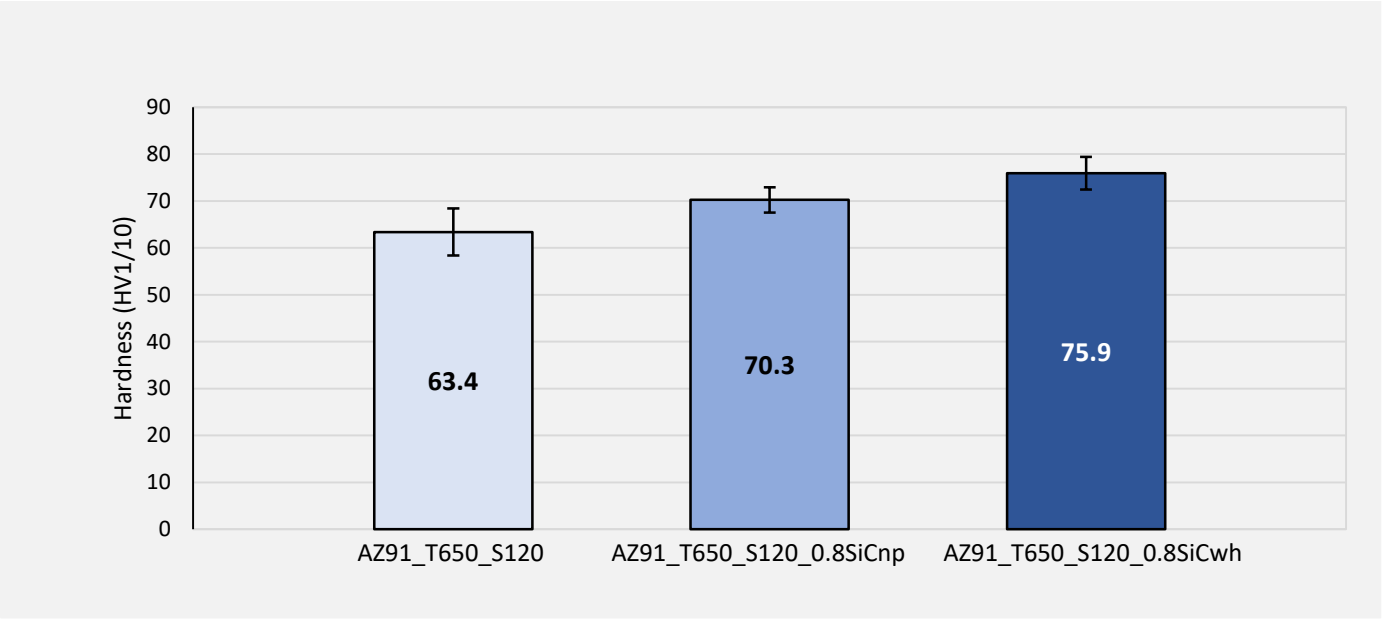

Figure 69. HV1/10 values measured for samples AZ91_T650_S120, AZ91_T650_S120_SiCnp and AZ91_T650_S120_0.8SiCwh.

4.2.3 Fractography

A hammer fracture surface was generated from an AZ91_T650_S120_0.8SiCwh composite, shown in Figure 70a. SiC whiskers were easily found within the fracture surface that appeared to be individually dispersed and well wetted with AZ91 matrix, with no whiskers being found within pores comparable to what was found in the Mg/AZ91 – MWCNT composites presented in sections 3.2.2. Figure 70b, c and d show two SiC whiskers embedded in the matrix. Figure 70c shows a whisker with a potentially clean interface, which would have to be confirmed with a TEM study, whereas Figure 70d shows either a poor interface or an interface that has de-bonded during the deformation prior to fracture.

Figure 71b shows a hexagonal socket that it was most likely formed by solidification of the AZ91 matrix around a SiC whisker followed by a secondary mechanism that occurred during the sample fracture, this will be discussed in section 4.3.1.

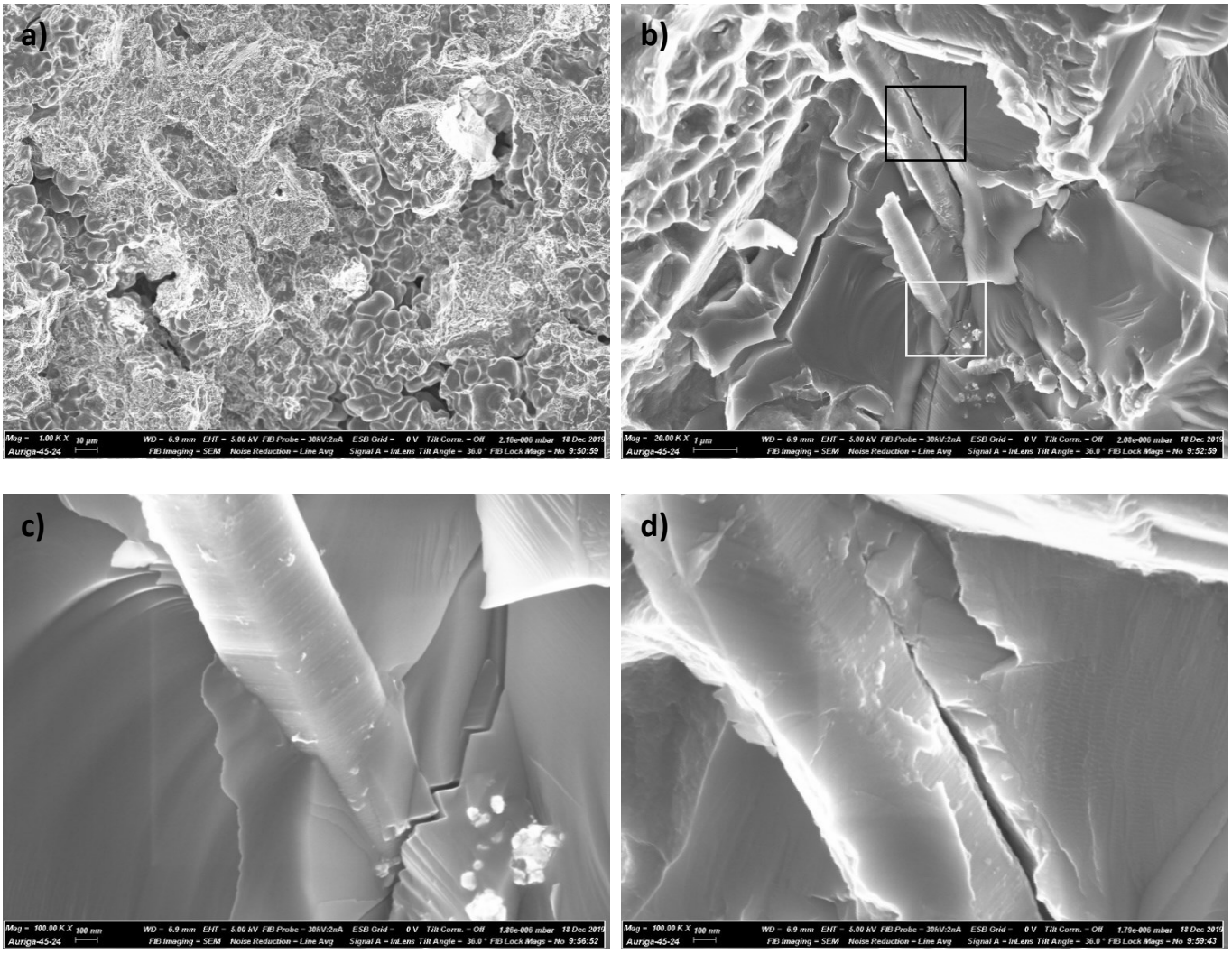

Figure 70. a) SEM image of a hammer fracture surface generated from an as-cast AZ91_T650_S120_0.8SiCwh composite. B) SEM image of two individualised SiC whiskers embedded in the AZ91D matrix. c) and d) SEM image showing the interface between the SiC whisker highlighted by the white and black square in b), respectively.

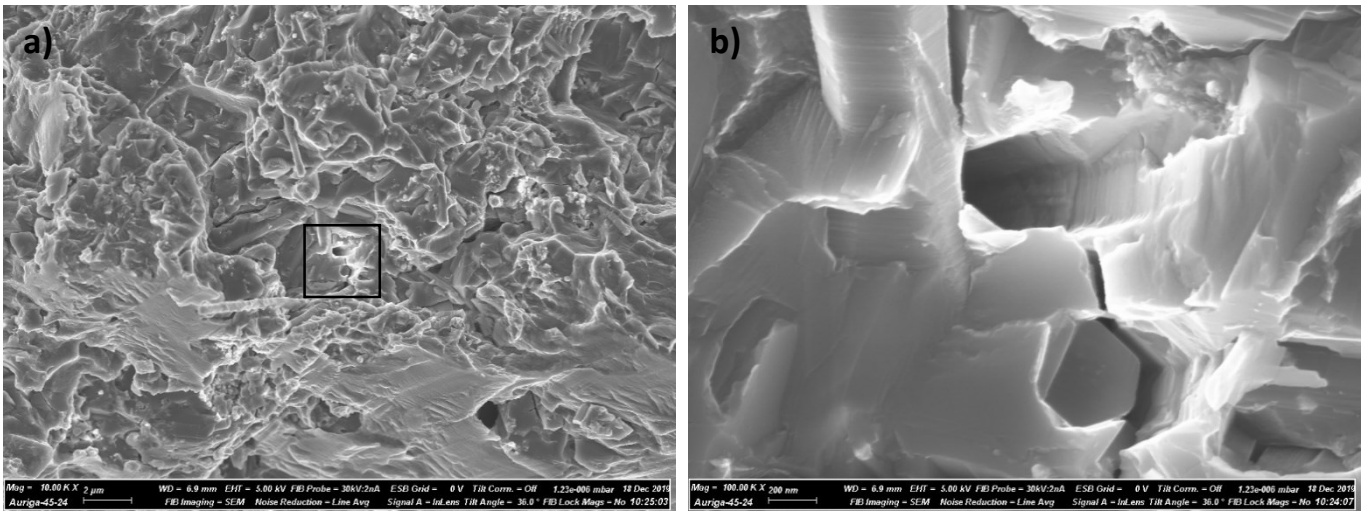

Figure 71. a) SEM image of a hammer fracture surface generated from an as-cast AZ91_T650_S120_0.8SiCwh composite. b) high magnification SEM image of the highlighted area in a) showing hexagonal sockets of where SiC whiskers are presumed to be located before fracture.

4.3 Discussion

4.3.1 Mechanical properties

Studying different types of reinforcing particles, such as whiskers and particles, allows one to start investigating what the ideal geometry for a MMNC reinforcement might be by comparing experimental data with predictive models that are currently used throughout the literature.

Table 13 shows the models and coefficients used to calculate the predicted increase in tensile yield strength by using the different reinforcements for a range of volume fractions used in this study with the results plotted in Figure 72a-f.

Table 13. Models and coefficients used for determining the theoretical increases in yield strength for the proposed composites in Figure 74.

Model/Coefficient/ Parameters			
Reinforcement	**MWCNT**	**SiC Whisker**	**SiC nanoparticles**
Thermal mismatch strengthening $\Delta\sigma_{y(T.M)}$	$= \alpha G_m b\sqrt{\frac{Bv_{re}\Delta CTE\Delta T}{bd(1-v_{re})}}$	$= \alpha G_m b\sqrt{\frac{Bv_{re}\Delta CTE\Delta T}{bd(1-v_{re})}}$	$= \alpha G_m b\sqrt{\frac{Bv_{re}\Delta CTE\Delta T}{bd(1-v_{re})}}$
Orowan strengthening $\Delta\sigma_{y(O)}$	$= \frac{0.8\, G_m bM}{\sqrt{\frac{\pi d^2}{2v_{re}}}}$	$= \frac{0.8\, G_m bM}{\sqrt{\frac{\pi d^2}{2v_{re}}}}$	$= \frac{0.8\, G_m bM}{\sqrt{\frac{\pi d^2}{6v_{re}}}}$ [40]
Load transfer $\Delta\sigma_{y(LT)}$	$= v_{re}\left(\frac{\tau l}{d}\right)$ as NC7000 $l < l_c$	$v_{re}\left(\frac{\tau l}{d}\right)$ as SiC whisker $l < l_c$	$= 0.5 v_{re}\sigma_m$ [82]
Summation model	$= \sigma_m + \sqrt{\Delta\sigma_{y(T.M)}{}^2 + \Delta\sigma_{y(LT)}{}^2 + \Delta\sigma_{y(O)}{}^2}$		
d **– reinforcement diameter (nm)**	9.5	650	100
l **– reinforcement length (µm)**	1.5	10	-
σ_{re} **– reinforcement yield strength (GPa)**	33 [24]	8.4 [178]	-
α **– Geometric constant**	1.25 [38]		
G_m **– Matrix shear modulus (GPa)**	16.4 [5]		
b **– Burgers vector (nm)**	0.32 [5]		
B **– Geometric constant**	4 [57]		12 [57]
ΔCTE **– Difference in coefficient of thermal expansion (x10^{-6} K^{-1})**	25 (MWCNT CTE = 1 [179]) (AZ91D CTE = 26 [180])	22 (β – SiC CTE = 4 [181])	22 (β – SiC CTE = 4 [181])
ΔT **– Change in processing to testing temperature (K)**	630	630	630
v_{re} **– Volume fraction of reinforcement**	0-0.01	0-0.01	0-0.01

Figure 72a-c show the predicted increase in yield strength with the contribution from each strengthening mechanism for AZ91D reinforced with MWCNTs, SiC whiskers and SiC nanoparticles, respectively, with the sums for all reinforcements compared in Figure 72d.

AZ91D – SiC whisker composites' dominant strengthening mechanism is load transfer and thermal mismatch strengthening with negligible contributions from Orowan, whilst for AZ91D – SiC nanoparticles, the dominant strengthening mechanisms are both Orowan and thermal mismatch strengthening, with a negligible contribution from load transfer. The main difference between the reinforcing particles that dictates the efficacy of different strengthening mechanisms is the relatively large diameter of the SiC whiskers used when compared (650nm) to the SiC nanoparticles (100nm).

Figure 72e shows a comparison for the predicted tensile yield strength for SiC whisker and nanoparticles of equal diameters of 20 and 100nm (The strengthening contributions for each mechanism and reinforcement were further introduced in Appendix A.3). The predicted tensile yield strengths were explored in an attempt to understand what the optimal nanoparticle reinforcement geometry for a given volume fraction loading would be. It is assumed that the theoretical SiC whiskers of 20 and 100nm are below the critical length, Figure 72e shows that for both particle geometries with decreasing particle diameter, the proportion of the strengthening contribution from the Orowan and thermal mismatch strengthening mechanisms significantly increase. For thermal mismatch, strengthening is greater for the nanoparticle due to the larger geometric constant, B. In Figure 72f, the Orowan strengthening and thermal mismatch for 20nm SiC nanoparticles becomes larger than the combined strengthening of thermal mismatch, load transfer and Orowan strengthening achieved for 20nm SiC whiskers due to the smaller interparticle distance realised by the SiC nanoparticles up until about 2vol.%, after which load transfer becomes dominant again for the SiC whiskers, as depicted in Figure 72f.

Therefore, in terms of maximising tensile strength for a %.vol of 0-2% of reinforcing particles, it is important to use equiaxed nanoparticles with minimised diameters in order to maximise the strengthening that can be achieved through thermal mismatch and Orowan strengthening. Additionally, if a manufacturing method can be devised that can achieve an ideal dispersion that allows the use of high vol.%, then the whisker shape is favourable compared to the particle as the increase in yield strength due to load transfer for the whisker is larger than the increase in Orowan and thermal mismatch strengthening for the particle. However, the effect of different particle geometries on other important material properties such as wear or fatigue resistance are yet to be deeply explored and therefore the ideal reinforcement may differ for different material requirements. Figure 72d shows how the mechanical and geometrical properties of MWCNTs, if dispersed and aligned properly, can take advantage of all the proposed strengthening mechanisms and provide the highest increase in tensile yield strength compared to SiC, making them the ideal reinforcement that is readily commercially available today.

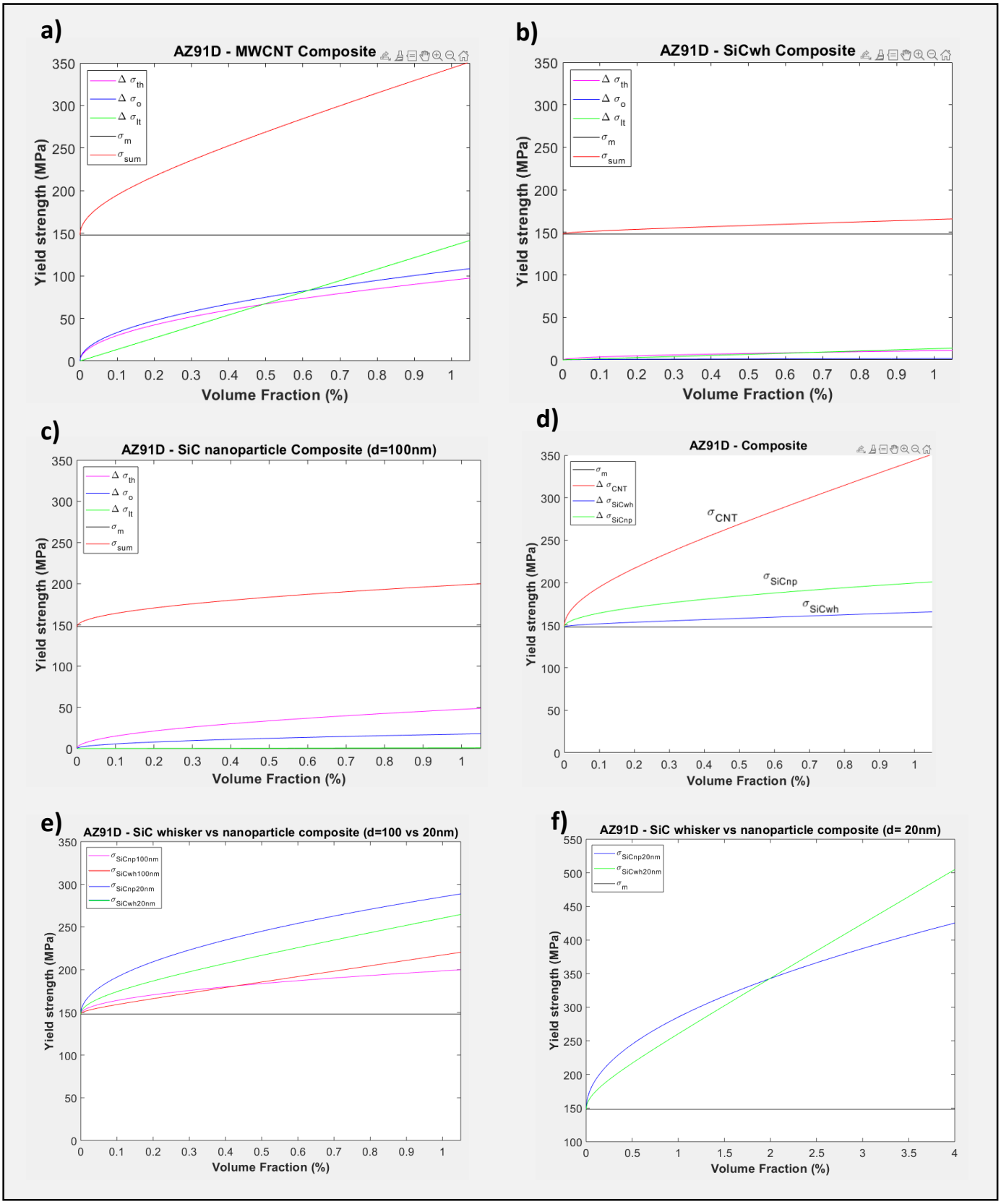

Figure 72. Theoretical yield strength increase for a AZ91D-MMNC using the models presented in Table 13 for a) AZ91D-NC7000, b) AZ91D – SiC whisker and c) AZ91D – SiC nanoparticle composites. d) compares the total yield strength increase for the composites presented in a), b) and c). e) Compares the theoretical yield strength increase for an AZ91D composite reinforced with SiC whisker and SiC nanoparticles with diameters of 20 and 100nm. f) shows the volume fraction transition point for where 20nm SiC whiskers offer a higher strengthening efficiency than 20nm SiC nanoparticles due to the load transfer becoming the dominant strengthening mechanism for whiskers at higher volume fractions.

The hardness of the samples reinforced with SiC nanoparticles and SiC whiskers were 11 and 20% higher than that of the pure AZ91D sample. The difficulty encountered when determining the source of the improvement in hardness in the NiCNT reinforced composites, where new intermetallics confound any potential improvement received from the reinforcing material itself, is also encountered with AZ91D composites reinforced with SiC. In the case of the SiC reinforced composites, the mechanics for the formation of Mg_2Si intermetallics (blue areas shown in Figure 73 [182] for sample AZ91_T650_S120_0.8SiCwh) are given by Equations 48 and 49. The SiO_2 for the reaction is provided by the native oxide layer that exists on the SiC particles. Mg_2Si formation can also have secondary benefits with regards to creep resistance due to its stability a high temperature, especially compared to $\beta - Mg_{17}Al_{12}$ [183].

$$2Mg_{(l)} + SiO_{2(s)} \rightarrow 2MgO_{(s)} + Si_{(l)} \quad (48)$$

$$2Mg_{(l)} + Si_{(l)} \rightarrow Mg_2Si_{(s)} \quad (49)$$

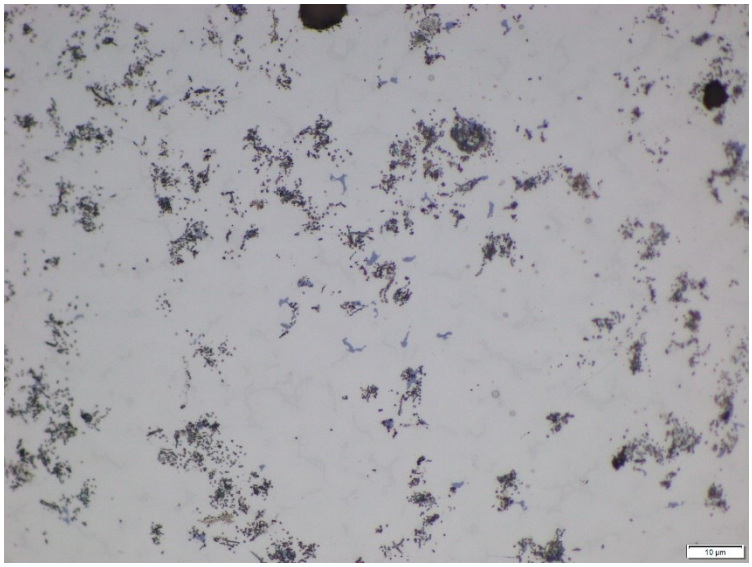

Figure 73. Microsctructure of AZ91_T650_S120_0.8SiCwh with the blue areas showing Mg_2Si formation.

Shi et al [184] found that for Mg – Al alloys where Mg mol.% was between 19.7 and 93.7% at 1173K, Equation 50 could occur, resulting in the further production of $Mg_2Si_{(s)}$ that would then be limited once the Al wt.% had been depleted below 5.3 wt.% during sessile drop tests. However, the dynamics of this reaction were not discussed, and the lower temperatures used in the manufacturing process in this study may inhibit or significantly slow the speed of this reaction. Al_4C_3 was not observed during microstructural studies, however, due to its decomposition upon contact with water, Al_4C_3 can be difficult to detect unless great care is taken during sample preparation.

SiC whiskers found in the fracture surface (Figure 70 and Figure 71) appear to show similar geometry to when they were observed in their as received state (Figure 64), and were seen to maintain their hexagonal shape (Figure 71) suggesting that dissolution of the SiC was not occurring or at a negligible rate and therefore that most of the $Mg_2Si_{(s)}$ was supplied from the native $SiO_{2(s)}$ oxide layer. Further TEM and XRD studies should be conducted to investigate whether any other carbides such as Al_2MgC_2 were formed to further understand the Mg-Al melt – SiC interaction.

$$6Mg_{(l)} + 4Al_{(s)} + 3SiC_{(s)} \rightarrow Al_4C_{3(s)} + 3Mg_2Si_{(s)} \quad (50)$$

Nevertheless, the AZ91D – SiC whisker sample showed the largest increase in hardness and if the increase was due to Mg_2Si intermetallic formation, the AZ91D – SiC nanoparticle sample should have shown the largest increase, despite the apparent poor dispersion of SiC nanoparticles, due to the approximately 5 times larger surface area of the SiC nanoparticles, and therefore SiO_2, relative to the SiC whiskers. Suggesting that the SiC whiskers themselves are acting as reinforcement. However, the poor wettability seen for a lot of the SiC nanoparticles suggest that maybe the surface of a significant proportion of the nanoparticles did not come into contact with the molten AZ91D and therefore did not form Mg_2Si. Figure 71 shows the formation of two hexagonal sockets, one hollow and another with potentially a SiC whisker still contained within. The hollow socket appears to be the result of fibre pull-out, however the other socket with the SiC whisker could be formed as the result of fibre fracture. The reasoning to support this view is that the matrix appears to maintain its hexagonal shape above the tip of the fractured SiC whisker, suggesting that some of the SiC whisker used to exist in this location. The uneven surface of the hexagonal fibres, shown in Figure 64, combined with the effective wetting of the fibres by the AZ91D shown in Figure 67 and Figure 70 would provide significant mechanical locking, again making fibre pull out for some whiskers unlikely. Figure 71 is believed to be showing crack bridging SiC whiskers that are acting to reinforce the AZ91D matrix through effective load transfer, and that this load transfer is at least, in some part, responsible for the increase in hardness measured for the AZ91D – SiC whisker composite.

4.3.2 Dispersion

One of the purposes of using SiC nanosized reinforcements with a long time of exposure to the AZ91D melt was to investigate whether the level of agitation that a mechanical stirrer can provide combined with the known wettability of SiC by AZ91D was enough to disperse the particles within the matrix, and achieve the 'self-stabilised' solution theorised in section 2.3.2.3. A significant difference in the quality of reinforcing particle dispersion can be seen between the AZ91D – SiC whisker and AZ91D – SiC nanoparticle composites from optical and SEM imaging. Whilst the SiC whiskers are very well distributed across the as-cast AZ91D ingot cross section, as shown in Figure 67, the whiskers still appear to be in small bundles. The SiC whiskers are shown to be individually wetted so they are either still bound by some van der Waals interaction through the AZ91D melt or they have been pushed together by local solidification fronts. T6 heat treatment of the AZ91D – SiC whisker composite could be employed to clearly show the grain boundaries under optical and SEM imaging, the location of the SiC whiskers can then be compared with the grain boundaries, allowing the influence of the solidification fronts to be assessed.

The lack of SiC nanoparticles found in the composite cross section could be due to a substantial separation of the AZ91D melt and SiC nanoparticles during the stirring stage, and if there are scenarios where separation can occur, the long stirring time of 2 hours would exacerbate the separation. The SiC nanoparticles could have either sunk, as their density of 3200kg/m^3 compared to AZ91D's of 1810kg/m^3 would suggest or they have floated to the surface of the melt due to entrapped gas, that might not be present in the whiskers, that could have then been removed by the turbulent cover gas. The much better dispersion achieved for the SiC whiskers in comparison to the SiC nanoparticles suggests the floating of the nanoparticles is more likely as the SiC nanoparticle and whiskers would have very similar densities. The SiC nanoparticles dispersion could also have been influenced by their interaction with incident

solidification fronts, SEM imaging of the AZ91D – SiC nanoparticle cross section, given in Figure 74, showed two different areas of shrinkage porosity, a porosity generated by the lack of molten material to feed a solidification front. Figure 74a and b show the surface of a clear AZ91D shrinkage porosity surface without any foreign particles. Figure 74c, d and e show the surface of a shrinkage porosity with a covering of unwetted SiC nanoparticles as suggested by Figure 74e,f and g.

The SiC nanoparticles being present in the shrinkage porosity suggests that they were pushed there by a solidification front. Figure 75 shows an SEM image taken of a solidification front found in the fracture surface of the AZ91D – SiC whisker composite where partially engulfed SiC whiskers can be seen that are parallel to the solidification front appear as though they have also been pushed to that final location. Ultimately, it appears as though the solidification of the composite has had an impact on the final dispersion of the SiC reinforcing particles. Therefore, the manufacturing parameters such as reinforcing particle selection/ surface modification or solidification speed that can minimise the impact of solidification front pushing should be investigated in order to produce metal composites with good particle dispersions and enhanced mechanical properties as a result.

The partial wetting of the SiC nanoparticles shown in Figure 74 suggest that even after 2 hours of stirring, the SiC nanoparticles were not infiltrated by the molten AZ91D. No unwetted SiC whiskers were found in their respective composites that shows that the two reinforcements show different wetting behaviour. The different wetting behaviour could have been due to trapped gas within a SiC nanoparticle agglomerate that retarded the infiltration of molten AZ91D or different SiC particle surfaces as a result of their different methods of manufacture. Nevertheless, a more intensive dispersion method or energetic environment may be required to achieve spontaneous infiltration of the SiC nanoparticles.

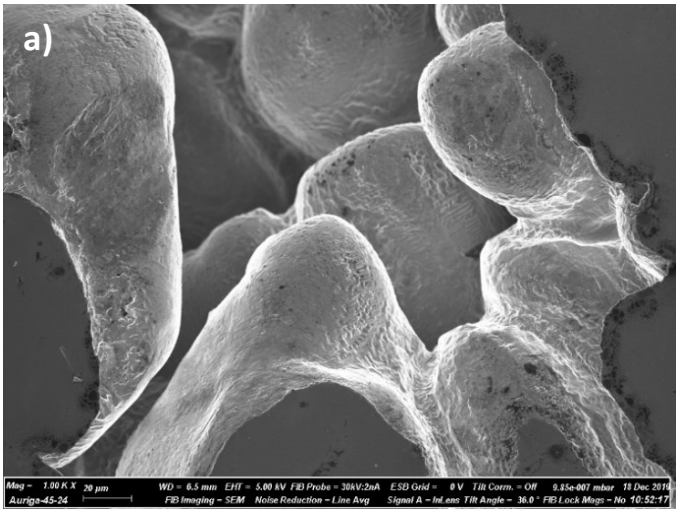
a)

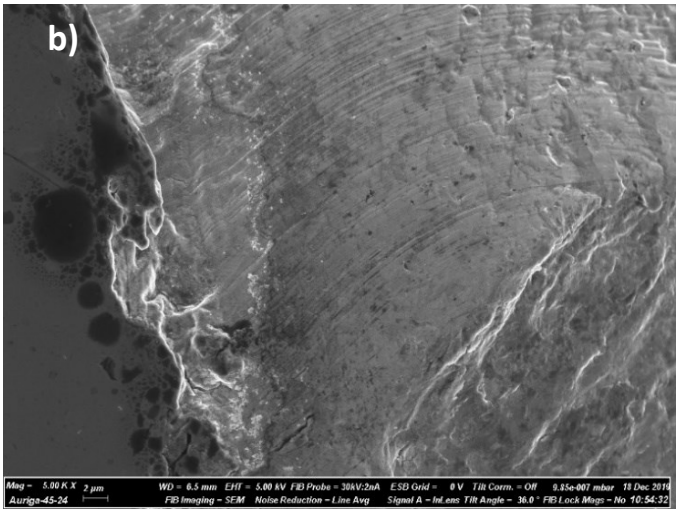
b)

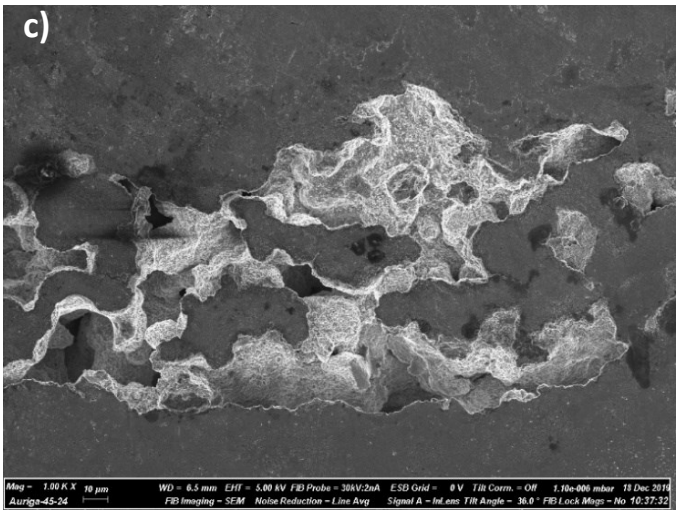
c)

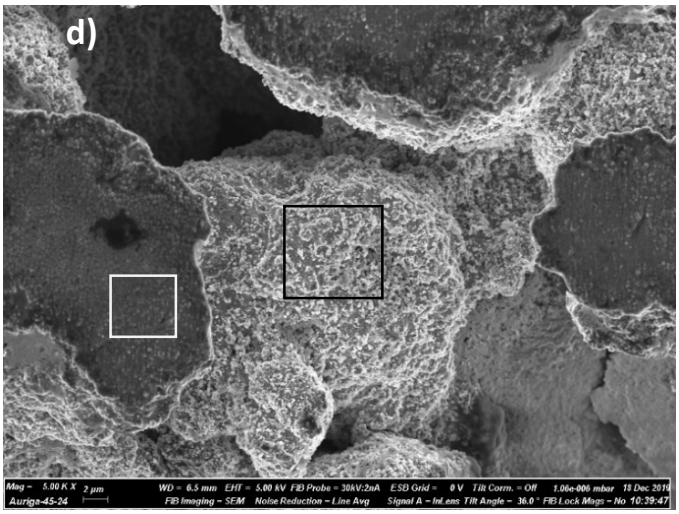
d)

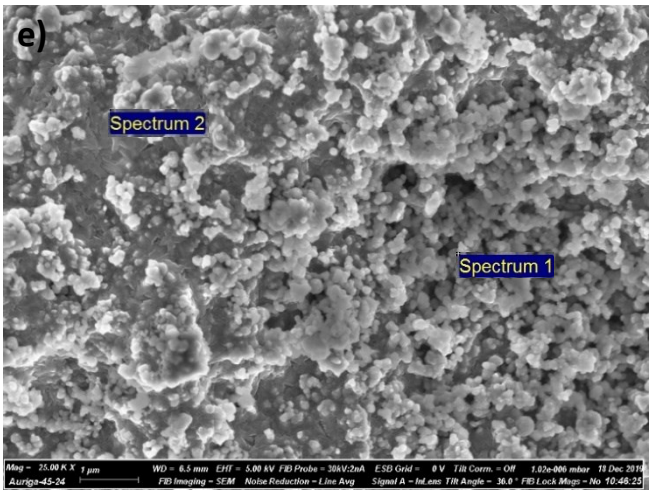
e)
Spectrum 2
Spectrum 1

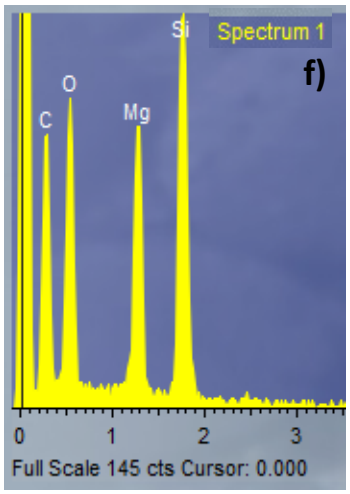
Si
Spectrum 1
f)
O
C
Mg
0
1
2
3
Full Scale 145 cts Cursor: 0.000

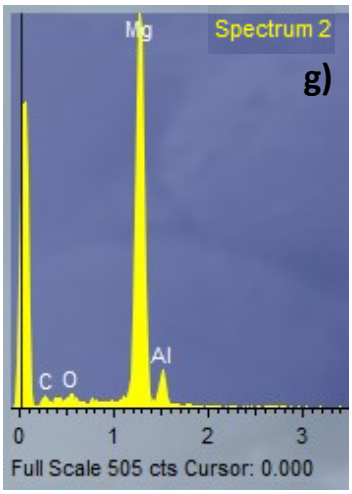
Mg
Spectrum 2
g)
Al
C O
0
1
2
3
Full Scale 505 cts Cursor: 0.000

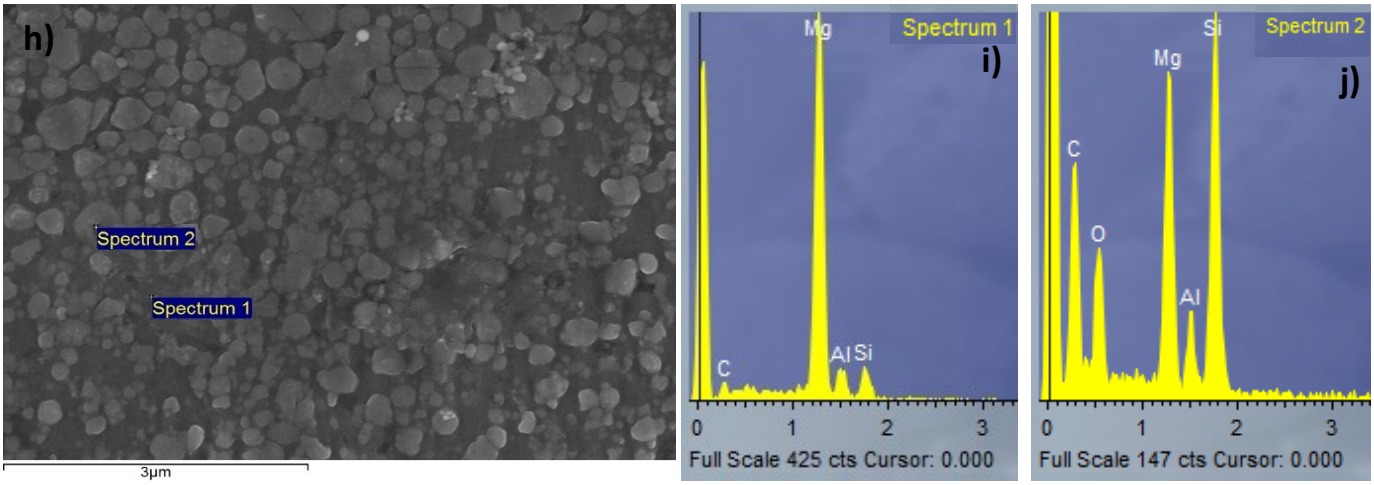

Figure 74. a) and b) show shrinkage porosity in AZ91_T650_S120_0.8SiCnp composite without the presence of SiC nanoparticles.c) and d) show shrinkage porosity found in AZ91_T650_S120_0.8SiCnp composite where a significant amount of unwetted SiC nanoparticles are situated on the surface of the shrinkage porosity suggesting they have been pushed here by a solidification front. e), f) and g) show a higher magnification image of the area highlighted in black in d) and the EDS spectra measured at the highlighted points in e), respectively. h), i) and j) show a higher magnification image of the area highlighted in white in d) and the EDS spectra measured at the highlighted points in h), respectively.

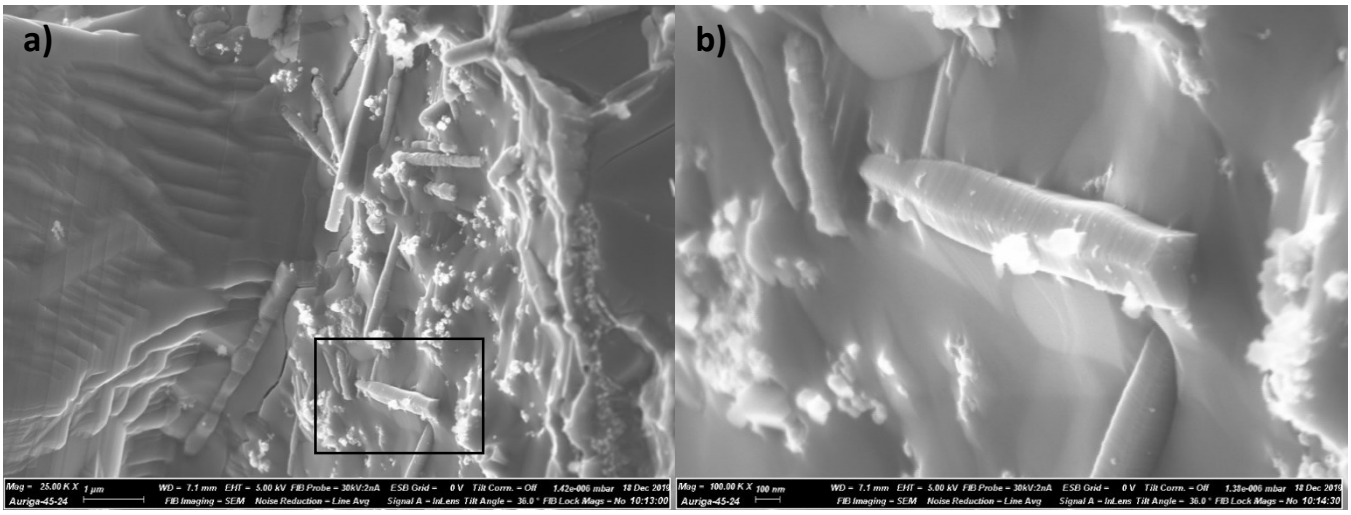

Figure 75. a) and b) SEM images of an internal solidifcation front found in the hammer fracture surface of a AZ91_T650_S120_0.8SiCwh composite, showing a relatively high concentration of SiC whiskers partially embedded, laying parallel to the solid surface, suggesting that they have been pushed here by a solidifcation front.

5 Conclusions and Future Work

This thesis provides methodologies for the fabrication of melt processed MMNCs reinforced with MWCNTs, NiCNTs, SiC whiskers and SiC nanoparticles using a melt stirring technique. The aim of this study was to assess the effectiveness of this fabrication route through the subsequent characterisation of the composites produced and as a result gain a further understanding into the interactions between the nanosized reinforcements and the metal matrix.

It was shown that the mechanical melt stirring utilised was not sufficient to further disperse MWCNTs following a pre-dispersion process, and therefore an alternative method such as ultrasonic-assisted stirring applied directly in metal melt is suggested for future investigation. Melt stirring an unstable metal melt-particle system with the equipment used in this study is most likely to induce nanoparticle re-agglomeration, therefore the wettability of the reinforcing nanoparticle with the metal melt is critical, as highlighted in section 3.2.4. Enhanced wettability of the MWCNTs with the Mg matrix appear to have been achieved by using Ni coated MWCNTs.

AZ91D – SiC whisker composites were produced realising a good distribution of individually wetted SiC whiskers, also achieving up to 20% increase in hardness. Mg alloy – SiC whisker composites are formed almost exclusively in the literature using a squeeze casting technique and a SiC whisker preform, the technique given in this study provides many advantages over squeeze casting in terms of cost effectiveness and scalability and is therefore very much worth investigation. However, this success was not reflected in the AZ91D – SiC nanoparticle composites, most likely due to the larger van der Waals interactions between the SiC nanoparticles than the SiC whiskers and entrapped gas that restricted molten AZ91D infiltration that led to matrix – nanoparticle separation. As a final study in this thesis, theoretical models used for the prediction of the increase in yield strength of MMNCs were used to determine the ideal particle geometry between a whisker or equiaxed shape. It was found that the ideal geometry was dependant on the diameter of the reinforcing particle and the %.vol fraction of ideally dispersed reinforcing particles that can be achieved.

5.1 Mg/AZ91D – MWCNT/NiCNT Composites

The pre-dispersion process was able to deposit some individualised MWCNTs on the Mg/AZ91 chip surface, however, bundles and big agglomerations were still found in the cracks and crevices of the AZ91 chips that would therefore be carried into the metal melt, prior to melt stirring. The bundles and agglomerations exist either because the ultrasonic bath was unable to disperse the bundles or that they have re-agglomerated during the stirring/drying stage of the pre-dispersion method. As large black agglomerates were visible when transferring the dispersion between vessels, it is likely the ultrasonic bath could not fully disperse the MWCNTs. In an attempt to solve this problem, probe sonication was used for MWCNT dispersion instead, as it is able to generate higher intensity cavitation zones than bath sonication [185], however, extensive damage can be bestowed onto the MWCNTs that increases defect density and/or length reduction via tube scission. The effect of the defect density of MWCNTs on the final mechanical properties of the metal composite is unknown and unstudied in the literature.

In addition to probe sonication, to omit the MWCNT reagglomeration that can occur during the stirring/drying stage, a rotary evaporator was used to significantly reduce the time of ethanol evaporation during pre-dispersion. This

process resulted in an enhanced pre-dispersion method, with a much higher proportion of individualised MWCNTs dispersed on the surface of the AZ91D chips. Pre-dispersion provides a 'head-start' in the dispersion process, nevertheless, the build-up of MWCNTs in the cracks and crevices of the AZ91 chips is an inherent symptom of the drying and stirring process. Therefore, a secondary dispersion method is necessary to further disperse the MWCNTs, as well as a method to overcome the instability of MWCNTs in Mg melt as discussed in section 3.2.4, otherwise a homogenous MWCNT dispersion will be incredibly difficult to achieve. Furthermore, the solidification front pushing of MWCNTs during composite solidification need to be equally addressed in order to benefit from the dispersion processes.

Whilst still serving to homogenise the metal melt on a macroscale, it has been calculated that the melt-stirring equipment used in this study does not supply a sufficient shear stress to the melt to de-bundle MWCNT agglomerates. Calculations performed in section 3.2.4 also show that MWCNTs are likely to re-agglomerate on contact due to their poor wettability with the metal melt. With these factors considered, it may be deduced that melt stirring would in fact stimulate MWCNT re-agglomeration.

A large degree of porosity, as much as 5%, is present in the as-cast ingots with shrinkage porosity appearing in the middle and top of the ingots. This characteristic makes the use of tensile testing inappropriate and could still add a high variability to the mechanical properties measured during compression testing, the testing method used as a way of overcoming the porosity issue. Whilst the variability of the as-cast ingots was reduced by using a ceramic plate placed under the permanent steel mould, shrinkage porosity was still present and can have a significant influence on the mechanical properties of the ingot. In this study, to overcome the porosity problem, hardness testing was used instead to investigate composite properties. As hardness testing is inherently highly localised, large variations in mechanical properties due to porosity can be avoided, allowing fairer, although more limited, comparisons to be made.

The compression mechanical properties of the monolithic AZ91 and AZ91-MWCNT composites were not affected in the range of casting temperatures tested. Furthermore, the effect of stirring time and MWCNT concentration appear to have no effect on the final composite mechanical properties. The stirring time appearing to be insignificant could be due to a number of reasons including an insignificant 'actual' MWCNT concentration in the composite due to processing issues such as unwetted MWCNTs that can therefore have no load transferred to them, porosity driven failures that supersede the effects of the nanoparticle additions or the MWCNTs floating to the top of the melt.

The UCS and CYS for all Mg – 0.05-1vol.% NC7000 composites show a slight increase, of up to 21%, when compared to pure Mg. The poor wettability and potential solidification front pushing observed in these composites suggest that the NC7000 MWCNTs would not contribute to the mechanical properties, as no load will be transferred through the poor interface and therefore act as pores instead of reinforcements. O_2 adsorbed onto the surface of the NC7000 MWCNTs and agglomerates could lead to the production of fine MgO particles that are then dispersed within the matrix through melt stirring that are acting as reinforcement instead.

Compression mechanical properties determined for AZ91-NiCNT composites were also found to be extremely similar, however, the hardness testing did in fact show a 13% and 15% improvement for AZ91D-0.8%NiCNT and Mg-0.8%NiCNT, respectively. Due to a significant change in the microstructure of the Mg/AZ91D – 0.8vol.%NiCNT composites, with new intermetallic formations occurring, a change in compression tested mechanical properties would be expected, therefore suggesting that the variation induced by the casting process is too large to detect any changes generated by the NiCNT addition. Unfortunately, due to time constraints of the project, the initial set of AZ91D/Mg – MWCNT composites were not hardness tested. An interesting study would be to hardness test the AZ91D/Mg – MWCNT samples and potentially detect trends in the material hardness that could not be detected by the compression testing.

The poor wettability of MWCNTs by AZ91D/Mg melt, that is apparent from the SEM images of the fracture surfaces in Figure 37, would suggest that in order to take advantage of the superior mechanical properties of MWCNTs, a coherent interface between the MWCNT and the Mg matrix is necessary. NiCNTs were used as a method to overcome this wettability challenge. Whilst signs of enhanced wettability between the AZ91D/Mg matrix and NiCNTs were detected during SEM inspection, the sample preparation technique to polish the surfaces of the MMNCs was devised late in the study and unable to be applied retrospectively to the AZ91D/Mg – MWCNT composites to investigate whether the same morphologies existed for MWCNT composites as did for NiCNT composites. Confirmation that the wetted morphologies do not exist in the AZ91D/Mg – MWCNT composites is required to confirm the enhanced wettability is due to the Ni coating.

5.2 AZ91D – SiC Composites

All of the observed SiC whiskers in the cross section of the AZ91D – SiC whisker composite appeared to be individually wetted by the AZ91D matrix. Whereas in the AZ91D – SiC nanoparticle composite, whilst well wetted nanoparticles were observed, a low amount were observed in the cross section of the composite. Unwetted nanoparticles were also found in shrinkage porosity, showing that the nanoparticles were poorly dispersed, especially compared to the AZ91D – SiC whisker composite. The presence of SiC nanoparticles in the shrinkage porosity shown in Figure 74 and the SiC whiskers laying parallel to a solidification front surface shown in Figure 75 suggest that there is some interaction between an AZ91D solidification front and the reinforcing SiC particles. A qualitative test could be conducted that generates a fast and a slow solidification speed by controlling the preheated temperature of the mould to investigate any impact on the dispersion of the reinforcing particles. Nevertheless, the increase in hardness of the AZ91D – SiC whisker composite is at least in part attributed to the well dispersed and clean interfaces observed between the SiC whiskers and the AZ91D matrix.

An increase in hardness of 11 and 20% was achieved for AZ91D alloy reinforced with SiC nanoparticles and SiC whiskers, respectively. However, it is difficult to exactly confirm the sources of the increase in hardness due to the significant difference in matrix microstructure as a result of the formation of additional Mg_2Si intermetallics in the composite materials when compared to the monolithic material.

Using the current state of the art models used for the prediction of the change of MMNC yield strength with reinforcing particle volume fraction, a whisker and an equiaxed nanoparticle were compared in order to understand what the ideal nanoparticle geometry for maximising yield strength is. It was shown that for whiskers and equiaxed particles with a diameter of 20nm and equal mechanical properties, in the %.vol region of 0-2%, equiaxed particles show the greatest strengthening potential. However, above 2%.vol, the whisker shape shows the greatest strengthening potential due to load transfer to whisker particles becoming the dominant strengthening mechanism. As the reinforcing particle diameter increases, the total strengthening potential decreases due to increased interparticle distance and load transfer becomes the dominant strengthening mechanism above particle %.vol of approximately 0.4%.vol. As more effective dispersion methods are developed, this study could aid with developing MMNCs by giving guidance on the most effective reinforcing particle to use to maximise mechanical properties. This work could be expanded to also consider 2D platelets, where graphene could be used as the reinforcement during experimental validation and compared to MWCNTs.

5.3 Future work

Suggestions for future work mainly revolve around the metal casting and nanoparticle dispersion processes used in this study in the form of improvements to experimental methodologies and equipment and complementary investigations.

The porosity observed in the as cast samples could have had a significant influence on the measured compression mechanical properties of the samples, if not at least the variance. Enhancing the quality of the as-cast material could be achieved by using a redesigned metal mould that makes use of classic mould design elements such as sprues, runners, risers, gates and bottom filling, as demonstrated in the ASTM B108 mould. However, a mould of this design would have to be carefully considered when adapting it to the volumes of melt that can be currently processed (~150g) to avoid filling issues. Alternative methods to omit porosity effects could include secondary processes such as hot rolling, that could be employed to aid in closing/reducing the shrinkage porosity found in the as-cast ingots. Hot rolling is a popular process that is also used in industry, it also provides a wealth of research opportunity into how the addition of nanoparticles can impact upon dynamic recrystallisation and induced texture, potentially valuable and relatively unexplored topics.

This study used Ar – 2% H_2 and Ar gas to provide an inert atmosphere for the molten metal processing, however, as the rig used was not air tight a constant source of O_2 was available to the Mg melt for oxidation which is then exacerbated by the porous nature of MgO, that allows further oxidation instead of building a protective layer. In order to achieve a high-quality Mg melt in an open system, a cover gas is essential. Traditionally in industry and academia, SF_6 gas is used that does indeed form a protective layer of MgF on the surface of the melt, however, the industrial use of SF_6 has recently been banned in the EU due to its extremely high global warming potential. Instead, alternative cover gases have been proposed and used with success, namely Novec 612.

Whilst the enhanced pre-dispersion method showed a much higher proportion of individualised MWCNTs dispersed on the metal chip surfaces, agglomerates were still present. Ultrasonic treatments that required to fully individualise

a sample of MWCNTs may require far too much time and resources to be practical. Therefore, to further enhance the pre-dispersion step, another potential solution would be to add a centrifugation step to remove a high proportion of the large agglomerates, however, this would require measuring the concentration of the supernatant to have a good estimate of the real concentration of MWCNTs in the final composite.

NiCNT agglomerates were found not being fully infiltrated and whilst improvements in hardness were measured, further testing is required to account for the change in hardness induced by interstitial Ni atoms and/or Mg_2Ni intermetallic formation as precipitants. A control sample could be made by measuring the composition of the composite matrix to determine the wt.% of Mg_2Ni and adding the appropriate amount of raw Ni to produce similar samples in which the reinforcing particles are absent.

The AZ91 composites reinforced with SiC whiskers showed a high degree of wetting between the matrix and whisker, making it very interesting system to study. Different volume loadings and geometries can be used to explore the different strengthening mechanisms used to model composite mechanical strength. Figure 72f shows an interesting scenario worth investigation, where whiskers offer a higher strengthening efficiency than equal diameter nanoparticles above a given .vol%. If SiC coated MWCNTs could be produced, being a similar dimension to available SiC nanoparticles, they could provide an exciting opportunity to explore the theoretical scenarios presented in Figure 72.

MMNC's have the potential to offer a step change in material properties with far reaching applications. There exist two main challenges in their melt processed manufacture; homogenous nanoparticle dispersion and nanoparticle wettability. Where homogenous nanoparticle dispersion maximises the strengthening potential, and nanoparticle wettability ensures load can be transferred to the nanoparticle as well as potentially allowing the nanoparticle dispersion to be maintained through solidification. By calculating that the melt stirring equipment would not provide sufficient shear force to disperse MWCNTs, another method for MWCNT dispersion in a metal melt is therefore required. To address the challenge of dispersion, ultrasonic-assisted stirring could supply the required shear stresses for nanoparticle dispersion in metal melt and could produce homogenously dispersed MWCNT-metal melt systems. To address the wettability challenge, Ni coated MWCNTs were used in this study with evidence of enhanced metal melt wettability and therefore offer an exciting avenue for future work.

6 References

1. *Reducing emissions from aviation*. 2015 [cited 2019 09/04/2019]; Available from: https://ec.europa.eu/clima/policies/transport/aviation_en.
2. *Challenges and Opportunities for Composite Materials Transitions in Aerospace.* in *ECCM18*. 2018. Aerospace Technology Institute.
3. Hinrich Helms, U.L., *The Potential Contribution of Light-Weighting to Reduce Transport Energy Consumption.* International Journal of Life Cycle Assessment, 2007.
4. Liu, G., Zhang, G. J., Jiang, F., Ding, X. D., Sun, Y. J., Sun, J. & Ma, E. (2013) Nanostructured high-strength molybdenum alloys with unprecedented tensile ductility. Nature Materials. 12 (4), 344-350. Available from: doi: 10.1038/nmat3544.
5. Chen, L., Xu, J., Choi, H., Pozuelo, M., Ma, X., Bhowmick, S., Yang, J., Mathaudhu, S. & Li, X. (2015) Processing and properties of magnesium containing a dense uniform dispersion of nanoparticles. Nature (London). 528 (7583), 539-543. Available from: doi: 10.1038/nature16445.
6. Kelton, K. and A.L. Greer, *Nucleation in condensed matter: applications in materials and biology*. Vol. 15. 2010: Elsevier.
7. Polmear, I.J., *Light alloys: Metallurgy of the light metals*. Third Edition ed. 1995, Londom: Arnold.
8. Polmear, I.J., *Light Alloys: From Traditional Alloys to Nanocrystals*. Fourth edition ed. 2006: Butterworth-Heinemann.
9. A. A. Luo, K., Sadayappan, *Technology for Magnesium Castings*. 2011, Schaumburg, IL USA: American Foundry Society.
10. Unal, O. & Tiryakioglu, M. (2015) On the ductility potential and assessment of structural quality in Mg alloy castings. Materials Science & Engineering. A, Structural Materials : Properties, Microstructure and Processing. 643 51-54. Available from: doi: 10.1016/j.msea.2015.07.003.
11. Mihriban O Pekguleryuz, K.K., A. Arslan Kaya, *Fundamentals of Magnesium Alloy Metallurgy*. 2013: Woodhead Publishing.
12. Wonsiewicz, B.C., *Plasticity of magnesium crystals*. 1966, Massachusetts Institute of Technology.
13. Taylor, G.I.J.J.I.M., *Plastic strain in metals.* 1938. 62: p. 307-324.
14. Kumar, A., Kumar, S. & Mukhopadhyay, N. K. (2018) Introduction to magnesium alloy processing technology and development of low-cost stir casting process for magnesium alloy and its composites. Journal of Magnesium and Alloys. 6 (3), 245-254. Available from: doi: 10.1016/j.jma.2018.05.006.
15. Dieringa, H. (2011) Properties of magnesium alloys reinforced with nanoparticles and carbon nanotubes: a review. Journal of Materials Science. 46 (2), 289-306. Available from: doi: 10.1007/s10853-010-5010-6.
16. Luo, A., Pekguleryuz, M.O. (1994) Cast magnesium alloys for elevated temperature applications. J Mater Sci 29, 5259–5271. Available from doi:10.1007/BF01171534
17. Pekguleryuz, M.O., *Development of Creep Resistant Magnesium Diecasting Alloys.* Materials Science Forum, 2000. 350-351: p. 131-140.
18. Mo, N., Tan, Q., Bermingham, M., Huang, Y., Dieringa, H., Hort, N. & Zhang, M. (2018) Materials and design. Materials and Design. 155 422-442. Available from: doi:10.1016/j.matdes.2018.06.032
19. Dieringa, H., et al., *Advances in manufacturing processes for magnesium alloys.* Magnesium Technology 2007, 2007: p. 19.
20. Philip L. Walker, P.A.T., *Chemistry and Physics of Carbon*. Vol. 14. 1978: Marcel Dekker Inc.
21. Iijima, S. & Ichihashi, T. (1993) Single-shell carbon nanotubes of 1-nm diameter. Nature. 363 (6430), 603-605. Available from: doi: 10.1038/363603a0.
22. Kroto, H. W., Heath, J. R., O'Brien, S. C., Curl, R. F. & Smalley, R. E. (1985) C 60 : Buckminsterfullerene. Nature. 318 (6042), 162-163. Available from: doi: 10.1038/318162a0.

23. Thostenson, E. T., Ren, Z. & Chou, T. (2001) Advances in the science and technology of carbon nanotubes and their composites: a review. Composites Science and Technology. 61 (13), 1899-1912. Available from: doi: 10.1016/S0266-3538(01)00094-X.
24. Yu, M. F., Lourie, O., Dyer, M. J., Moloni, K., Kelly, T. F. & Ruoff, R. S. (2000) Strength and breaking mechanism of multiwalled carbon nanotubes under tensile load. Science (New York, N.Y.). 287 (5453), 637-640. Available from: doi: 10.1126/science.287.5453.637.
25. Tjong, S.C., *Carbon Nanotube Reinforced Composites: Metal and Ceramic Matrices*. 2009: Wiley-VCH Verlag GmbH & Co.
26. Treacy, M. M. J., Gibson, J. M. & Ebbesen, T. W. (1996) Exceptionally high Young's modulus observed for individual carbon nanotubes. Nature (London). 381 (6584), 678-680. Available from: doi: 10.1038/381678a0.
27. Laurent, C., Flahaut, E. & Peigney, A. (2010) The weight and density of carbon nanotubes versus the number of walls and diameter. Carbon. 48 (10), 2994-2996. Available from: doi: 10.1016/j.carbon.2010.04.010.
28. Beke, D., Szekrényes, Z., Balogh, I., Czigány, Z., Kamarás, K. & Gali, A. (2013) Preparation of small silicon carbide quantum dots by wet chemical etching. Journal of Materials Research. 28 (1), 44-49. Available from: doi: 10.1557/jmr.2012.223.
29. Aldrich, S. *Silicon Carbide nanopowder, <100 nm particle size*. 2020 18/04/2020]; Available from: https://www.sigmaaldrich.com/catalog/product/aldrich/594911?lang=en&region=GB.
30. Kelsall, R.W., *Silicon-Based Nanomaterials: Technology and Applications*. 2019: Multidisciplinary Digital Publishing Institute.
31. haydale. *About Haydale*. 2020 18/04/2020]; Available from: https://haydale.com/about-haydale/.
32. Deng, K. K., Wu, K., Wu, Y. W., Nie, K. B. & Zheng, M. Y. (2010) Effect of submicron size SiC particulates on microstructure and mechanical properties of AZ91 magnesium matrix composites. Journal of Alloys and Compounds. 504 (2), 542-547. Available from: doi: 10.1016/j.jallcom.2010.05.159.
33. Zheng, M. Y., Wu, K., Kamado, S. & Kojima, Y. (2003) Aging behavior of squeeze cast SiCw/AZ91 magnesium matrix composite. Materials Science and Engineering: A. 348 (1), 67-75. Available from: doi: 10.1016/S0921-5093(02)00638-X.
34. Zheng, M., Wu, K. & Yao, C. (2001) Effect of interfacial reaction on mechanical behavior of SiCw/AZ91 magnesium matrix composites. Materials Science and Engineering: A. 318 (1), 50-56. Available from: doi: 10.1016/S0921-5093(01)01338-7.
35. Chen, L., Xu, J., Choi, H., Pozuelo, M., Ma, X., Bhowmick, S., Yang, J., Mathaudhu, S. & Li, X. (2015) Processing and properties of magnesium containing a dense uniform dispersion of nanoparticles. Nature (London). 528 (7583), 539-543. Available from: doi: 10.1038/nature16445.
36. D. Hull, D.J.B., *Dislocations*. Fifth Edition ed. 2011: Elsevier.
37. Orowan, E., *Zur Kristallplastizitt. III.* Zeitschrift fr Physik, 1934. **89**(9-10): p. 634-659.
38. Li, Q., Viereckl, A., Rottmair, C. A. & Singer, R. F. (2009) Composites science and technology. 69 (7), 1193-1199. Available from: doi: 10.1016/j.compscitech.2009.02.020
39. Tjong, S. C. (2013) Recent progress in the development and properties of novel metal matrix nanocomposites reinforced with carbon nanotubes and graphene nanosheets. Materials Science and Engineering: R: Reports. 74 (10), 281-350. Available from: doi: 10.1016/j.mser.2013.08.001.
40. Kelly, P. M. (1972) The effect of particle shape on dispersion hardening. Scripta Metallurgica. 6 (8), 647-656. Available from: doi: 10.1016/0036-9748(72)90120-2.
41. Chen, B., Shen, J., Ye, X., Jia, L., Li, S., Umeda, J., Takahashi, M. & Kondoh, K. (2017) Length effect of carbon nanotubes on the strengthening mechanisms in metal matrix composites. Acta Materialia. 140 317-325. Available from: doi: https://doi.org/10.1016/j.actamat.2017.08.048.
42. Miller, W.S. and F.J. Humphreys, *Strengthening Mechanisms in Particulate Metal Matrix Composites.* Scripta Metallurgica Et Materialia, 1991. **25**(1): p. 33-38.

43. Uozumi, H., Kobayashi, K., Nakanishi, K., Matsunaga, T., Shinozaki, K., Sakamoto, H., Tsukada, T., Masuda, C. & Yoshida, M. (2008) Fabrication process of carbon nanotube/light metal matrix composites by squeeze casting. Materials Science and Engineering: A. 495 (1), 282-287. Available from: https://doi.org/10.1016/j.msea.2007.11.088.
44. Smith, S.W., (1951) *Surface Tension of Liquid Metals.* Nature. **168**(4269): p. 343-344. Available from: https://doi.org/10.1038/168343b0
45. Dujardin, E., et al., (1994) *Capillarity and Wetting of Carbon Nanotubes.* Science. **265**(5180): p. 1850-1852. Available from: doi: 10.1126/science.265.5180.1850
46. Cox, H. L. (1952) The elasticity and strength of paper and other fibrous materials. British Journal of Applied Physics. 3 (3), 72–79. Available from: doi: 10.1088/0508-3443/3/3/302.
47. Kelly, A. & Tyson, W. R. (1965) Tensile properties of fibre-reinforced metals: Copper/tungsten and copper/molybdenum. Journal of the Mechanics and Physics of Solids. 13 (6), 329-350. Available from: doi: https://doi.org/10.1016/0022-5096(65)90035-9.
48. Ryu, H. J., Cha, S. I. & Hong, S. H. (2003) Generalized shear-lag model for load transfer in SiC/Al metal-matrix composites. Journal of Materials Research. 18 (12), 2851-2858. Available from: doi: 10.1557/JMR.2003.0398.
49. Park, J. G., Keum, D. H. & Lee, Y. H. (2015) Strengthening mechanisms in carbon nanotube-reinforced aluminum composites. Carbon. 95 690-698. Available from: doi: https://doi.org/10.1016/j.carbon.2015.08.112.
50. Zhou, W., Yamamoto, G., Fan, Y., Kwon, H., Hashida, T. & Kawasaki, A. (2016) In-situ characterization of interfacial shear strength in multi-walled carbon nanotube reinforced aluminum matrix composites. Carbon. 106 37-47. Available from: doi: https://doi.org/10.1016/j.carbon.2016.05.015.
51. Kurita, H., Estili, M., Kwon, H., Miyazaki, T., Zhou, W., Silvain, J. & Kawasaki, A. (2015) Load-bearing contribution of multi-walled carbon nanotubes on tensile response of aluminum. Composites Part A: Applied Science and Manufacturing. 68 133-139. Available from: doi: https://doi.org/10.1016/j.compositesa.2014.09.014.
52. Zhou, W., Bang, S., Kurita, H., Miyazaki, T., Fan, Y. & Kawasaki, A. (2016) Interface and interfacial reactions in multi-walled carbon nanotube-reinforced aluminum matrix composites. Carbon. 96 919-928. Available from: doi: https://doi.org/10.1016/j.carbon.2015.10.016.
53. Yi, C., Chen, X., Gou, F., Dmuchowski, C. M., Sharma, A., Park, C. & Ke, C. (2017) Direct measurements of the mechanical strength of carbon nanotube - Aluminum interfaces. Carbon. 125 93-102. Available from: doi: https://doi.org/10.1016/j.carbon.2017.09.020.
54. Zhang, Z. & Chen, D. L. (2008) Contribution of Orowan strengthening effect in particulate-reinforced metal matrix nanocomposites. Materials Science and Engineering: A. 483-484 148-152. Available from: doi: https://doi.org/10.1016/j.msea.2006.10.184.
55. Zhang, Z. & Chen, D. L. (2006) Consideration of Orowan strengthening effect in particulate-reinforced metal matrix nanocomposites: A model for predicting their yield strength. Scripta Materialia. 54 (7), 1321-1326. Available from: doi: https://doi.org/10.1016/j.scriptamat.2005.12.017.
56. Hansen, N. (1977) The effect of grain size and strain on the tensile flow stress of aluminium at room temperature. Acta Metallurgica. 25 (8), 863-869. Available from: doi: https://doi.org/10.1016/0001-6160(77)90171-7.
57. Arsenault, R. J. & Shi, N. (1986) Dislocation generation due to differences between the coefficients of thermal expansion. Materials Science and Engineering. 81 175-187. Available from: doi: https://doi.org/10.1016/0025-5416(86)90261-2.
58. Taya, M., Arsenault, R. J *Metal Matrix Composites: Thermomechanical behavior*. First Edition ed. 1989: Pergamon Press.
59. Dong, S., Zhou, J., Hui, D., Wang, Y. & Zhang, S. (2015) Size dependent strengthening mechanisms in carbon nanotube reinforced metal matrix composites. Composites Part A: Applied Science and Manufacturing. 68 356-364. Available from: doi: https://doi.org/10.1016/j.compositesa.2014.10.018.

60. Vogt, R., Zhang, Z., Li, Y., Bonds, M., Browning, N. D., Lavernia, E. J. & Schoenung, J. M. (2009) The absence of thermal expansion mismatch strengthening in nanostructured metal–matrix composites. Scripta Materialia. 61 (11), 1052-1055. Available from: doi: https://doi.org/10.1016/j.scriptamat.2009.08.025.
61. Baig, Z., Mamat, O. & Mustapha, M. (2018) Recent Progress on the Dispersion and the Strengthening Effect of Carbon Nanotubes and Graphene-Reinforced Metal Nanocomposites: A Review. Null. 43 (1), 1-46. Available from: doi: 10.1080/10408436.2016.1243089.
62. Bakshi, S. R., Lahiri, D. & Agarwal, A. (2010) Carbon nanotube reinforced metal matrix composites - a review. Null. 55 (1), 41-64. Available from: doi: 10.1179/095066009X12572530170543..
63. Munir, K. S., Kingshott, P. & Wen, C. (2015) Carbon Nanotube Reinforced Titanium Metal Matrix Composites Prepared by Powder Metallurgy—A Review. Null. 40 (1), 38-55. Available from: doi: 10.1080/10408436.2014.929521.
64. Hall, E. O. (1951) The Deformation and Ageing of Mild Steel: III Discussion of Results. Proceedings of the Physical Society. Section B. 64 (9), 747–753. Available from: doi: 10.1088/0370-1301/64/9/303.
65. Yuan, Q., Zeng, X., Liu, Y., Luo, L., Wu, J., Wang, Y. & Zhou, G. (2016) Microstructure and mechanical properties of AZ91 alloy reinforced by carbon nanotubes coated with MgO. Carbon. 96 843-855. Available from: doi: https://doi.org/10.1016/j.carbon.2015.10.018.
66. Thangaraju, S., Heilmaier, M., Murty, B. S. & Vadlamani, S. S. (2012) On the Estimation of True Hall–Petch Constants and Their Role on the Superposition Law Exponent in Al Alloys. Advanced Engineering Materials. 14 (10), 892-897. Available from: doi: 10.1002/adem.201200114.
67. Choi, H. J., Kim, Y., Shin, J. H. & Bae, D. H. (2010) Deformation behavior of magnesium in the grain size spectrum from nano- to micrometer. Materials Science and Engineering: A. 527 (6), 1565-1570. Available from: doi: https://doi.org/10.1016/j.msea.2009.10.035.
68. Kim, W. T. & Cantor, B. (1992) Solidification behaviour of Pb droplets embedded in a Cu matrix. Acta Metallurgica Et Materialia. 40 (12), 3339-3347. Available from: doi: https://doi.org/10.1016/0956-7151(92)90047-I.
69. Kim, W. T. & Cantor, B. (1994) Heterogeneous nucleation of Al2Cu in Al•Cu eutectic liquid droplets embedded in an al matrix. Acta Metallurgica Et Materialia. 42 (9), 3045-3053. Available from: doi: https://doi.org/10.1016/0956-7151(94)90401-4.
70. Quested, T. E. (2004) Understanding mechanisms of grain refinement of aluminium alloys by inoculation. Null. 20 (11), 1357-1369. Available from: doi: 10.1179/026708304225022359.
71. de Cicco, M. P., Turng, L., Li, X. & Perepezko, J. H. (2011) Nucleation Catalysis in Aluminum Alloy A356 Using Nanoscale Inoculants. Metallurgical and Materials Transactions A. 42 2323-2330. Available from: doi: 10.1007/s11661-011-0607-1.
72. Günther, R., Hartig, C. & Bormann, R. (2006) Grain refinement of AZ31 by (SiC)P: Theoretical calculation and experiment. Acta Materialia. 54 (20), 5591-5597. Available from: doi: https://doi.org/10.1016/j.actamat.2006.07.035.
73. Novikov, V. Y. (2000) On zener pinning in 3-D polycrystals. Scripta Materialia. 42 (5), 439-443. Available from: doi: https://doi.org/10.1016/S1359-6462(99)00379-6.
74. Rohrer, G.S. (1948) “Introduction to Grains, Phases, and Interfaces—an Interpretation of Microstructure” Trans. AIME, vol. 175, pp. 15–51, by C.S. Smith. Metall Mater Trans A 41, 1063–1100. Available from https://doi.org/10.1007/s11661-010-0215-5.
75. Mokhtari, O., Roshanghias, A., Ashayer, R. et al. (2012) Disabling of Nanoparticle Effects at Increased Temperature in Nanocomposite Solders. Journal of Elec Materi 41, 1907–1914. Available from https://doi.org/10.1007/s11664-012-1976-y
76. Han, G., Wang, Z., Liu, K., Li, S., Du, X. & Du, W. (2015) Synthesis of CNT-reinforced AZ31 magnesium alloy composites with uniformly distributed CNTs. Materials Science and Engineering: A. 628 350-357. Available from: doi: https://doi.org/10.1016/j.msea.2015.01.039.

77. Morisada, Y., Fujii, H., Nagaoka, T. & Fukusumi, M. (2006) MWCNTs/AZ31 surface composites fabricated by friction stir processing. Materials Science and Engineering: A. 419 (1), 344-348. Available from: doi: https://doi.org/10.1016/j.msea.2006.01.016.
78. Sanaty-Zadeh, A. (2012) Comparison between current models for the strength of particulate-reinforced metal matrix nanocomposites with emphasis on consideration of Hall–Petch effect. Materials Science and Engineering: A. 531 112-118. Available from: doi: https://doi.org/10.1016/j.msea.2011.10.043.
79. Hull, D. and T.W. Clyne, *An introduction to composite materials*. 1996: Cambridge university press.
80. Goh, C. S., Wei, J., Lee, L. C. & Gupta, M. (2007) Properties and deformation behaviour of Mg–Y2O3 nanocomposites. Acta Materialia. 55 (15), 5115-5121. Available from: doi: https://doi.org/10.1016/j.actamat.2007.05.032.
81. Ramakrishnan, N. (1996) An analytical study on strengthening of particulate reinforced metal matrix composites. Acta Materialia. 44 (1), 69-77. Available from: doi: https://doi.org/10.1016/1359-6454(95)00150-9.
82. Nardone, V. C. & Prewo, K. M. (1986) On the strength of discontinuous silicon carbide reinforced aluminum composites. Scripta Metallurgica. 20 (1), 43-48. Available from: doi: https://doi.org/10.1016/0036-9748(86)90210-3.
83. Nardone, V. C. (1987) Assessment of models used to predict the strength of discontinous silicon carbide reinforced aluminum alloys. Scripta Metallurgica. 21 (10), 1313-1318. Available from: doi: https://doi.org/10.1016/0036-9748(87)90105-0.
84. Mirza, F.A. and D.L. Chen, (2015*) Unified Model for the Prediction of Yield Strength in Particulate-Reinforced Metal Matrix Nanocomposites.* Materials (Basel),. **8**(8): p. 5138-5153. Available from: https://doi.org/10.3390/ma8085138
85. Li, J.C.M., (1963) *Citation Classic - Petch Relation and Grain-Boundary Sources.* Current Contents/Engineering Technology & Applied Sciences, (49): p. 16-16.
86. Mirza, F. A. & Chen, D. L. (2012) An Analytical Model for Predicting the Yield Strength of Particulate-Reinforced Metal Matrix Nanocomposites with Consideration of Porosity. Nanoscience and Nanotechnology Letters. 4 (8), 794-800. Available from: doi: 10.1166/nnl.2012.1394.
87. Goh, C. S., Wei, J., Lee, L. C. & Gupta, M. (2005) Development of novel carbon nanotube reinforced magnesium nanocomposites using the powder metallurgy technique. Nanotechnology. 17 (1), 7–12. Available from: https://doi.org/10.1088/0957-4484/17/1/002.
88. Goh, C. S., Wei, J., Lee, L. C. & Gupta, M. (2006) Effect of Fabrication Techniques on the Properties of Carbon Nanotubes Reinforced Magnesium. Solid State Phenomena. 111 179-182. Available from: doi: 10.4028/www.scientific.net/SSP.111.179.
89. Goh, C. S., Wei, J., Lee, L. C. & Gupta, M. (2006) Simultaneous enhancement in strength and ductility by reinforcing magnesium with carbon nanotubes. Materials Science and Engineering: A. 423 (1), 153-156. Available from: doi: https://doi.org/10.1016/j.msea.2005.10.071.
90. W. D. Callister, D.G.R., *Materials Science and Engineering*. Eighth Edition ed. 2011: Wiley.
91. Bohlen, J., Letzig, D. & Kainer, K. U. (2007) New Perspectives for Wrought Magnesium Alloys. Materials Science Forum. 546-549 1-10. Available from: doi: 10.4028/www.scientific.net/MSF.546-549.1.
92. Cui, Y., Li, Y., Sun, S., Bian, H., Huang, H., Wang, Z., Koizumi, Y. & Chiba, A. (2015) Enhanced damping capacity of magnesium alloys by tensile twin boundaries. Scripta Materialia. 101 8-11. Available from: doi: https://doi.org/10.1016/j.scriptamat.2015.01.002.
93. Huang, Y. Y. & Terentjev, E. M. (2012) Dispersion of carbon nanotubes: Mixing, sonication, stabilization, and composite properties. Polymers. 4 275-295. Available from: http://publications.eng.cam.ac.uk/444861/.
94. Han, G., Du, W., Ye, X., Liu, K., Du, X., Wang, Z. & Li, S. (2017) Compelling mechanical properties of carbon nanotubes reinforced pure magnesium composite by effective interface bonding of Mg2Ni.

Journal of Alloys and Compounds. 727 963-969. Available from: doi: https://doi.org/10.1016/j.jallcom.2017.08.133.
95. Morsi, K., Esawi, A. (2007) Effect of mechanical alloying time and carbon nanotube (CNT) content on the evolution of aluminum (Al)–CNT composite powders. J Mater Sci 42, 4954–4959. Available from: https://doi.org/10.1007/s10853-006-0699-y
96. Hashim, J., Looney, L. & Hashmi, M. S. J. (1999) Metal matrix composites: production by the stir casting method. Journal of Materials Processing Technology. 92-93 1-7. Available from: doi: https://doi.org/10.1016/S0924-0136(99)00118-1.
97. Zeng, X., Zhou, G., Xu, Q., Xiong, Y., Luo, C. & Wu, J. (2010) A new technique for dispersion of carbon nanotube in a metal melt. Materials Science and Engineering: A. 527 (20), 5335-5340. Available from: doi: https://doi.org/10.1016/j.msea.2010.05.005.
98. Li, Q., Rottmair, C. A. & Singer, R. F. (2010) CNT reinforced light metal composites produced by melt stirring and by high pressure die casting. Composites Science and Technology. 70 (16), 2242-2247. Available from: doi: https://doi.org/10.1016/j.compscitech.2010.05.024.
99. Lan, J., Yang, Y. & Li, X. (2004) Microstructure and microhardness of SiC nanoparticles reinforced magnesium composites fabricated by ultrasonic method. Materials Science and Engineering: A. 386 (1), 284-290. Available from: doi: https://doi.org/10.1016/j.msea.2004.07.024.
100. Barbosa, J., Puga, H. (2019) Ultrasonic Melt Treatment of Light Alloys. Inter Metalcast 13, 180–189. Available from: https://doi.org/10.1007/s40962-018-0248-x
101. Eskin, G. (1997) Principles of Ultrasonic Treatment: Application for Light Alloys Melts. Advanced Performance Materials 4, 223–232. Available from: https://doi.org/10.1023/A:1008603815525
102. Dieringa H. (2018) Processing of Magnesium-Based Metal Matrix Nanocomposites by Ultrasound-Assisted Particle Dispersion: A Review. Metals.; 8(6):431. Available from: https://doi.org/10.3390/met8060431
103. Chen, L., Peng, J., Xu, J., Choi, H. & Li, X. (2013) Achieving uniform distribution and dispersion of a high percentage of nanoparticles in metal matrix nanocomposites by solidification processing. Scripta Materialia. 69 (8), 634-637. Available from: doi: https://doi.org/10.1016/j.scriptamat.2013.07.016.
104. Wang, Z., Wang, X., ZHAO, Y. & DU, W. (2010) SiC nanoparticles reinforced magnesium matrix composites fabricated by ultrasonic method. Transactions of Nonferrous Metals Society of China. 20 s1029-s1032. Available from: doi: https://doi.org/10.1016/S1003-6326(10)60625-5.
105. Liu, S., Gao, F., Zhang, Q., Zhu, X. & LI, W. (2010) Fabrication of carbon nanotubes reinforced AZ91D composites by ultrasonic processing. Transactions of Nonferrous Metals Society of China. 20 (7), 1222-1227. Available from: doi: https://doi.org/10.1016/S1003-6326(09)60282-X.
106. Zhang, L., Eskin, D.G. & Katgerman, L. (2011) Influence of ultrasonic melt treatment on the formation of primary intermetallics and related grain refinement in aluminum alloys. J Mater Sci 46, 5252–5259. Avaialble from: https://doi.org/10.1007/s10853-011-5463-2
107. Pasumarthi, P., Absar, S. & Choi, H. (2016) The effect of geometrical parameters on the characteristics of ultrasonic processing for metal matrix nanocomposites (MMNCs). Journal of Manufacturing Processes. 24 382-390. Available from: doi: https://doi.org/10.1016/j.jmapro.2016.06.019.
108. Bang, J. H. & Suslick, K. S. (2010) Applications of Ultrasound to the Synthesis of Nanostructured Materials. Advanced Materials. 22 (10), 1039-1059. Available from: doi: 10.1002/adma.200904093.
109. Yusa, M., Mathur, G. P. & Stager, R. A. (1977) Viscosity and compression of ethanol-water mixtures for pressures up to 40,000 psig. Journal of Chemical & Engineering Data. 22 (1), 32-35. Available from: https://doi.org/10.1021/je60072a020.
110. Culpin, M. F. (1957) The Viscosity of Liquid Magnesium and Liquid Calcium. Proceedings of the Physical Society. Section B. 70 (11), 1079–1086. Available from: doi: 10.1088/0370-1301/70/11/308.
111. Eskin, G.I., *Ultrasonic Treatment of Light Alloy Metallic Melts*. 1998, The Netherlands: Gordon and Breach Science Publishers.

112. Ruirun, C., Deshuang, Z., Tengfei, M., Hongsheng, D., Yanqing, S., Jingjie, G. & Hengzhi, F. (2017) Effects of ultrasonic vibration on the microstructure and mechanical properties of high alloying TiAl. Scientific Reports. 7 (1), 41463. Available from: doi: 10.1038/srep41463.
113. Song, S., Zhou, X., Li, L. & Ma, W. (2015) Numerical simulation and experimental validation of SiC nanoparticle distribution in magnesium melts during ultrasonic cavitation based processing of magnesium matrix nanocomposites. Ultrasonics Sonochemistry. 24 43-54. Available from: doi: https://doi.org/10.1016/j.ultsonch.2014.12.010.
114. Li, X. & Xu, J. (2018) 6.5 Metal Matrix Nanocomposites. In: Beaumont, P. W. R. & Zweben, C. H. (eds.). Comprehensive Composite Materials II. [e-book] Oxford, Elsevier. pp. 97-137. Available from: https://www.sciencedirect.com/science/article/pii/B9780128035818100281.
115. Xu, J. Q., Chen, L. Y., Choi, H. & Li, X. C. (2012) Theoretical study and pathways for nanoparticle capture during solidification of metal melt. Journal of Physics: Condensed Matter. 24 (25), 255304.. Available from: doi: 10.1088/0953-8984/24/25/255304.
116. Visser, J. (1972) On Hamaker constants: A comparison between Hamaker constants and Lifshitz-van der Waals constants. Advances in Colloid and Interface Science. 3 (4), 331-363. Available from: doi: https://doi.org/10.1016/0001-8686(72)85001-2.
117. Fadavi Boostani, A., Tahamtan, S., Yazdani, S., Khosroshahi, R. A., Wei, D., Sahamirad, H., Zhang, X. M. & Jiang, Z. Y. (2016) Graphene tweaking Hamaker constant of SiC nanoparticles: A new horizon to solve the conflict between strengthening and toughening. Scripta Materialia. 118 65-69. Available from: doi: https://doi.org/10.1016/j.scriptamat.2016.02.028.
118. Chen, X. J., Levi, A. C. & Tosatti, E. (1991) Hamaker constant calculations and surface melting of metals. Surface Science. 251-252 641-644. Available from: doi: https://doi.org/10.1016/0039-6028(91)91070-E.
119. Xiang, S., Wang, X., Gupta, M., Wu, K., Hu, X. & Zheng, M. (2016) Graphene nanoplatelets induced heterogeneous bimodal structural magnesium matrix composites with enhanced mechanical properties. Scientific Reports. 6 (1), 38824. Available from: doi: 10.1038/srep38824.
120. Israelachvili, J.N., *Intermolecular and Surface Forces*. 2011.
121. Médout-Marère, V., Partyka, S., Dutartre, R., Chauveteau, G. & Douillard, J. M. (2003) Surface heterogeneity of passively oxidized silicon carbide particles: vapor adsorption isotherms. Journal of Colloid and Interface Science. 262 (2), 309-320. Available from: doi: 10.1016/S0021-9797(03)00198-X.
122. Egerton, R.F., *Electron Energy-Loss Spectroscopy in the Electron Microscope*. 2011.
123. Yao, Y., Xu, Z., Sugio, K., Choi, Y., Kang, S., Fu, R. & Sasaki, G. (2015) Nickel Formation on Graphite Sheet Surface for Improving Wettability with Magnesium Alloy. Materials Transactions. 56 (10), 1693-1697. Available from: doi: 10.2320/matertrans.MAW201506.
124. Ip, S. W., Sridhar, R., Toguri, J. M., Stephenson, T. F. & Warner, A. E. M. (1998) Wettability of nickel coated graphite by aluminum. Materials Science and Engineering: A. 244 (1), 31-38. Available from: doi: https://doi.org/10.1016/S0921-5093(97)00823-X.
125. Rams, J., Ureña, A., Escalera, M. D. & Sánchez, M. (2007) Electroless nickel coated short carbon fibres in aluminium matrix composites. Composites Part A: Applied Science and Manufacturing. 38 (2), 566-575. Available from: doi: https://doi.org/10.1016/j.compositesa.2006.02.010.
126. Nasiri, S., Wang, K., Yang, M. et al. (2019) Nickel coated carbon nanotubes in aluminum matrix composites: a multiscale simulation study. Eur. Phys. J. B 92, 186. Available from: https://doi.org/10.1140/epjb/e2019-100243-6
127. Stein, J., Lenczowski, B., Anglaret, E. & Fréty, N. (2014) Influence of the concentration and nature of carbon nanotubes on the mechanical properties of AA5083 aluminium alloy matrix composites. Carbon. 77 44-52. Available from: doi: https://doi.org/10.1016/j.carbon.2014.05.001.
128. Jiang, L., Li, Z., Fan, G., Cao, L. & Zhang, D. (2012) The use of flake powder metallurgy to produce carbon nanotube (CNT)/aluminum composites with a homogenous CNT distribution. Carbon. 50 (5), 1993-1998. Available from: doi: https://doi.org/10.1016/j.carbon.2011.12.057.

129. Fan, G., Jiang, Y., Tan, Z., Guo, Q., Xiong, D., Su, Y., Lin, R., Hu, L., Li, Z. & Zhang, D. (2018) Enhanced interfacial bonding and mechanical properties in CNT/Al composites fabricated by flake powder metallurgy. Carbon. 130 333-339. Available from: doi: https://doi.org/10.1016/j.carbon.2018.01.037.
130. Xu, R., Tan, Z., Xiong, D., Fan, G., Guo, Q., Zhang, J., Su, Y., Li, Z. & Zhang, D. (2017) Balanced strength and ductility in CNT/Al composites achieved by flake powder metallurgy via shift-speed ball milling. Composites Part A: Applied Science and Manufacturing. C (96), 57-66. Available from: doi: 10.1016/j.compositesa.2017.02.017.
131. Xiang, S., Wang, X., Gupta, M., Wu, K., Hu, X. & Zheng, M. (2016) Graphene nanoplatelets induced heterogeneous bimodal structural magnesium matrix composites with enhanced mechanical properties. Scientific Reports. 6 (1), 38824. Available from: doi: 10.1038/srep38824.
132. Munir, K. S., Zheng, Y., Zhang, D., Lin, J., Li, Y. & Wen, C. (2017) Microstructure and mechanical properties of carbon nanotubes reinforced titanium matrix composites fabricated via spark plasma sintering. Materials Science and Engineering: A. 688 505-523. Available from: doi: https://doi.org/10.1016/j.msea.2017.02.019.
133. Kónya, Z., Zhu, J., Niesz, K., Mehn, D. & Kiricsi, I. (2004) End morphology of ball milled carbon nanotubes. Carbon. 42 (10), 2001-2008. Available from: doi: https://doi.org/10.1016/j.carbon.2004.03.040.
134. Ghasemi, A., Penther, D. & Kamrani, S. (2018) Microstructure and nanoindentation analysis of Mg-SiC nanocomposite powders synthesized by mechanical milling. Materials Characterization. 142 137-143. Available from: doi: https://doi.org/10.1016/j.matchar.2018.05.023.
135. Fukuda, H., Kondoh, K., Umeda, J. & Fugetsu, B. (2011) Interfacial analysis between Mg matrix and carbon nanotubes in Mg–6wt.% Al alloy matrix composites reinforced with carbon nanotubes. Composites Science and Technology. 71 (5), 705-709. Available from: doi: https://doi.org/10.1016/j.compscitech.2011.01.015.
136. Shimizu, Y., Miki, S., Soga, T., Itoh, I., Todoroki, H., Hosono, T., Sakaki, K., Hayashi, T., Kim, Y. A., Endo, M., Morimoto, S. & Koide, A. (2008) Multi-walled carbon nanotube-reinforced magnesium alloy composites. Scripta Materialia. 58 (4), 267-270. Available from: doi: https://doi.org/10.1016/j.scriptamat.2007.10.014.
137. Nai, M.H., J. Wei, and M. Gupta, Interface tailoring to enhance mechanical properties of carbon nanotube reinforced magnesium composites. Materials & Design, 2014. 60: p. 490-495.
138. Miettinen, J. (2008) Thermodynamic description of Cu–Mg–Ni and Cu–Mg–Zn systems. Calphad. 32 (2), 389-398. Available from: doi: https://doi.org/10.1016/j.calphad.2008.03.005.
139. Quang, P., Jeong, Y. G., Yoon, S. C., Hong, S. H. & Kim, H. S. (2007) Consolidation of 1vol.% carbon nanotube reinforced metal matrix nanocomposites via equal channel angular pressing. Journal of Materials Processing Technology. 187-188 318-320. Available from: doi: https://doi.org/10.1016/j.jmatprotec.2006.11.116.
140. Srivatsan, T.S., Godbole, C., Paramsothy, M. et al. (2012) Influence of nano-sized carbon nanotube reinforcements on tensile deformation, cyclic fatigue, and final fracture behavior of a magnesium alloy. J Mater Sci 47, 3621–3638. Available from: https://doi.org/10.1007/s10853-011-6209-x
141. Goh, C. S., Wei, J., Lee, L. C. & Gupta, M. (2008) Ductility improvement and fatigue studies in Mg-CNT nanocomposites. Composites Science and Technology. 68 (6), 1432-1439. Available from: doi: https://doi.org/10.1016/j.compscitech.2007.10.057.
142. Paramsothy M, Hassan SF, Srikanth N, Gupta M. (2010) Simultaneous enhancement of tensile/compressive strength and ductility of magnesium alloy AZ31 using carbon nanotubes. J Nanosci Nanotechnol. 956-64. Available from: doi: 10.1166/jnn.2010.1809.
143. Paramsothy, M., Tan, X. H., Chan, J., Kwok, R. & Gupta, M. (2013) Carbon nanotube addition to concentrated magnesium alloy AZ81: Enhanced ductility with occasional significant increase in strength. Materials & Design. 45 15-23. Available from: https://doi.org/10.1016/j.matdes.2012.09.001.

144. Arab, M., Marashi, S.P.H. (2018) Graphene Nanoplatelet (GNP)-Incorporated AZ31 Magnesium Nanocomposite: Microstructural, Mechanical and Tribological Properties. Tribol Lett 66, 156. Available from: https://doi.org/10.1007/s11249-018-1108-9
145. Asadi, P., Faraji, G., Masoumi, A. et al. Experimental Investigation of Magnesium-Base Nanocomposite Produced by Friction Stir Processing: Effects of Particle Types and Number of Friction Stir Processing Passes. (2011) Metall Mater Trans A 42, 2820–2832. Available from: https://doi.org/10.1007/s11661-011-0698-8
146. Asadi, P., Faraji, G. & Besharati, M.K. (2010) Producing of AZ91/SiC composite by friction stir processing (FSP). Int J Adv Manuf Technol 51, 247–260. Available from: https://doi.org/10.1007/s00170-010-2600-z
147. Faraji, G. & Asadi, P. (2011) Characterization of AZ91/alumina nanocomposite produced by FSP. Materials Science and Engineering: A. 528 (6), 2431-2440. Available from: doi: https://doi.org/10.1016/j.msea.2010.11.065.
148. Chen, L., Konishi, H., Fehrenbacher, A., Ma, C., Xu, J., Choi, H., Xu, H., Pfefferkorn, F. E. & Li, X. (2012) Novel nanoprocessing route for bulk graphene nanoplatelets reinforced metal matrix nanocomposites. Scripta Materialia. 67 (1), 29-32. Available from: doi: https://doi.org/10.1016/j.scriptamat.2012.03.013.
149. Thakur, S.K., Kwee, G.T. & Gupta, M. (2007) Development and characterization of magnesium composites containing nano-sized silicon carbide and carbon nanotubes as hybrid reinforcements. J Mater Sci 42, 10040–10046. Available from: https://doi.org/10.1007/s10853-007-2004-0
150. Carreño-Morelli, E., Yang, J., Couteau, E., Hernadi, K., Seo, J. W., Bonjour, C., Forró, L. & Schaller, R. (2004) Carbon nanotube/magnesium composites. Physica Status Solidi (a). 201 (8), R53-R55. Available from: doi: 10.1002/pssa.200409045.
151. Yuan, Q., Fu, D., Zeng, X. & Liu, Y. (2017) Fabrication of carbon nanotube reinforced AZ91D composite with superior mechanical properties. Transactions of Nonferrous Metals Society of China. 27 (8), 1716-1724. Available from: doi: https://doi.org/10.1016/S1003-6326(17)60194-8.
152. Nourbakhsh, S.H., et al., *Investigation of mechanical and microstructural properties of AZ31/SiC nanocomposite fabricated by squeeze stir casting.* Materials Research Express, 2018. **5**(8).
153. Ferkel, H. and B.L. Mordike, *Magnesium strengthened by SiC nanoparticles.* Materials Science and Engineering a-Structural Materials Properties Microstructure and Processing, 2001. **298**(1-2): p. 193-199.
154. Luo, A., Pekguleryuz, M.O. (1994) Cast magnesium alloys for elevated temperature applications. J Mater Sci 29, 5259–5271. Available from: https://doi.org/10.1007/BF01171534
155. Luo, A.A., *Recent magnesium alloy development for elevated temperature applications.* International Materials Reviews, 2004. **49**(1): p. 13-30.
156. Haghshenas, M. & Gupta, M. (2019) Magnesium nanocomposites: An overview on time-dependent plastic (creep) deformation. Defence Technology. 15 (2), 123-131. Available from: doi: https://doi.org/10.1016/j.dt.2018.08.008.
157. Kassner, M.E., *Fundamentals of creep in metals and alloys*. 2015: Butterworth-Heinemann.
158. Dieter, G.E. and D.J. Bacon, *Mechanical metallurgy*. Vol. 3. 1986: McGraw-hill New York.
159. Somekawa, H., Hirai, K., Watanabe, H., Takigawa, Y. & Higashi, K. (2005) Dislocation creep behavior in Mg–Al–Zn alloys. Materials Science and Engineering: A. 407 (1), 53-61. Available from: doi: https://doi.org/10.1016/j.msea.2005.06.059.
160. Maruyama, K., Suzuki, M. & Sato, H. (2002) Creep strength of magnesium-based alloys. Metall and Mat Trans A 33, 875–882. Available from: https://doi.org/10.1007/s11661-002-1020-6
161. Gupta, M. and S.N.M. Ling, *Magnesium, magnesium alloys, and magnesium composites*. 2011: John Wiley & Sons.
162. Mordike, B. L. (2001) Development of highly creep resistant magnesium alloys. Journal of Materials Processing Technology. 117 (3), 391-394. Available from: doi: https://doi.org/10.1016/S0924-0136(01)00793-2.

163. Sandlöbes, S., Friák, M., Korte-Kerzel, S., Pei, Z., Neugebauer, J. & Raabe, D. (2017) A rare-earth free magnesium alloy with improved intrinsic ductility. Scientific Reports. 7 (1), 1-8. Available from: doi: 10.1038/s41598-017-10384-0.
164. Mahajan, A., Kingon, A., Kukovecz, Á, Konya, Z. & Vilarinho, P. M. (2013) Studies on the thermal decomposition of multiwall carbon nanotubes under different atmospheres. Materials Letters. 90 165-168. Available from: doi: https://doi.org/10.1016/j.matlet.2012.08.120.
165. Katsarou, L., Mounib, M., Lefebvre, W., Vorozhtsov, S., Pavese, M., Badini, C., Molina-Aldareguia, J. M., Jimenez, C. C., Pérez Prado, M. T. & Dieringa, H. (2016) Microstructure, mechanical properties and creep of magnesium alloy Elektron21 reinforced with AlN nanoparticles by ultrasound-assisted stirring. Materials Science and Engineering: A. 659 84-92. Available from: doi: https://doi.org/10.1016/j.msea.2016.02.042.
166. Michael Avedesian, H.B., *ASM Specialty Handbook : Magnesium and Magnesium Alloys*. 1998, Ohio: ASM INTERNATIONAL.
167. Chen, B., Kondoh, K., Imai, H., Umeda, J. & Takahashi, M. (2016) Simultaneously enhancing strength and ductility of carbon nanotube/aluminum composites by improving bonding conditions. Scripta Materialia. 113 158-162. Available from: doi: https://doi.org/10.1016/j.scriptamat.2015.11.011.
168. Hutchinson, W. B. & Barnett, M. R. (2010) Effective values of critical resolved shear stress for slip in polycrystalline magnesium and other hcp metals. Scripta Materialia. 63 (7), 737-740. Available from: doi: https://doi.org/10.1016/j.scriptamat.2010.05.047.
169. *Rotavapor® R-300 Convenient and efficient rotary evaporation*. 2020 [cited 2020 13/04/2020]; Available from: https://www.buchi.com/gb-en/products/laboratory-evaporation/rotavapor-r-300.
170. *VCX 500 / VCX 750 Ultrasonic Processors for Small and Medium Volume Applications*. 2020 [cited 2020 13/04/2020]; Available from: https://www.sonics.com/liquid-processing/products/vibra-cell-processors/vcx-500-vcx-750/.
171. Ross, R.B., *Metallic materials specification handbook*. Fourth Edition ed. 1992, Glasgow: Chapman & Hall.
172. Nicolas Eustathopoulus, M.G.N., Béatrice Drevet, *Wettability at High Temperatures*, ed. R.W. Cahn. Vol. 3. 1999: Elsevier Science Ltd.
173. Nuriel, S., Liu, L., Barber, A. H. & Wagner, H. D. (2005) Direct measurement of multiwall nanotube surface tension. Chemical Physics Letters. 404 (4), 263-266. Available from: doi: https://doi.org/10.1016/j.cplett.2005.01.072.
174. Hashim, J., Looney, L. & Hashmi, M. S. J. (2001) The enhancement of wettability of SiC particles in cast aluminium matrix composites. Journal of Materials Processing Technology. 119 (1), 329-335. Available from: doi: https://doi.org/10.1016/S0924-0136(01)00919-0.
175. Zhang, D., Shen, P., Shi, L., Lin, Q. & Jiang, Q. (2010) Wetting and evaporation behaviors of molten Mg on partially oxidized SiC substrates. Applied Surface Science. 256 (23), 7043-7047. Available from: doi: https://doi.org/10.1016/j.apsusc.2010.05.022.
176. Liang, J., Li, H., Qi, L., Tian, W., Li, X., Zhou, J., Wang, D. & Wei, J. (2016) Influence of Ni-CNTs additions on the microstructure and mechanical properties of extruded Mg-9Al alloy. Materials Science and Engineering: A. 678 101-109. Available from: doi: https://doi.org/10.1016/j.msea.2016.09.089.
177. H. E. Friedrich, B.L.M., *Magnesium Technology - Metallurgy, Design Data, Applications*. 2006, Germany: Springer.
178. Petrovic, J.J., Milewski, J.V., Rohr, D.L. et al. (1985) Tensile mechanical properties of SiC whiskers. J Mater Sci 20, 1167–1177. Available from: https://doi.org/10.1007/BF01026310
179. Yoo, S. J., Han, S. H. & Kim, W. J. (2013) Strength and strain hardening of aluminum matrix composites with randomly dispersed nanometer-length fragmented carbon nanotubes. Scripta Materialia. 68 (9), 711-714. Available from: doi: https://doi.org/10.1016/j.scriptamat.2013.01.013.
180. Dynacast. *AZ91D*. 2019 20/11/2019 [cited 2020 07/01/2020]; Available from: https://www.dynacast.co.uk/az91d.

181. Harris, G.L., *Properties of Silicon Carbide*, ed. G.L. Harris. 1995, London: INSPEC, the Institution of Electrical Engineers.
182. A. J. Dolata, M.D., *Light Metals and their Alloys II - Technology, Microstructure and Properties*. 2012, Switzerland: Trans Tech Publications Ltd.
183. Srinivasan, A., Ajithkumar, K. K., Swaminathan, J., Pillai, U. T. S. & Pai, B. C. (2013) Creep Behavior of AZ91 Magnesium Alloy. Procedia Engineering. 55 109-113. Available from: https://doi.org/10.1016/j.proeng.2013.03.228.
184. Shi, L., Shen, P., Zhang, D. & Jiang, Q. (2011) Wetting and evaporation behaviors of molten Mg–Al alloy drops on partially oxidized α-SiC substrates. Materials Chemistry and Physics. 130 (3), 1125-1133. Available from: doi: https://doi.org/10.1016/j.matchemphys.2011.08.051.
185. Hugo Miguel Santos, C.L., Prof. José-Luis Capelo-Martínez, *The Power of Ultrasound*, in *Ultrasound in Chemistry*, J. Capelo-Martínez, Editor. 2009, Wiley-VCH Verlag GmbH & Co. KGaA.

7 Appendix

A.1 Crucible dimensions

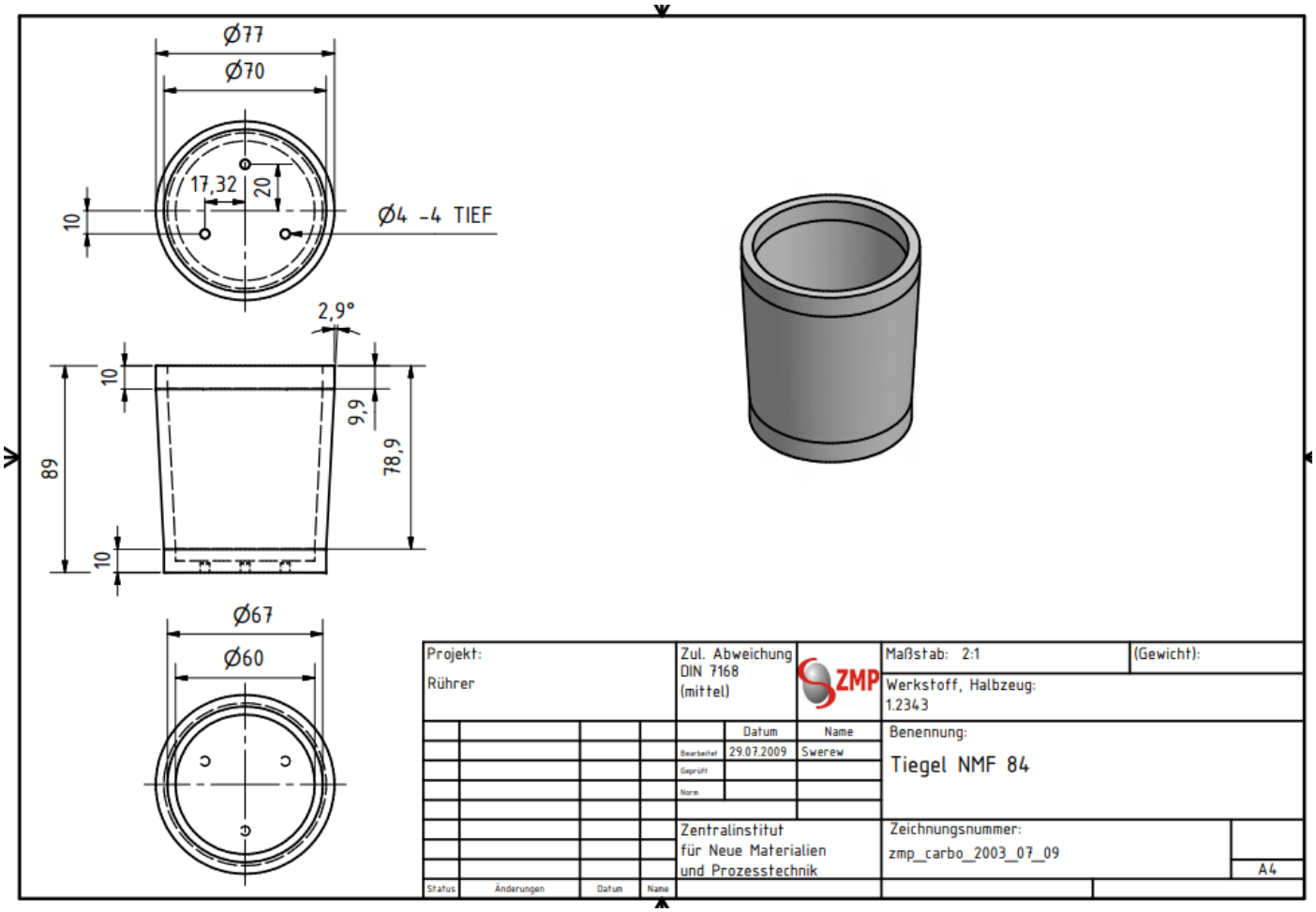

Figure A1. H13 tool steel crucible used in the presented study.

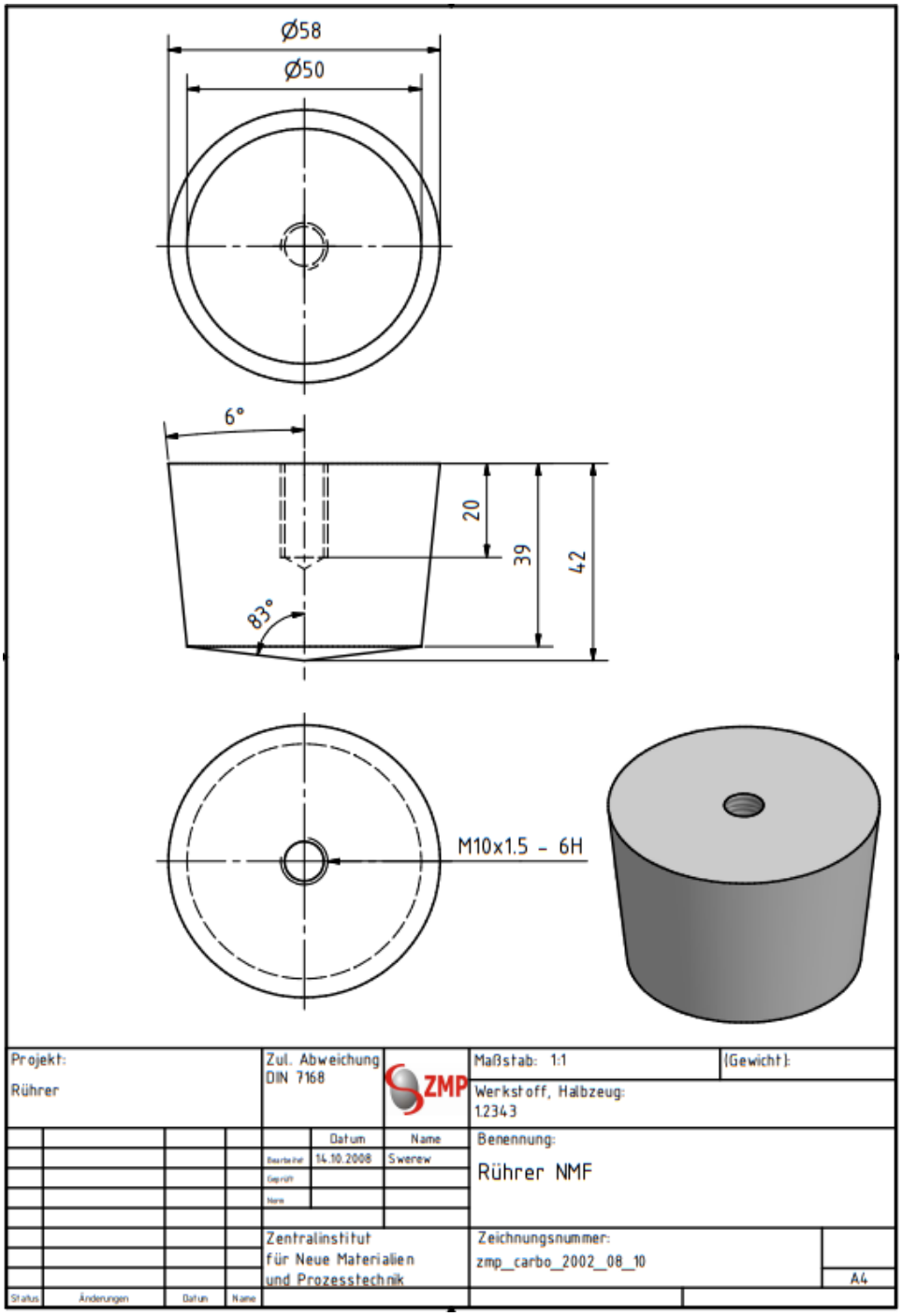

Figure A1.1. Melt stirring head dimensions used in the presented study.

A.2 AZ91D – MWCNT

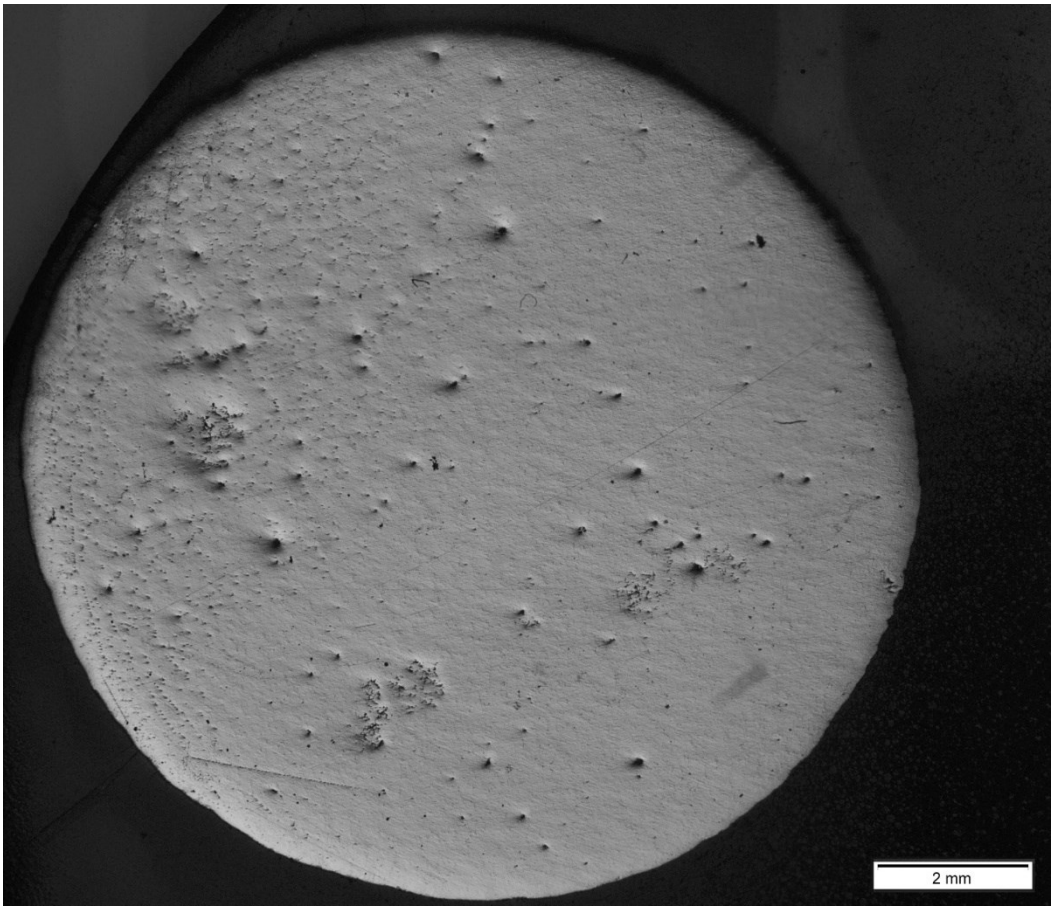

Figure A 1. Polishing cross section taken from the middle of a cylindrical as-cast ingot showing gas and shrinkage porosities.

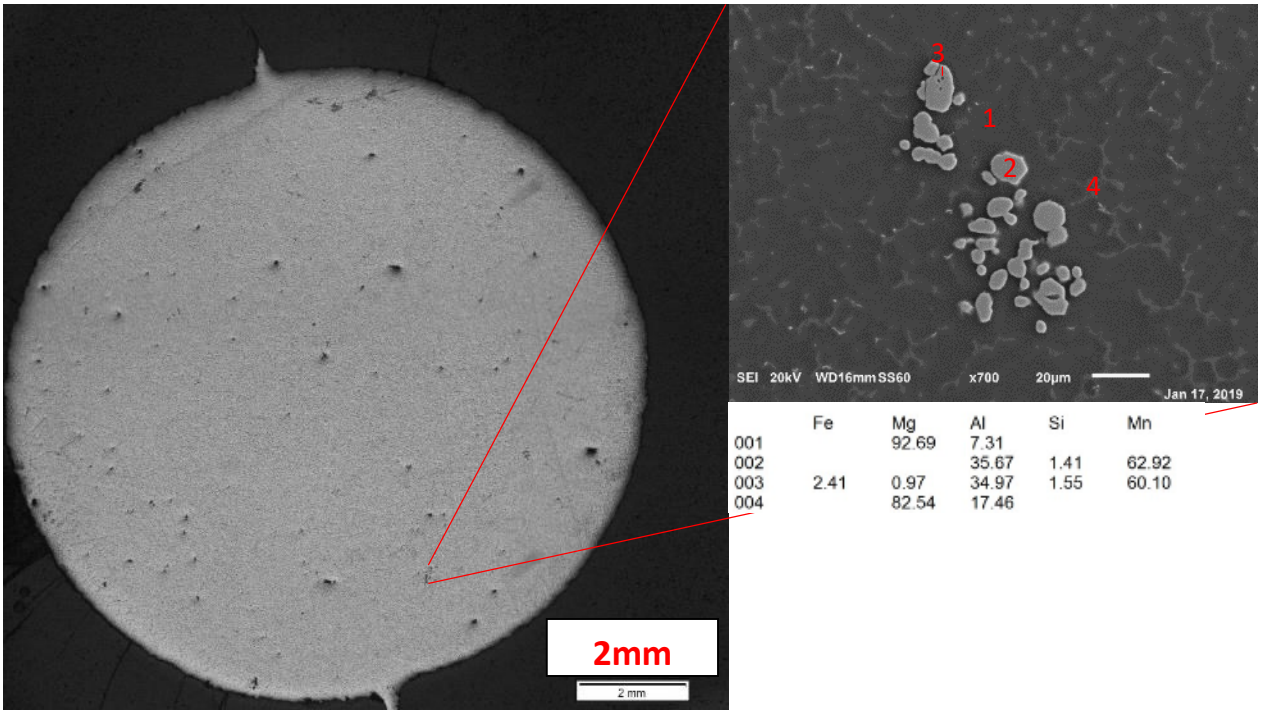

Figure A 2. Al_8Mn_5 intermetallic found in the as-cast AZ91 microstructure.

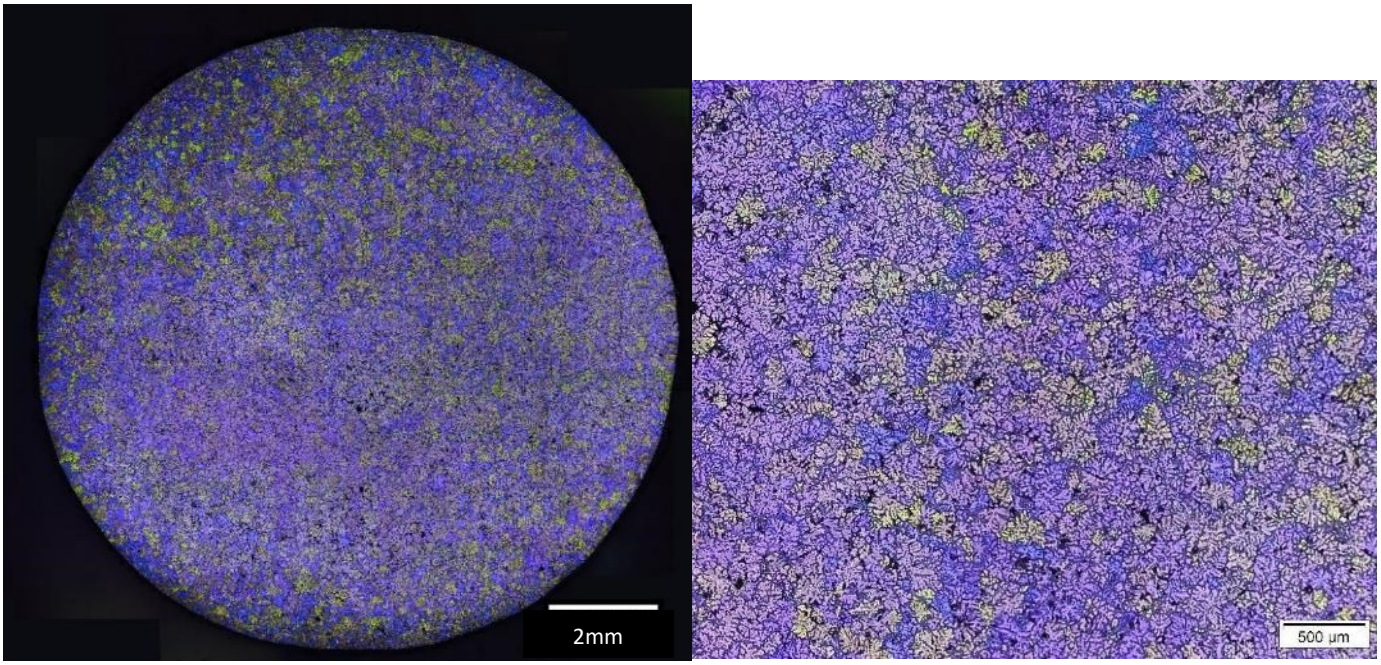

Figure A2.1. Colour etched cross section of the top of an as-cast ingot showing a dendritic grain structure.

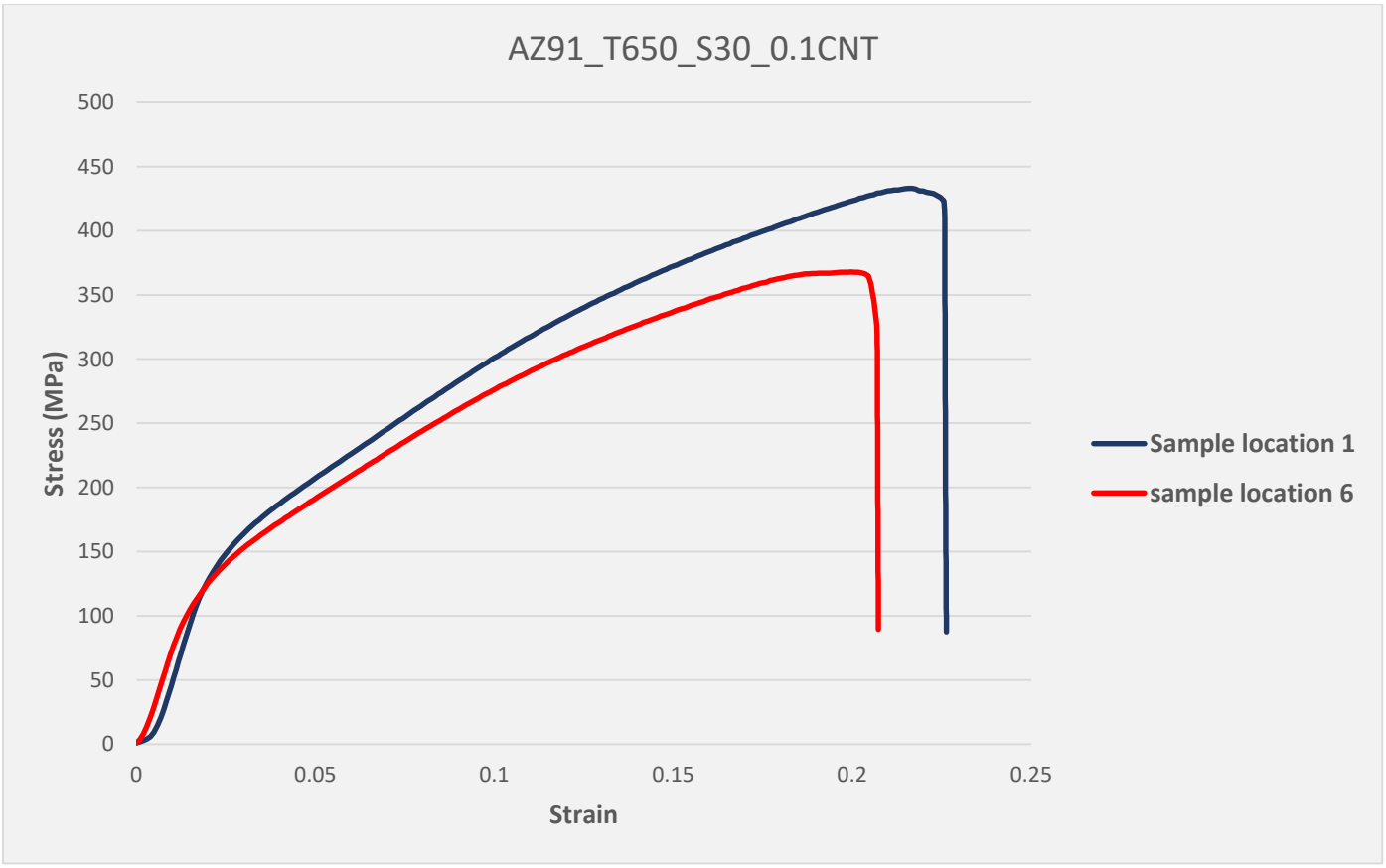

Figure A2.2. Stress strain curves for samples taken from the same casting but from different positions within the casting. Sample location 1 is taken from the bottom of the casting, whilst sample 6 is taken from the middle.

A.3 Predicted increase in tensile yield strength curves

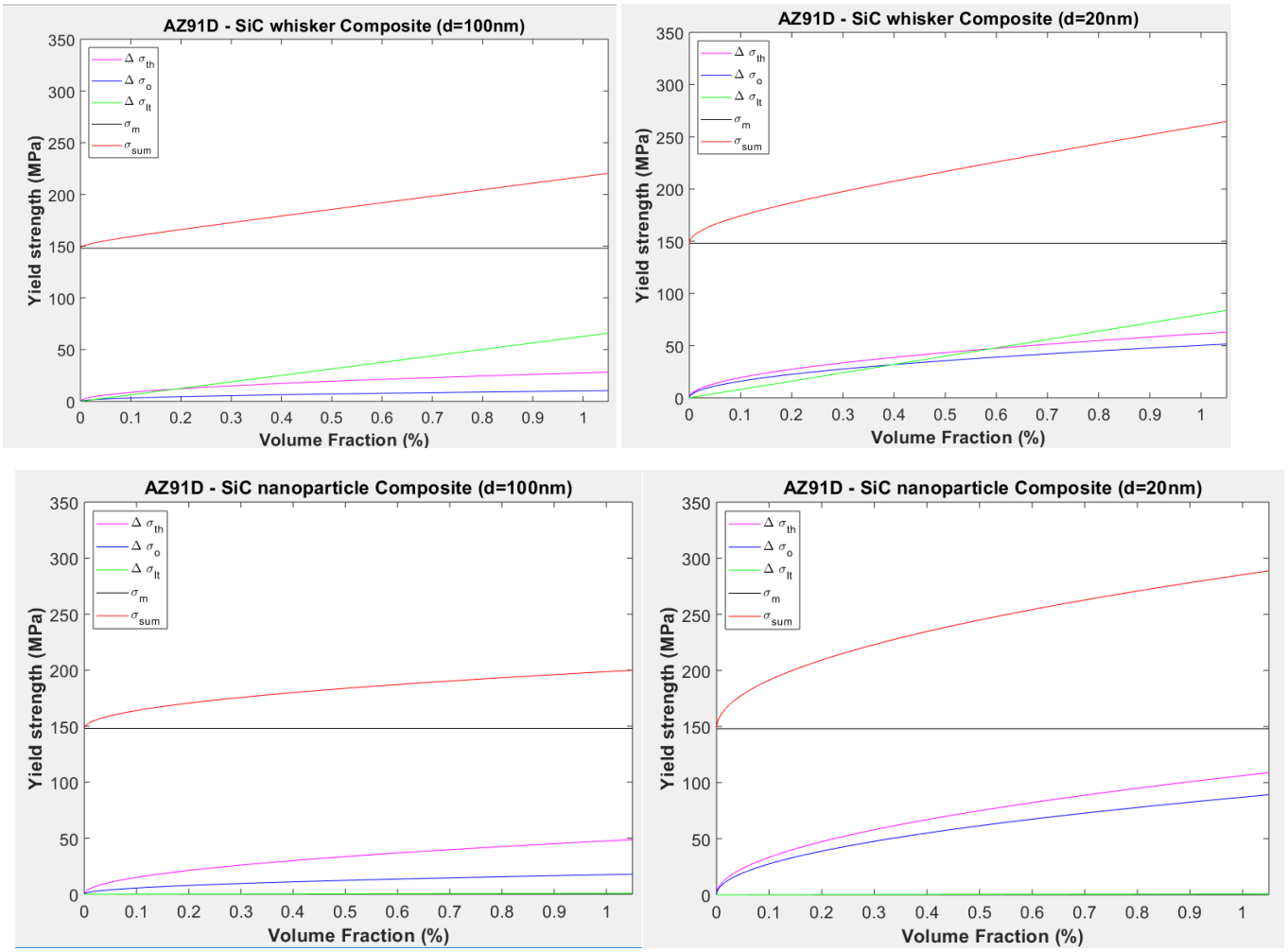

Figure A3. Theoretical yield strength increase for a AZ91D-MMNC using the models presented in

Table 13 for a) AZ91D-SiCwh 100nm, b) AZ91D–SiCwh 20nm, c) AZ91D–SiCnp 100nm composites and d AZ91D–SiCnp 20nm composites.